AD

AD-A221 692

E-GUN TECHNOLOGY

FINAL TECHNICAL REPORT

J. E. Eninger, H. W. Friedman and K. E. Williams

AVCO EVERETT RESEARCH LABORATORY, INC.

Contract No. DAAK40–78–C–0127

July 1981

sponsored by

DEFENSE ADVANCED RESEARCH PROJECTS AGENCY
DARPA Order No. 3498

Approved for public release; distribution unlimited

The views and conclusions in this document are those of the authors and should not be interpreted as necessarily representing the official policies, either expressed or implied, of the Defense Advanced Research Projects Agency or the U. S. Government.

90 05 18 101

E-GUN TECHNOLOGY

Final Technical Report

J.E. Eninger, H.W. Friedman and K.E. Williams

AVCO EVERETT RESEARCH LABORATORY, INC.
A Subsidiary of Avco Corporation
2385 Revere Beach Parkway
Everett, MA 02149

Accession For
NTIS GRA&I
DTIC TAB
Unannounced
Justification
By
Distribution/
Availability Codes
Avail and/or
Dist Special
A-1

Contract No. DAAK40-78-C-0127

July 1981

prepared for

DEFENSE ADVANCED RESEARCH PROJECTS AGENCY
DEPARTMENT OF DEFENSE

and

monitored by

U.S. Army Missile Command
Redstone Arsenal, AL 35809

DTIC COPY INSPECTED 4

Approved for public release; distribution unlimited.

TABLE OF CONTENTS

Section		Page
	List of Illustrations	vii
I.	INTRODUCTION AND EXECUTIVE SUMMARY	I-1
	A. Background	I-1
	B. Program Objectives	I-2
	C. Experimental Approach	I-2
	D. Experimental Results	I-4
	1. Cold Cathodes	I-4
	2. Photoemissive Cathodes	I-9
	3. Small Area Thermionic Cathodes	I-13
	4. Large Area Thermionic Cathodes	I-13
	5. Foil Cooling	I-22
	E. Conclusions and Recommendations	I-22
	Section I - References	I-29
II.	TECHNICAL BACKGROUND	II-1
	A. Introduction	II-1
	1. Cathode Technology	II-1
	2. E-Beam Window Technology	II-3
	3. Guide Magnetic Fields	II-3
	B. Field Emitting Cathodes	II-5
	1. Diode Closure	II-5
	2. Loss of Emission Sites	II-14
	3. Emission Site Density	II-19
	4. Fast Beam Current Density Fluctuation	II-21
	C. Photoelectric Cathodes	II-31
	1. Photoelectric E-Gun Efficiency	II-36
	2. Flashlamp Shields	II-38
	D. Thermionic Cathodes	II-42
	1. General	II-42
	2. Dispenser Type Cathodes	II-49

Section		Page
	E. Magnetic Fields	II-60
	1. Beam Pinching	II-60
	2. Guide Magnetic Field	II-63
	F. E-Beam Windows	II-72
	1. Foil Heating and Cooling	II-72
	2. Foil Window Design	II-96
	Section II - References	II-109
III.	DESCRIPTION OF EXPERIMENTAL APPARATUS AND TECHNIQUES	III-1
	A. Single-Pulse Apparatus	III-1
	B. Repetitively-Pulsed E-Gun Facility	III-7
	1. Line Pulser System	III-7
	2. Vacuum Chamber	III-14
	C. Field Emission Cathodes	III-21
	1. Tantalum Blade Cathode	III-21
	2. Carbon Felt Cathodes	III-21
	D. Photoemissive Cathodes	III-27
	E. Small Area Thermionic Cathodes	III-32
	F. Large Area Thermionic Cathodes	III-36
	G. Foil and Foil Support Structure (Repped Facility)	III-41
IV.	EXPERIMENTAL RESULTS	IV-1
	A. Tantalum Blade Cathodes	IV-1
	B. Carbon Felt Cathodes	IV-6
	C. Photoemissive Cathodes	IV-11
	D. Small Area Dispenser Cathodes	IV-17
	1. Cathode Activation	IV-17
	2. Beam Expansion	IV-18
	3. Magnetic Field Effects	IV-23
	4. No Diode Closure	IV-23
	5. Comparison of Cathode Performance	IV-23

Section	Page
E. Large Area Dispenser Cathodes	IV-28
1. Spatial Uniformity	IV-38
2. Repped Testing	IV-44
3. Outgassing	IV-48
F. Foil Testing	IV-48
G. Gas Poisoning Tests	IV-52
Section IV References	IV-55

LIST OF ILLUSTRATIONS

Figure		Page
I-1	AERL-DARPA E-Gun Test Facility	I-3
I-2	Cathode Array Using Tantalum Blades with Outgassing Capability	I-5
I-3	Effect of Cathode Outgassing on Diode Closure Characteristics of a Tantalum Blade, Cold Cathode Array	I-6
I-4	Current Density Distribution with Guide Magnetic Fields for a Tantalum Blade, Cold Cathode Array	I-7
I-5	Random Emission Sites "Grown" along the Edge of a 1/2 mil Tantalum Blade after 75 (Single Shot) Pulses	I-8
I-6	Carbon Felt Cold Cathode	I-10
I-7	Felt Cathode Diode Closure vs Magnetic Field	I-11
I-8	Magnesium Photocathode Mounted on High Voltage Terminal with Close Proximity Flashlamps	I-12
I-9	Small Area Dispenser Cathode of the Barium Dispenser Type	I-14
I-10	Dispenser Cathode Voltage and Current Waveforms (a) without Guide Magnetic Field (b) with Guide Magnetic Field	I-15
I-11	Current Densities Under Single-Pulse Conditions	I-17
I-12	100 Shot Overlays of Voltage and Current at 25 Hz	I-18
I-13	Dispenser Cathode Emission with No Guide Magnetic Field	I-19
I-14	Dispenser Cathode Emission with a Guide Magnetic Field	I-20
I-15	Water Cooled Foil Support Structure	I-23

Figure		Page
I-16	Copper Clad (0.5 μm, One Side) Titanium Foil (25 μm) Tested up to 30 W/cm^2	I-24
I-17	Actively Cooled Foil Concept Using Phase Change	I-25
II-1	Debye Length Plotted Against Electron Density for Electron Temperatures of 1 and 10 eV	II-7
II-2	Potential Distribution Near the Cathode of a Cold Cathode E-Gun at a Time t After the Formation of The Cathode Plasma	II-8
II-3	Beam Voltage and Current Oscillograms from the Maxwell E-Gun for Anode-Cathode Spacings of 6, 7 and 8 cm	II-11
II-4	Constraints on Beam Pulse Length as a Function of Beam Current Density for Beam Energies of 150, 300 and 500 keV	II-13
II-5	Edge of a Grooved Carbon Cold Cathode Showing Evidence of Erosion During Operation	II-16
II-6	Emission Sites "Grown" Along the Edge of a 1/2 mil Tantalum Foil During Single Shot Operation	II-17
II-7	Close-Up of Emission Sites Showing Growth Rings	II-18
II-8	Effects of External B_o on Cold Cathode Blade Emission	II-20
II-9	Beam Current Density Variations in the Maxwell E-Gun	II-22
II-10	The Beam Collectors in the Faraday Cup Array are Constructed from Graphite to Minimize Albedo	II-23
II-11	Potentials for Both Unipolar and Bipolar Diodes are Shown	II-25
II-12	Equipotential Contours for the Case of Local Anode Ion Sources	II-26
II-13	Averaging Fast Beam Current Fluctuation by Foil Scattering	II-28
II-14	Averaging Fast Beam Current Fluctuation by Scattering through Anode Foil	II-29

Figure		Page
II-15	Fraction of E-beam Energy Absorbed by the Foil as a Function of Foil Scattering Angle	II-30
II-16	Photocathode E-Beam Generator	II-32
II-17	E-Gun Efficiency, P_{out}/P_{in} as a Function of Cathode Quantum Efficiency	II-37
II-18	Broad Area Photoelectric E-Gun Using a Multiplicity of Coaxial Flashlamps	II-39
II-19	Magnetic Shield for Flashlamps	II-40
II-20	Emission Density Plotted Against Cathode Temperature for Various Cathode Materials	II-44
II-21	Power Radiated from a Surface Plotted Against Surface Temperature	II-45
II-22	Cross-Sectional View of a Thermionic Electron Gun	II-47
II-23	Effects of Steady-State and Pulsed Heat Loads on Maximum Current Density for Conduction Cooled Windows	II-50
II-24	Dispenser Type Thermionic Cathode	II-51
II-25	Dispenser Cathode Surface Reactions	II-53
II-26	Projected Dispenser Thermionic Cathode Life and Emission Density vs Temperature	II-54
II-27	Cathode Poisoning by Background Gas	II-55
II-28	Direct Secondary Ion Backstreaming	II-58
II-29	Sputtering Yield of High Energy Backstreaming Ions	II-59
II-30	The Larmor Radius of a Beam Electron at the Gun Anode is Plotted Aganist the Product of Beam Current Density and Beam Height	II-61
II-31	Scaling Constraints on E-Beam Height (No External Magnetic Field	II-62
II-32	Transverse Beam Profiles for Gun Anode-Cathode Spacings of 6 and 8 cm	II-64
II-33	Externally Applied Magnetic Field Used to Reduce Beam Pinching	II-65

Figure		Page
II-34	Effects of Applied Magnetic Field	II-67
II-35	Magnetic Steering of the E-Beam (1 mil Titanium Foil)	II-68
II-36	KrF* Laser Burn Pattern (No Magnetic Field)	II-69
II-37	KrF* Laser Burn Pattern (800 G Magnetic Field)	II-70
II-38	Magnetic Field Coil	II-71
II-39	Typical E-Beam Window Configuration	II-73
II-40	Foil Losses as a Function of Initial Electron Energy	II-75
II-41	Conduction Cooled E-Beam Window	II-80
II-42	Mid-Foil Temperature Due to Single Pulse	II-81
II-43	Mid-Foil Temperature Due to Multiple Pulses	II-83
II-44	Maximum Current Density as a Function of Repetition Rate for Conduction Cooled Windows	II-86
II-45	Maximum Current Density as a Fucntion of Repetition Rate for Conduction Cooled Windows with Different Foil Support Bar Spacings and Foil Thickness	II-88
II-46	Convection Cooled Window Concept	II-89
II-47	Comparison of Convection Cooling and Conduction Cooling of E-Beam Windows as a Function of Cooling Gas Pressure and Flow Mach Number	II-93
II-48	Ulitmate Stress Temperature Curves for Candidate Foil Materials	II-95
II-49	Fraction of E-beam Energy Absorbed	II-98
II-50	Schematic Showing Foil and Support Bars, Showing Average Temperatures	II-100
II-51	Dependence of Foil Temperature on Support Bar Spacing	II-101
II-52	Foil Heating Constraints on Pulse Repetition Rate as a Function of Beam Current Density, for a Copper Clad Titanium Foil	II-102

Figure		Page
II-53	Foil Stress as a Function of Support Spacing for Various Initial Elongations	II-105
II-54	Trade-off Between Foil Heating and Stress, for $J_{eb} = 10\ A/cm^2$	II-106
II-55	Trade-off Between Foil Bar Spacing and PRF	II-108
III-1	Room Layout for the Single-Pulse Test Apparatus	III-2
III-2	Electrical Schematic for the Single-Shot Test Configuration	III-3
III-3	Single-Shot Marx Generator Current Pulse into a 73 Ω Resistive Load	III-5
III-4	Schematic of Experiment for Single-Pulse Tests	III-6
III-5	Schematic Diagram of the Repetitively-Pulsed E-Gun Facility	III-8
III-6	Output Voltage Across a 50 Ω Resistive Load Under Repetitively-Pulsed Conditions	III-11
III-7	Output Voltage Across a 50 Ω Resistive Load for Single-Shot Conditions	III-12
III-8	Time Response of a Sensitive Rogowski Current Probe	III-13
III-9	Schematic Diagram of the Vacuum Chamber	III-15
III-10	E-Gun Test Chamber	III-16
III-11	Vapor Pressure Curve of EPOM 828	III-18
III-12	Mass Spectrometer Scah of the Base Vacuum in the Vacuum Chamber	III-19
III-13	Photographs of the Water-Cooled Foil Anode and Support Bars	III-20
III-14	Cold Cathode Concept with Outgassing Capability	III-22
III-15	Cold Cathode Array with Outgassing Preheaters	III-23
III-16	Electrical Isolation of Heated Blades	III-24
III-17	Cold Cathode Mounted Behind Electrostatic Cover Plate	III-25

Figure		Page
III-18	Carbon Felt Cold Cathode	III-26
III-19	Magnesium Photoemissive Cathode (10 x 20 cm)	III-28
III-20	Magnesium Photocathode Mounted on Aluminum Support Plate which is Attached to the High-Voltage	III-29
III-21	Coaxial Flashlamps Used to Farodiate the Photocathode	III-30
III-22	Current Button Plate Used to Measure E-Beam Current Density Distribution	III-31
III-23	Experimental Configuration for the Small Area Dispenser Cathode	III-33
III-24	Small Area Dispenser Cathode	III-34
III-25	Large Area Dispenser Cathode	III-37
III-26	Large Area Cathode Temperature vs Input Power	III-38
III-27	Temperature Profiles of 150 cm^2 along Horizontal and Vertical Scans	III-40
III-28	Foil Support Structure	III-42
III-29	Photomicrograph of Copper Clad Titanium Foil (Vapor Deposition)	III-44
III-30	Photomicrograph of Aluminum Clad Titanium Foil (Plasma Spraying)	III-45
IV-1	Effect of Cathode Outgassing on the Closure	IV-2
IV-2	E-Gun Voltage and Current Waveforms of Tantalum Blade Cathode	IV-4
IV-3	Spatial Distribution of Current Density in a Tantalum Blade Cold Cathode with Guide Magnetic Fields	IV-5
IV-4	Tilt Compensation in a Blade Cathode Array	IV-7
IV-5	Time Resolved E-Beam Current Density Distributions	IV-8
IV-6	Emission Sites "Grown" along the Edges of a 1/2 mil Tantalum Cold Cathode Balde after 50 (Single-Pulse)	IV-9

Figure		Page
IV-7	Emission Profile of a Carbon Felt Cathode	IV-10
IV-8	V-I Characteristics for a Space Charge Limited Diode with Diode Closure Present	IV-12
IV-9	Diode Closure Velocity vs Guide Field	IV-13
IV-10	Constraint on E-Beam Pulse Length as a Result of Diode Closure	IV-14
IV-11	Cathode Illumination Due to One and Two Flashlamps, Including the Effects of r^{-1} Fall Off and the Oblique Capacity of the Screen	IV-15
IV-12	Total E-Beam Current Flowing to 13 Current Buttons	IV-16
IV-13	Activation of the Small Area Dispenser Cathode	IV-19
IV-14	Small Area Dispenser Cathode at Different Temperatures	IV-20
IV-15	Defocussing Effects in the Diode Region	IV-22
IV-16	Effects of Axial Magnetic Guide Field on the Current of the Small Area Dispenser Cathode	IV-24
IV-17	Distorted Beam Profile Resulting from Interaction of the Current with the Self-Magnetic Field	IV-25
IV-18	Long Pulse, High Current Density Results from the Small Area Dispenser Cathode	IV-26
IV-19	Volt-Ampere Characteristics of E-Guns Using (a) Dispenser and (b) Field Emission Cathodes	IV-27
IV-20	Temperature and Pressure History of Large Area Dispenser Cathode Activation	IV-30
IV-21	Mass Spectrometer Scan During the Activation Process	IV-31
IV-22	Voltage and Current Characteristics Measured for a a 100 cm^2 Dispenser Cathode (d_{ak} = 4 cm) (a) 10^{-6} torr (b) 10^{-7} torr	IV-32
IV-23	Votlage and Current Characteristics at Reduced Spacing (d_{ak} = 3 cm)	IV-34
IV-24	Voltage and Current Waveforms at 2200 A Emission	IV-35

Figure		Page
IV-25	Thermionic Dispenser Cathode Emission Characteristics Measured and Projected	IV-37
IV-26	Richardson Plot for the Dispenser Cathode	IV-39
IV-27	Fluorescence from Dispenser Cathode Emission without Guide Magnetic Field (B=0)	IV-41
IV-28	Densitometer Traces at Dispenser Cathode Emission	IV-42
IV-29	Fluorescnece from Dispenser Cathode Emission in a Guide Magnetic Field (B = 800 G)	IV-43
IV-30	Test Conditions for Repped, Large Area Dispenser Cathode	IV-45
IV-31	Voltage and Current Waveforms of a Dispenser Cathode a) with and b) without a Clipper Gap (100 Shot Overlay)	IV-46
IV-32	Voltage and Current Waveforms of a 1000 Shot Overlay	IV-47
IV-33	Outgassing Constraints for Large-Scale Dispenser Cathodes	IV-49
IV-34	Poisoning by Pure Titanium Foils	IV-51
IV-35	25 μm Titanium Foil Clad with 0.5 μm Thick Copper Operated up to 30 W/cm^2	IV-53

I. INTRODUCTION AND EXECUTIVE SUMMARY

A. BACKGROUND

Two key technical issues in the scaling of e-beam pumped visible and near UV lasers to high average powers are 1) the development of cathodes which can emit high current densities for long-pulse durations and high repetition rates and 2) the development of high transmission foil windows which can dissipate the heat load which results from e-beam absorption. Large area cold cathodes do presently exist which can supply the tens of A/cm^2 of current density which is needed but these devices are limited to 1-2 μsec pulse width because of diode closure effects. These cold cathodes have not been repped for long durations, i.e., > 50-100 pulses, because of the high outgassing rates associated with their design. The development of broad area cathodes which can emit 10-20 A/cm^2 for pulse durations of $\sim$ 5 μsec at $\sim$ 100 Hz repetition rate is crucial to attain the high average power required for DARPA applications.

At these performance levels, the heat load which must be dissipated by the thin foil which serves as the vacuum to laser gas interface is in excess of 100 W/cm^2. The sources of the heat load are the e-beam deposition, the heated laser gas (both ambient and post pulse), and the direct radiation from the emitter surface in the case of thermionic cathodes. The availability of suitable foil materials, active methods of heat removal and high transmission support structures are areas of technical concern for the high-power visible lasers. Several laser programs would benefit from developments in cathode and foil technology, including XeF scale-up, high repetition-rate XeF, KrF lasers for ICF, HgBr lasers for space applications, pulsed HF and DF and conventional CO_2 pulsed lasers.

B. PROGRAM OBJECTIVES

This program has two main objectives: the first is to develop broad area cathodes which can deliver current densities of 10-20 A/cm^2 for several microseconds in duration and for pulse repetition rates of 25 Hz (near term) and up to 100 Hz (long term); the second objective is to develop techniques for foil cooling in the regime $\gtrsim$ 100 W/cm^2. These techniques include foil materials, both singular and composite structures, active methods of heat removal and support structures which provide good heat conductivity, proper support for the thin foils and high e-beam transmission and efficiency.

C. EXPERIMENTAL APPROACH

Several different types of cathodes were investigated initially and one was selected for more detailed evaluation. Candidates included cold cathodes (tantalum blade arrays and carbon felt) with procedures to reduce the effects of diode closure, photoemissive broad area cathodes (with close proximity flashlamps for initiation) and broad area thermionic cathodes. The most promising technology was found to be the broad area thermionic cathode of the dispenser type wherein a barium-calcium-aluminate compound is impregnated into a tungsten matrix. Heating dispenses fresh barium to the surface, thereby replenishing the surface with a low work function material. With this action, long lifetimes and insensitivity to poisoning from exposure to laser gas may be achieved.

The apparatus used in this program for the testing of large area dispenser cathodes is a vacuum chamber with high-voltage pulse modulator shown in Figure I-1. Procedures to activate the cathodes were developed and high current densities at high pulse repetition rates were demonstrated.

Methods of foil cooling were studied as part of this program. For the cases where the ambient temperature of the laser gas is high and where the foil must be heated to avoid thermal boundary layers, foil materials such as titanium must be used. To

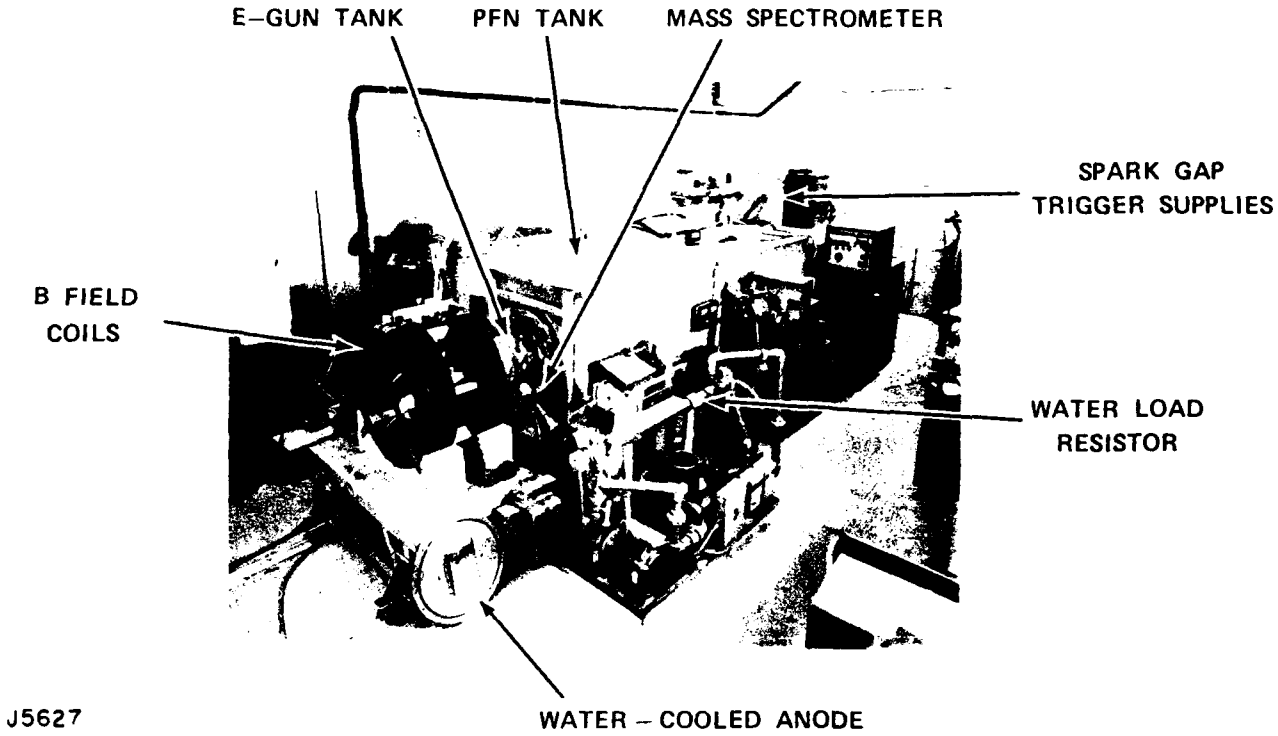

Figure I-1 AERL-DARPA E-Gun Test Facility

improve the thermal conductivity of titanium, a cladding material can be applied which, for reasons of compatibility with dispenser cathodes, must be copper. Methods of cladding titanium foils were investigated and their performance studied.

Another promising technique to improve the thermal capabilities of thin foils is convection cooling by a flowing gas. In this scheme, two foils are used with a thin space between through which a cooling gas, e.g., helium, is flowed. A variation of this technique is to seed the cooling gas with liquid droplets and allow a phase change at the foil surface to substantially improve the heat conduction of the gas coolant.

D. EXPERIMENTAL RESULTS

1. Cold Cathodes

A cold cathode array with dimensions of 10 x 20 cm was built using spring mounted tantalum blades as the field emitting element, as shown in Figure I-2. The blades were heated by a separate electric current in order to drive off absorbed hydrogen, the presence of which is known to increase the closure velocity of the diode. The effect of outgassing the cold cathode array is evident from the oscillograms of Figure I-3. When the cathode blades are heated, the effect of diode closure; namely, a rise in current for fixed applied voltage, disappears for the first microsecond. It was not possible to extend this result to longer pulse durations because of arcing conditions which could not be corrected with the existing design.

The current density distribution with increasing guide magnetic field is shown in Figure I-4. The most notable features in this photograph are the slant angle of the e-beam, a result of the interaction of the beam with the total field present, and the non-uniformity of the emission along the blades, a result of the random nature of the field emitting sites. The latter effect is shown clearly in a photomicrograph of a tantalum blade, Figure I-5.

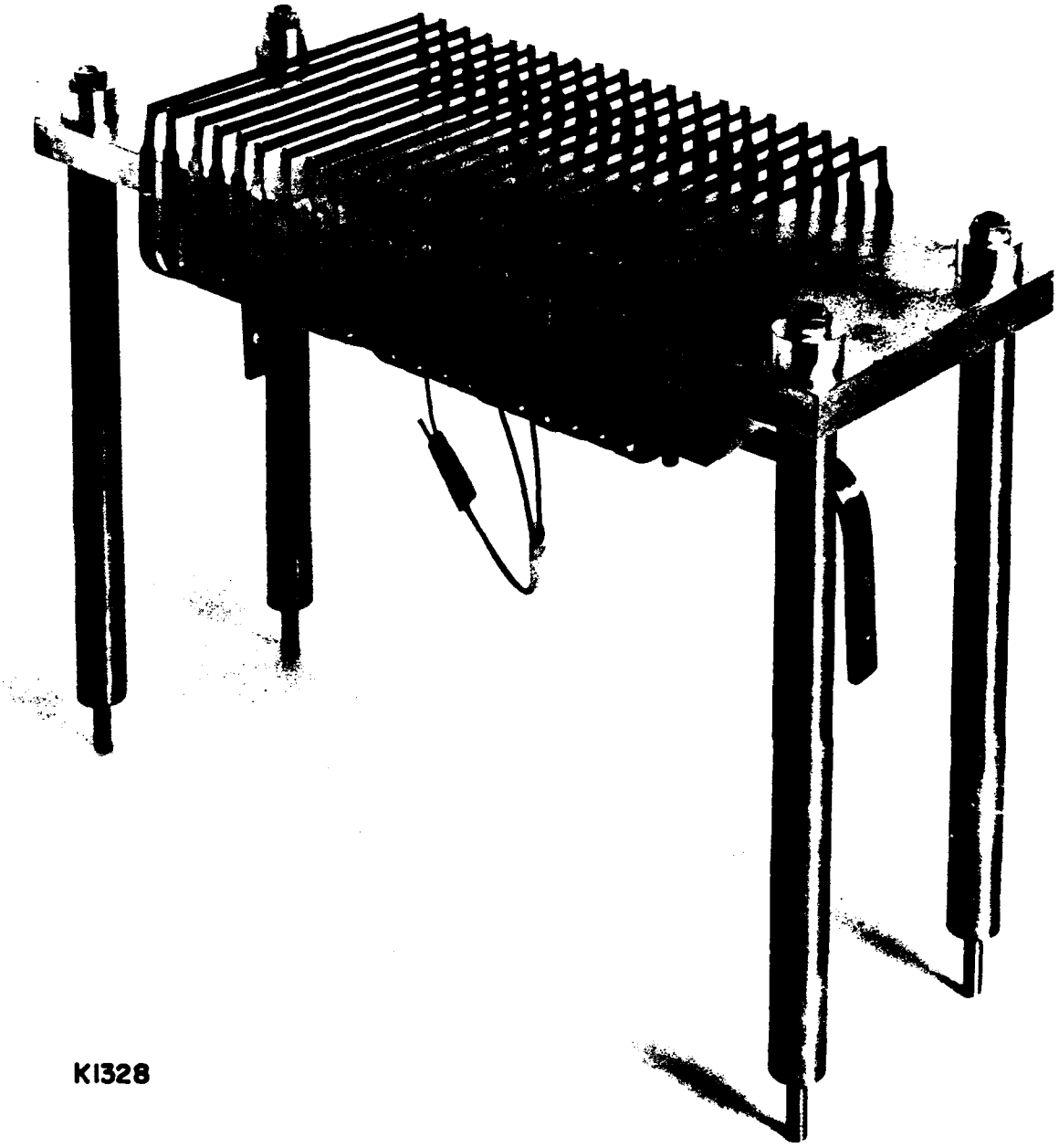

Figure I-2 Cathode Array Using Tantalum Blades with Outgassing Capability.

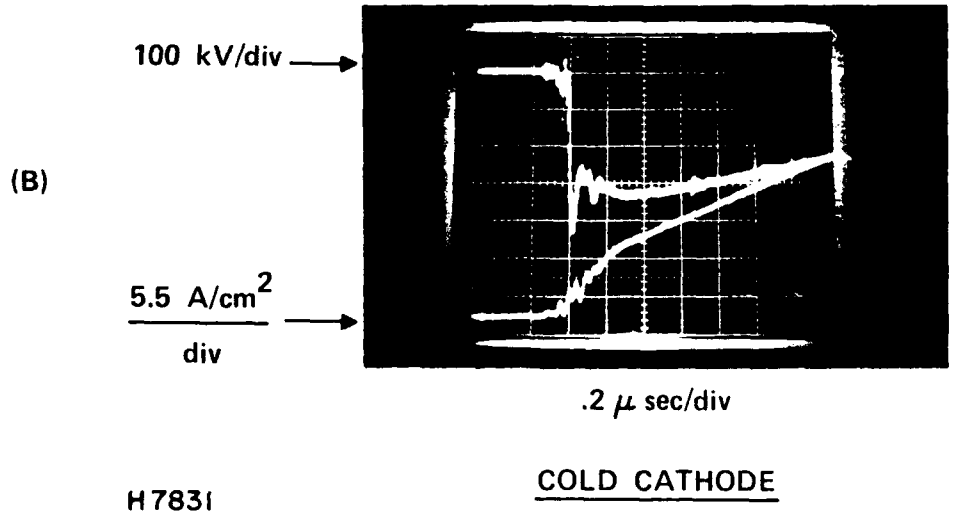

Figure I-3 Effect of Cathode Outgassing on Diode Closure Characteristics of a Tantalum Blade, Cold Cathode Array.

ANODE/CATHODE SPACING = 1.9 cm
E-BEAM CURRENT DENSITY = 40A/cm^2
E-BEAM ENERGY = 150 keV
FOIL 2 MIL KAPTON
TANTALUM CATHODES SPACED 1.2 cm APART

B = 0.75 kG

B = 1.5 kG

B = 3.4 kG

Figure I-4 Current Density Distribution with Guide Magnetic Fields for a Tantalum Blade, Cold Cathode Array.

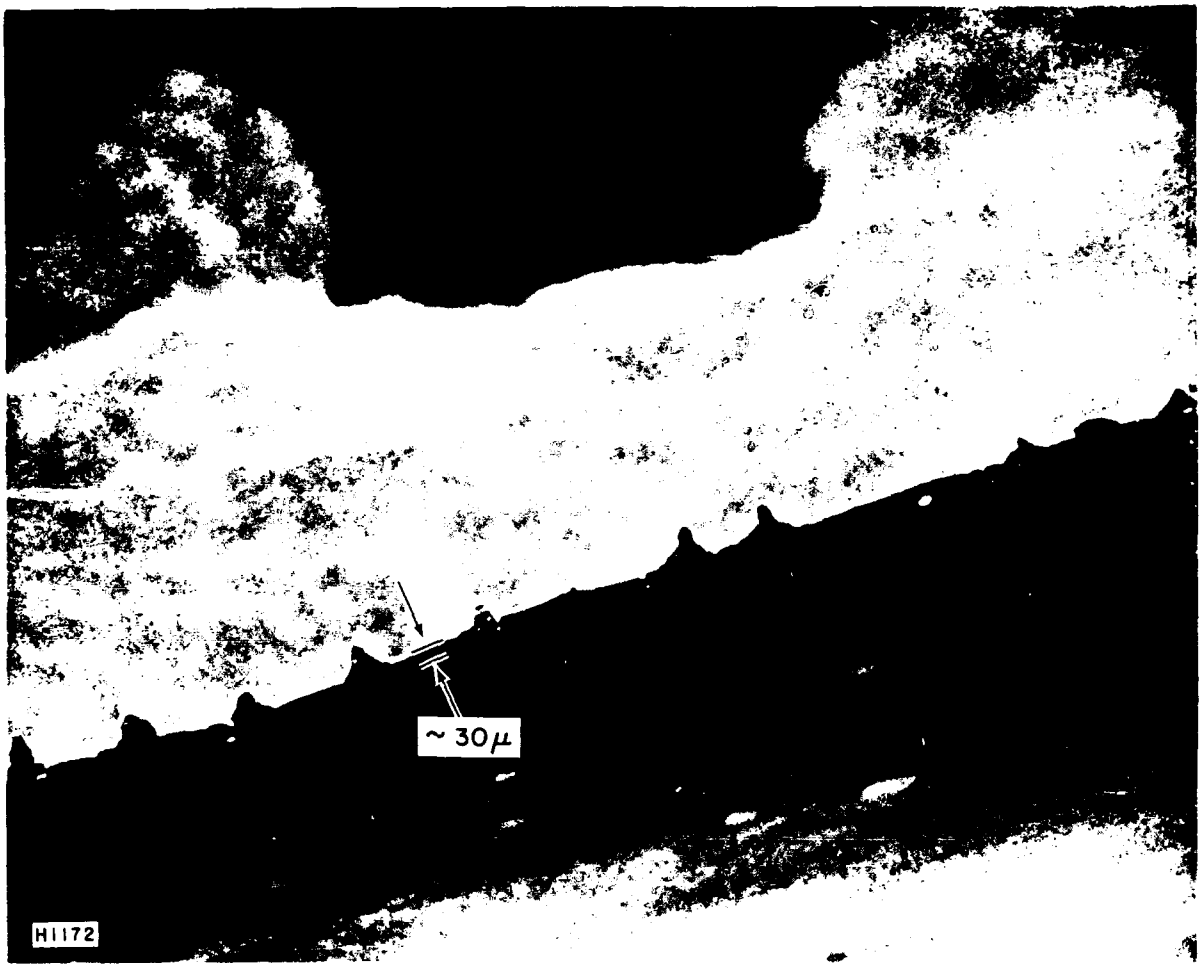

Figure I-5 Random Emission Sites "Grown" along the Edge of a 1/2 mil Tantalum Blade after 75 (Single-Shot) Pulses.

The slant effect can be corrected by tilting the blades in the opposite direction but the nonuniformity of the emission density, which is accentuated at high guide magnetic fields, limits the usefulness of this design. Aside from nonuniform energy deposition in the gas, nonuniform emission density will locally overheat the foil, thereby limiting the useful range of this technology.

Another cold cathode technology, broad area carbon felt was also investigated. The tested 10 x 100 cm cathode is shown in Figure I-6. Although the uniformity of the emission of this cathode was better than $\pm$ 10%, the closure velocity was found to increase with increasing magnetic guide field as shown in Figure I-7. At multikilogauss fields, the measured closure velocity of ~ 2 cm/μsec limits this (space charge limited) cold cathode to pulse durations of $\lesssim$ 2 μsec.

Although no repped operation of felt cathodes was investigated in this effort, tests elsewhere have exhibited large outgassing rates which resulted in diode failure after 40-100 pulses.[1] Substantial reduction of this outgassing will be necessary for large repetitively-pulsed systems.

2. Photoemissive Cathodes*

The feasibility of using photoemissive cathodes for high current density, broad area e-guns was investigated. Materials such as aluminum and magnesium are well suited for this purpose because they are not poisoned by exposure to air. A 10 x 20 cm magnesium photocathode, mounted on an aluminum high-voltage terminal and irradiated by two xenon flashlamps in close proximity is shown in Figure I-8. The total e-beam current waveform replicated that of the flashlamp with a peak current density of ~ 0.15 A/cm^2 corresponding to an average quantum efficiency of ~ 5 x 10^{-5} electrons per incident photon (which is within the range expected for pure metals). Current densities in the 5-10 A/cm^2 range could

*This work was funded by AERL-IRAD.

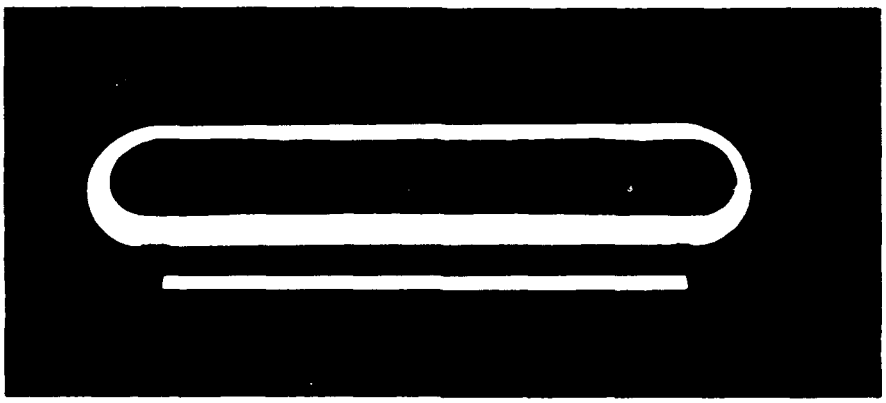

100 cm

CARBON FELT COLD CATHODE

J4563

Figure I-6 Carbon Felt Cold Cathode

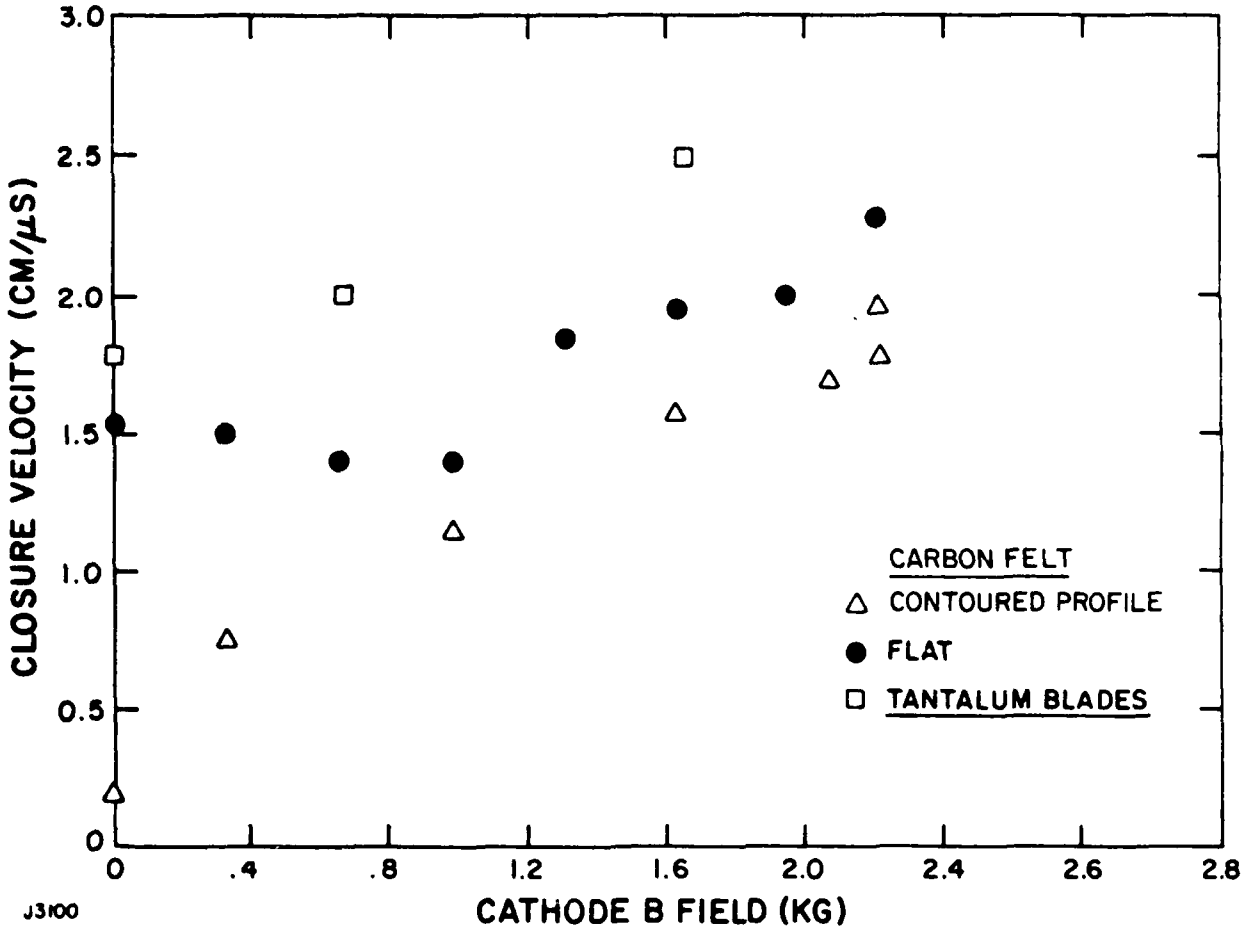

Figure I-7 Felt Cathode Diode Closure vs. Magnetic Field

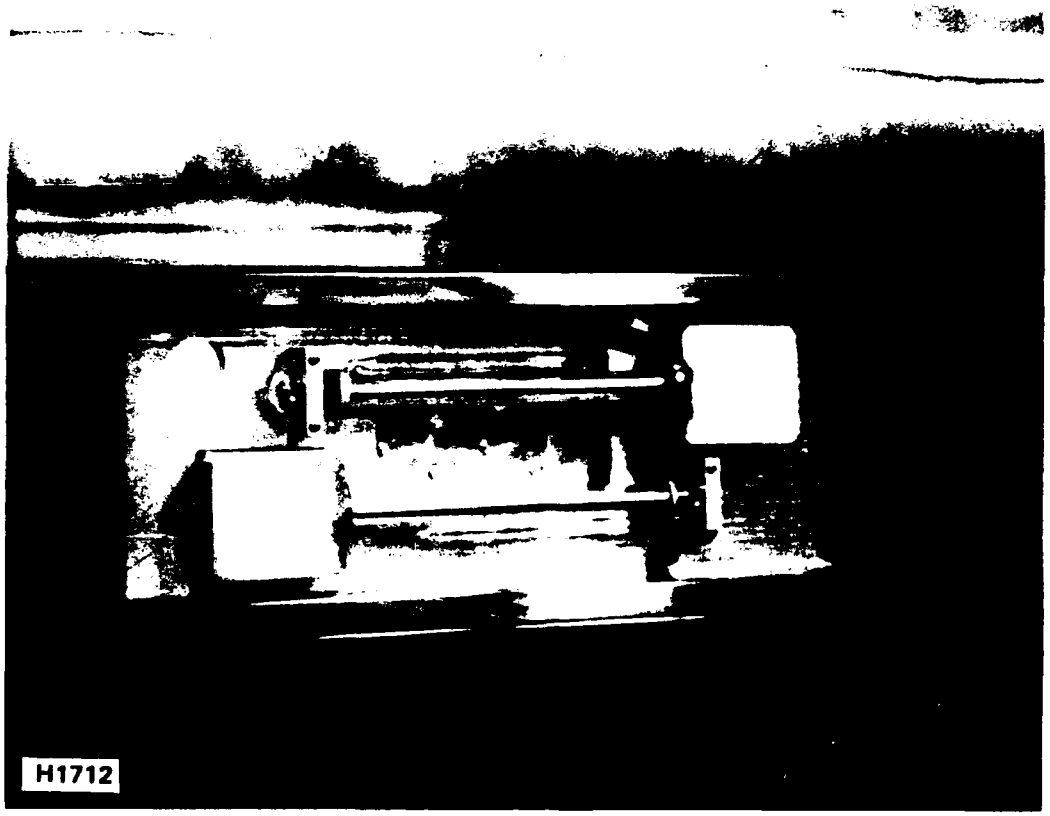

Figure I-8 Magnesium Photocathode Mounted on High Voltage Terminal with Close Proximity Flashlamps.

conceivably be reached with refined techniques and higher flash-lamp energies but significantly more work in this area is required before large efficient e-guns can be designed and built.

3. Small Area Thermionic Cathodes

A small area thermionic cathode of the barium dispenser type,[2] as shown in Figure I-9, was investigated under single-pulse conditions to determine activation procedures and basic performance. Higher activation and operating temperatures than normal were required to overcome the high arrival rate of contaminants such as oxygen for the relatively high background pressure used here ($> 10^{-6}$ torr). Efforts to overcome this problem were undertaken in a large scale facility. At the highest temperature, an emission density of ~ 30 A/cm^2 was achieved, which is limited by applied voltage, i.e., space charge or Child-Langmuir dependence.

A key property of thermionic cathodes is the absence of diode closure as evidenced by the flat current waveforms of Figure I-10a for a pulse duration in excess of 5 μsec. The elimination of diode closure and therefore the availability of a long-pulse electron source with constant impedance and constant emission, is of prime importance for the development of efficient high-power visible lasers.

The total emission remains unchanged with the application of a guide magnetic field, Figure I-10b. The guiding effect of the magnetic field is observed from the fluorescence measurements: in the absence of a guide field, the diameter of the fluorescence pattern is larger than the catnode area due to the spreading effects of e-beam space charge. With a guide field the fluorescence pattern is the same size as the cathode area and the edges are more sharply defined.

4. Large Area Thermionic Cathodes*

Large area, 100 cm^2, dispenser cathodes[2] were investigated in both single-pulse and repetitively-pulsed modes using the

*Part of this work was finished by AERL-IRAD

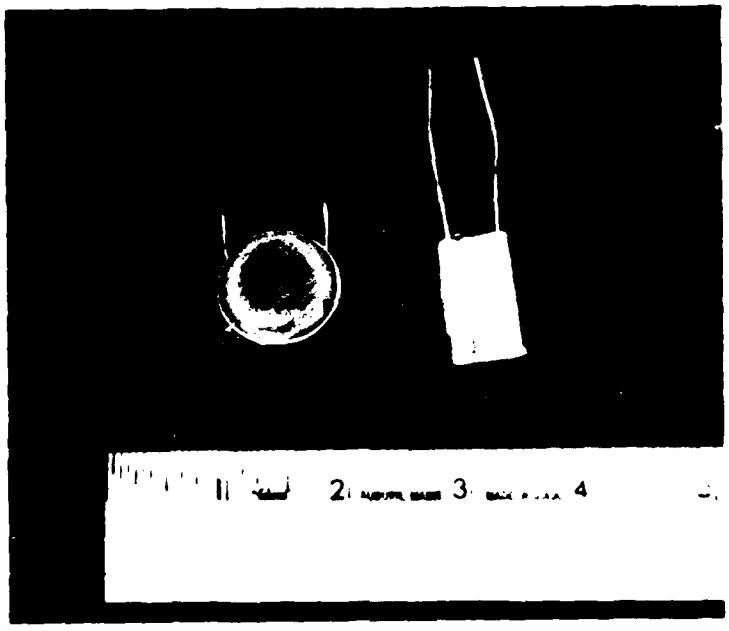

SMALL AREA DISPENSER CATHODE

J4563 (THERMIONIC)

Figure I-9 Small Area Dispenser Cathode of the Barium Dispenser Type.

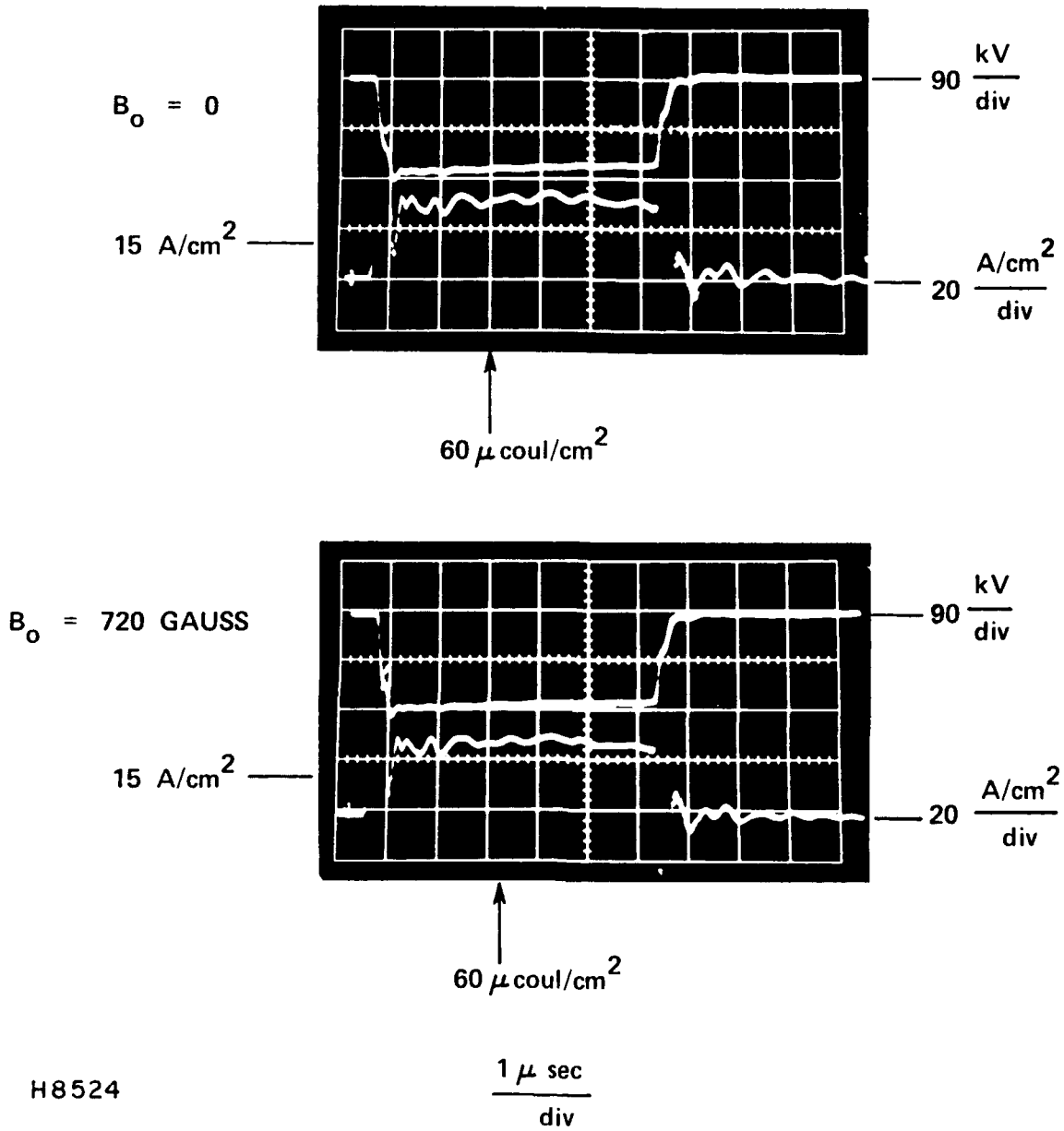

Figure I-10 Dispenser Cathode Voltage and Current Waveforms
a) without Guide Magnetic Field
b) with Guide Magnetic Field

line pulser[3] and vacuum chamber apparatus shown in Figure I-1. Under single-pulse conditions, peak current densities of up to 30 A/cm^2 were demonstrated for this large cathode as well, as shown in Figure I-11. Under repetitively-pulsed conditions, pulse current densities of 10 A/cm^2 for several successive bursts of ~ 1000 pulses at 25 Hz were demonstrated with no decrease in performance as evident in the 100 shot overlays of Figure I-12. The uniformity of the cathode emission is excellent as indicated by Figure I-13 which is a photograph of e-beam induced fluorescent emission from a polystyrene target (single pulse). With a guide magnetic field, the spreading of the beam is reduced and imaging of cathode is evident, as shown in Figure I-14.

An important requirement for a laser e-beam cathode is its ability to survive exposure to air or laser gas in the event of a foil rupture. Results of poisoning experiments with the 100 cm^2 dispenser cathodes, summarized in Table I-1 are encouraging, showing that dispenser cathodes can survive exposure to typical laser gas mixtures and be reactivated without significant loss of performance. Further work is necessary to determine the effect of repeated exposures.

A property of the dispenser cathodes we have tested thus far is that the temperature which is required for high current operation is about 100°C higher than quoted by the manufacturer.[2] We believe that the problem lies with the inability to fully activate the entire surface rather than a higher valve of work function for the area which is activated. Conclusions are that lower vacuum levels, lower desorption rates and the ability to bake the cathode, anode and vacuum chamber may be required to fully activate the surface. Our present activation procedure consists of heating the cathode for several hours at background pressure levels of 10^{-7} to 10^{-6} torr. System bakeout is not possible without substantial redesign of the vacuum chamber, pumping system and high-voltage bushing.

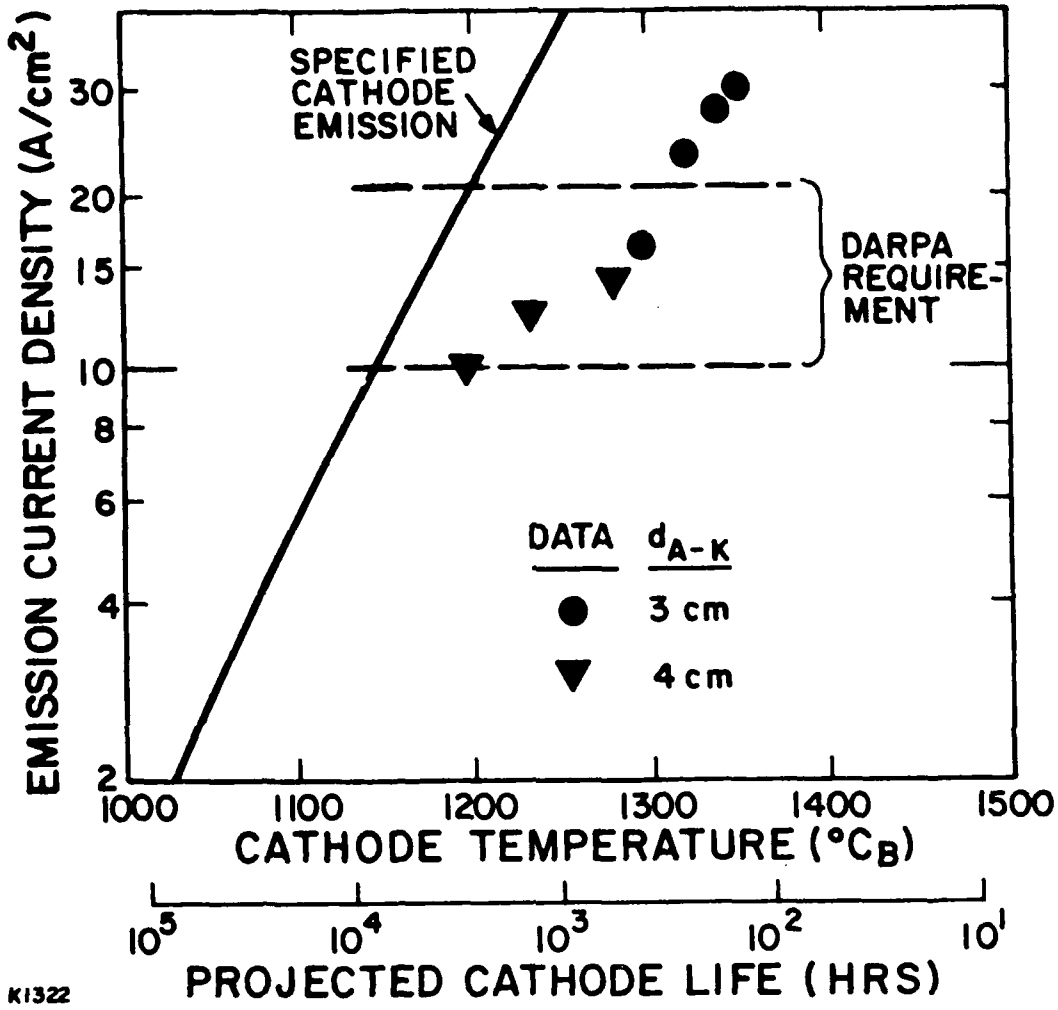

Figure I-11 Current Densities Under Single-Pulse Conditions

80 kV/DIV

0.5 μ SEC/DIV

370 A/DIV

(A)

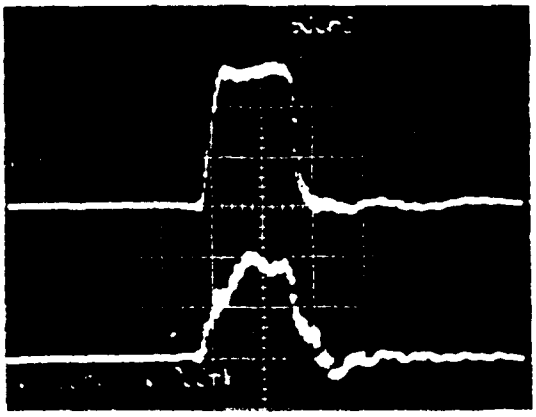

100 SHOTS, 25 Hz
215 kV

80 kV/DIV

0.5 μ SEC/DIV

370 A/DIV

(B)

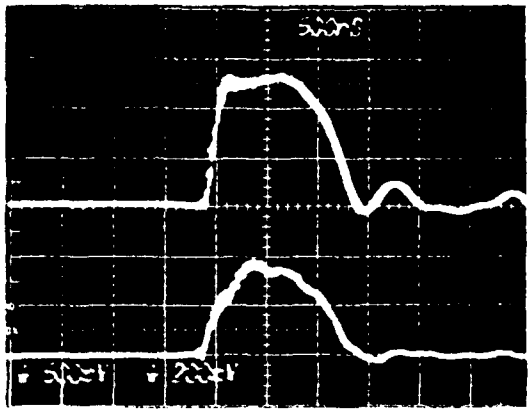

100 SHOTS, 25 Hz
215 kV

J9761

Figure I-12 100 Shot Overlays of Voltage and Current at 25 Hz

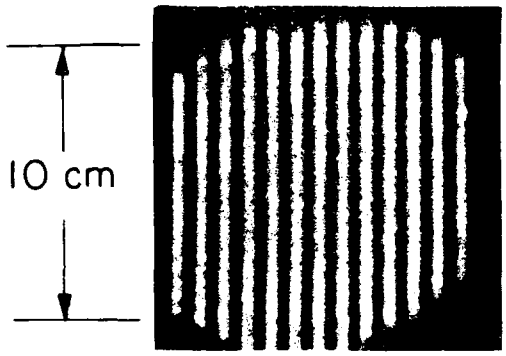

J5612

Figure I-13 Dispenser Cathode Emission with No Guide Magnetic Field.

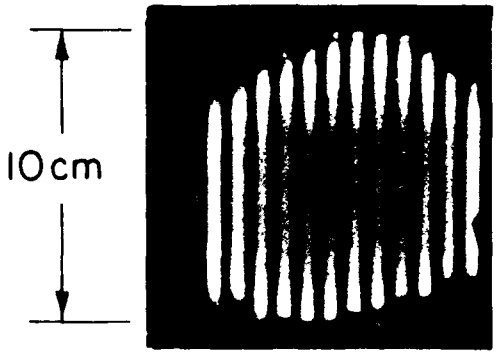

Figure I-14 Dispenser Cathode Emission with a Guide Magnetic Field.

TABLE I-1

CATHODE EXPOSURE TO LASER GAS MIXTURES

GAS MIX (1 atm)	TEST CONDITIONS (150 kV, 380 amps 1230°C)	RESULTS
CO_2/N_2	273°C	Full Reactivation
1:1	1230°C	Full Reactivation After Reheat
Ar/NF_2	273°C	Full Reactivation After Reheat
1: .01	1230°C	90% Reactivation After Reheat

5. Foil Cooling*

The high gas temperatures (> 200°C) which are encountered in visible lasers will require a high-temperature foil material such as titanium. The poor thermal conductivity of titanium, however, will require cladding of these foils with copper or aluminum. Under the present program, different methods were tried for coating titanium foil with copper. Uniform coatings with good adhesion up to 1 μm thickness were applied by vacuum deposition. These coatings were shown to eliminate the poisoning effects of pure titanium. Attempts to apply the 5 μm needed on 25 μm thick titanium to achieve ~ 100 W/cm^2 cooling capability were not successful.

Uncoated and coated foils were tested using the water cooled support structure shown in Figure I-15, constructed from OFHC copper for high thermal conductivity as well as compatibility with dispenser cathodes. The 1 μm coating was tested successfully up to ~ 20 W/cm^2 for long duration runs. At 30 W/cm^2 and a foil temperature close to 1000°C, puckering of the foil and delamination of the copper cladding occurred, as shown in Figure I-16.

An alternate method of removing the heat deposited in foils is shown in Figure I-17 where two foils are used and a coolant gas is flowed between them. The coolant can be a gas such as helium or a gas seeded with water droplets which undergo a phase change at the heated foil surface. The high heat capacity associated with a phase charge greatly increases the cooling capability of the gas. Recent studies indicate that this foil cooling technique may dissipate in excess of 100 W/cm^2 for reasonable flow geometries.[4]

E. CONCLUSIONS AND RECOMMENDATIONS

Conclusions derived from the present work are in the two main areas of cathode technology and e-beam window technology.

*Part of this work was funded by AERL-IRAD

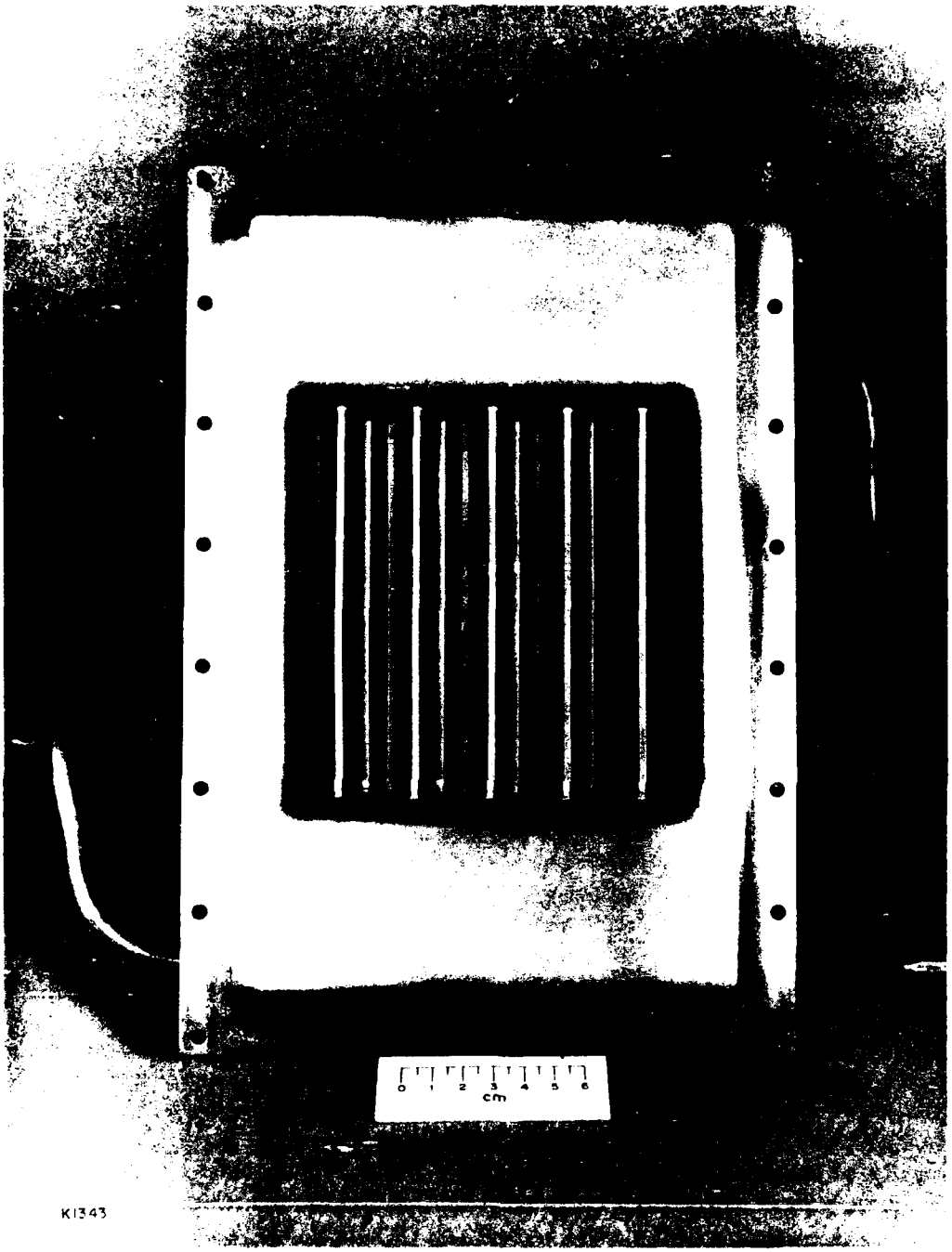

CONDUCTION COOLED
FOIL SUPPORT STRUCTURE

Figure I-15 Water Cooled Foil Support Structure

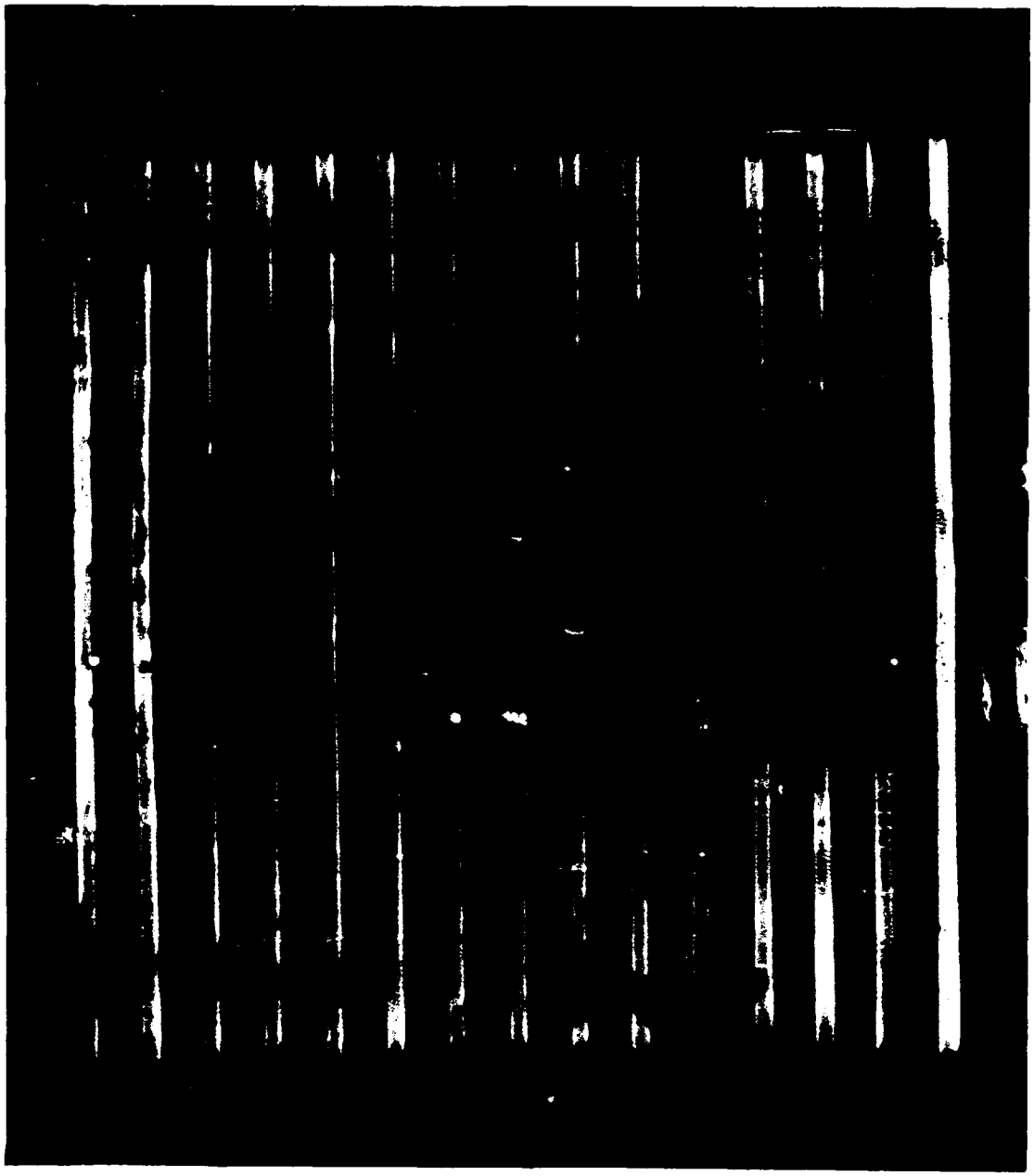

K1321

Figure I-16 Copper Clad (0.5 μm, One Side) Titanium Foil (25 μm) Tested up to 30 W/cm^2

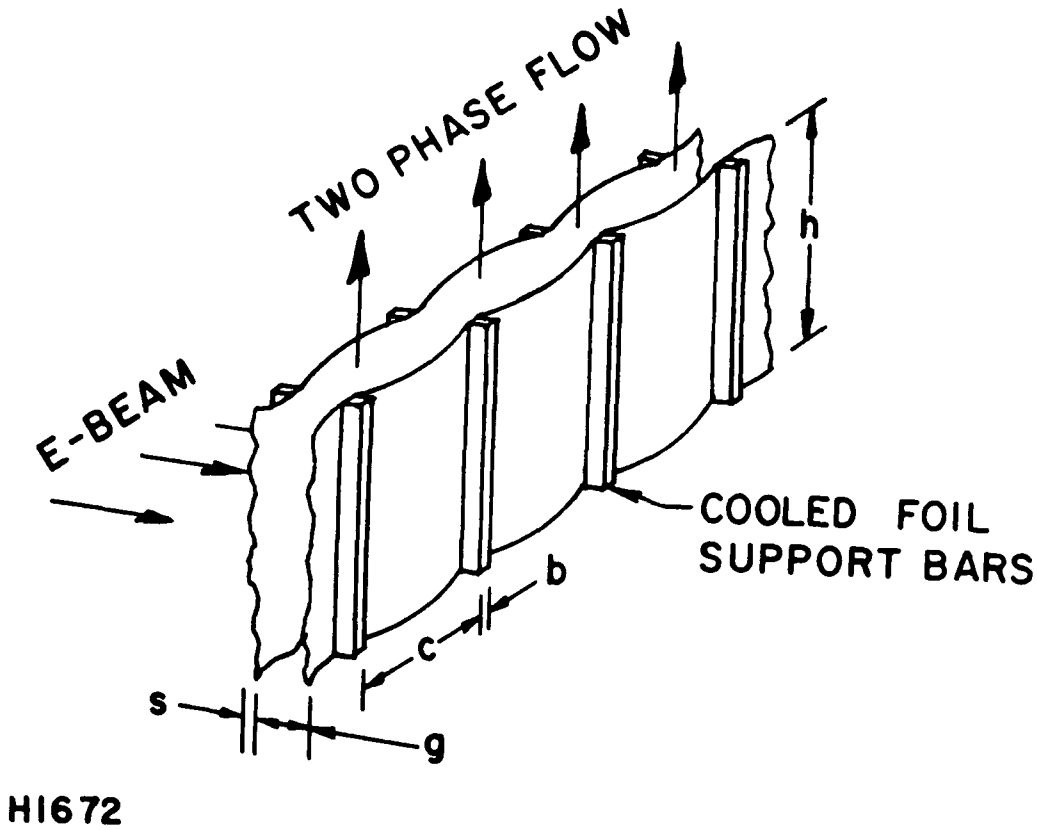

Figure I-17 Actively Cooled Foil Concept Using Phase Change

With regard to cathodes, we have evaluated several different types including field emitting blade cathodes and carbon felt cathodes, photoemissive cathodes, and thermionic cathodes. Based on experiments and analysis, the thermionic dispenser cathode was judged to be the most promising candidate for DARPA's UV/visible laser applications, and was selected for more detailed tests and characterization of performance. Main reasons for selecting thermionic over cold emitters were the high closure velocity and poor emission uniformity from cold cathodes in the presence of applied magnetic fields. Also, questions remain on repetitive pulse performance of cold cathodes, i.e., limited run and life time due to high outgassing rates and cathode erosion. Both thermionic and photoemitting cathodes can avoid these limitations of field emitting cathodes, however, thermionics were chosen over photo cathodes because of their more advanced state of development, easier implementation, and higher efficiency.

The large area thermionic cathode selected for testing is of the barium oxide dispenser type. This system has longer life expectancy and is easier to handle and operate than other oxide cathodes. It can also be obtained commercially in modular shapes and sizes suitable for broad area arrays. Pulse current densities of up to 30 A/cm^2 with good emission uniformity in the presence of a guide magnetic field were demonstrated in the present program. Constant emission with no evidence of diode closure effects was observed for pulse durations up to 5 μsec.

Repetitive pulsing at up to 25 Hz was demonstrated for voltages in the 200-300 kV range. Long duration runs with successive bursts of ~ 1000 pulses showed excellent pulse-to-pulse reproducibility and no signs of cathode degradation due to effects such as ion back-streaming. The repetition-rate and run duration in these tests were limited by the line pulser and not by cathode performance. However, since DARPA applications will require ~ 100 Hz operation, it is recommended that the line pulser be upgraded for higher repetition-rate and increased reliability for future cathode development and testing.

Poisoning tests have shown that dispenser cathodes can survive exposure to laser gases, especially those containing NF_3, and still retain the ability to be reactivated. Further tests are needed, however, to explore the full degree of resistance to poisoning. These tests should include the frequency of exposure and the ability to recover to higher levels of emission. Also, full activation has not yet been achieved and the cathode temperature is higher than is required according to manufacturer's specifications. It remains to be demonstrated that dispenser cathodes can recover to full emission at the projected lower temperature.

Based on observed operating temperatures, being $\sim 100^{\circ}C$ higher than specified, cathode lifetimes of 10^2-10^3 hr can be projected for current densities of 10-20 A/cm^2. This is about one order of magnitude shorter life than can be obtained with better controlled environmental conditions, i.e., with lower base vacuum and system bakeout capability. Better vacuum will lead to higher degree of cathode activation and will allow operation at lower temperature. Also, the observed outgassing rate of ~ 1 molecule/electron is two to three orders of magnitude higher than practical for scaling to larger e-beam systems. We recommend that these issues be addressed and resolved in the near term by upgrading the vacuum test chamber of the repped facility for demonstration of higher cathode efficiency and lower outgassing. These results are essential inputs for the engineering of large devices. Another engineering issue related to the life and reliability of cathodes is the heater design. Separation of the heaters from the impregnated tungsten body could improve reliability as well as lead to a substantial reduction of cathode cost.

In the area of e-beam window technology, the present effort has addressed several design issues related to foil materials and cooled foil support structurers, including their compatibility with dispenser cathodes. Fabrication techniques for titanium foils clad with copper or aluminum were investigated. Thin copper coatings of up to 1 μm thickness were applied by vapor deposition

and were shown to prevent cathode poisoning by titanium. Efforts to achieve, the thicker ~ 5 μm coatings needed for ~ 100 W/cm^2 heat loads have so far not been successful. Thick aluminum coatings applied by plasma spraying, although well bonded, were found too uneven to be considered as a solution for foil cooling.

A 12 x 12 cm water cooled foil structure was designed, fabricated and tested with different kinds of foil, including pure copper, pure titanium and clad titanium. Tests were performed with heat loads up to 30 W/cm^2, limited by the available foil materials and by the capability of the 25 Hz line pulser.

It is recommended that the effort to find suitable foil cladding methods continue. At the same time, phase transition convective cooling appears to have significant potential, which, if combined with conduction cooling, should ensure a cooling capability that is sufficient to meet the > 100 W/cm^2 DARPA requirement. An upgrade of the present line pulser to 100 Hz and 2-4 μsec pulse length would provide the necessary test conditions for this. Finally, an important issue that was not specifically addressed in the present program, but should be pursued forcefully, is the development of nonintercepting window structures. This will not only have significant payoff in terms of e-beam efficiency, but would also eliminate constraints of heat removal from the foil support structure.

SECTION I. REFERENCES

1. Shannon, J., Maxwell Labs, Inc. Presentation given at the DARPA Eximer Laser Review Meeting, Naval Research Laboratory 1-2 July 1980.

2. Spectra-Mat, Inc. Watsonville, CA.

3. Systems, Science and Software, Hayward, CA.

4. Loda, G. and Forcier, D., "Phase Transition Cooled Window Slides for High Average Power Electric Guns," Final Report, DARPA Contract DAAK 40-79-C-0258, December 1980.

II. TECHNICAL BACKGROUND

A. INTRODUCTION

The overall objective of the present program is the development of the component technologies necessary to build broad area, high current density e-guns that are free from the constraints that limit efficient, repetitively-pulsed operation. These component technologies include the appropriate choice of cathode, means of scaling these cathode structures to large area, grid switching techniques to ease the design of pulsed-power systems and highly transparent foil structures which can withstand the high incident electron fluxes. This background section discusses the key technology issues of e-beam cathodes and foil windows and also describes the need for, and advantages of using guide magnetic fields in broad area e-guns.

1. Cathode Technology

The e-beam sources considered by AERL for use in these guns are cold cathodes, thermionic cathodes, and photoelectric cathodes.

Cold cathodes have been used almost exclusively in UV and visible laser research primarily due to their large current density capability (hundreads of A/cm^2). The primary disadvantages of cold cathodes are associated with the propagation of the cathode plasma across the anode-cathode gap. This propagation is called diode closure and leads to large variations in e-gun current density and impedance. Typically diode closure limits the useful pulse duration to 1-2 μsec. Since the diode closure velocity varies inversely as the square root of the mass of the lightest ion present, the use of clean, high-Z cathode material can lead to an order of magnitude increase in maximum useful pulse width and a corresponding decrease in e-gun impedance and current density

variation. This would significantly increase the usefulness of cold cathodes for use in UV and visible laser e-guns as they are scaled to large average powers.

Another way to avoid diode closure is to use thermionic cathodes which do not rely on plasma formation for their operation and are perhaps the most technologically advanced of all electron sources considered. Its one main drawback is that the peak current density (tens of A/cm^2) is determined by the maximum allowable cathode temperature which, in turn, determines the rate at which oxide coatings are evaporated from its surface. The evaporation of cathode material may adversely affect useful cathode life, as well as emission uniformity and high-voltage standoff capability.

A concept for producing broad areas, homogeneous, high current density e-beams using photoelectric cathodes has been developed at AERL under an IRAD-funded program and was included for consideration in future DARPA-funded e-gun technology programs. The incentive for investigating photoelectric cathodes lies in its potential advantage over cold cathodes and oxide coated thermionic cathodes. Because photoelectric cathodes do not require the formation of a cathode plasma nor the use of high-temperature heaters for their operation, they do not suffer from the primary disadvantages of either the cold cathode or the thermionic cathode. Also, illumination and photoemission uniformity may be adequate to make e-gun operation in the space charge limited mode unnecessary. This would eliminate the need for high-voltage, high-current switches and allow the anode-to-cathode spacing to be substantially increased over the Child-Langmuir limit thereby reducing the probability of high-voltage breakdown. This allows the repetitively-pulsed e-beam energy to be supplied from a dc source by simply pulsing the light source. This advantage is shared by a grid-controlled thermionic source which also eliminates the need for full energy PFNs and switches.

2. E-Beam Window Technology

The foil window of an e-beam gun absorbs beam energy to an extent determined largely by the thickness, density and atomic number of the material. This energy deposition causes an instantaneous increase in foil temperature. In single-pulse operation, with comparatively long intervals between pulses, the heat is conducted through the foil to the support bars and dissipated in the surrounding structure. For a repetitively-pulsed laser there is insufficient time between pulses for passive cooling to be effective and active cooling must be used by pumping coolant through the foils support bars.

The design problem is to provide for the maximum transparency of the foil within the constraints of the foil materials available. Successful design of the foil and foil support structures depends on correct evaluation of a number of parameters which are not necessarily directly related. Because of the complex interdependence of these parameters, an iterative procedure is necessary.

The stress in the foil is determined by (a) the distance between the support bars, and (b) the laser gas pressure and temperature, while the foil temperature is determined by (c) the e-beam power absorbed by the foil and (d) the thermal conductivity of the foil. The combination of these parameters determines the lifetime of the foil.

3. Guide Magnetic Fields

The application of an external guide magnetic field can have several beneficial effects on e-beam as well as overall laser performance. First, a B-field can be used to prevent e-beam pinching and therefore permit scaling to large areas at high current densities. Second, an applied magnetic field helps to control the energy deposition in the laser gas which leads to increased medium uniformity and higher laser efficiency. Third, the effective transmission factor and efficiency of the e-beam can be increased with non-intercepting anode-foil design, which also requires a magnetic guide field.

To avoid pinching, the strength of the applied magnetic field must be 3-4 times the maximum self-magnetic field at the e-beam. For good discharge confinement, the field must be strong enough to make the electron Larmor radius much smaller than the cavity dimension. These criteria typically lead to B-fields in the 1-3 kG range. Magnet power is not a fundamental issue since large dc superconducting coils for these and significantly higher fields are commercially available.

B. FIELD EMITTING CATHODES

1. Diode Closure

Recently, considerable theoretical and experimental work has gone into understanding the dominant mechanisms leading to the generation of a cold cathode e-beam after the formation of the cathode plasma.[1,2] This work complements the earlier Russian work which was primarily concerned with the formative ($\leq$ 10 nsec) stages of the cathode plasma. Mesyats and Proskurovskii[3] showed that the cathode plasma is formed when field emission currents successively heat, vaporize and ionize whisker-like projections from the cathode surface. For most cathode materials, this process occurs within 10 nsec after the application of the voltage as long as the applied anode-cathode electric field is enhanced macroscopically and microscopically to be $\gtrsim 10^7$ V/cm at the whisker tips. In the absence of an externally applied magnetic field, a uniform cathode plasma is formed by the merging of individual flares (from each whisker) across the surface of the cathode.[1] The dense plasma which forms the gun cathode also moves toward the gun anode. The plasma closure velocity which has been measured at AERL and elsewhere[1] lies between 2 and 3 cm/μsec for most cathode materials. Orzechowski and Bekefi[2] have made a computer model for the closure of the cathode plasma. This model has been used to predict the V-I characteristics of their e-gun and to determine the identity of the plasma ion which determines the closure velocity. The electron density and temperature of the cathode plasma were determined spectroscopically to lie between 10^{17} and 10^{19} electrons/cm^3 and 1 and 10 eV respectively.[4] The model also shows that the electron density and temperature at the front of the expanding plasma vary in time. Typically the electron density and temperature of the plasma front decrease as the plasma expands toward the anode. The results of the spectroscopic measurements (Stark shift and broadening of H^+ lines) are in agreement with the rough calculation of Mesyats and Proskurovskii for the plasma density and temperature.

With these data a simple physical model for the closure of the cathode plasma toward the anode can be formulated. As the plasma moves toward the anode, the anode to cathode electric field is shielded from the interior of the plasma in several Debye shielding distance, λ_D.

$$\lambda_D = 7.43 \times 10^2 \left(\frac{T_e}{N_e}\right)^{1/2} \text{cm} \qquad \text{(II-1)}$$

In Figure II-1 the Debye shielding distance is plotted against electron density, N_e, for electron temperatures, T_e, equal to 1 and 10 eV. As can be seen in Figure II-1, the Debye shielding distance is many orders of magnitude smaller than the distance the cathode plasma propagates during a beam pulse. Consequently the potential distribution near a plasma cathode can be roughly estimated at some time after formation of the cathode plasma to be shown in Figure II-2. The potential across the Debye sheath is typically a few times kT_e and the gradient produces an electric field which tends to retard all those electrons not in the high energy tail of the distribution from leaving the plasma. Therefore, the electric field produced is just that necessary to provide ambipolar expansion of the ions and electrons. The high-energy electrons which leave create a positive plasma space charge. This space charge generates an electric field which tends to prevent electrons from leaving the plasma surface. The expansion of the plasma is then controlled by the velocity at which plasma ions fall through the Debye sheath potential. This velocity is given by

$$V_c = \alpha \sqrt{\frac{kT_e}{M_i}} \qquad \text{(II-2)}$$

where values of α lie typically between 1 and 2.

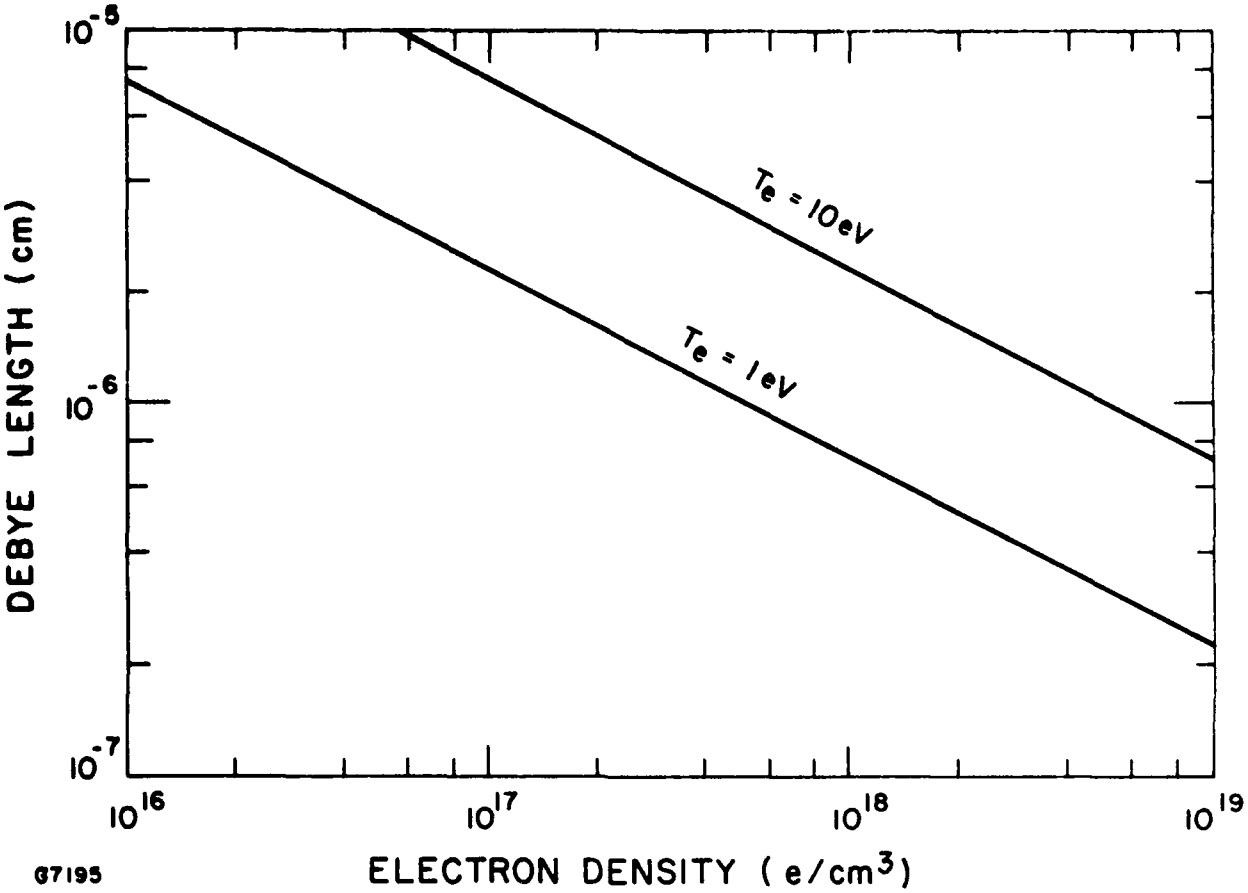

Figure II-1 Debye Length Plotted Against Electron Density for Electron Temperatures of 1 and 10 eV.

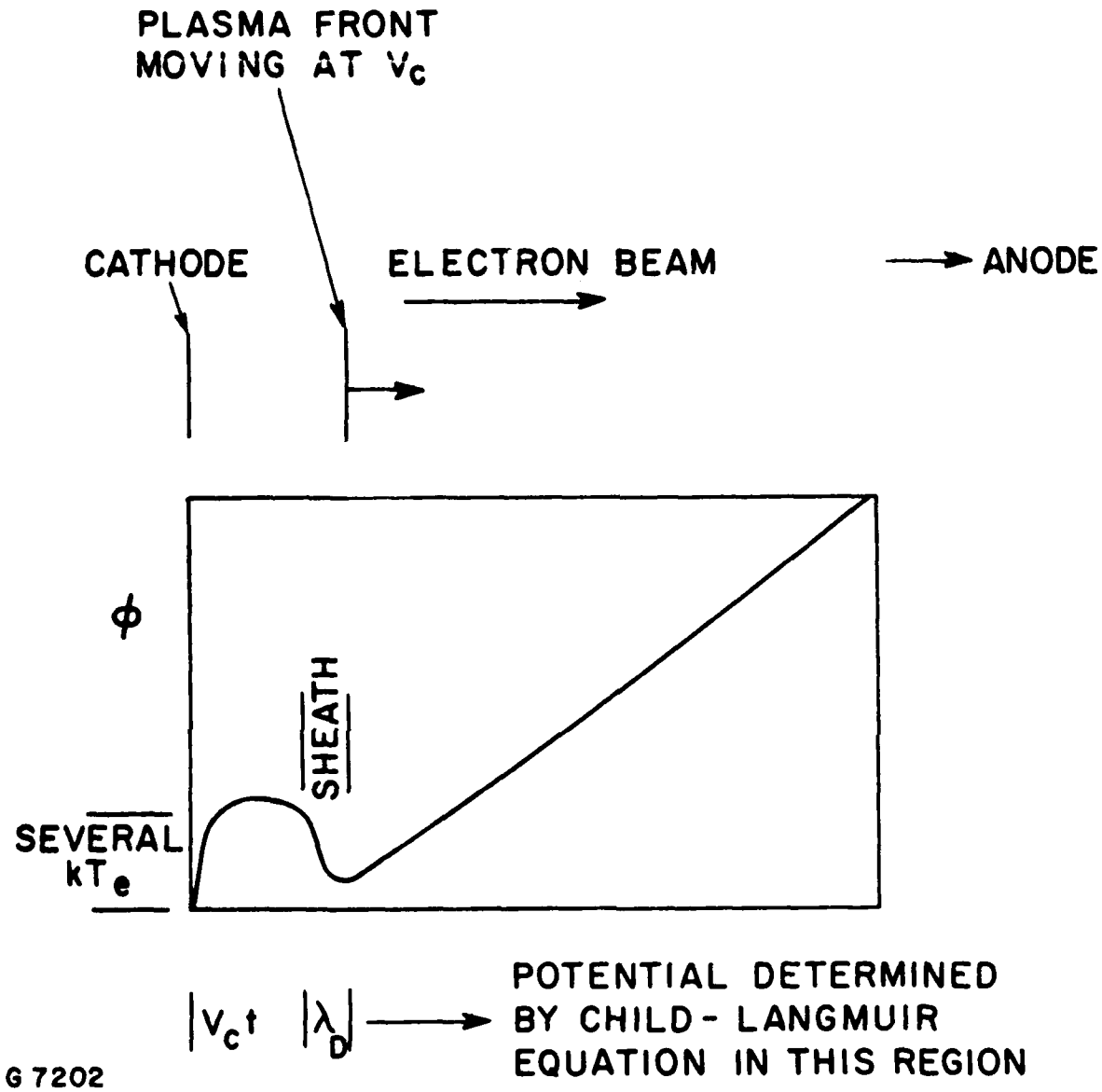

Figure II-2 Potential Distribution Near the Cathode of a Cold Cathode E-Gun at a Time t After the Formation of the Cathode Plasma.

As the electrons leave the surface of the plasma they are accelerated by the main field in the diode. The motion of the electrons and the potential distribution in this region are determined by the Child-Langmuir theory since space-charge-limited conditions prevail.

The fastest closure velocity is, of course, determined by the mass of the lightest positive ion in the plasma. In the vacuum environment of most cold cathode guns where pump oil, water vapor and hydrogen are often absorbed on the cathode surface, the positive ion determining closure is generally H^+. During an AERL-IRAD program the closure velocity was measured for both graphite and tantalum strip cathodes. This measurements was performed at a cathode voltage of 150 kV and at a beam current density of 15 A/cm^2. For these conditions the closure velocity was measured to be 2.3 $\pm$ 0.1 cm/μsec independent of cathode material. This value for the closure velocity is in good agreement with that measured by Parker et al.[1] for a plane graphite cathode at a beam energy of ~ 250 keV and a current density of ~ 10^3 A/cm^2. Orzechowski and Bekefi[2] have estimated the cathode plasma electron temperature to be 1-10 eV. This estimate together with Eq. (II-2) implies that the lightest plasma ion is H^+.

Cold cathode e-beam with $\leq$ 500 keV of energy obey the non-relativistic Child-Langmuir law so that

$$I_{eb}(t) = \frac{2.34 \times 10^{-6} \, V_{eb}^{3/2} \, A(t)}{d^2(t)} \qquad \text{(II-3)}$$

where

$I_{eb}(t)$ = total beam current
V_{eb} = beam acceleration potential
$d(t)$ = anode-plasma cathode spacing
$A(t)$ = effective cathode area

Consequently, the beam current grows with time since d(t) decreases and A(t) increases as the cathode plasma expands. The temporal behavior of d(t) can be approximated as

$$d(t) = d_o - V_c t \qquad \text{(II-4)}$$

where d_o is the initial anode-cathode spacing. For a pulse length t_p, the beam current density increases by $d_o^2/(d_o - V_c t_p)^2$ if the anode-cathode voltage is held constant. For example, an initial beam current density of 5 A/cm^2 achieved at 300 keV implies a current density growth to 7.6 A/cm^2 during a 1 μsec pulse (V_c = 2.3 cm/μsec). The temporal behavior of A(t) can be approximated as

$$A(t) = (h_o + 2V_c t)(w_o + 2V_c t) \qquad \text{(II-5)}$$

where h_o and w_o are the initial transverse dimensions of the cathode. The subsequent transverse expansion of the cathode plasma can lead to substantial increases in the total beam current density for long beam pulse lengths

$$(t_p \gtrsim 0.25 \frac{w_o}{V_c} \text{ or } 0.25 \frac{h_o}{V_c} \qquad \text{(II-6)}$$

Oscillograms of the cathode current and voltage obtained with a typical Marx driven, cold cathode gun are shown in Figure II-3 for anode-cathode spacings of 6, 7 and 8 cm. These oscillograms show that for a relatively constant acceleration voltage the e-beam current increases significantly during the pulse and that its peak value just prior to crowbarring the gun increases for decreasing anode-to-cathode spacing. These traces clearly illustrate the constraint on maximum pulse width imposed by diode closure. The effect of this constraint is shown quantitatively by the following analysis.

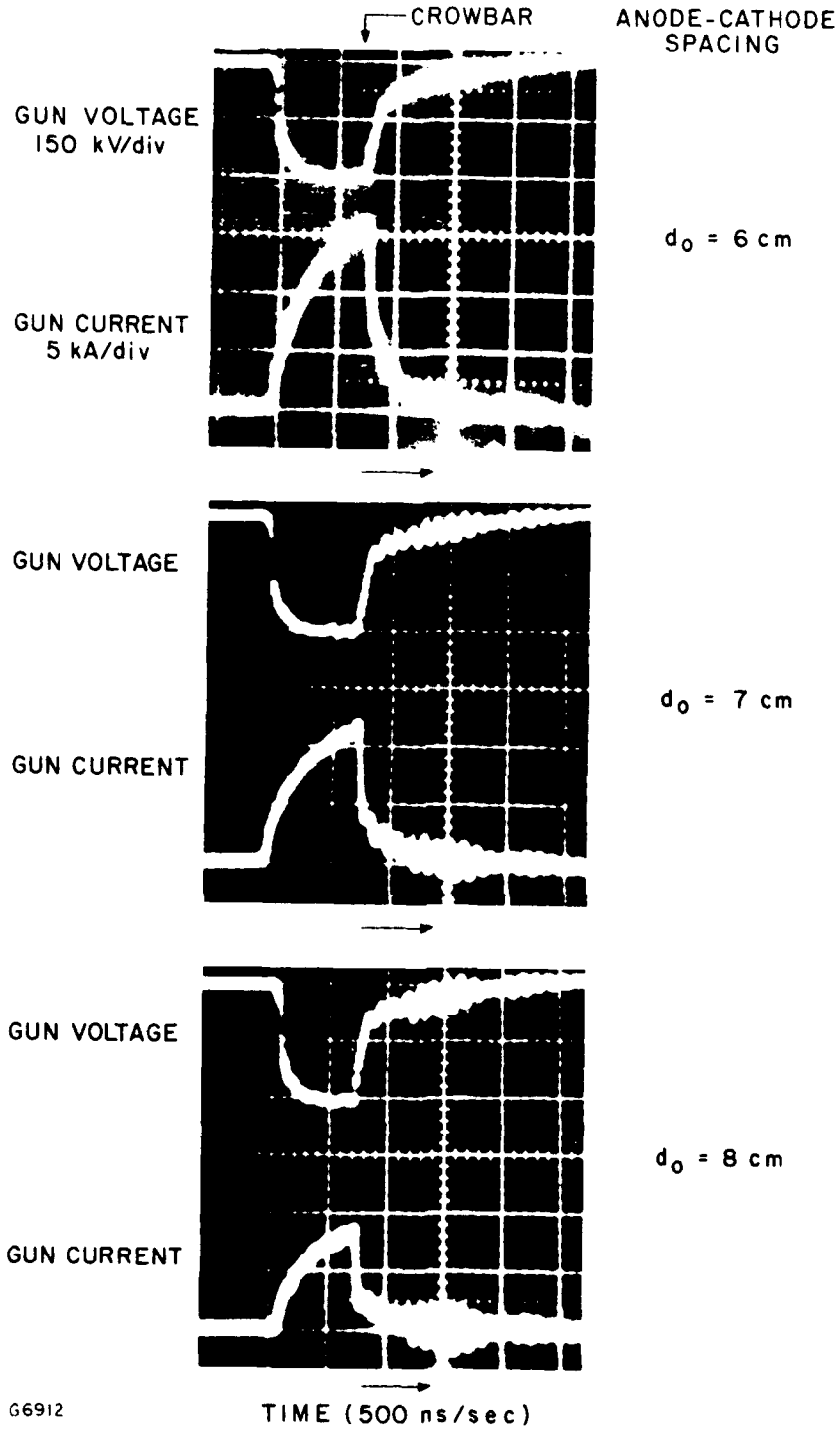

Figure II-3 Beam Voltage and Current Oscillograms From the Maxwell E-Gun for Anode-Cathode Spacings of 6, 7 and 8 cm.

The nonrelativistic Child-Langmuir law can be used to relate the beam current density J_{eb} to the acceleration potential V_{eb} in these guns for $V_{eb} \leq 500$ keV. In the gas

$$J_{eb} = 2.34 \times 10^{-6} F \frac{V_{eb}^{3/2}}{d^2} \text{ A/cm}^2 \qquad \text{(II-7)}$$

where F is the transparency of the foil and foil support structure. As discussed above diode closure implies that the anode-cathode plasma spacing, d, decreases nearly linearly with time so that

$$d(t) = d_o - V_c t \qquad \text{(II-8)}$$

where d_o is the initial anode-cathode spacing. For a closure velocity, 3×10^6 cm/sec, the initial anode-cathode spacing must be

$$d_o \geq 10^7 t_p \qquad \text{(II-9)}$$

if J_{eb} is to vary be less than a factor of two over the pulse duration t_p. Thus we estimate that

$$J_{eb} \leq 2.34 \times 10^{-20} \frac{F V_{eb}^{3/2}}{t_p^2} \text{ A/cm}^2 \qquad \text{(II-10)}$$

to avoid severe limitations on gun performance. This approximate constraint is shown in Figure II-4 for 150, 300 and 500 keV design energies with F = 0.75. In general, this constraint is most severe when high beam current densities are required at relatively low beam voltages. For example, at a beam voltage of 300 kV and a beam current density of 10 A/cm^2, the beam pulse length is limited to be $\leq$ 600 nsec.

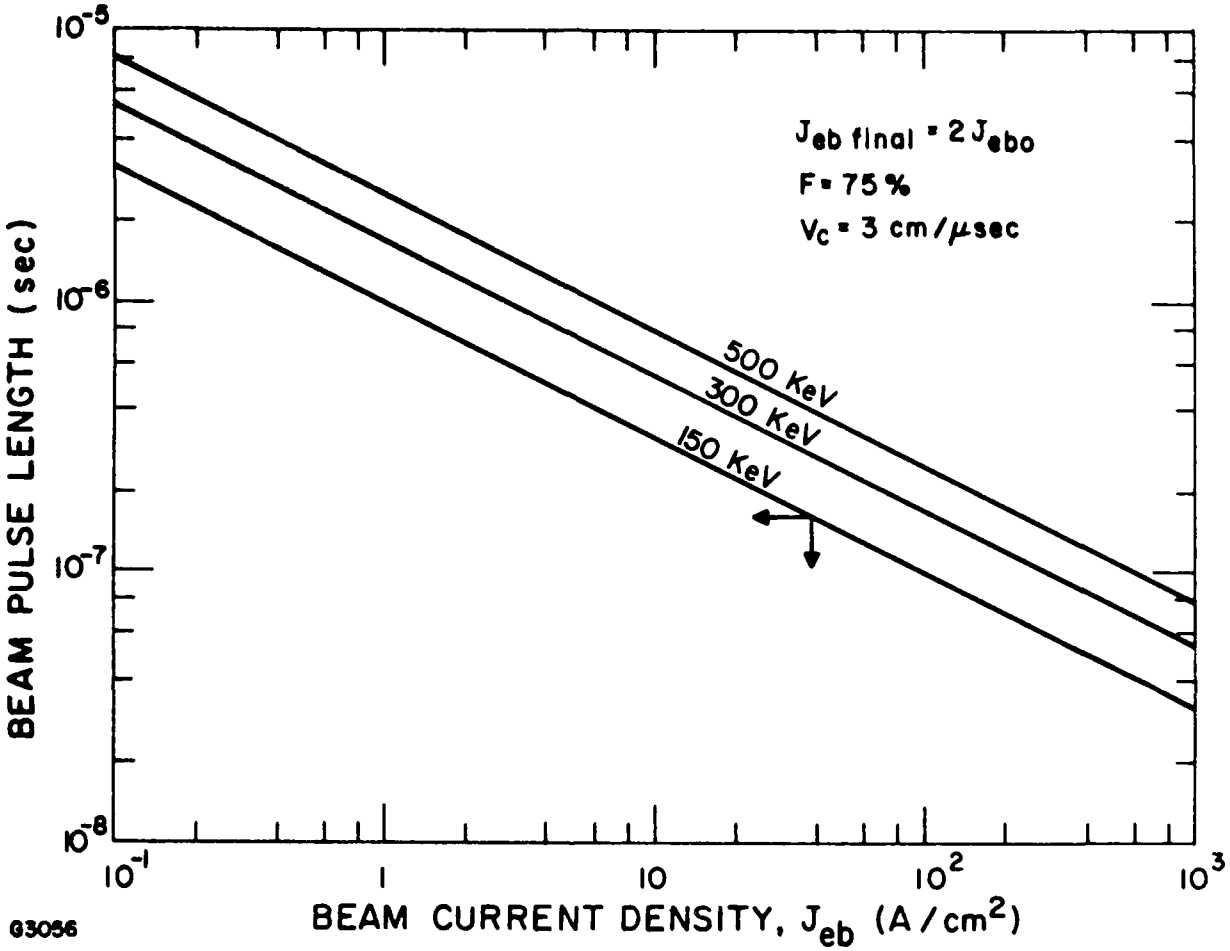

Figure II-4 Constraints on Beam Pulse Length as a Function of Beam Current Density for Beam Energies of 150, 300 and 500 keV. The beam current density rises by less than a factor of 2 if the gun is operated below the lines. A closure velocity of 3 cm/μsec was used in these calculations.

The large current variations seen in the data in Figure II-3 are caused by diode closure. These variations in cathode current during the beam pulse create large gain variations in direct e-beam systems and lead to reduced extraction efficiency in the presence of cavity losses. For e-beam controlled discharge pumping these current density variations lead to even more severe problems since the discharge stability in these lasers depend critically on the power density input to the laser mixture. The large variations in gun and discharge impedance also leads to difficulties in matching pulse forming networks to these devices and hence to reduced efficiency. Consequently, a method must be found to slow down or eliminate diode closure in cold cathode guns.

2. Loss of Emission Sites

To understand the concern over this issue, one must consider the microscopic mechanisms involved in the production of the cathode plasma formed during the initial turn-on stages of the cold cathode. The applied anode-cathode electric field is enhanced by macroscopic irregularities at the cathode surface. These irregularities are typically the edge of 1/2 mil tantalum foils spaced $\sim$ 1 cm apart or the sharp edge along the ridges of a grooved carbon cathode. Microscopic irregularities or whiskers that occur on the macroprotrusions further intensify the local electric field to values exceeding 10^7 V/cm. These large gradients cause field emission from the whiskers and their subsequent ohmic heating leads to a thermal instability and eventual whisker explosion and thermal ionization. In the absence of an externally applied magnetic field, the local cathode plasma flares formed at each emission site spread rapidly in all directions and quickly fill the region between emission sites. Space charge limited current emission then takes place from the anode side of this plasma as described in Section B.1.

The fact that cathode whiskers are vaporized in this process suggests that eventually all the emission sites will be vaporized and that the electro-polished cathode will supply cease to emit. Experinece with carbon cathodes tend to support this argument. After ~ 50 pulses, the current rise time from a grooved carbon cathode was found to slowly increase. The original fast current rise time of 20 nsec could be re-established by roughening the cathode with emery cloth so that the field emission sites were restored. Evidence of this is seen in Figure II-5. Note that the sharp corner has begun to show evidence of rounding after only 10 shots. This electro-polishing reduces the field enhancement and subsequent field emission and plasma formation and would eventually lead to unacceptably long current rise times or, perhaps, no emission at all.

There has been no noticeable increase in rise time as a function of total shots when 1/2 mil tantalum strips are used. In fact, the data shown in Figures II-6 and II-7 indicate emission sites are "grown" during operation. These photographs of the edge of a 1/2-mil tantalum foil were taken after ~ 50 shots. The growth rings shown in Figure II-7 may be formed on each shot. Calculations indicate the electrostatic pressure associated with the gradients necessary to cause field emission from protrusions of the size shown, exceeds the surface tension pressure of liquid tantalum. Hence, the protrusions may grow under the influence of the electrostatic field, tugging at the surface of a molten pool of tantalum. Calculations also show that during a 1 μsec pulse, the molten tantalum can move distance comparable to several times the protrusion diameter.

These photographs and the lack of any observed increase in current rise time, suggest that for single shot operation loss of emission sites will not be a problem for cold cathodes using tantalum foils. However, because of tantalum's high affinity for hydrogen and the need to eliminate light ions to reduce diode closure velocity, emission site growth must be looked for on other suitable cathode materials such as molybdenum and tungsten.

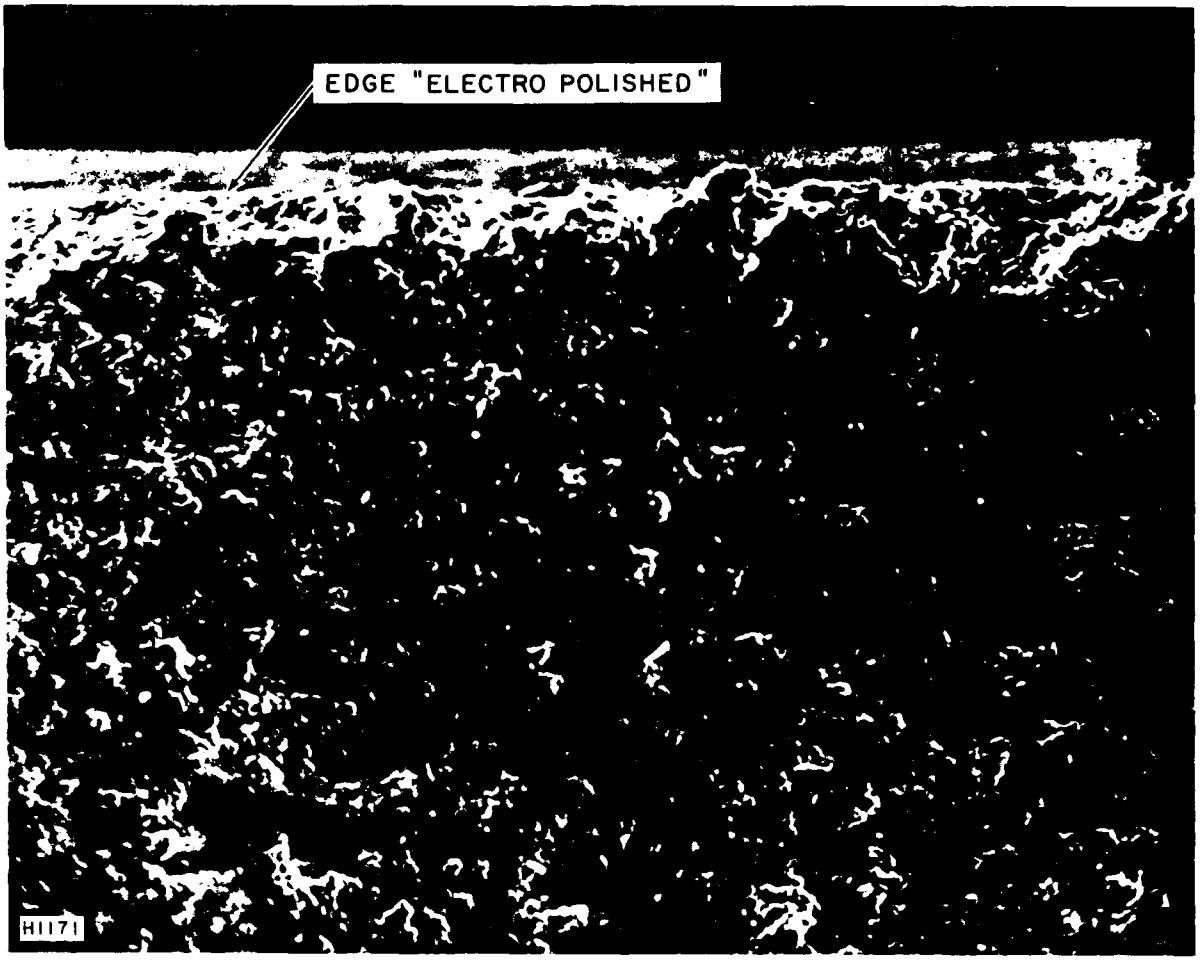

Figure II-5 Edge of a Grooved Carbon Cold Cathode Showing Evidence of Erosion During Operation.

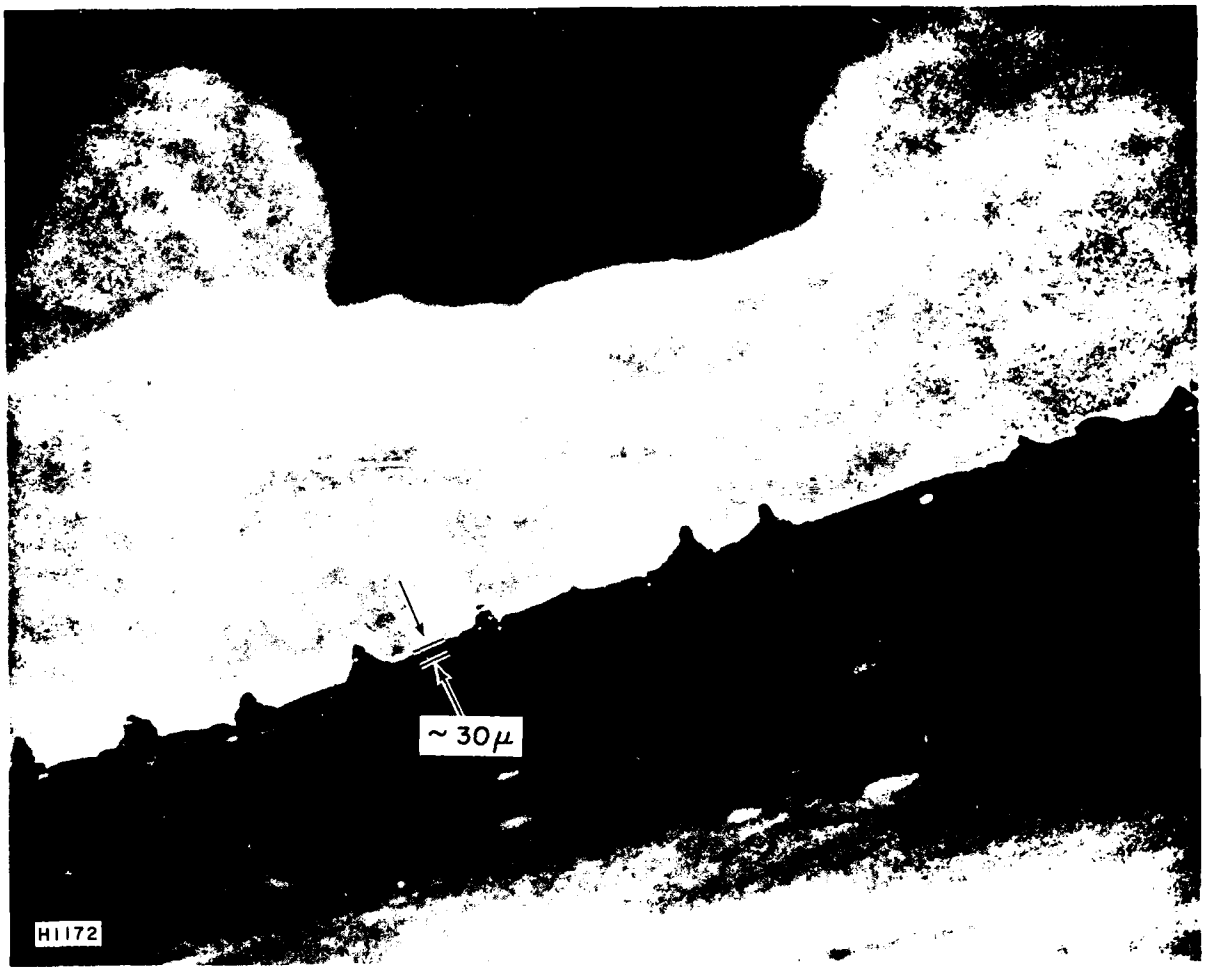

Figure II-6 Emission sites "Grown" Along the Edge of a 1/2 mil Tantalum Foil During Single Shot Operation.

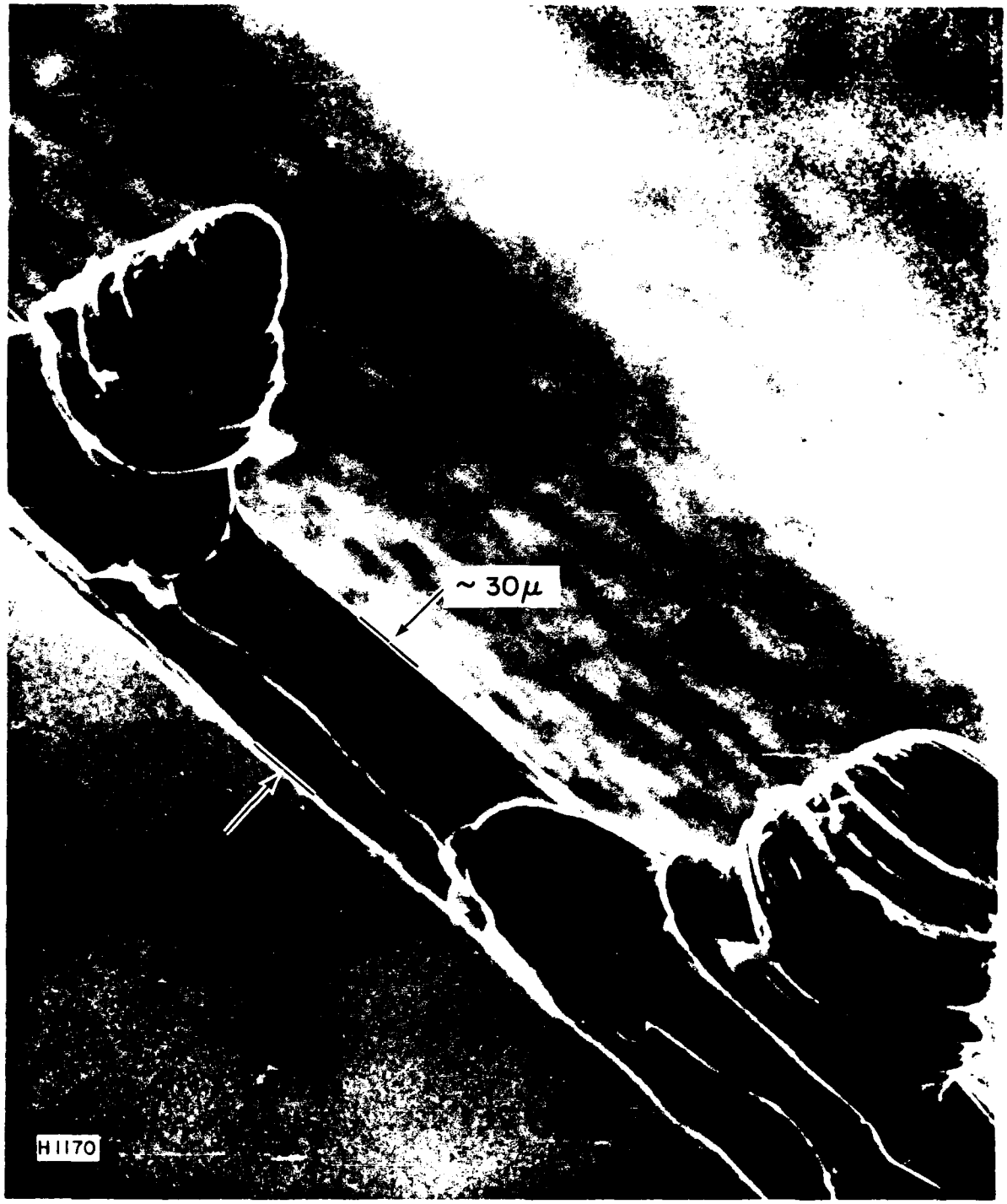

Figure II-7 Close-Up of Emission Sites Showing Growth Rings

The emission sites which are melted during the current pulse must cool by radiation and conduction during the interpulse period. The thermal diffusion time constant for heat flow from the tip to the base of the emission cone is on the order of 40 μsec, however, nearly 12 sec is required for heat to diffuse the 1.4 cm distance between the cone base and the foil support structure. The cooling rate of emission sites may constrain the maximum repetition rate of high current density cold cathode. This phenomenon clearly must be investigated under repetitively pulsed conditions because it involves raising the emission site temperatures beyond its melting point.

3. Emission Site Density

The spacing between the emission sites shown in the photographs of Figure II-6 can lead to spatial inhomogeneity in the e-beam current when an applied magnetic field is used to prevent pinching. In the presence of an applied magnetic field, the cathode plasma expands until the plasma pressure equals the local magnetic pressure. Thus, complete transverse spreading of the cathode plasma is prevented and the local regions of high current density are preserved by the applied magnetic field as the beam strikes the e-beam window. This situation is shown schematically in Figure II-8. Experiments at AERL have shown that for a applied magnetic fields as low as 500 G, the cathode blade pattern is visible at the foil. When the applied magnetic field is removed, the blade pattern is no longer discernable. This suggests a non-intercepting gun could be made by simply centering the emitting tantalum blades midway between the foil support bars. With the applied magnetic field turned on, the electrons from each emitting blade would be constrained magnetically to flow between the foil support bars. As the electrons pass through the foil into the laser medium, the scattering by the gas and foil would cause the electron to spread in the laser gas. If the foil support bar is constructed so that its thickness is on the order

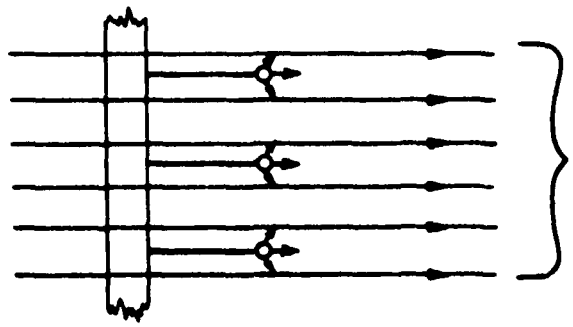

$$2 n_e k T_e > \frac{1}{2} \frac{B_o^2}{\mu_o}$$

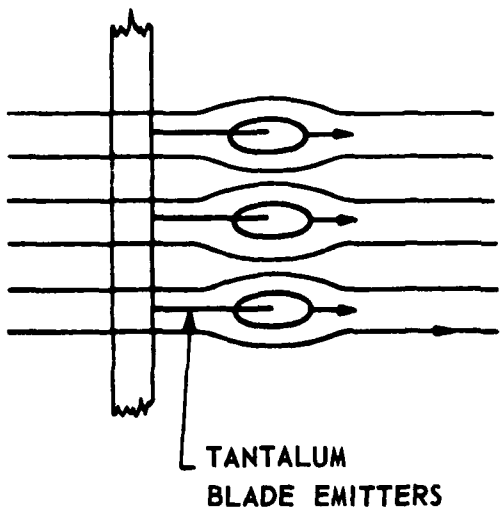

$$2 n_e' k T_e' \simeq \frac{1}{2} \frac{B'^2}{\mu_o}$$

- EVEN AT B_o = 500 GAUSS, THE BLADE PATTERN IS VISIBLE AT THE FOIL

G7958

EFFECTS OF EXTERNAL B_o ON

COLD CATHODE BLADE EMISSION

Figure II-8 Effects of External B_o on Cold Cathode Blade Emission.

of the electron gyroradius, the homogeneity of the transmitted beam is restored. Since energy is lost by electrons striking the foil support bars, this concept can significantly reduce the total power dissipated in the e-beam window.

In order to produce e-beams with high uniformity, the cold cathode must propagate along the cathode blade as well as transverse to it. This motion also is impeded by the applied magnetic field. Therefore, it the emission site density is too low, uniform high-current density e-beam may not be possible using simple cold cathode sources.

4. Fast Beam Current Density Fluctuation

In addition to the spatial inhomogeniety caused by beam pinching, a fast beam fluctuation is observed, typically, 2 to 1 variations in beam current density averaged over a beam area of 1 cm^2, is seen. Beam current variations are shown in Figure II-9 for three consecutive beam pulses. These data were obtained with the Faraday cup shown in Figure II-10 for a gun anode-cathode spacing of 7.5 cm. Generally, the instability increases in amplitude to unacceptable levels $\sim$200 to 300 nsec into the beam pulse. The instability is characterized by increases in beam current density by a factor of 2 in a time which can be as short as 25 nsec. Currently at AERL we have found that there is no apparent temporal correlation in these fluctuations between 1 cm^2 samples taken 2 cm apart. In addition, there is essentially no shot-to-shot correlation between beam samples taken at the same transverse position.

These fluctuations can be caused by positive ions which are created at the gun anode. The ions can be generated when the surface of the solid anode sections is heated by the e-beam. In 200-300 nsec, these parts are heated by $\sim 100^{\circ}C$ so that some of the surface contaminants are vaporized and absorbed gases are

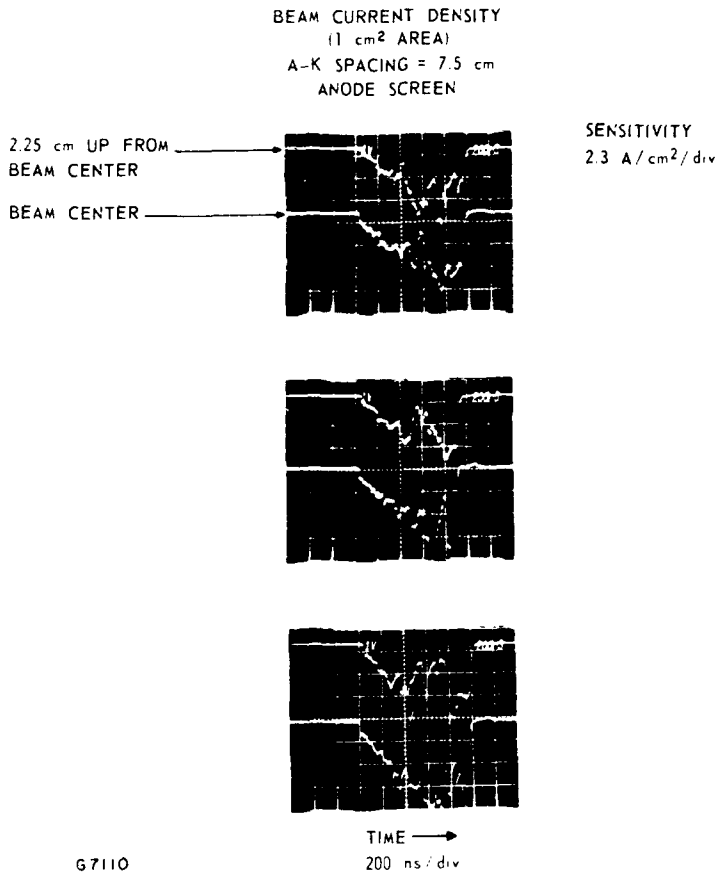

Figure II-9 Beam Current Density Variations in the Maxwell E-Gun. Data, which are from three consecutive shots, show the stochastic nature of these fluctuations.

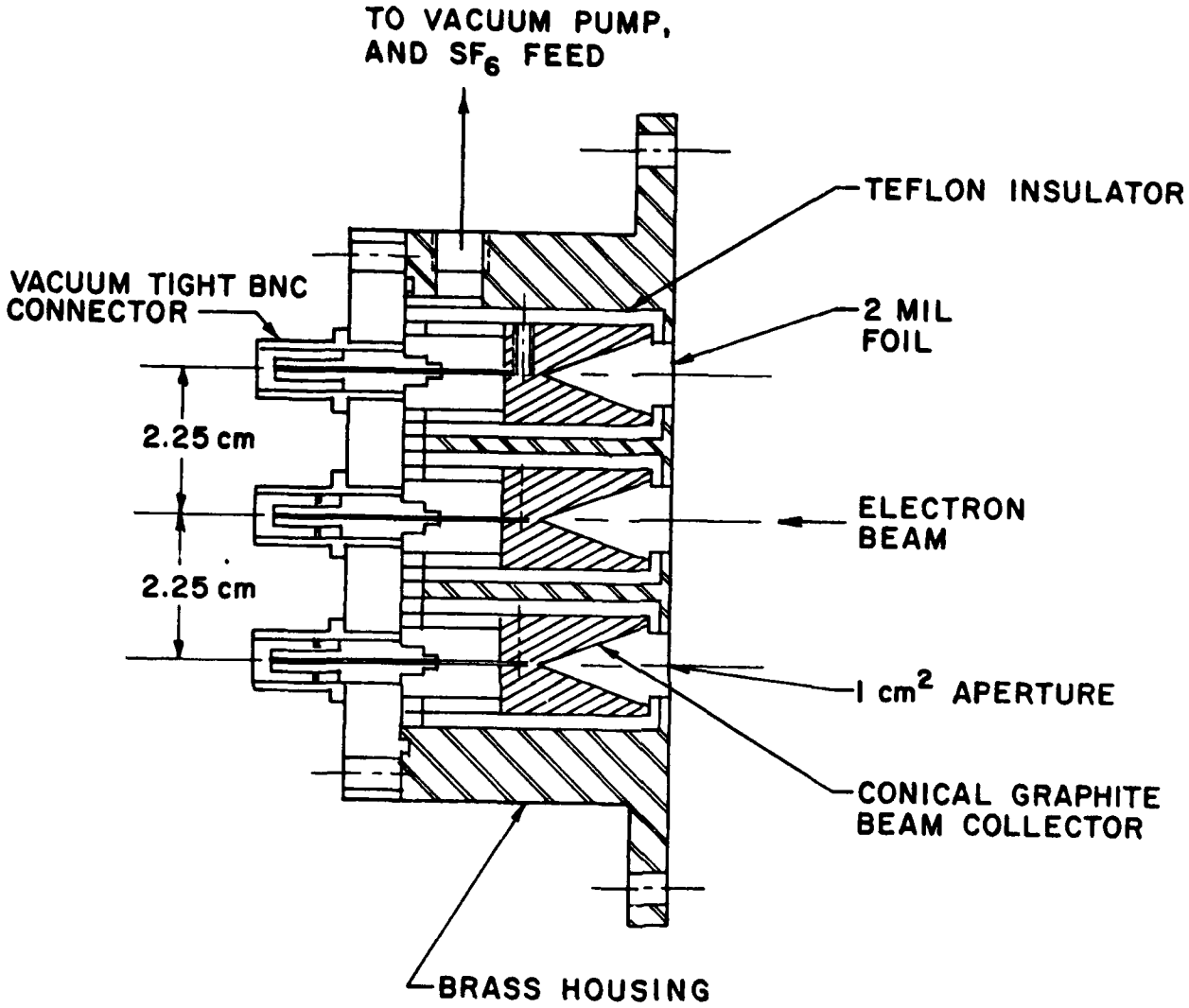

G6735

Figure II-10 The Beam Collectors in the Faraday Cup Array are Constructed from Graphite to Minimize Albedo. Each collector is terminated in 50 Ω and the voltage across these resistors are monitored. The Faraday cup array is typically evacuated and backfilled with ~ 100 torr of SF_6 to eliminate plasma return current effects.

desorbed. The e-beam and local electric fields can then ionize the evolved gases and produced positive ions. These ions are then accelerated by the diode field and can partially neutralize the electron space charge. A new quasi-equilibrium results in which both the electron and ion current densities are space-charge-limited. Langmuir[5] has shown that for a planar "bipolar diode," the space-charge-limited electron current density can reach 1.86 times that obtained with no positive ions. The potential across the diode gap is plotted in Figure II-11 for both electron space-charge-limited conditions and for the bipolar diode case.

In the case where a planar plasma electron source is present at the cathode but where only small patches of ions are generated at the anode, an even larger change in the electron current density is possible. This current focusing is illustrated graphically by Figure II-12. The fastest time scale on which the local beam current density can increase is just the transit time of these ions across the anode-cathode gap. Assuming a typical anode-cathode spacing of 7 cm and a cathode potential of -300 kV, the transit time for a H^+ ion across this gap when accelerated by the space-charge-modified electric field is ~ 28 nsec. If the electron space charge were completely neutralized by the positive ions, the ion transit time would be ~ 19 nsec. Therefore, the ion transit time across the diode gap is found to be consistent with the shortest observed beam current growth time of ~ 25 nsec. The local re-establishment of the original diode conditions then depends upon the time history of ion creation at the anode and the density of the plasma. Positive ions can be created randomly at the gun anode by desorbtion and vaporization followed by beam and electric field ionization. However, at the gun anode, the plasma formation time is longer (heating time by beam) and the plasma is likely to be spatially nonuniform across the anode surface. Again, this hypothesis is consistent with the experimental fact that the beam current fluctuations develop 200 to 300 nsec into the beam pulse and have small spatial correlation lengths.

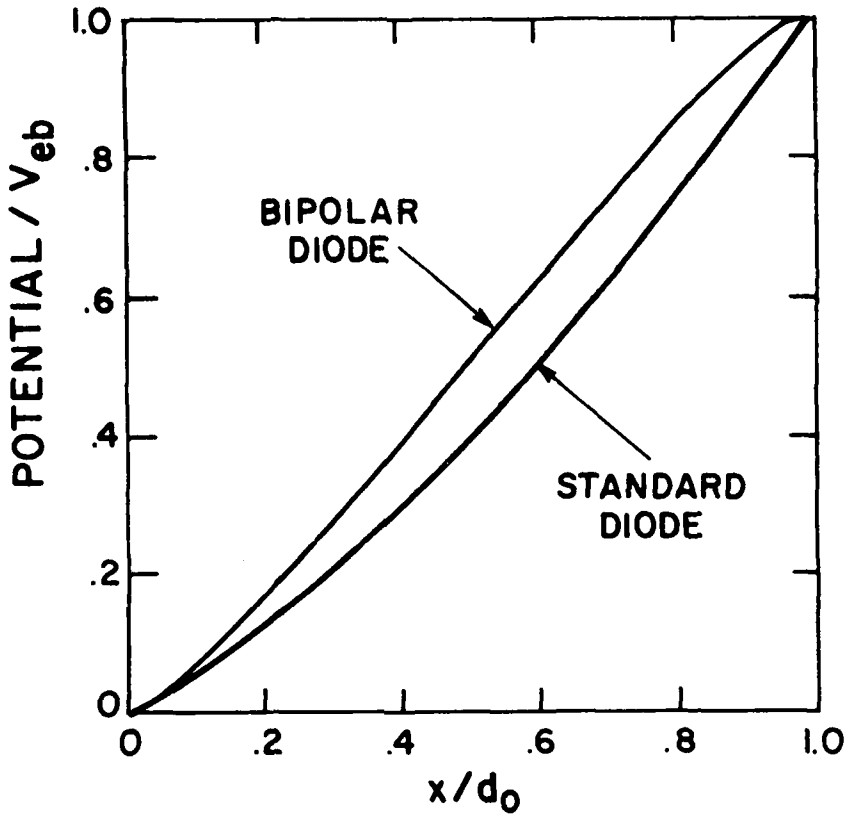

- ELECTRON EMISSION FROM CATHODE ONLY

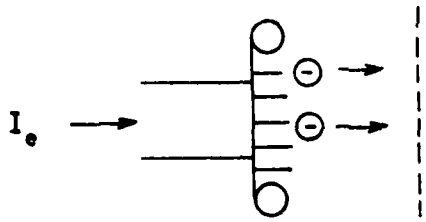

$I_{e\ BIPOLAR} = 1.86\ I_e$

- BIPOLAR EMISSION

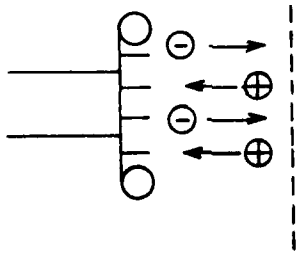

G7208

Figure II-11 Potentials for Both Unipolar and Bipolar Diodes are Shown. In the planar case the electron current density in the bipolar case is 1.86 times the electron current density in the unipolar case.

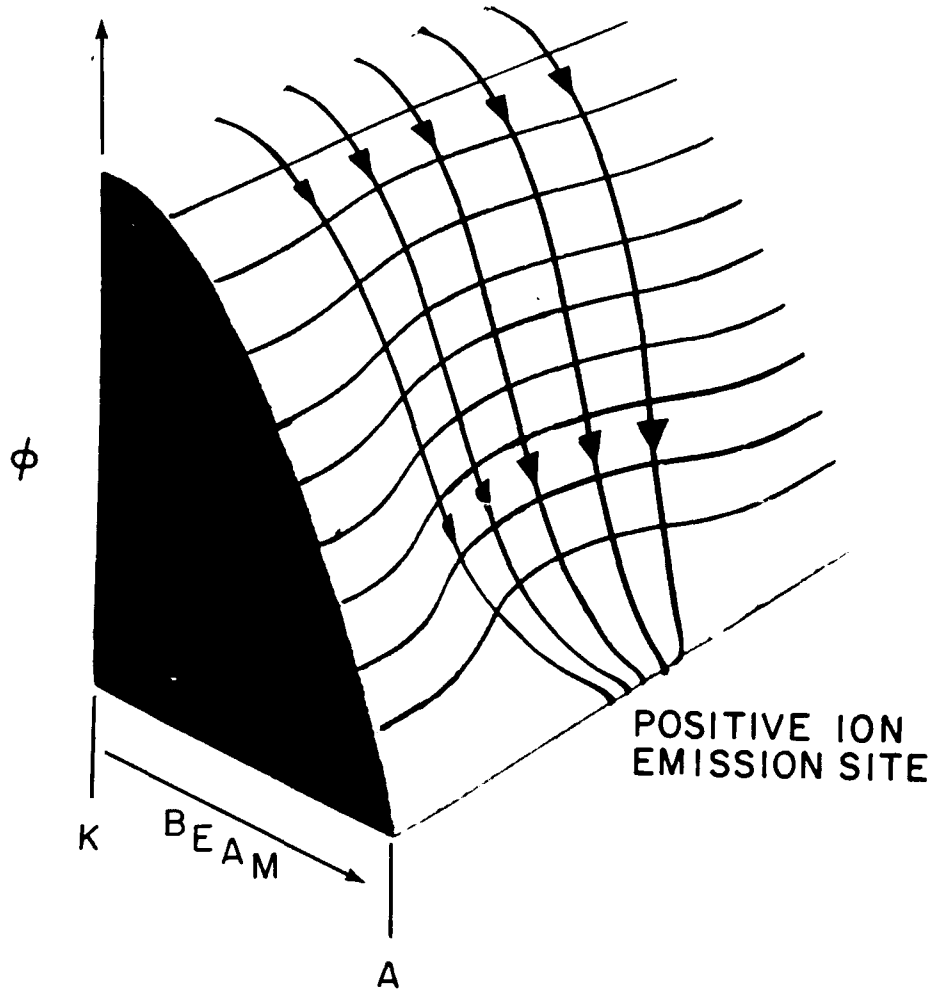

G7217

Figure II-12 Equipotential Contours for the Case of Local Anode Ion Sources.

It is possible to smooth these spatial fluctuations by scattering the beam through an anode prefoil as shown diagramatically in Figure II-13. The results of this experiment are shown in Figure II-14 where it is seen that the anode foil effeccively averages the fast beam current fluctuations. There are, however, two drawbacks to this solution. First, in order to achieve significant foil scattering angle of ~ 30 to 40 degrees, a large fraction of the total e-beam energy is absorbed by the foil. This is shown in Figure II-15 where it is seen that even for low-Z foils such an aluminum (Z = 13) over half the e-beam energy is absorbed in the foil for scattering angles $< 45^{\circ}$. The second drawback to this solution is that the applied magnetic field required to eliminate beam pinching will inhibit this averaging process. Hence, the solution to the problem of fast beam current fluctuation is to use low-Z materials for anode components and clean high vacuum techniques. Since the range of electrons increases as Z decreases, the use of low-Z anode parts reduces the surface temperature rise during the pulse. This will reduce the amount of gas desorbed during a given pulse period and prolong the maximum allowable pulse width before fast beam current fluctuation begins. This use of clean high vacuum techniques, of course, simply reduces the amount of gases absorbed by the anode parts.

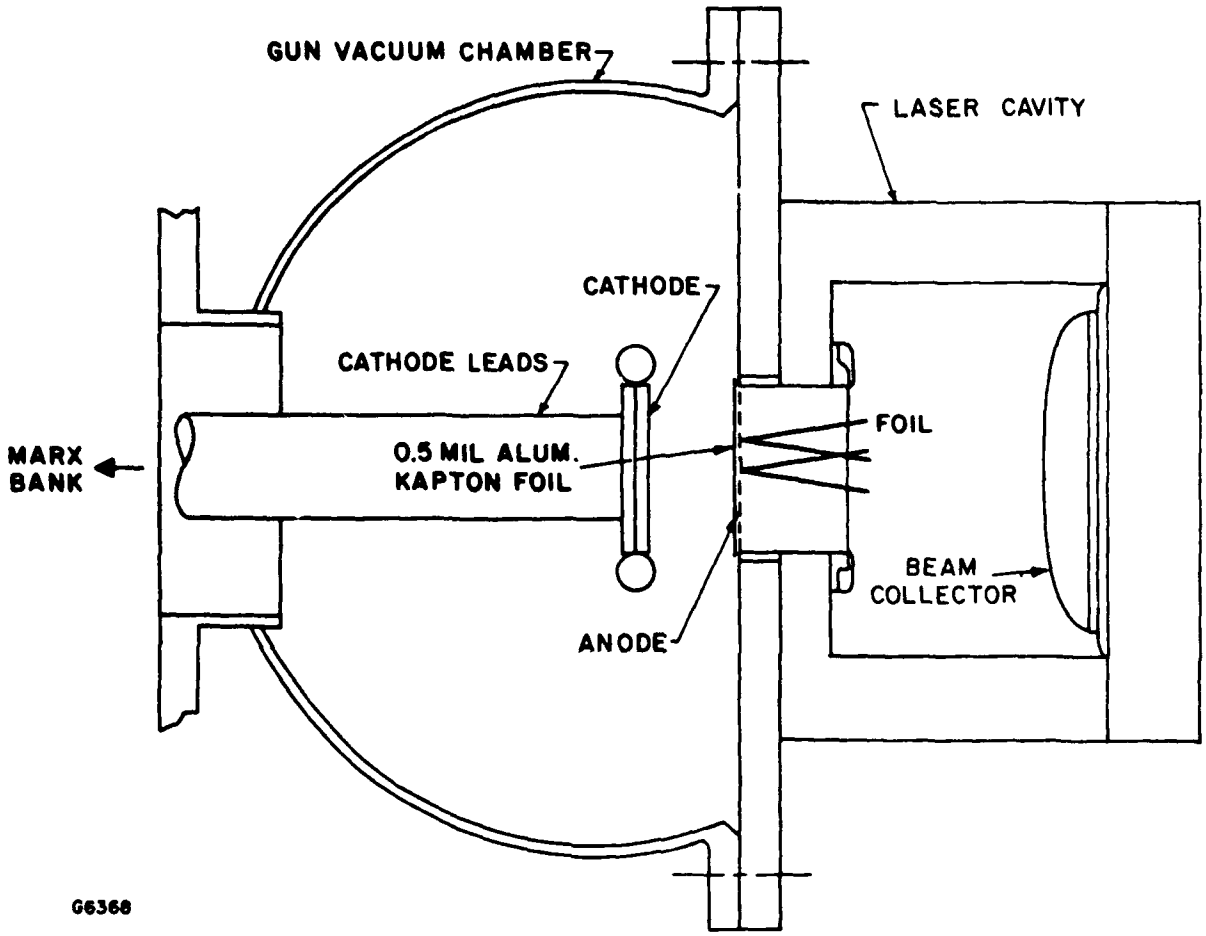

Figure II-13 Averaging Fast Beam Current Fluctuation by Foil Scattering.

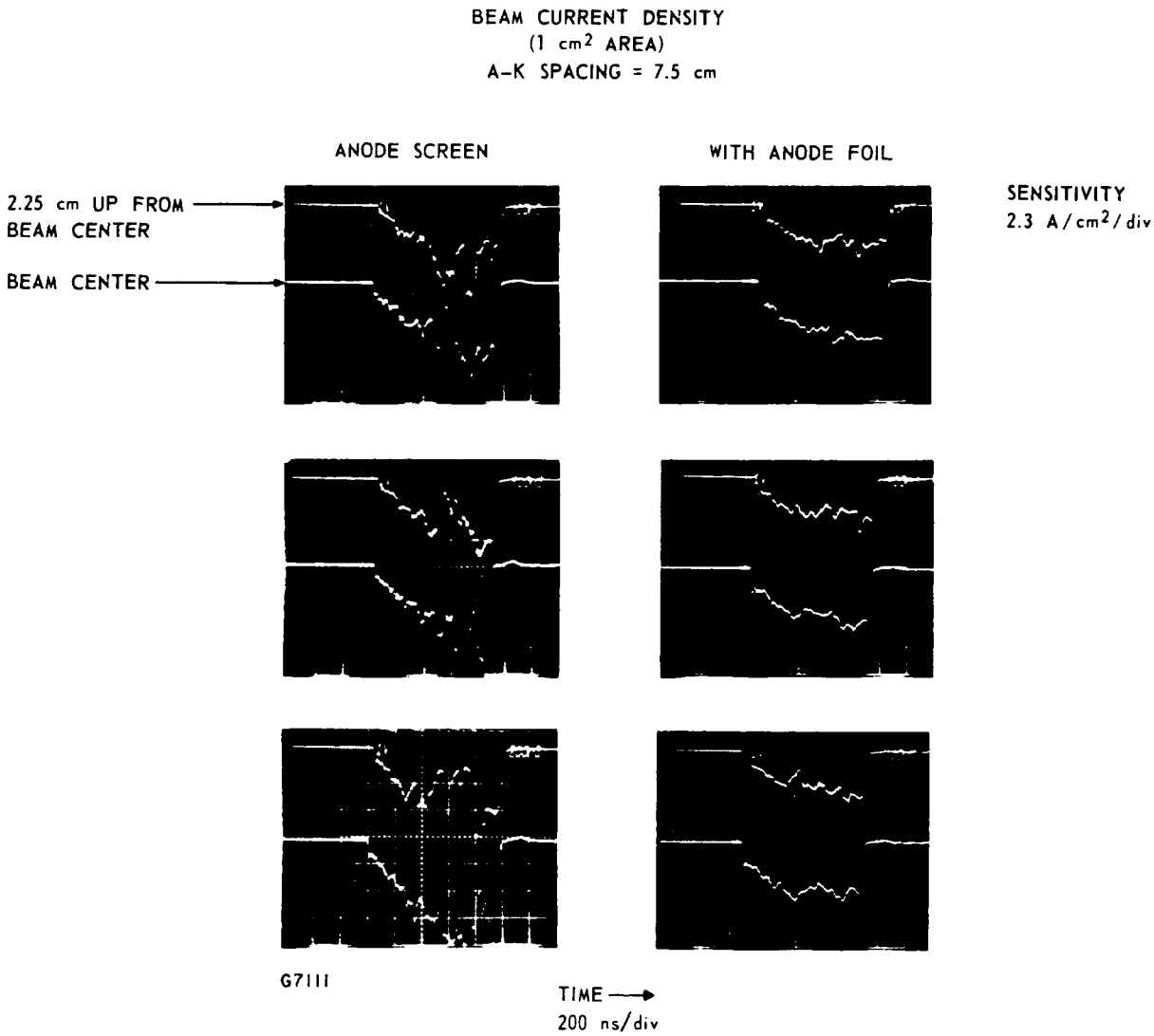

Figure II-14 Averaging Fast Beam Current Fluctuation by Scattering Through Anode Foil.

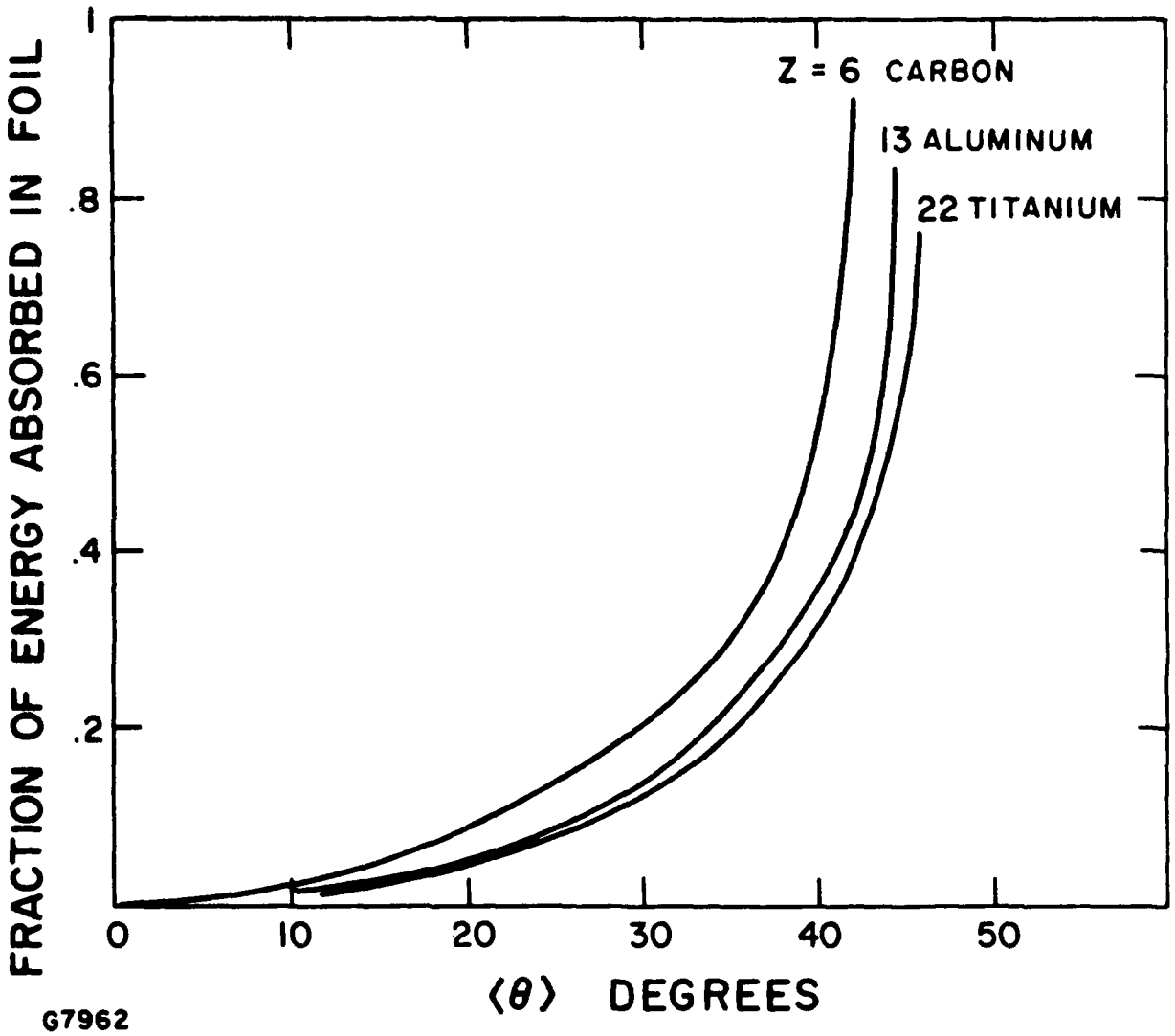

Figure II-15 Fraction of E-Beam Energy Absorbed by the Foil as a Function of Foil Scattering Angle.

C. PHOTOELECTRIC CATHODES

The photoelectric effect was first noticed in 1887 when Hertz[6] initiated a spark between two widely separated electrodes by exposing the negative electrode to ultraviolet radiation. Nearly 18 years later Einstein[7] successfully explained the photoelectric phenomenon as a quantum effect having the following properties for metals.

(a) for constant spectral composition of the radiation source, the photoelectric current density, J is proportional to the source irradiance, H.

$$J = kH \tag{II-11}$$

(b) The maximum kinetic energy of photoelectrons is independent of source irradiance and varies linearly with radiation frequency, ν above some threshold frequency $_o$

$$\frac{1}{2}(mv^2)_{max} = h(\nu - \nu_o) \tag{II-12}$$

(c) The time delay between incident radiation and emitted photoelectrons is immeasurably short. Subsequent data shows this time to be < 3 nsec.[8]

Using these properties a concept for producing broad area, high current density e-beams using photoelectric cathodes has been developed under an AERL-IRAD sponsored program. An embodiment of this concept is shown in Figure II-16 where it is seen that current flow is initiated by uniformly illuminating the cathode with flashlamps enclosed in a Faraday cage formed by the anode screen and e-beam window. The electrons so liberated are accelerated by the potential applied between the anode and cathode. This potential can be maintained by a simple capacitor blank since current flow is coincident with the light pulse. Since this capacitor bank must store at least 20 times the e-beam pulse energy, a

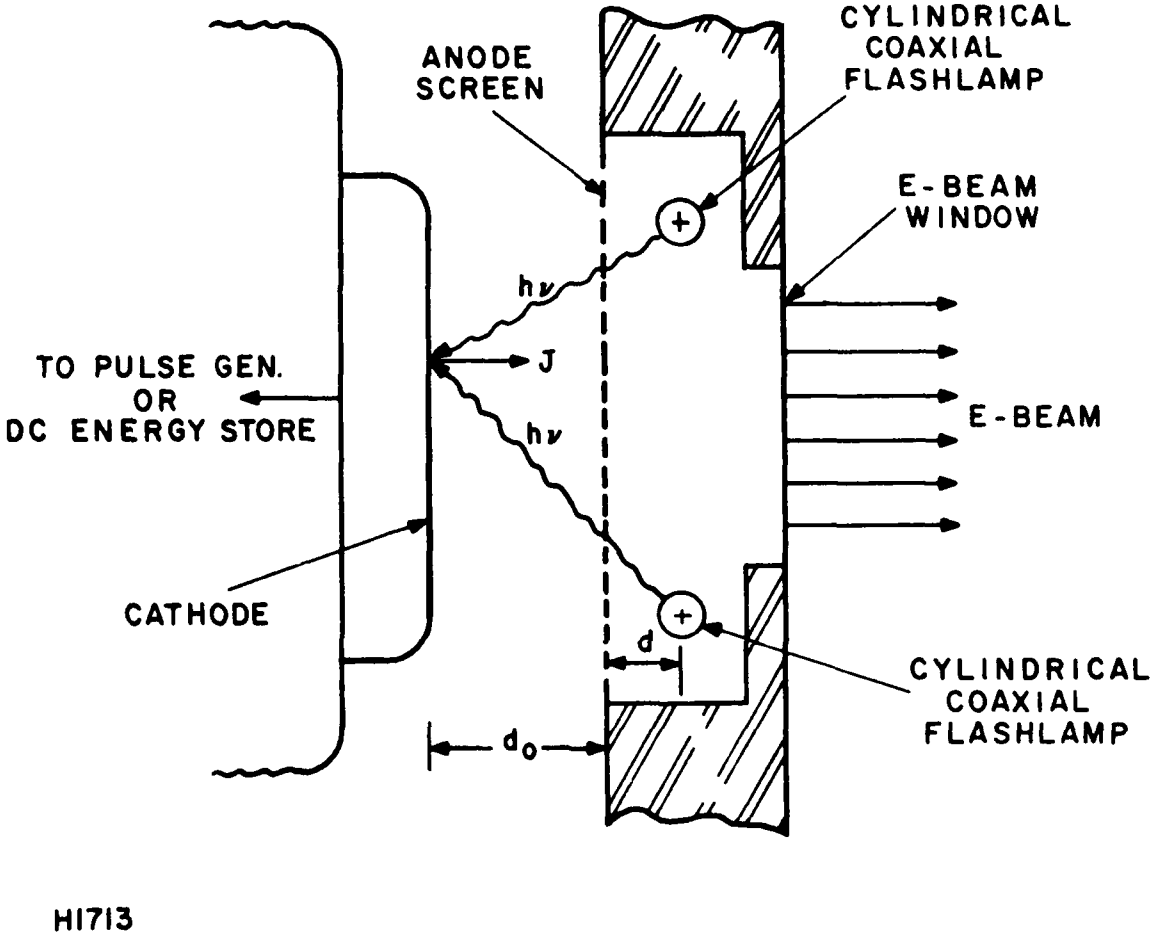

Figure II-16 Photocathode E-Beam Generator

smaller energy storage system could be made by using a pulse forming network (PFN) for which the stored energy is approximately equal to the e-beam pulse energy. Of course, in order to match PFN and e-gun impedances, the cathode should be illuminated for the entire electrical pulse.

Photocathodes do not require the formation of a cathode plasma for their operation, and hence the problem of diode closure which presently limits the pulse widths of cold cathodes is eliminated. Also the current density (pulsed or cw) obtainable from thermionic cathodes is determined by its operating temperature which also determines the rate at which thermal emissive materials (e.g., barium and strontium oxides) are evaporated from the cathode surface. Evaporation of these materials can adversely affect useful cathode life, emission uniformity and vacuum high-voltage standoff capability. By operating at room temperature, photoemitting cathodes do not exhibit either of these limitations.

The current density leaving an illuminated cathode is estimated to be

$$J = \frac{e}{hc} \langle\lambda\rangle \langle\gamma\rangle \langle H_n\rangle \qquad \text{(II-13)}$$

where

$\langle\gamma\rangle$ = average cathode quantum efficiency (electrons per incident photon) in the spectral range between and $(\lambda + \Delta\lambda)$

$\langle\lambda\rangle$ = average spectral wavelength = $\lambda + (\lambda + \Delta\lambda)/2$

$\langle H_n\rangle$ = average normal irradiance of the cathode surface in the spectral range between λ and $(\lambda + \Delta\lambda)$

e = electronic charge

h = Planks constant

c = speed of light

Both lasers and high intensity flashlamps can be used to illuminate photocathodes. If flashlamps are used, they almost certainly have to be coaxial in order to reduce the total circuit inductance. This allows the flashlamp gas to be heated to high temperatures ($> 20{,}000^{o}K$) by loading it with large amounts of energy (hundred's of J) in times on the order of a few microseconds. Such flashlamps were developed[9] ~ 10 years ago and have an average brightness of ~ 250 W/cm^2 in the range between 2000 Å and 3000 Å. The lamp-to-cathode spacing, $(d_o + d)$ in Figure II-16 should be minimized in order to reduce the r^{-1} decrease in lamp irradiance. The dimension d_o is determined by the Child-Langmuir relation for space charge limited current and the dimension d is determined by the electrostatic requirements of the lamps (lamp electrical gradients exceed 1 kV/cm of active length). The opacity as a function of viewing angle of the anode screen is appreciable and must be accounted for in determining the normal irradiance of the cathode surface. Both the r^{-1} decrease in lamp irradiance and the effect of screen opacity can be accounted for by a single effect attenuation factor G such that

$$\langle H_n \rangle = G\, B_o\, \Delta\lambda \qquad \text{(II-14)}$$

where

G = effective geometric attenuation factor

B_o = lamp brightness in spectral range between and $(\lambda + \Delta\lambda)$

For lamp-to-cathode spacings typical of 300 kV, 10 A/cm^2 e-beams using 25 cm lamps and anode screens with wire spacing to diameter ratios of 40, G = 0.26. Thus, for the described flashlamp,

$$\langle H_n \rangle = 0.26 \times 250 \times 1000 = 65\ kW/cm^2 \qquad \text{(II-15)}$$

In the spectral range between 2000 Å and 3000 Å, many metals such as aluminum and magnesium have quantum efficiencies[10] between 10^{-5} and 10^{-3} electrons per photon. Thus, using $\langle\lambda\rangle = 2500$ Å,

$$J = \frac{e}{hc} \times (2500 \times 10^{-10}) \times (10^{-3}) \times (65 \times 10^{-3}) = 13 \text{ A/cm}^2 \qquad \text{(II-16)}$$

Thus, it is seen that appreciable photoelectric currents can be generated in a practical system using cathodes with extremely low quantum efficiencies. More sensitive photoemissive materials with quantum efficiencies approaching 100% are presently used in conventional vacuum photodiodes. Many of these materials also are capable of emitting high current densities and, if cooled properly, could do so at high-repetition rates. The principle difficuly with these materials, however, is that they are poisoned upon contact with air and other reactive gases used in UV and visible lasers. By poisoning, it is meant that their quantum efficiencies are reduced to zero. Thus, in order to realize the advantages of high quantum yield materials, one must:

(a) fabricate and/or expose sensitive photoemissive cathodes only in the evacuated e-gun vacuum chamber.

(b) develop air-exposable materials which have high quantum efficiencies over a broad spectral range.

The first approach is a viable option for the end use applications of UV and visible lasers where the consequences of e-beam window foil rupture extend far beyond the attendent cathode poisoning.

The second option has not been explored simply because up to this time there has not been a need to develop efficient photocathodes for use outside the vacuum enclosures in which they are fabricated. Developments in this area would be most beneficial since efficient air exposable photocathodes would greatly facilitate e-gun fabrication and use.

1. Photoelectric E-Gun Efficiency

Increasing quantum yield also improves overall e-gun efficiency. Efficiency is defined as

$$\eta = \frac{P_{eb}}{P_{eb} + P} \qquad \text{(II-17)}$$

where

$$\begin{aligned} P_{eb} &= J\phi_o = \text{e-beam power density} \\ J &= \text{e-beam current density} \\ \phi_o &= \text{e-beam energy} \end{aligned} \qquad \text{(II-18)}$$

$$\begin{aligned} P_f &= J(h\nu)/G\langle\gamma\rangle\eta_{el} = \text{flashlamp power density} \\ h\nu &= \text{initial energy of photoelectrons} \\ \eta_{el} &= \text{electrical efficiency of flashlamp in the spectral range between } \lambda \text{ and } (\lambda + \Delta\lambda) \end{aligned} \qquad \text{(II-19)}$$

By combining Eq. (II-16) through Eq. (II-18) the photoelectric e-gun efficiency is found to be

$$= 1 + \frac{1}{\frac{h\nu}{\phi_o} \quad \frac{1}{G\eta_{el}\langle\gamma\rangle}} \qquad \text{(II-20)}$$

This relation is plotted in Figure II-17. Coaxial flashlamps of the type used in the AERL-IRAD program have electrical efficiencies of ~ 8% for the spectral range between 2000 Å and 3000 Å and, therefore, liberated photoelectrons have an average maximum energy of ~ 5 eV. From Figure II-17 it is seen that the overall e-gun efficiency is quite acceptable for quantum yields > 10^{-2} electrons/photon.

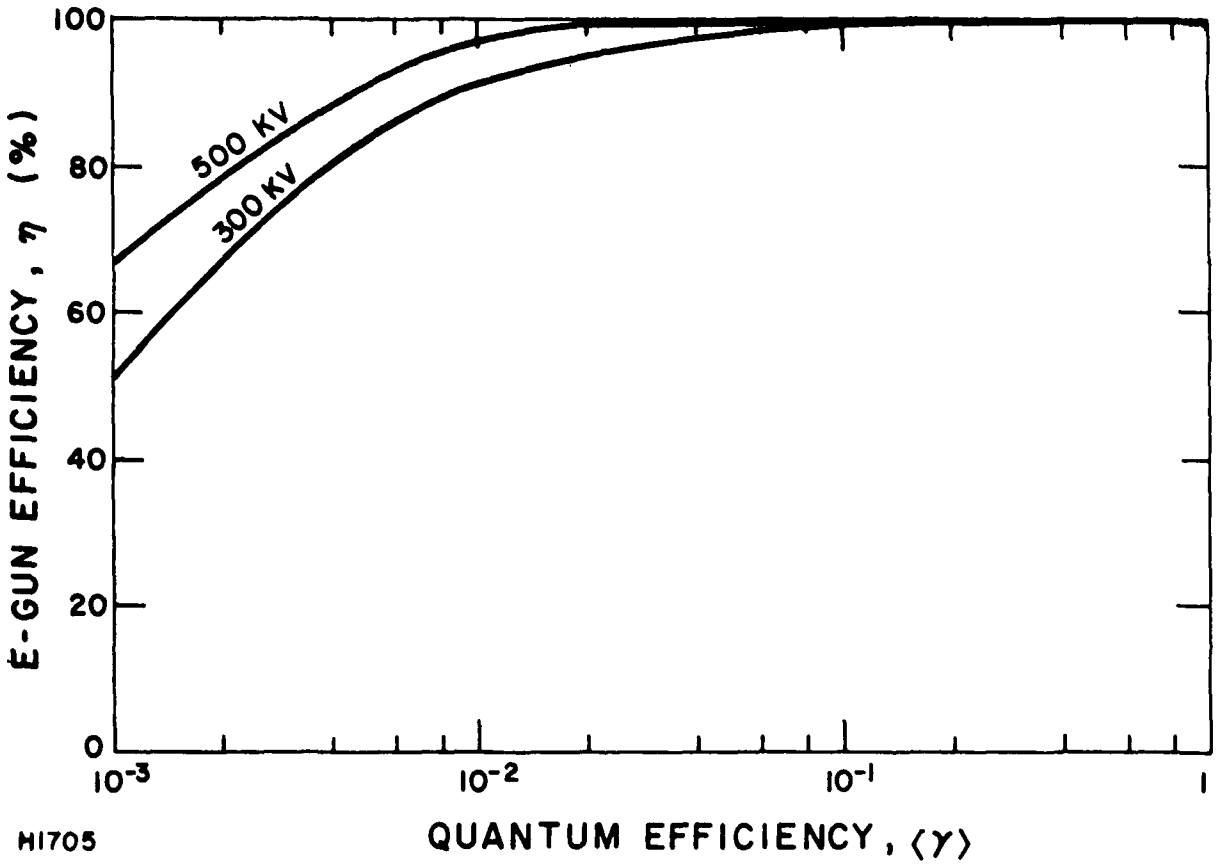

Figure II-17 E-Gun Efficiency, P_{out}/P_{in} as a Function of Cathode Quantum Efficiency.

2. Flashlamp Shields

An embodiment of a broad area photoelectric e-gun concept is shown in Figure II-18. Very uniform cathode illumination is achieved by appropriately adjusting the ratio s/y. In this scheme, however, there must be some method devised to protect the quartz envelope of the flashlamp from high energy electron bombardment. E-beam electrons will very quickly darken this envelope and substantially reduces light transmission. One method of shielding the flashlamps is shown in Figure II-19. In Figure II-19(a), only the axial guide B-field applied. This magnetic field is required to avoid beam pinching as described in Section E.1. By passing a current through a conductor running axially through the flashlamp center, a circular magnetic field is produced which surrounds the flashlamp center, a circular magnetic field is produced which surrounds the flashlamp as shown in Figure II-19(b). As shown, this circular field opposes the guide field on the top of the flashlamp and adds to the guide field below the flashlamp bottom. When both fields are applied the total magnetic field goes around the flashlamps as shown in Figure II-19(c). Similarly electrons spiralling about these magnetic field lines will also miss the flashlamps. Magnetic fields on the order of several kilogauss must be produced at distances of ~ 1 cm from the quartz envelope to produce an electron spin radius small enough to miss the flashlamp envelope. This requires a magnetomotive force of 10,000 to 20,000 ampereturns in the flashlamp center conductor. This net current flows transverse to the applied guide field and, therefore, the flashlamp must be built to withstand forces of up to 12 lbs/cm which for a 2 cm diameter flashlamp is comparable to a differential pressure of 1 atm.

Another method of shielding the flashlamps is to apply a non-emissive coating on the cathode surface directly opposite each flashlamp. The transverse dimension of this coating should be slightly larger than the flashlamp diameter so that electrons constrained to follow the applied guide field would miss each

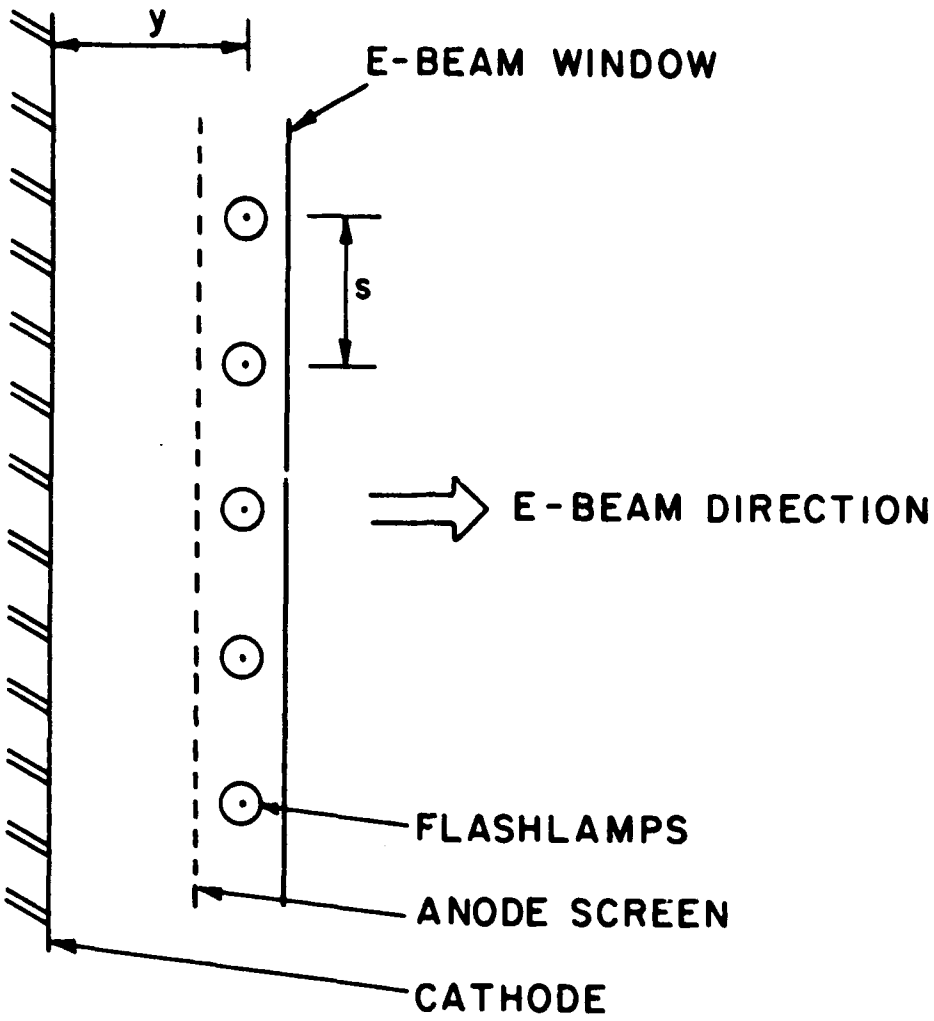

H1706

Figure II-18 Broad Area Photoelectric E-Gun Using a Multiplicity of Coaxial Flashlamps.

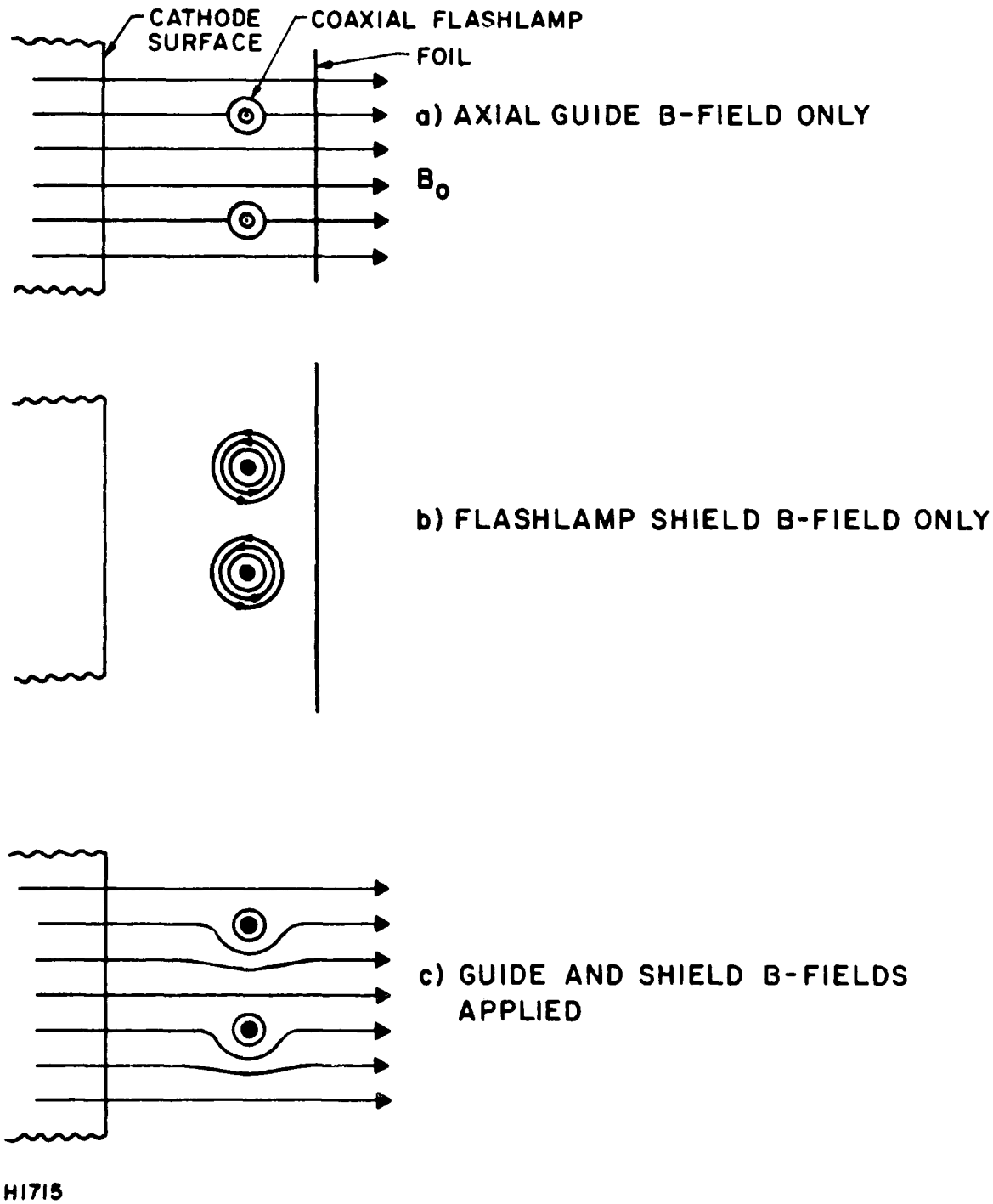

Figure II-19 Magnetic Shield for Flashlamps

flashlamp. A disadvantage to this approach not shared by the previous method is that the masked area of the cathode is lost to the conduction process. For large diameter flashlamps with the ratio $s/y \sim 1$ required for uniform illumination, this area could become appreciable. Thus the first method, although not as simple, might be considered for very large current density e-guns.

D. THERMIONIC CATHODES

1. General

Thermionic cathodes have been used to generate e-beams for over 60 years.[11,12] Small area thermionic cathodes have found extensive use in both low and high-power hard tube rectifiers and gridded amplifiers, thyratrons, klystrons and magnetrons and have performed very reliably. In these applications, high repetition rates ($\geq 10^3$ Hz) at high beam current densities ≥ 10 A/cm^2 have been achieved in sealed off tubes for thousands of hours of operation. These e-guns can be operated at pulse lengths up to 1 msec since diode closure does not limit pulse length.

In recent years, broad area ($> 10^4$ cm^2), low current density (≤ 1 A/cm^2) e-beams have been required for CO_2 and CO laser applications. These e-beams have been produced most reliably by filamentary tungsten emitters operated at very high temperatures (2800°K). For the high beam current densities required for visible and UV lasers, however, tungsten emitters, though rugged and dependable, produce insufficient current per unit of filament power. This is shown by considering the current density obtainable from a thermionic emitter at temperature T is given by the Richardson equation

$$J_p = \frac{4 \pi m Ce}{h^3} (kT)^2 e^{-\phi/kT} \qquad \text{(II-21)}$$

where

ϕ = Work Function

h = Planck's Constant

k = Boltzmann's Constant

At a given cathode temperature, T, the current density obtainable varies as the inverse exponential of the work function ϕ. Since BaO and SrO-coated cathodes have considerably lower work functions than tungsten ($\sim$ 1.5 eV for barium as compared to $\sim$ 4.6 eV for

tungsten), much lower cathode temperatures can be used to obtain a given current density.

A comparison of emitted beam current densities plotted against cathode temperature is given in Figure II-20 for various cathode materials. The filament power required for a given emission density is balanced by the power lost to radiation and conduction. At high temperature the radiation power dominates. Since the power radiated which varies according to the Stefan-Boltzmann law as T^4, the filament power required for tungsten is much larger than that required for oxide-coated cathodes. A plot of the power radiated per cm^2 of surface area as a function of cathode temperature is given in Figure II-21. For example, at a cathode emission density of 10 A/cm^2, tungsten cathodes must be operated at $\sim 2800^oK$ and oxide coated cathodes at $\sim 1100^oK$. At 2800^oK, tungsten has a total emissivity of 0.4 and at 1100^oK oxide-coated cathodes have an emissivity of ~ 0.3. Consequently, with tungsten emitters a total filament power of at least 139 W/cm^2 of emission are required while for oxide-coated emitters 2.5 W/cm^2 are required. For a tungsten cathode with an area of 10^4 cm^2, at least 1.39 MW of filament power would be needed while for a similar oxide-coated cathode the corresponding power is only 25 kW. The large additional filament requirements for tungsten cathodes lead to heating of internal gun insulators and the e-beam window. For example, direct radiative heating of the foil from the cathode surface (with a flux of ≥ 100 W/cm^2) can, when added to e-beam foil heating, severely limit the repetition rate of the gun and can lead to reduced pulse widths for single pulses of high current densities. Severe heating of the insulators can lead to increased conductivity, thermal runaway and eventual voltage breakdown. The large filament voltage and/or currents required for tungsten can also lead to filament voltage breakdown or unacceptable deformation of the beam by the magnetic fields created by the filament current.

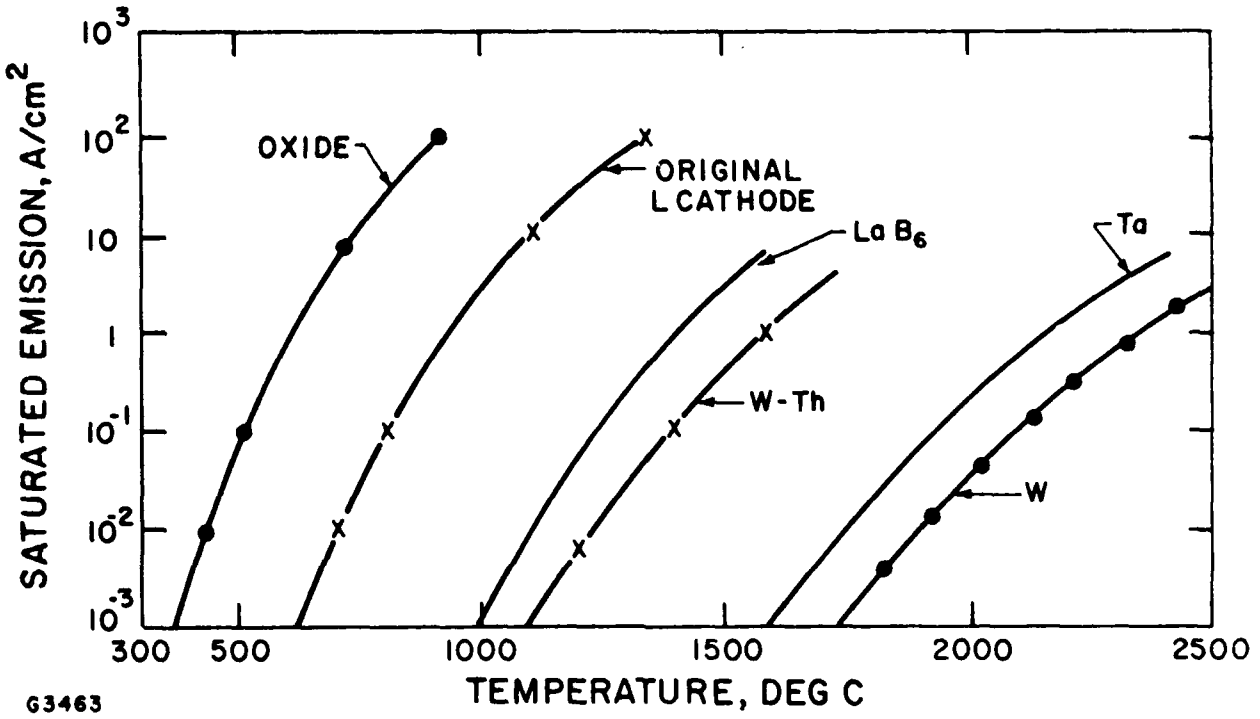

Figure II-20 Emission Density Plotted Against Cathode Temperature for Various Cathode Materials.

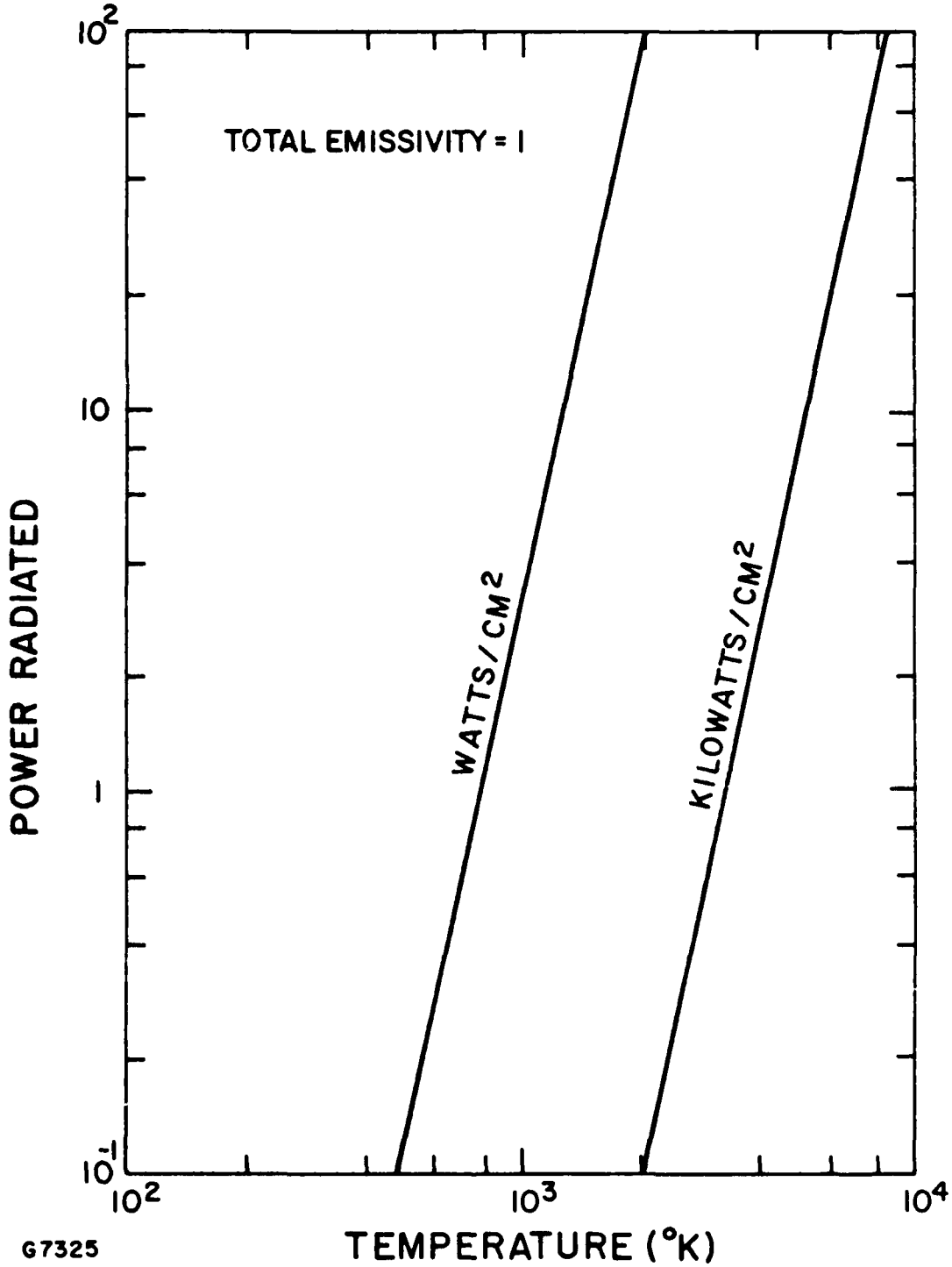

Figure II-21 Power Radiated From a Surface Plotted Against Surface Temperature. Unit surface emissivity is assumed.

The principal advantages of thermionic cathodes when compared to cold cathodes arise because no cathode plasma is necessary for beam formation. Consequently, many of the constraints imposed upon cold cathode gun design by the formation of this plasma (diode closure, etc.) are avoided if thermionic cathodes are used. Since diode closure is not present with thermionic cathodes, gridded gun control using low voltage switches becomes possible. A typical thermionic gun configuration with grid control is shown in Figure II-22. In this particular design, as relatively low voltage, high current density e-beam is formed in an "inner box" which is held at a large negative potential. The low energy beam is then accelerated in the region between the inner box and the grounded screen to full energy. The accelerating field in this region is on continuously and consequently no high-voltage, high repetition rate switch is required. In the off condition, the control grid is biased ~ 1 kV with respect to the potential of the cathode and the inner box. To turn the gun on, the cathode is pulsed negatively to the desired voltage. If the cathode pulse voltage is chosen sufficiently low, the PFN driving the cathode can be switched with hydrogen thyratrons and high repetition rates are possible. At the same time this pulse voltage allows space charge limited cathode-grid spacings of ≥ 1 cm with reasonable tolerances of ≤ 0.05 cm. With a constant negative bias of ~ 1 kV on the grid, the beam electrons are not significantly intercepted by the grid wires and heating of these wires is minimized.

a. Life at High Current Densities

Several excellent review papers have been written detailing the performance of thermionic cathodes. A review of past work[11,12] indicates that much of the work on thermionic cathodes performed prior to the 1940s concentrated on the dc emission properties of these cathodes. Under dc operating conditions it was found that the maximum current density which could be drawn from oxide coated cathodes under cw and dc operation was

DUAL CHAMBER THERMIONIC GUN DESIGN

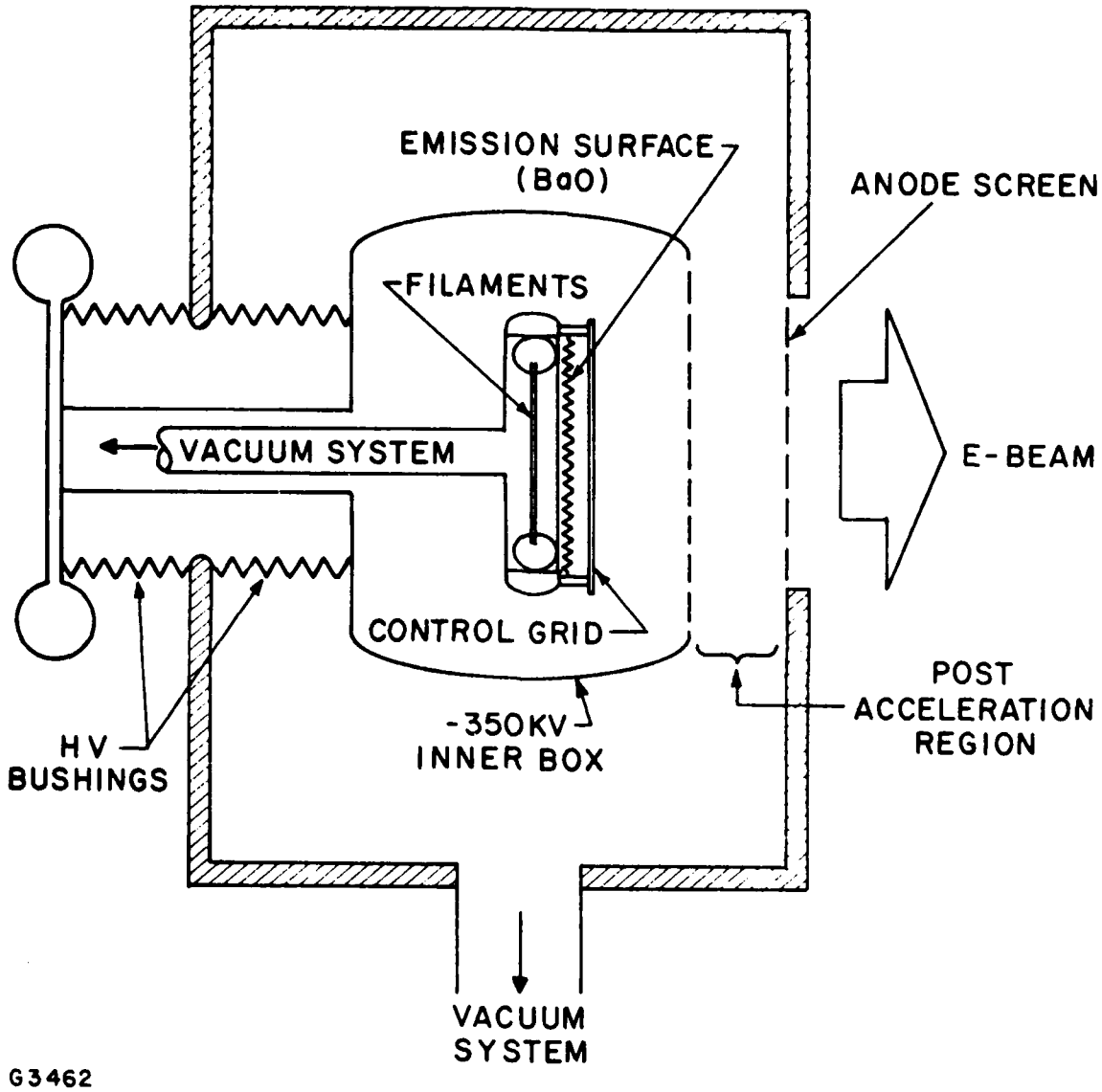

Figure II-22 Cross-Sectional View of a Thermionic Electron Gun. The e-beam is formed at relatively low voltage in the inner box and gains most of its energy in the post-acceleration region.

$\sim 1\ A/cm^2$. The current density is limited by the finite conductivity of the low work function oxide coating from which electron emission is obtained. In general, at dc current densities above $1\ A/cm^2$, the resistive (I^2R) heating of the oxide layer leads to thermal runaway and the oxide coating is rapidly boiled away.

In the 1940s, however, the short pulse ($\sim 1\ \mu sec$) performance of these cathodes for magnetron applications was studied. It was found that very high current densities ($\geq 100\ A/cm^2$) could be extracted from these cathodes for tens and hundreds of microseconds at high repetition rates. In fact Buck and Clogston[12] have shown that small area, oxide-coated cathodes can be run at $10\ A/cm^2$ for 500 hrs at a repetition rate of 10^3 Hz and a pulse length of $10\ \mu sec$. These data indicate that the lifetime of oxide-coated cathodes for current densities up to $20\text{-}30\ A/cm^2$ is ≥ 100 hrs as long as the average current density, $J_p\ t_p\ f_o$, is $\leq 1\ A/cm^2$. Since e-beams for visible and UV lasers are likely to require average beam current densities of $10^{-2} A/cm^2$ ($10\ A/cm^2 \times 10^3\ Hz \times 10^{-6}$ sec) heating of the oxide coating is not expected to be a problem.

b. Homogeneity at High Current Densities

Positive ions can be formed at the gun anode if gas is evolved when the solid parts of the anode structure are heated by the beam. The electric field stress concentrations at the anode can ionize this gas and the resulting positive ions can be accelerated through 300 to 500 kV to the oxide-coated cathode. Small positive ions currents can actually help keep the cathode activatd by dissociating the alkaline earth oxides to produce the free alkaline earth metal which is thought to be the electron source. The fact that cathode activation is greatly facilitated by application of a positive potential to the anode in processing is considered sufficient evidence of this action. Experiments[13] indicate that large, pulsed ion current densities with ion energies of up to 20 keV can bombard oxide-coated cathodes for hundreds of hours with no serious deterioration of the coating.

Large average positive ion currents however can anomalously heat the oxide coating and destroy its emission properties. In the present applications ions formed at the cathode will gain roughly 10 times as much energy than is typical in most microwave tube applications, and positive ion formation must be carefully controlled. Clean vacuum conditions must be maintained and a vacuum operating pressure of $\leq 10^{-6}$ torr will be required to insure that no positive ions are formed by ambient gas ionization. The gun anode should be constructed so that few positive ions are generated at its surface. Nonintercepting grid and anode designs will be investigated. With these precautions, positive ion bombardment of the oxide-coated cathode should be maintained at acceptable levels.

c. Power Dissipation

The average filament power required to generate a 300 keV, 5 A/cm^2, 1 μsec e-beam repetitively-pulsed at 10^3 Hz should be less than the average power in the e-beam for oxide-coated cathodes. As discussed above, under fully activated conditions and neglecting any conduction losses, the average power density radiated in this case $\sim$ 2.5 W/cm^2. If the radiating area of the hot cathode surface is approximately twice the area of the electron emitting surface (a worst case assumption since radiation shields can be used) $\sim$ 5.0 W/cm^2 of emission surface is required to drive the heater filaments. For the e-beam described above, 1500 W/cm^2 of beam power is obtained from the emitting surface. Therefore, the filaments may, under optimum conditions, require a negligible amount of electrical power.

The power radiated from the thermionic emitter can heat the beam transmission foil. The magnitude of this effect can be seen by comparing curves (3) and (5) in Figure II-23.

2. Dispenser Type Cathodes

The thermionic cathode selected for the present test program is of the dispenser type shown schematically in Figure II-24. This cathode type, first used in gaseous discharge tubes in

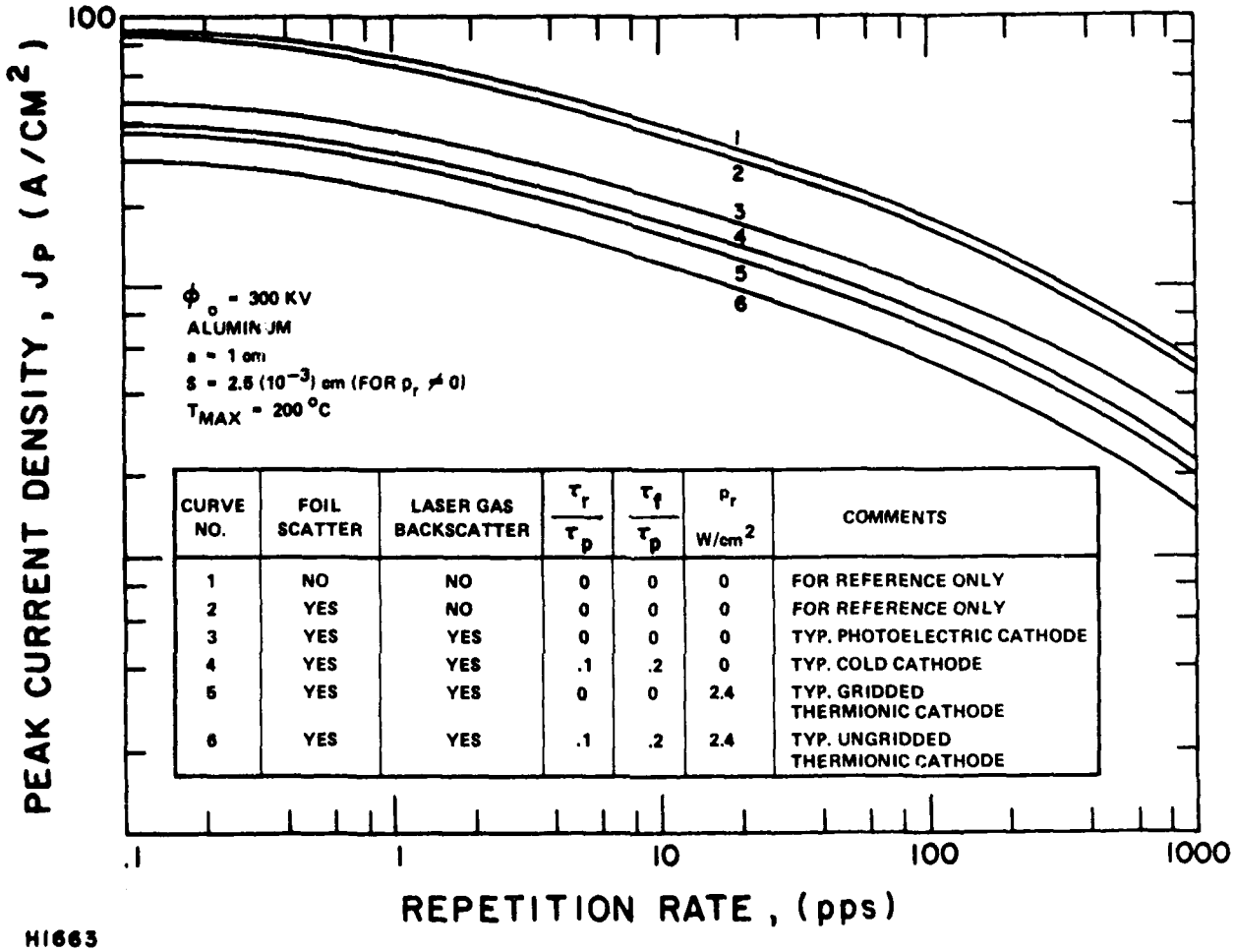

CURVE NO.	FOIL SCATTER	LASER GAS BACKSCATTER	τ_r / τ_p	τ_f / τ_p	p_r W/cm²	COMMENTS
1	NO	NO	0	0	0	FOR REFERENCE ONLY
2	YES	NO	0	0	0	FOR REFERENCE ONLY
3	YES	YES	0	0	0	TYP. PHOTOELECTRIC CATHODE
4	YES	YES	.1	.2	0	TYP. COLD CATHODE
5	YES	YES	0	0	2.4	TYP. GRIDDED THERMIONIC CATHODE
6	YES	YES	.1	.2	2.4	TYP. UNGRIDDED THERMIONIC CATHODE

Figure II-23 Effects of Steady-State and Pulsed Heat Loads on Maximum Current Density for Conduction Cooled Windows.

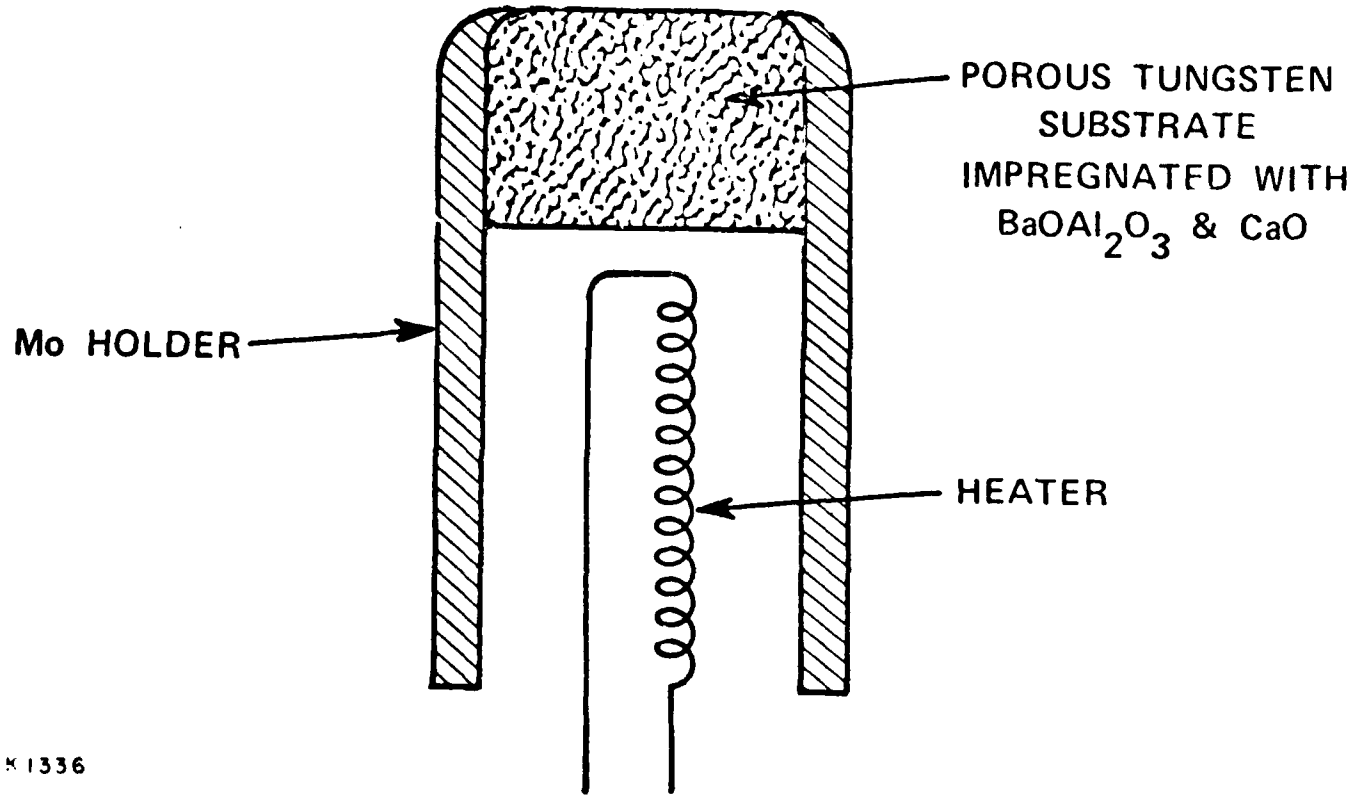

Figure II-24 Dispenser Type Thermionic Cathode

1939[14] was developed and refined[15-36] during the period 1950 to 1970 principally to overcome the limitations of oxide-coated cathodes. More recent developments were reported at the Tri-Service Cathode Workshop in 1978.[39-52]

In operation, an impregnant, usually consisting of various combinations of barium-aluminum oxides and calcium oxides, is continuously diffused to the vacuum surface of the heated porous tungsten substrate. With 20 to 40 percent porosity and small hole size, rapid transverse migration establishes a continuous low work function emitting surface. In the event of cathode damage (e.g., by backstreaming ions) the low work function cathode surface is very quickly re-established by the migration process. This "self-healing" capability is one of the major advantages of the dispenser-type thermionic cathode.

The surface reactions of importance for dispenser thermionic cathode operation are shown in Figure II-25. The cathode temperature must be raised to the point where the arrival rate of diffused barium exceeds the rate of barium removal caused by evaporation, neutral reaction, ion reaction and ion sputtering.

The evaporation rate determines the operating life of the cathode as projected in Figure II-26. For example, in order to achieve a saturation current density of 20 A/cm^2, the cathode surface must be maintained at $\sim 1200^{\circ}C$. The barium evaporation rate at that temperature is such that all the barium in the 31180-cathode is evaporated in $\sim$ 200 hr, an exceptable lifetime for many DARPA applications.

The neutral reaction rate determines the required operating vacuum level of the e-gun. The arrival rate of chemically active elements must be considerably less than the arrival rate of barium diffused to the surface from the volume of the porous tungsten matrix. The worst offender of the commonly present elements is oxygen. However, as shown in Figure II-27, if the partial pressure of oxygen is kept below 10^{-6} torr, then no appreciable oxygen poisoning occurs for cathode temperatures corresponding to operation at tens of A/cm^2.

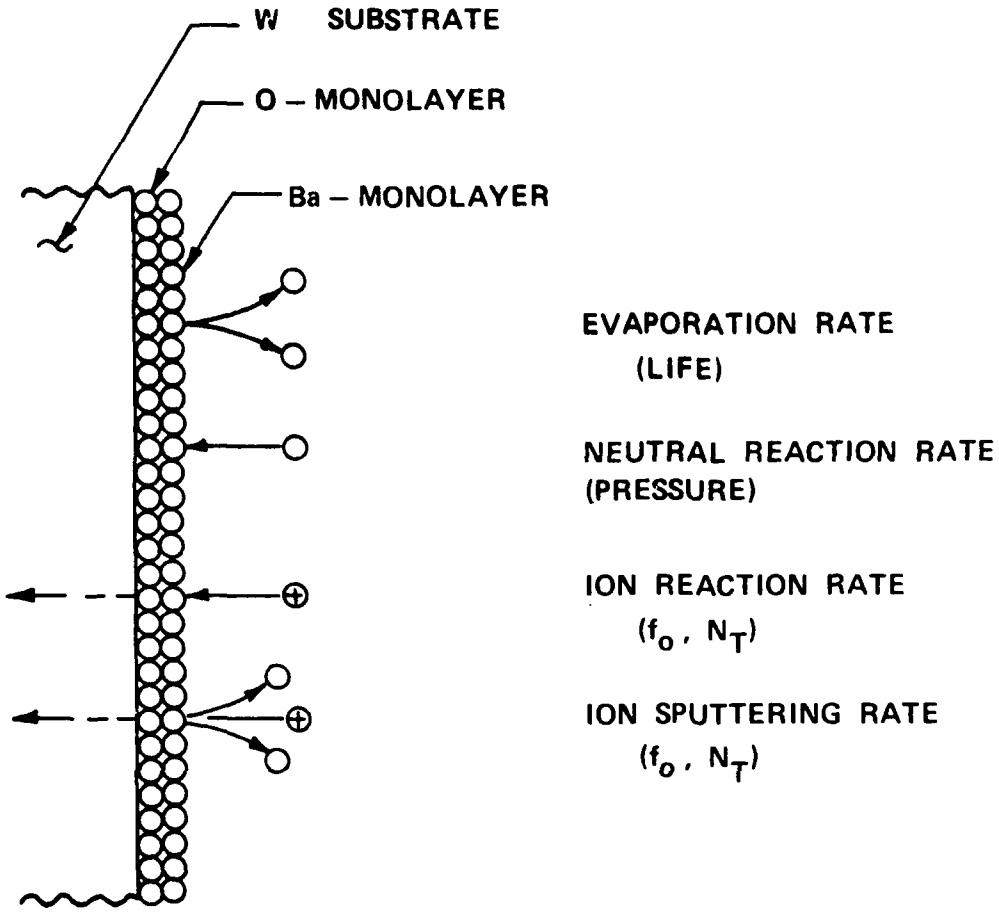

POISONING MECHANISMS CONSIDERED

1. IMPLANTATION OF ~1 MONOLAYER OF HIGH ENERGY IONS
2. AVERAGE ARRIVAL RATE $\gtrsim$ Ba DIFFUSION RATE

H7112

Figure II-25 Dispenser Cathode Surface Reactions

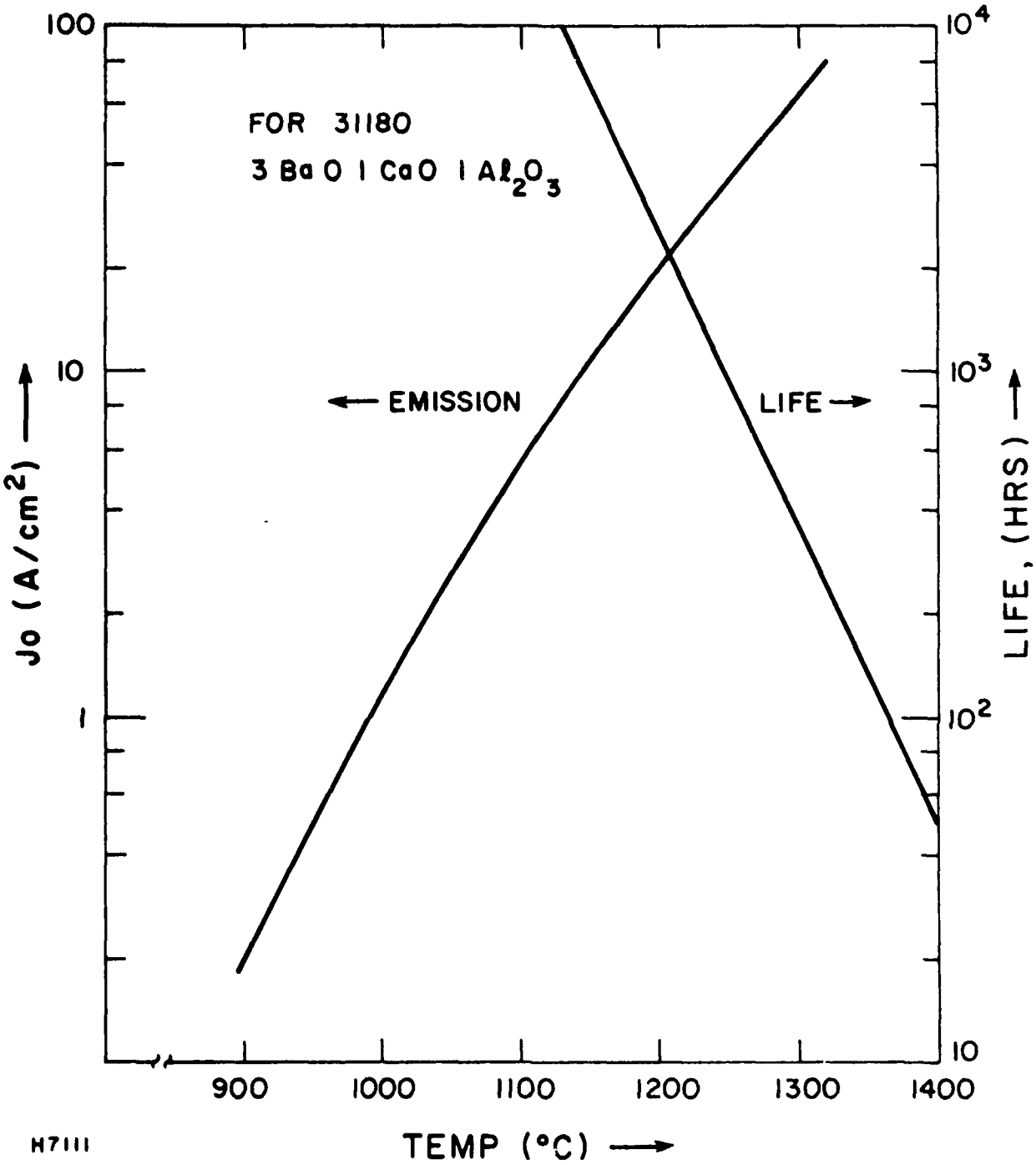

Figure II-26 Projected Dispenser Thermionic Cathode Life and Emission Density vs. Temperature.

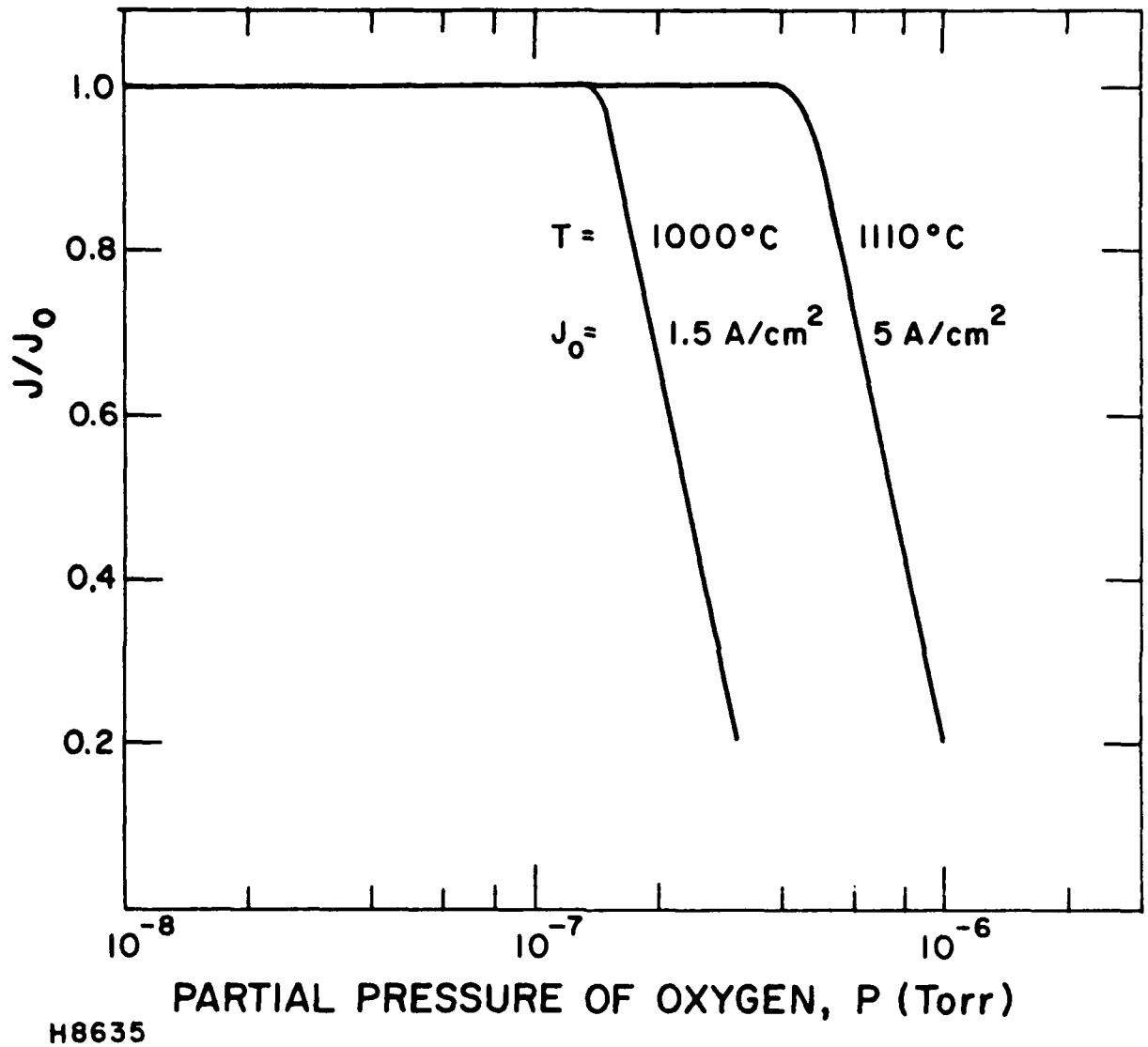

Figure II-27 Cathode Poisoning by Background Gas

Backstreaming ions have several detrimental effects on cathode operation. In general, ions are slightly more chemically active than their parent neutral atoms. Therefore, there is a maximum ion reaction rate allowable that is very similar to the neutral reaction rate just described.

High energy ions also cause sputtering and poisoning by implanted ions which cannot be subsequently evaporated. The ion sources encounted in e-guns and their relative contribution to ions arrving at the cathode is shown in Table II-1. As seen in this table the most severe source is direct secondary ions generated when high energy electrons strike the anode.

On the basis of an assumption that ion poisoning can occur when one monolayer of ions has been implanted in the cathode surface (using ion generation rates measured by Trump and Van De Graff[53] then the effect of backstreaming high energy ions can be seen in Figure II-28. At 20 A/cm^2, the repetition rate is constrained to < 600 Hz with a total shot limitation of ~ 2000 pulses.

While sputtering removes atoms from the cathode surface barium will rediffuse over the affected area unless extreme melting has taken place. For displacement energies in the range of 10 to 40 eV, 500 keV ions can sputter 40 to 100 cathode atoms as indicated by Figure II-29.

TABLE II-1

- VOLUME IONIZATION OF BACKGROUND GAS

$$\frac{Ni}{N_e} = n_o \int_o^{do} \sigma(\phi)\, dx = \frac{n_o}{\sqrt{Jo}} \times 10^{-14} = \underline{\underline{6 \times 10^{-6}}}$$

- SURFACE IONIZATION OF BACKGROUND GAS

$$\frac{Ni}{N_e} = \alpha_s \sigma_i\, n_o\, 2 \left(\frac{\phi_s}{\phi o}\right) do = 3.6 \times 10^{-8}$$

- SURFACE IONIZATION OF DESORBED GAS

$$\frac{Ni}{N_e} = \alpha_s \sigma_i \left(\alpha_s \sigma_d \frac{Ng}{vg} \frac{Jo}{e}\right) 2 \left(\frac{\phi_s}{\phi_o}\right) do = 7.5 \times 10^{-9}$$

- DIRECT SECONDARY ION GENERATION

$$\frac{Ni}{N_e} = \underline{\underline{2.2 \times 10^{-3}}}$$ TRUMP & VAN DE GRAAFF

H8507

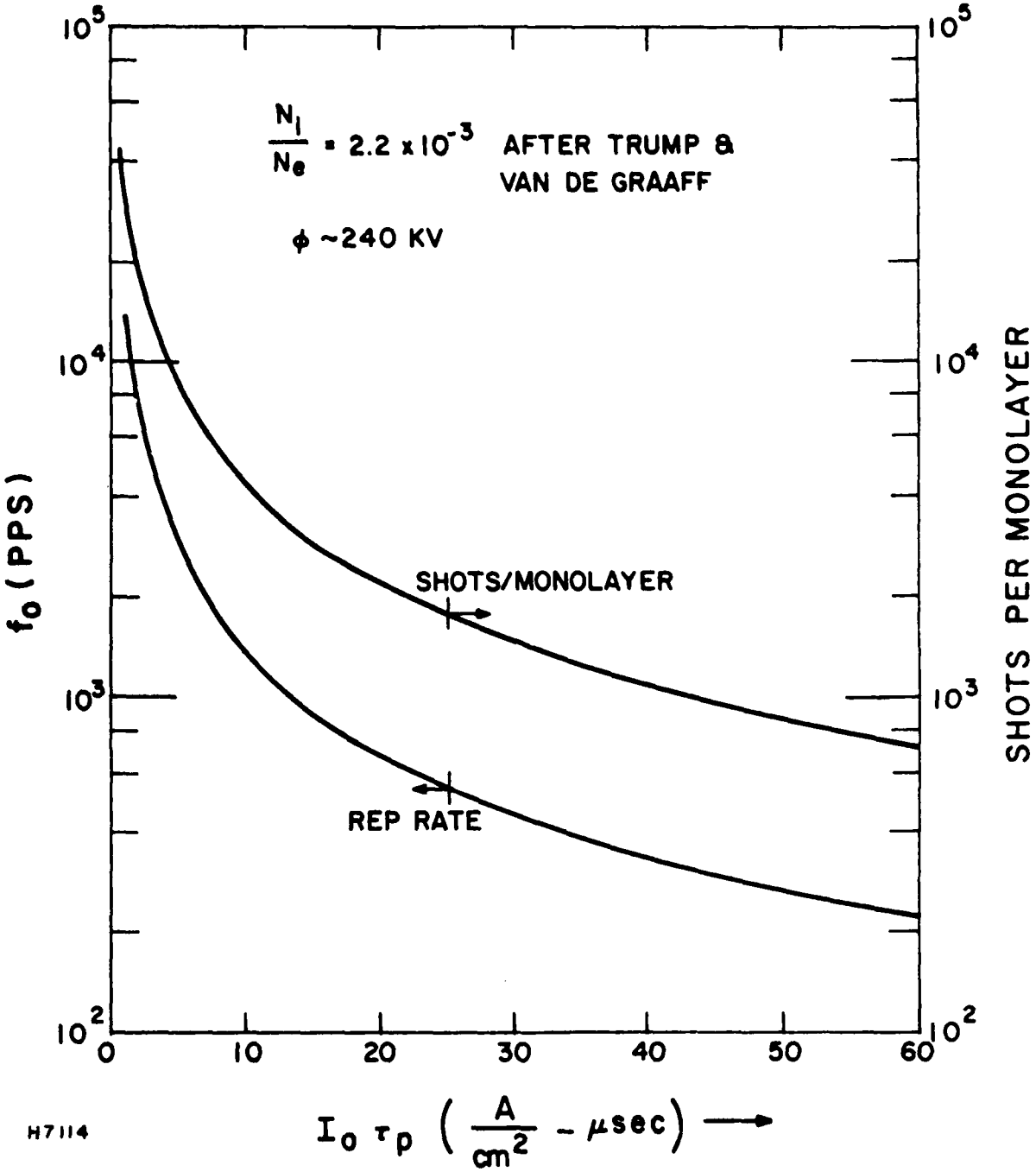

Figure II-28 Direct Secondary Ion Backstreaming

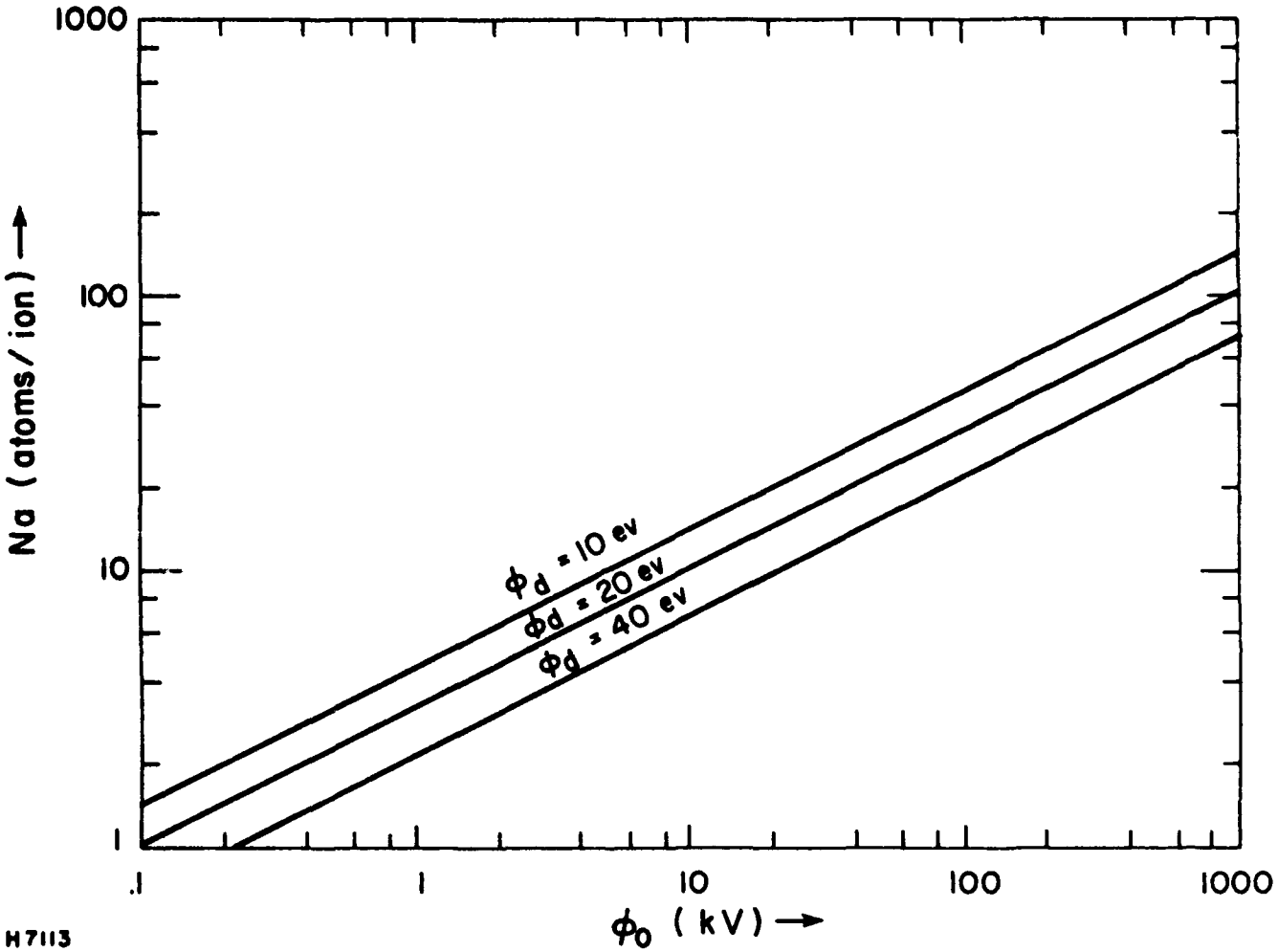

Figure II-29 Sputtering Yield of High Energy Backstreaming Ions.

E. MAGNETIC FIELDS

1. Beam Pinching

A limitation common to broad area, high current density e-beams is beam pinching. The propagation of high current density e-beams is determined by space charge and self-magnetic field forces. In free space, the electrostatic forces which tend to diverge the beam are always larger than the magnetic field forces which tend to converge (pinch) the beam. However, in the usual e-gun configuration, the transverse electric field generated by the beam space charge is substantially reduced by the conduction anode and cathode structures so that essentially only the self-magnetic field force acts on the beam. Therefore, high current density, broad area e-beams are known to pinch rather than diverge as they propagate for short distances in metallic drift tubes. The pinching of a broad area beam under the influence of its self-magnetic field can produce large transverse nonuniformities as illustrated schematically in Figure II-30.

For e-beam pumped lasers, these large transverse nonuniformities appreciably reduce overall laser efficiency. In lassers pumped by e-beam controlled discharge pumped lasers, the effects of beam pinching is more serious. Spatial inhomogeneities in the discharge are amplified and beam pinching can lead to uncontrolled arcs.

The magnetic field acting on the edge beam electons and the resulting Larmor radius of these electrons are plotted as a function of $J_{eb}h$ in Figure II-30. As shown in this figure, the beam electrons pass through the anode screen obliquely. In the drift region between the anode screen and foil, the e-beam continue to converge because of its self-magnetic field. The scaling constraints imposed by this self-magnetic field are shown in Figure II-31 where it is seen that current densities on the order of 20 to 40 A/cm^2 limit the cathode transverse dimension, h, to < 20 cm.

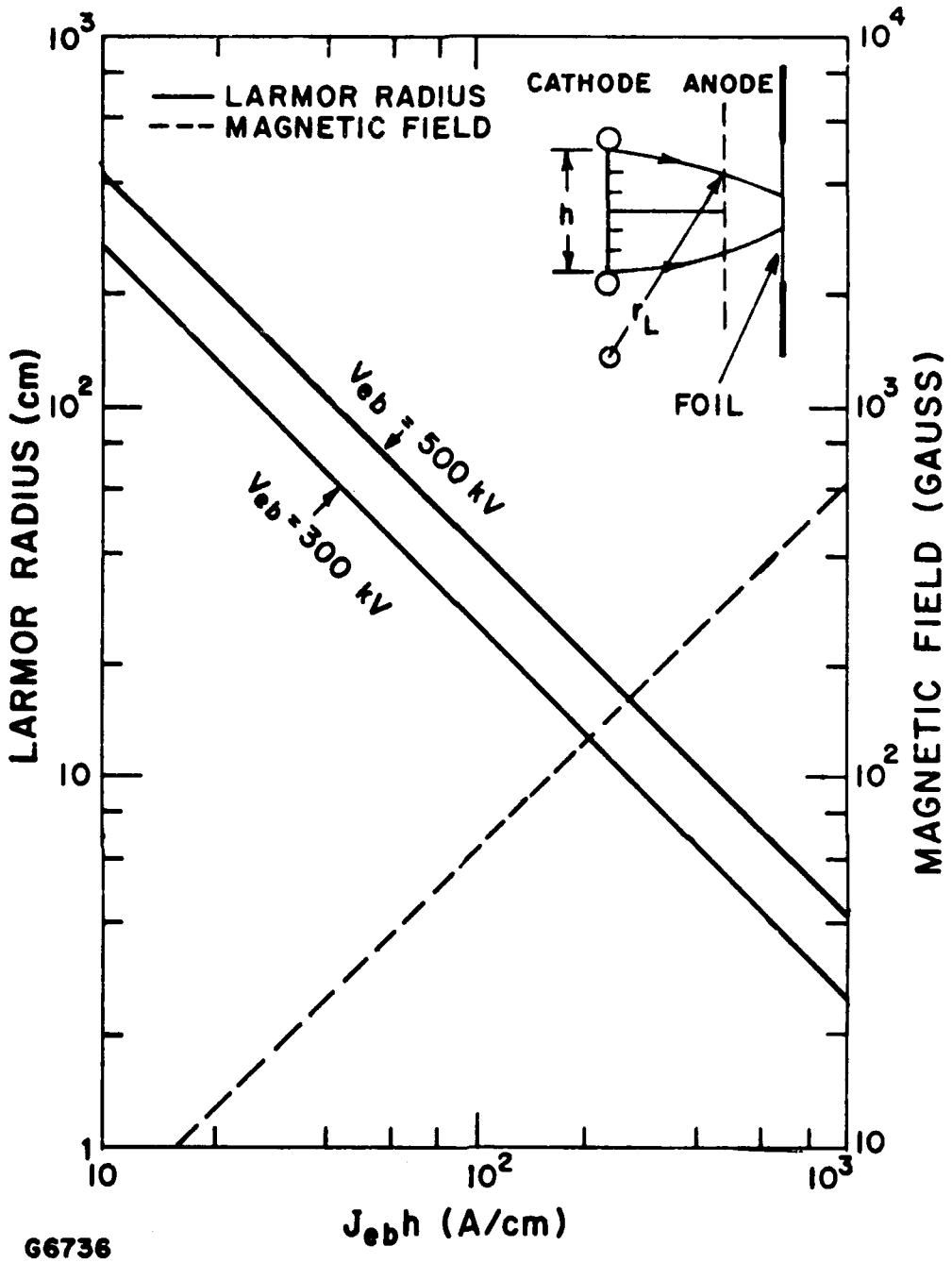

Figure II-30 The Larmor Radius of a Beam Electron at the Gun Anode is Plotted Against the Product of Beam Current Density and Beam Height. The magnetic field seen by the edge beam electrons is also plotted.

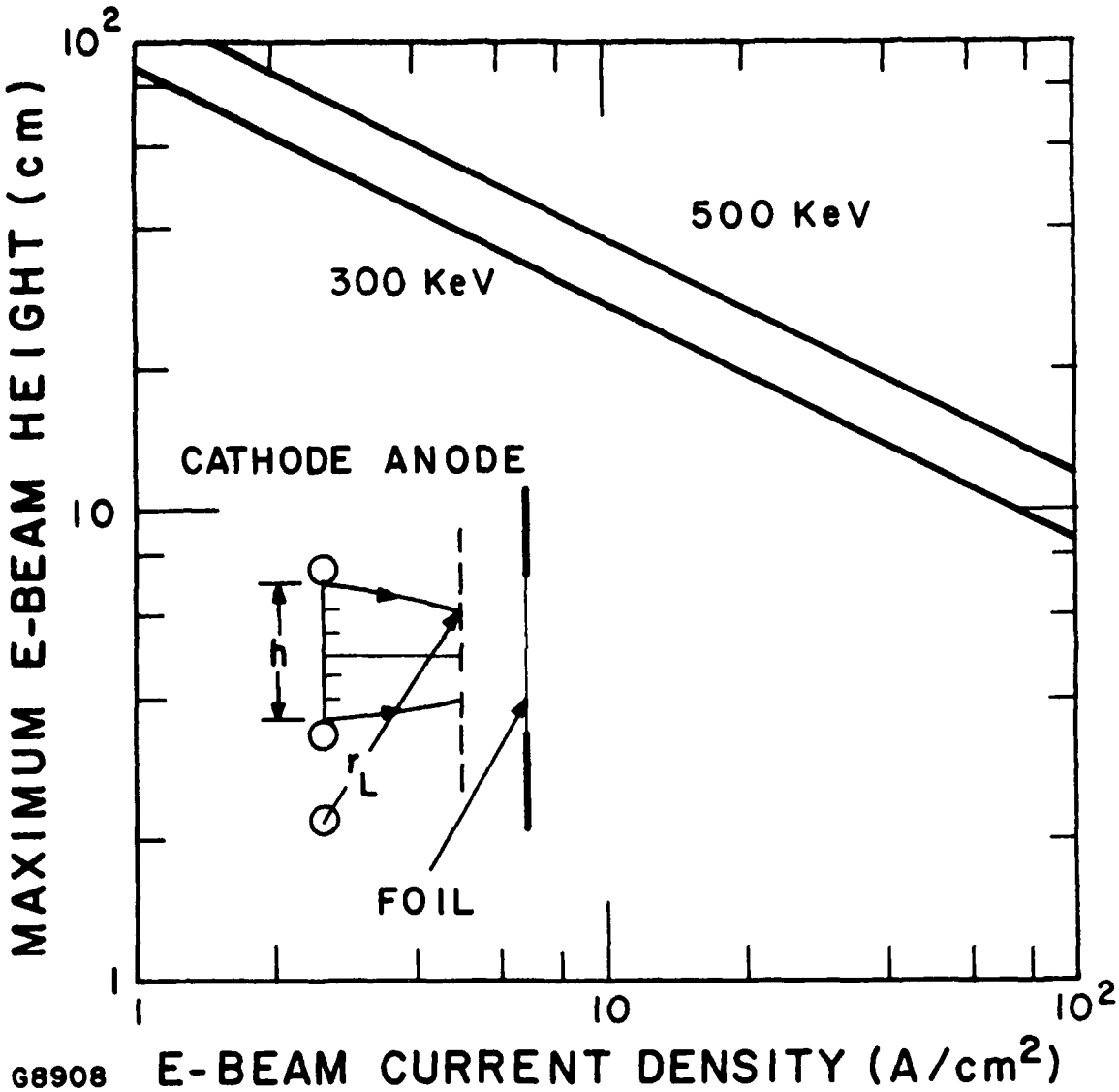

Figure II-31 Scaling Constraints on E-Beam Height (No External Magnetic Field).

Beam pinching is evident in the transverse profile of the e-beam shown in Figure II-32 for anode-cathode spacings, d_o of 6 and 8 cm at a cathode voltage of 300 kV. These data, obtained by microdensitometering Cinamoid™ strips which were exposed to the beam, show that the beam profile converges as the current density increases. The peak diode current density determined by Child's law varies as d_o^{-2} and was 16 and 9 A/cm^2 for the 6 and 8 cm cases respectively.

The large transverse nonuniformities for the higher current densities lead to large nonuniformities in the small signal gain of direct e-beam pumped lasers such as KrF. The result is that the extraction efficiency is reduced significantly.

2. Guide Magnetic Field

In order to produce a more uniform transverse e-beam density profile, AERL developed the use of a strong external magnetic field applied parallel to the desired beam direction. This magnetic field must be much larger than the self-magnetic field felt by the edge beam electrons at the highest beam current densities of interest. For example, if a maximum beam current density of 15 A/cm^2 is desired in the laser medium and the anode and foil support structures have a transparency of 70%, the magnetic field seen by the edge beam electron is 130 G (from Figure II-30 with h = 10 cm). To produce the applied magnetic field, two copper coils are placed outside the gun vacuum chamber as shown in Figure II-33. These coils provide a magnetic field of ~1000 G to guide the beam electrons as shown in this figure. The coils are driven by commercially-avaiable welding supplies capable of producing 1500 A at 40 Vdc.

The magnetic field generated with these coils guide the e-beam from the cathode surface to the anode and prevent the pinching of the beam under the influence of its own magnetic field. In addition, in discharge-pumped experiments, this external magnetic field will guide the beam and prevent pinching due to the magentic field associated with the discharge current.

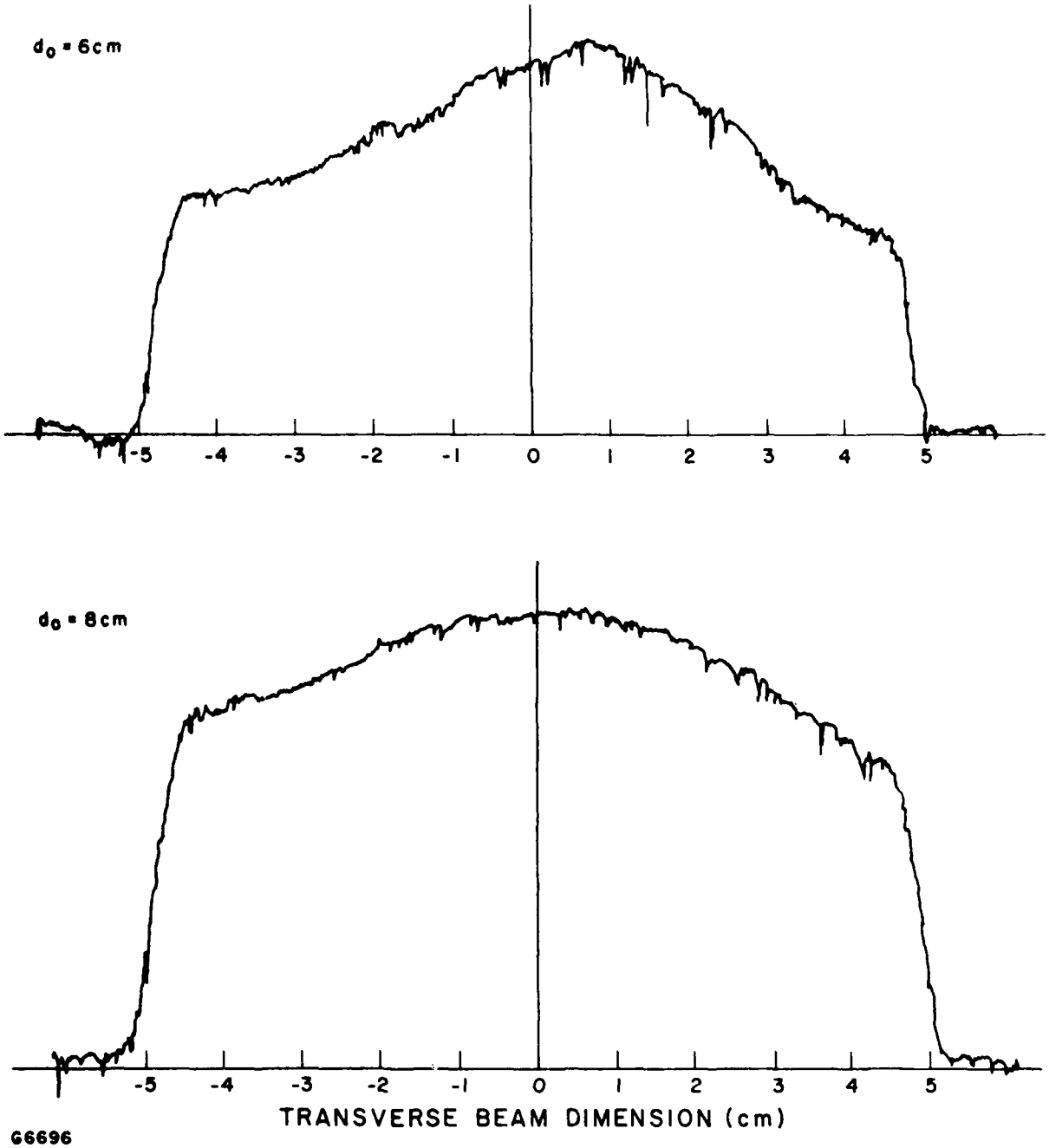

Figure II-32 Transverse Beam Profiles for Gun Anode-Cathode Spacings of 6 and 8 cm.

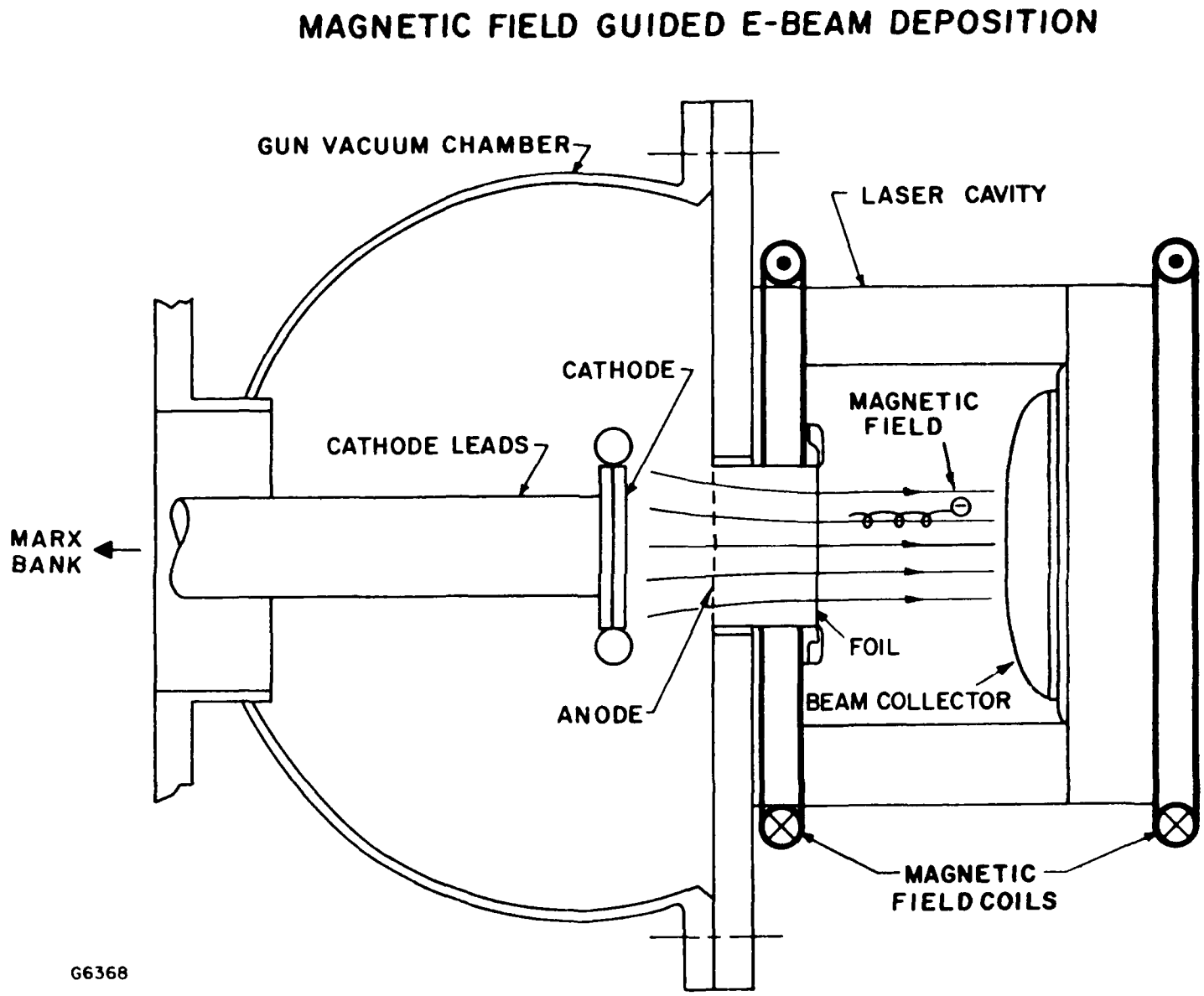

Figure II-33 Externally Applied Magnetic Field Used to Reduce Beam Pinching.

AVCO EVERETT

The effects of the applied magnetic field are shown in Figure II-34. The lower oscilloscope traces show the beam current transmitted through a 1 mil titanium foil. These currents were measured with Faraday cups placed at the beam center (h = 0) and at the beam edge (h = 2.5 cm). The current density at the beam center is ~ 1-1/2 times as large as the current density near the beam edge without an applied magnetic field and that they are nearly equal with an applied magnetic field of (~ 800 G).

Additional advantages to using an applied magnetic field are illustrated in Figures II-35 through II-37. Figure II-35 shows the luminescence produced by the e-beam as it passed through the laser medium with and without an externally applied magnetic field. As electrons pass through the foil and laser medium, they are scattered through large angles as shown in the left photograph of Figure II-35. There is a corresponding decrease in the energy deposited in the active (central) portion of the laser medium. With an externally applied magnetic field, the electrons cannot scatter and remain concentrated in the active laser medium as shown in the right photograph of Figure II-35.

The laser burn pattern shown in Figure II-36 shows the effect of beam pinching on laser output. With no applied field, the laser burn pattern is limited to the central region of the cavity. With external magnetic field applied, the laser energy fills the cavity to a larger extent as shown in Figure II-37. The incomplete filling shown in both photographs is, in part, due to insufficient e-beam accelerating voltage for the anode-to-cathode spacing used.

The coils used to produce the applied magnetic field are constructed using flat copper, insulated conductors as shown in Figure II-38. The design and mounting of these coils takes into account the large magnetic forces which occur when they are energized.

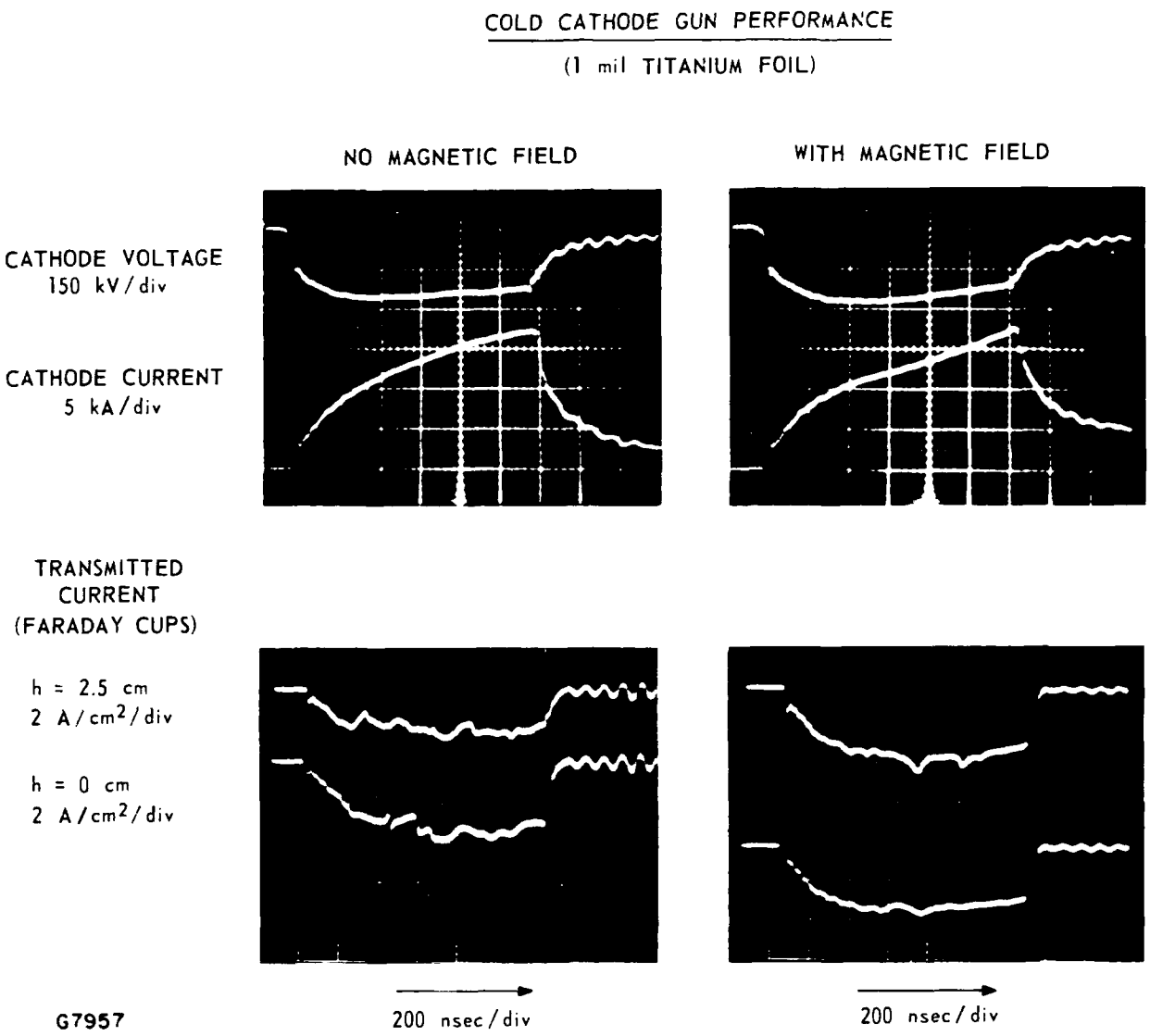

Figure II-34 Effects of Applied Magnetic Field

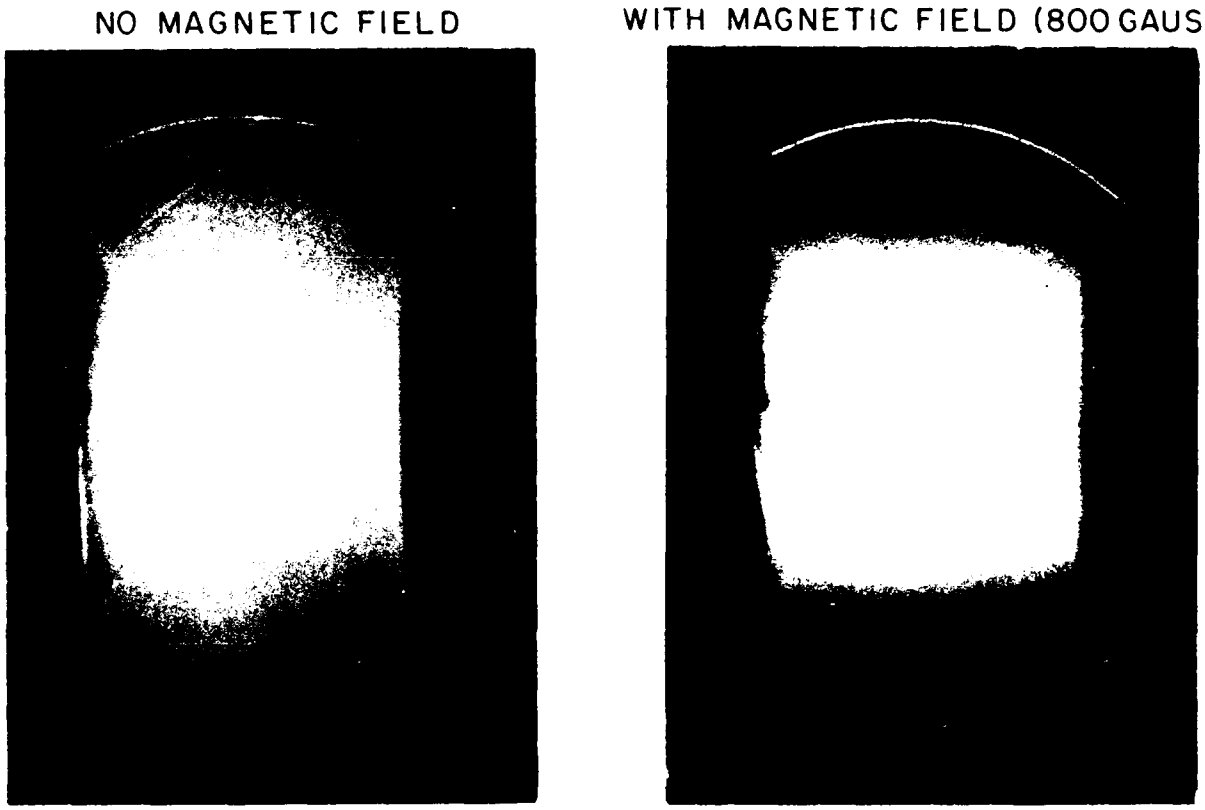

Figure II-35 Magnetic Steering of the E-Beam (1 mil Titanium Foil)

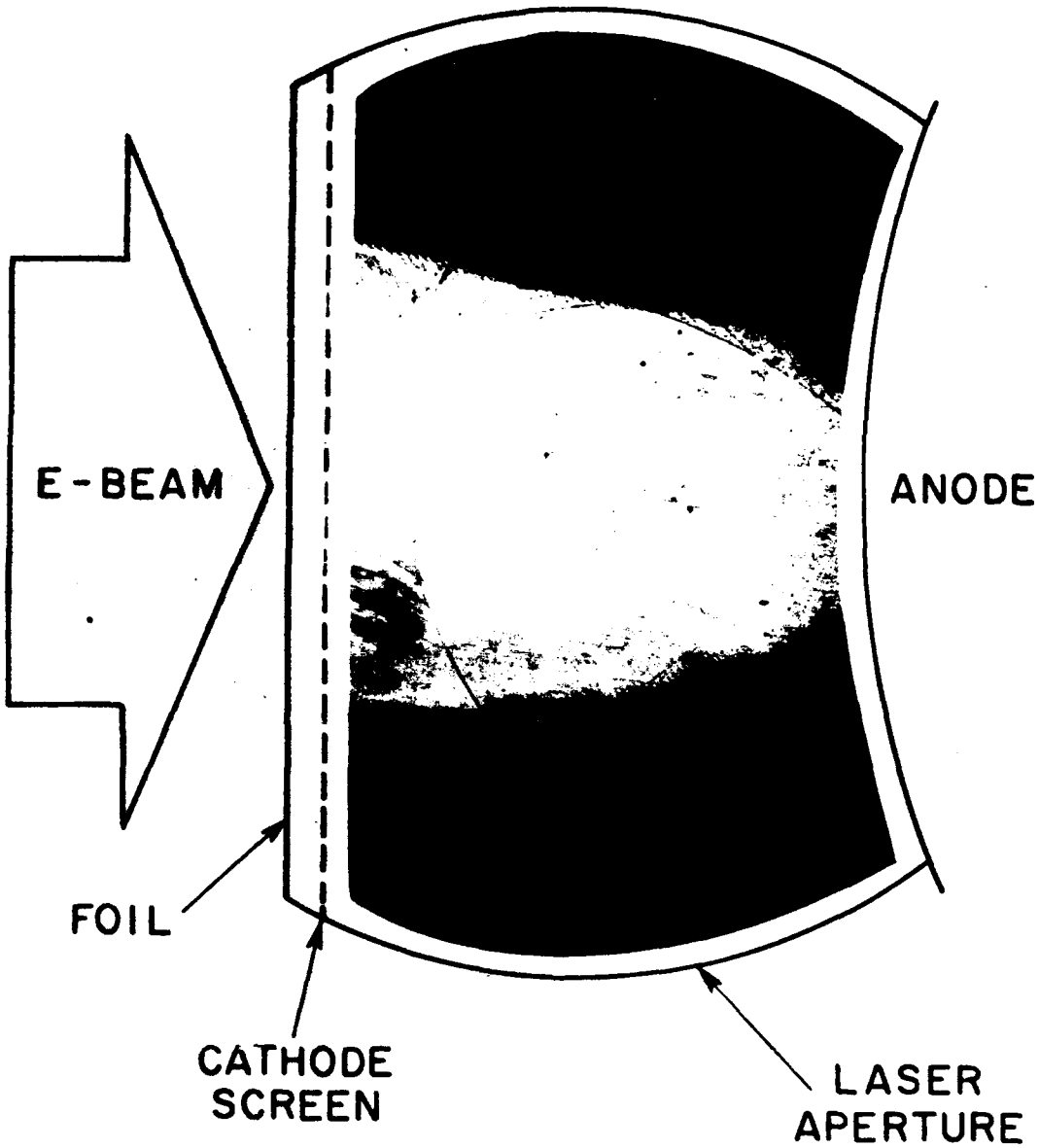

H1126

Figure II-36 KrF* Laser Burn Pattern (No Magnetic Field

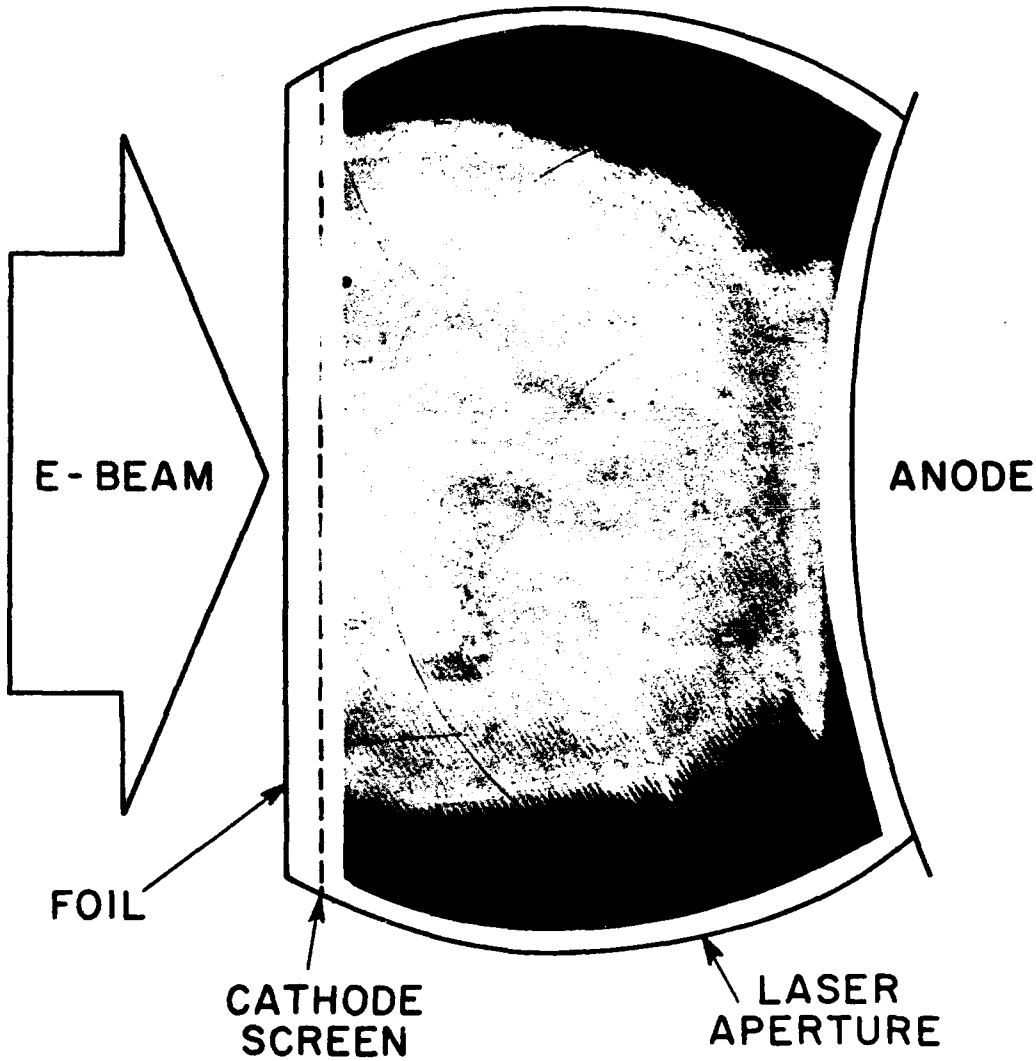

H1127

Figure II-37 KrF* Laser Burn Pattern (800 G Magnetic Field)

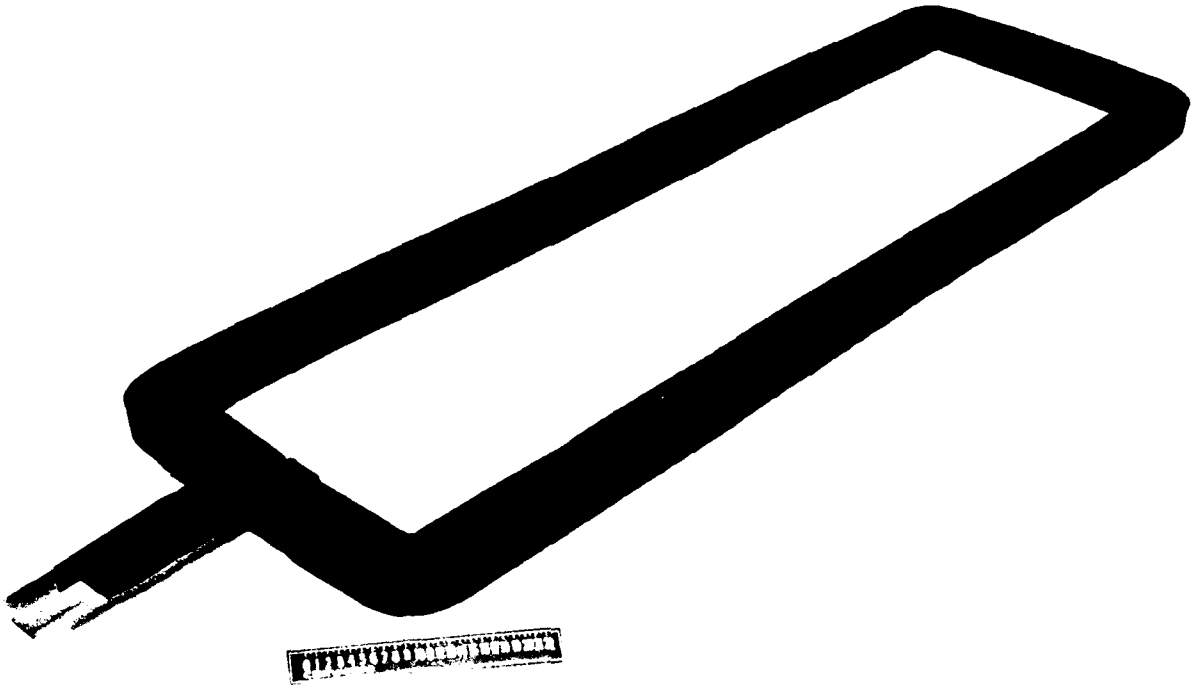

G7247

Figure II-38 Magnetic Field Coil

F. E-BEAM WINDOWS

1. Foil Heating and Cooling

The lasing media of both direct e-beam pumped and e-beam controlled discharge UV and visible lasers must be irradiated with a uniform, broad area beam of high-energy electrons. In order to efficiently produce these beams, electrons must be generated and accelerated in vacuum through potentials on the order of 300 kV to 500 kV. Since the lasing media pressures are typically on the order of a few atmospheres, it must be separated from the e-beam vacuum chamber by an electron-permeable material. This function is provided by the e-beam window as shown schematically in Figure II-39. The e-beam window consists of the foil and foil support assembly. The window support structure must incorporate a means of cooling both the foil and foil support to prevent foil failure.

The use of materials such as Nimonic and titanium which have a very high allowable stress at temperatures approaching 1000°C (see Figure II-48) have been suggested for use in e-beam windows. However, since the laser medium contacts the e-beam window, the average window temperature also must be maintained low enough to avoid inducing thermal gradients ($\Delta\rho/\rho < 10^{-4}$) in the active laser medium. Hence the superior high temperature characteristics of these materials cannot be fully exploited for UV and visible laser e-beam applications. The cooling system must maintain the window temperature below that which will adversely affect medium homogeneity. Factors influencing the design of such a system fall into three major categories; heat loading, heat removal, and failure mode criteria.

a. Heat Loading

The significant e-beam window heat load sources which have been identified to date are:

(1) Direct high energy electron heating during the relatively invariant period of the accelerating potential pulse.

(2) Direct low energy electron heating during the rise and fall time of the accelerating potential pulse.

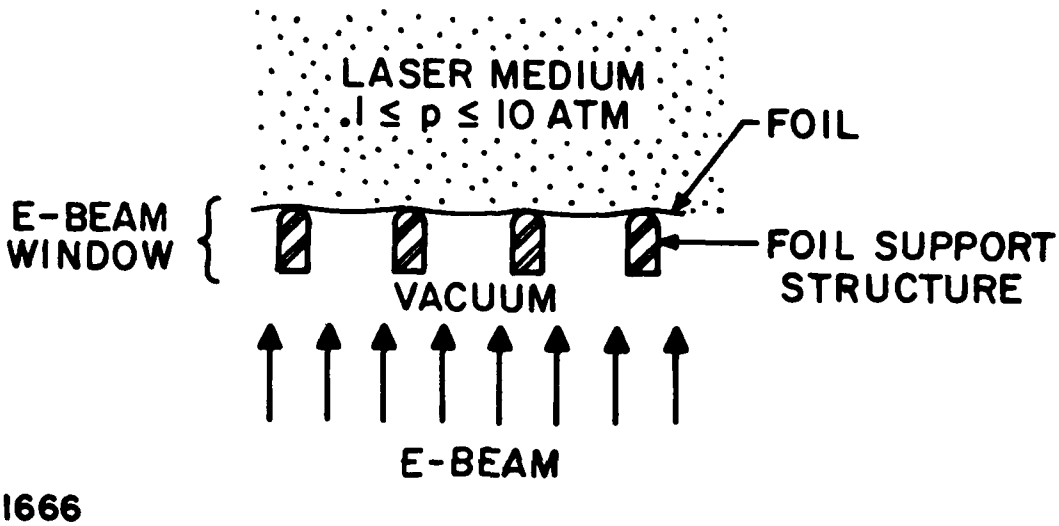

Figure II-39 Typical E-Beam Window Configuration

(3) Electron backscattering from the laser medium.

(4) Thermal radiation from hot laser medium, thermonic cathodes, or repetitively pulsed flashlamps.

Direct Electron Heating Including Backscatter

Foil heating may be estimated for the first three heat load sources by considering the data shown in Figure II-40. Curve (1) shows the mean electron energy loss in a 1 mil aluminum foil using the stopping power given by Berger and Seltzer.[54] This curve is presented here for reference since it is used many times to estimate foil losses. However, at low electron energies, where the electron range is comparable to the foil thickness, elastic electron scattering in the foil contributes significantly to foil heating as shown by curve (2). When the effects of coulombic electron backscattering from the laser gas are included, the foil losses are found to be appreciably greater than those predictd by Berger and Seltzer at all initial electron energies. For example, the foil loss predicted by curve (3) are approximately double those predicted by Berger and Seltzer even for initial electron energies > 300 kV. It is clear, then, that foil heating due to backscattering must be accounted for at all e-beam energies.

It is also clear from Figure II-40, that foil heating due to e-beam current flowing during the rise and fall time of the applied voltage pulse (i.e., at low electron energy) are greater than foil heating caused by current flow at high accelerating potentials. These loses can be substantially reduced with appropriate grid pulsing techniques which reduce the rise and fall times of the voltage pulse.

Cold cathodes do not share in this advantage because they cannot be operated in a grid-controlled mode. Except for the first few nanoseconds of the voltage rise time required for plasma formation, cold cathode current flows during the entire voltage pulse. An estimate of the low energy foil heating can be made by multiplying the foil loss as a function of electron energy by the

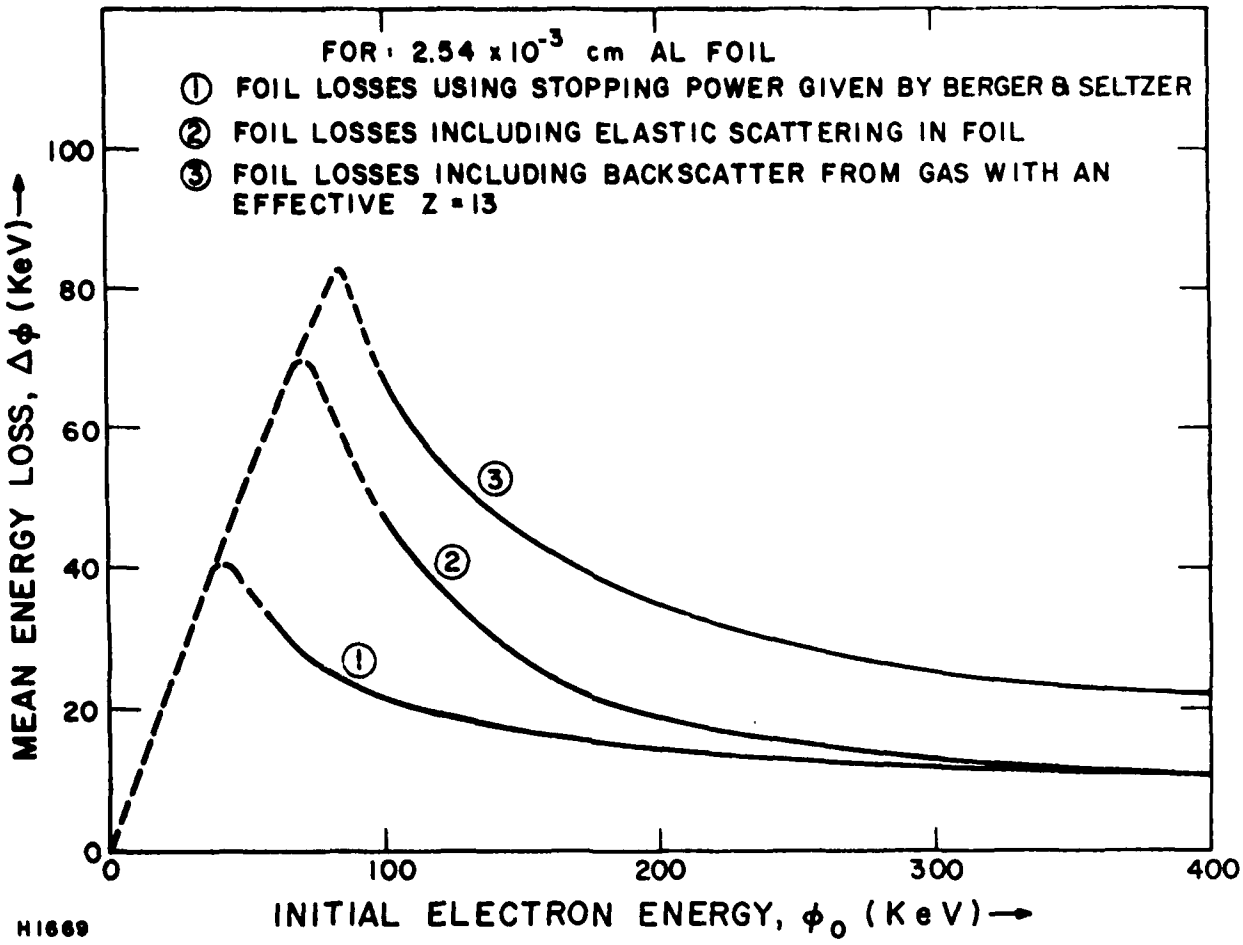

Figure II-40 Foil Losses as a Function of Initial Electron Energy.

space charge limited current that flows during the rise and fall time of the voltage pulse. By integrating this product from zero to full e-beam energy, the effective foil stopping power can be determined from the relation

$$\psi_e = \frac{1}{\rho S J_p} \int_o^{\phi_o} \Delta\phi J \, d\phi \qquad \text{(II-22)}$$

where

$J = J_p (\phi/\phi_o)^{3/2}$
ϕ_o = maximum electron energy
$\Delta\phi$ = mean energy loss from curve (3), Figure II-39
ρ = foil density
S = foil thickness

For aluminum, using curve (3) of Figure II-40, this integral yields ψ_e = 2.19 MeV cm^2/g which is ~ 2/3 the stopping power of aluminum for 300 keV electrons. This equivalent stopping power can be used in determining the single pulse foil temperature rise due to direct electron heating including the effects of rise and fall time heating by low energy electrons and coulombic back-scatter given by:

$$\Delta T_o = \frac{J_p \tau_p \psi}{C} \left[1 + \frac{\psi_e}{\psi} \frac{\tau_r + \tau_f}{\tau_p} \right] \qquad \text{(II-23)}$$

where

J_p = peak current density
C = specific heat of foil
ψ = stopping power at full energy

ψ_e = effective stopping power during rise and fall time
τ_p = pulse duration
τ_r = rise time
τ_f = fall time

In order to deliver energy efficiently to large e-guns operating at high-repetition rates, pulse forming networks or cables may be used. The characteristic rise and fall times of either PFNs or PFCs are typically 0.1 τ_p and 0.2 τ_p, respectively. Under these conditions, for aluminum

$$\Delta T_o = 1.2 \frac{J_p \tau_p \psi}{C} \qquad \text{(II-24)}$$

Thus, for conditions that are typical of a 300 kV e-gun using an aluminum foil window, the <u>foil temperature rise in a single pulse</u>

(1) ~ <u>doubles</u> due to <u>electron backscatter and</u>
(2) increases by <u>~ 20%</u> due to <u>low energy electron heating</u> during typical voltage rise and fall times.

<u>Thermal Radiation</u>

An additional heat load imposed upon the e-beam window is caused by thermal radiation from thermionic cathodes, hot laser gases, or pulsed flashlamps used to irradiate photoelectric cathodes. The radiational foil heating from laser gases at a few hundred degrees centigrade will be much smaller than from thermionic cathodes heated to ~ 1000°C. The radiation from flashlamps can be shielded by the reflectors used to focus light on the photo cathode. Thus, in a well designed e-gun, the main source of thermal radiation to the foil will be from thermionic cathodes. These losses can be estimated using the relation

$$p_r = e\sigma \ (T_1^4 - T_2^4) \qquad \text{(II-25)}$$

where

$$e = \frac{1}{\frac{1}{e_1} + \frac{1}{e_2} - 1} = \text{effective emissivity of two parrallel radiators}$$

e_1 = emissivity of cathode at cathode temperature, T_1
e_2 = emissivity of foil at foil temperature, T_2
σ = Boltzmann's Constant.

For example, for an oxide impregnated porous tungsten cathode heated to 1000°C, e_1 = 0.45 and for aluminum at 200°C, e_2 = 0.2, resulting in a net heat transfer to the aluminum of 2.4 W/cm^2. This, of course, is a steady-state heat load on the foil and is not a function of repetition rate. It does, however, raise the steady-state foil temperature which lowers the maximum allowable temperature rise due to direct electron heating during pulsed operation.

b. Heat Removal

The significant heat loads on the e-beam window fall into two categories:

(1) pulsed heat load sources
- direct high energy electron heating
- direct low energy electron heating
- electron backscatter

(2) continuous heat load sources
- thermal radiation from thermionic cathodes

The effects of these heat load sources on repetitively-pulsed e-beam window performance can be demonstrated by considering example cases of a conduction cooled and a forced convection cooled aluminum foil e-beam window. Since the total e-beam energy is absorbed by the foil support bars, it is assumed they are liquid or

heat pipe-cooled. No optimization of e-beam performance has been attempted in the following example cases since they are presented for illustrative purposes only.

Conduction Cooling

The essential elements of the conduction cooled e-beam window are shown in Figure II-41 where it is seen that the energy dissipated in the foil is conducted along the foil to the cooled foil support bars. These bars are liquid cooled to reduce thermal gradients along their length so that e-beam window scaling is a function only of the free span dimension, a.

For e-beam pulses on the order of a few microseconds, the foil temperature is raised by an amount T_o as shown in Figure II-42. Since the energy absorbed by the foil is conducted along the foil, the temperature along the foil is greatest at its midpoint and, hence, will ultimately limit the mechanical integrity of the e-beam window.

Neglecting convection and radiational foil cooling, the decay of the mid-foil temperature after the first pulse is given by

$$T(t) = T_o \exp\left(\frac{t - \tau_p}{\tau_d}\right) \operatorname{erfc}\left(\frac{t - \tau_p}{\tau_d}\right)^{1/2} \qquad \text{(II-26)}$$

$$T_o = \frac{J_p \tau_p \psi}{C}\left[1 + \frac{\psi_e}{\psi}\left(\frac{\tau_r + \tau_f}{\tau_p}\right)\right] \qquad \text{(II-27)}$$

T_o = single-pulse temperature rise

J_p = peak current density

ψ = stopping power for high energy electrons

ψ_e = effective stopping power for low energy electrons flowing during pulse rise time, τ_r and fall time, τ_f

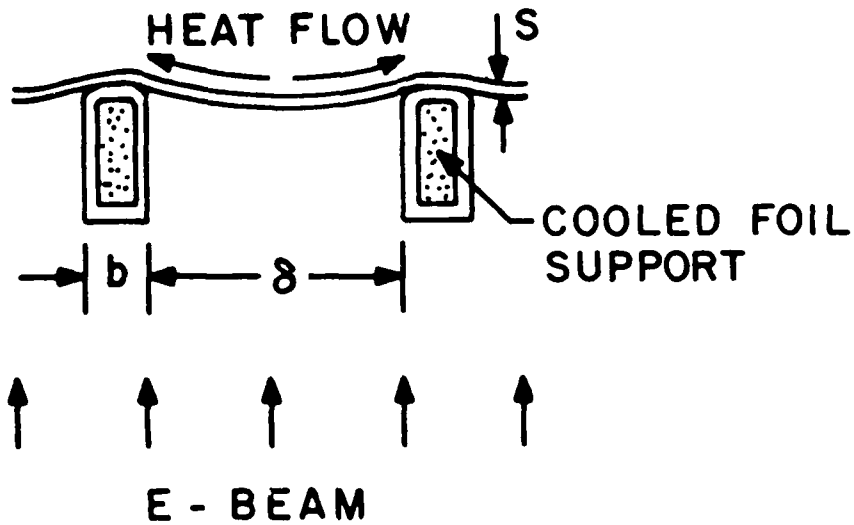

H 1668

Figure II-41 Conduction Cooled E-Beam Window

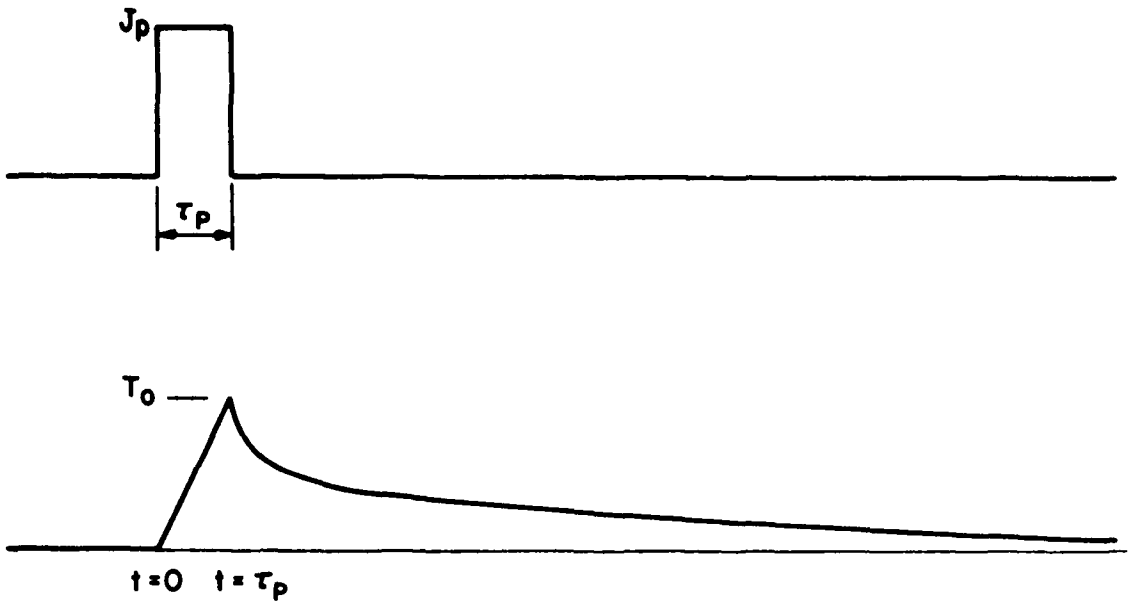

H1670

TIME →

Figure II-42 Mid-Foil Temperature Due to Single Pulse

τ_p = pulse width

τ_d = $(a/2\ \ )^2$ = thermal diffusion time constant of foil

a = foil free span

α = $(k/\rho C)^{1/2}$ = thermal diffusivity of foil

k = thermal conductivity of foil

ρ = foil density

C = foil specific heat

erfc = (1 - erf) = complimentary error function

The mid-foil temperature as a function of time for a single pulse is shown in Figure II-42. Note that the temperature decays very fast just after the pulse when the temperature gradients are large but decays less rapidly as the temperature distribution along the foil becomes more uniform. If a second heat load pulse occurs before the mid-foil temperature returns to its initial value, then the peak temperature at the end of the second pulse is given by

$$T(t_o + \tau_p) = (1 + \beta)\ T_o \qquad \text{(II-28)}$$

where

$$\beta = \frac{T(t_o)}{T_o} \qquad \text{(II-29)}$$

$$t_o = \frac{1}{f_o} = \text{interpulse period}$$

This is shown in Figure II-43 from which it can be deduced that the peak temperature after the nth pulse is

$$T_n = T_o \sum_{n=0}^{n} \beta^n \qquad \text{(II-30)}$$

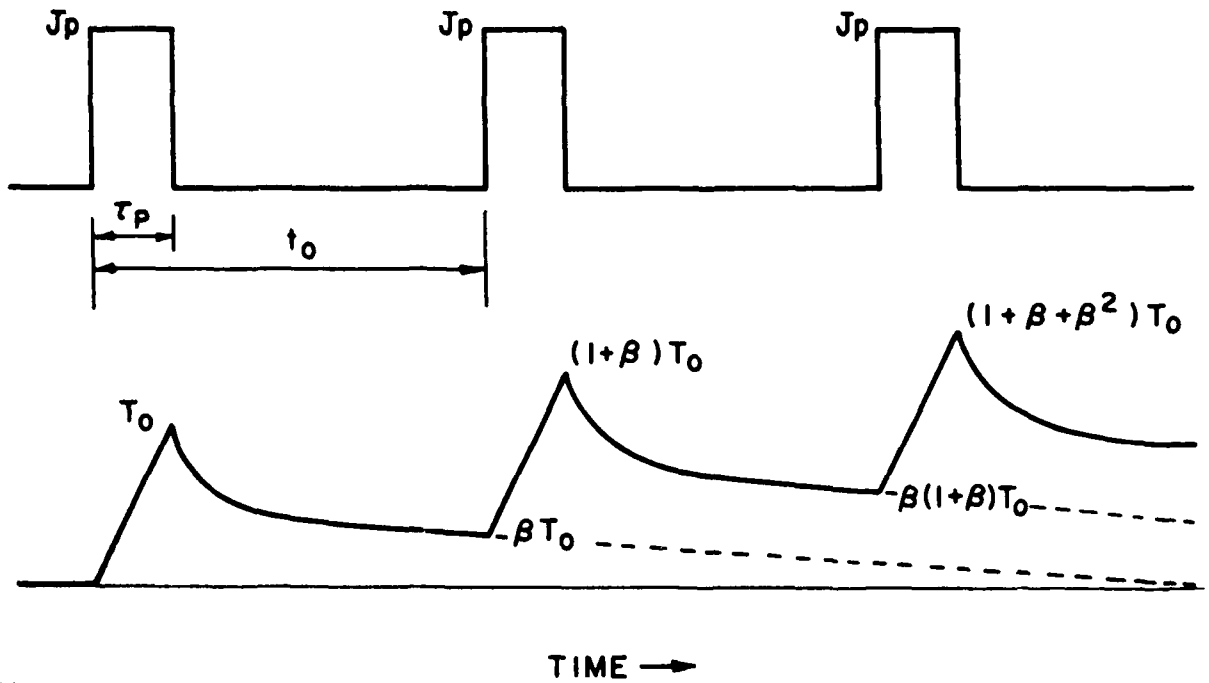

Figure II-43 Mid-Foil Temperature Due to Multiple Pulses

The equilibrium mid-foil temperature rise is found by taking the limit of T_n as $n \to \infty$

$$T_m = \lim_{n \to \infty} (T_n) = T_o \lim_{n \to \infty} \sum_{n=0}^{n} \beta^n$$

or

$$T_m = \frac{T_o}{1 - \beta} \qquad \text{(II-31)}$$

In order to avoid structural damage, this temperature must not exceed the maximum allowable temperature rise of the foil for the operating conditions that prevail (i.e., foil material, transparency, differential pressure, required $\Delta\rho/\rho$, etc.). Thus, the maximum charge density that can be transmitted by conduction cooled foil is found by combining Eqs. (II-26, (II-27), (II-29), and (II-30) yielding,

$$J_p\, p = \frac{C}{\psi}\left[\frac{1-\exp\left(\frac{1-\tau_p f_o}{\tau_d f_o}\right)\operatorname{erfc}\left(\frac{1-\tau_p f_o}{\tau_d f_o}\right)^{1/2}}{1+\frac{\psi_e}{\psi}\left(\frac{\tau_r+\tau_f}{\tau_p}\right)}\right]\left[T_m - \frac{a^2 p_r}{8kS}\right] \qquad \text{(II-32)}$$

The second bracketed term in this expression shows the effect of steady-state radiational heating from thermionic cathodes or any other source for which p_r is appreciable. The denominator of the first bracketed term reflects the effect of low energy electron heating that occurs during the rise and fall time of the applied voltage pulse. The stopping power, ψ, used in this expression must include collisional, scattering and bremsstrahlung

foil losses and coulombic backscatter losses from the laser medium (i.e., curve (3) of Figure II-40). When composite foils are considered, effective values should be defined for each parameter in Eq. (II-32). The maximum allowable mid-foil temperature is T_m.

The effect on conduction cooled window performance of the various heat loads described by Eq. (II-32) is demonstrated in Figure II-23 for a 300 kV, 1 μsec e-beam passing through a 1 mil aluminum foil with a free span of 1 cm. The maximum mid-foil temperature allowed is 200°C. Curves (1) and (2) are shown for reference only because they are used quite often to predict foil heating. However, because they do not include the effects of elastic foil scattering and electron backscattering from the laser medium, the error in predicted foil performance can be appreciable. This magnitude of this error can be seen by comparing curves (1) and (2) with curve (3) which includes the effects of foil scatter and gas backscatter and would be typical of the e-beam window performance expected when photoelectric cathodes are used. The effects of low energy rise time and fall time losses is shown by curve (4). This curve would be typical of the performance of e-beam windows used with cold cathodes for which space-charge limited current flow for the entire voltage pulse. The rise time and fall time losses can be reduced by grid-pulsing a thermionic cathode or by pulsing the photoelectric cathode flashlamps during the steady-state portion of the applied voltage pulse. When, gridded thermionic cathodes are used, however, the radiational heat load on the foil must be accounted for as shown by curve (5). The effects of all the significant heat loads is shown by curve (6) which would be typical of ungridded thermionic cathode operation or operation with significant radiational or convection heat loading from hot laser gases.

The effect of long pulse widths for cold cathode operation is shown in Figure II-44 where it is seen that the single-pulse heating limit is only approached for repetition rates as low as 0.1 pps.

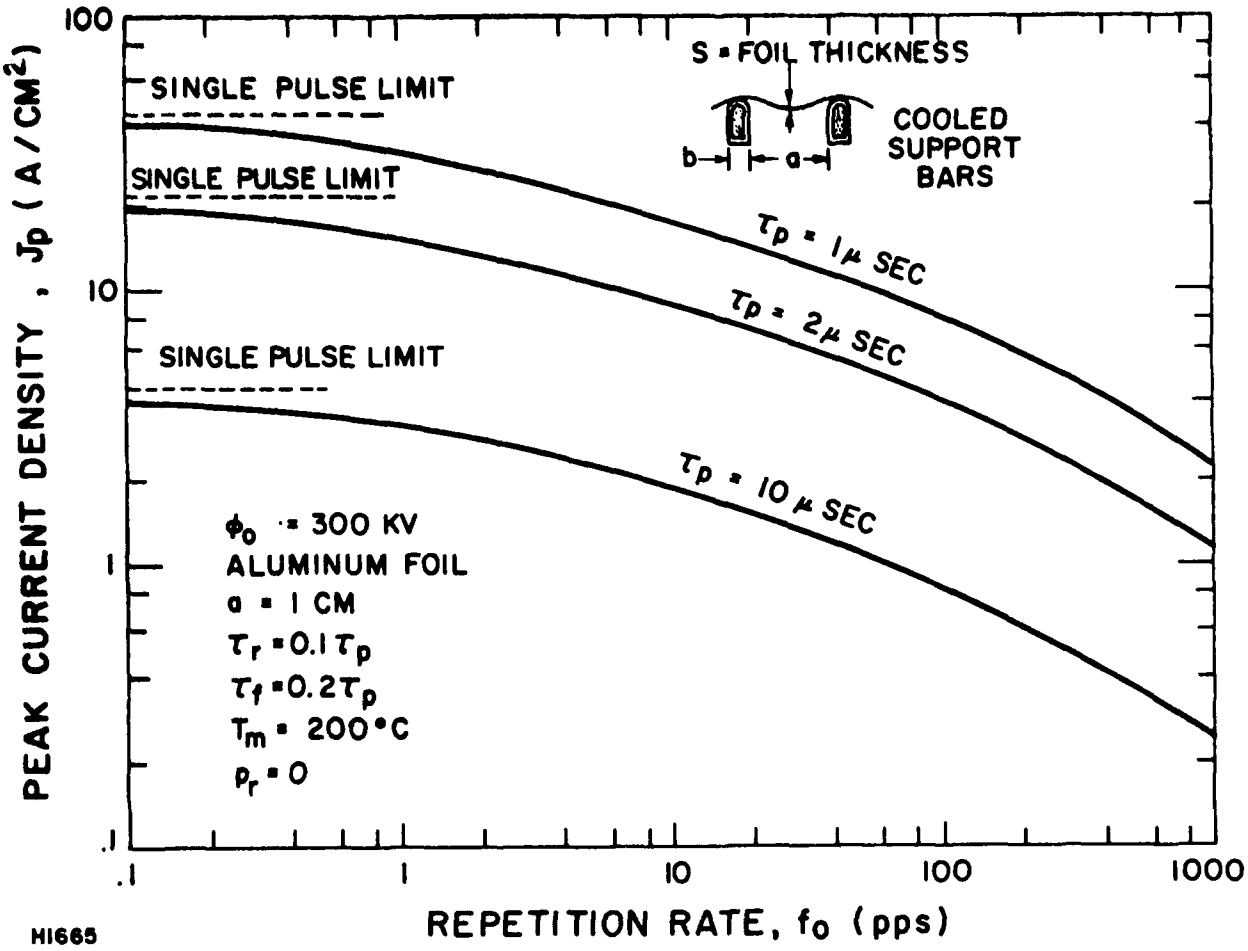

Figure II-44 Maximum Current Density as a Function of Repetition Rate for Conduction Cooled Windows.

It should be noted that, in the absence of steady-state radiational or convection heating, the $(J_p \tau_p)$ - product is independent of foil thickness, S. However, when either radiational or convection heat loads are present as in the case of radiational heating from thermionic cathodes, the foil thickness is important. This is shown in Figure II-45 where it is seen that quadrupling the foil thickness with constant foil span has the same fact as doubling the foil span with constant foil thickness.

Forced Convection Cooling

Another method of cooling e-beam windows is to force a high velocity stream of low-Z gas over the foil surface. A low-Z gas is desirable in order to minimize the e-beam energy lost directly in the gas. An embodiment of this concept is shown in Figure II-46 where it is seen that foil losses are carried away by the cooling gas flowing transverse to the e-beam. The advantage of this heat removal method is that the rate at which heat can be removed is no longer dependent upon the foil span, a, as is the case for conduction cooled windows. This allows a greater separation between cooled support bars and, therefore, e-beam window transparency and e-gun efficiency are increased. In this section a comparison is made between conduction and convection cooling.

The rate of heat removal from the surface of the e-beam window foil is given by

$$p = h(T - T_g) \qquad \text{(II-33)}$$

where

h = film coefficient for flow boundary layer
T = foil surface temperature
T_g = free stream gas temperature

Neglecting radiational and conduction heat transfer, the rate of change of foil temperature is

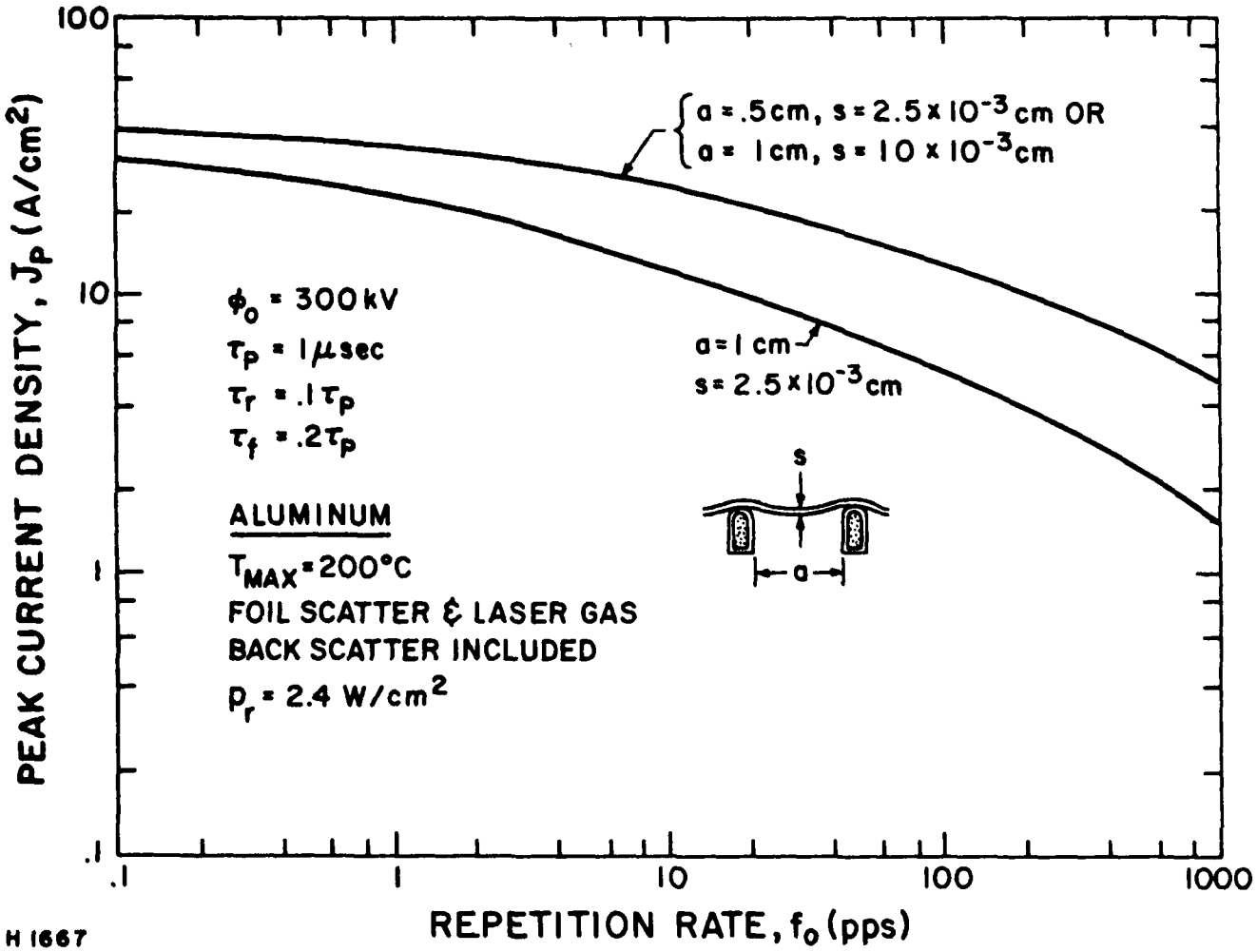

Figure II-45 Maximum Current Density as a Function of Repetition Rate for Conduction Cooled Windows with Different Foil Support Bar Spacings and Foil Thickness.

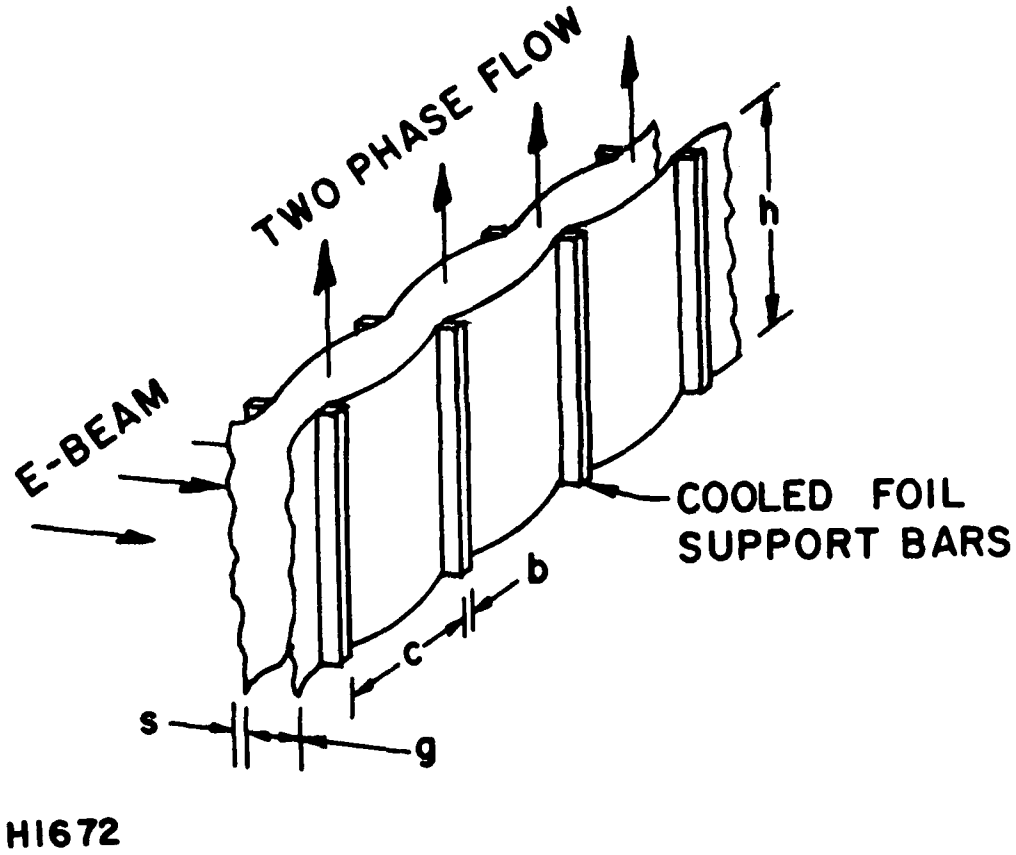

Figure II-46 Convection Cooled Window Concept

$$\frac{dT}{dt} = \frac{-p}{\rho SC} \qquad \text{(II-34)}$$

such that the foil temperature decay after the e-beam current pulse is found to be

$$\Delta T = T_o \exp \left[- \left(\frac{t - \tau_p}{\tau_c} \right) \right] \qquad \text{(II-35)}$$

where

T_o = single-pulse temperature rise

$\tau_c = \rho CS/h$ = thermal convection time constant

$\Delta T = T - T_g$

Under repetitively-pulsed conditions the foil temperature reaches a maximum given by

$$T_m = \frac{T_o}{1 - \beta} \qquad \text{(II-36)}$$

where

$$\beta = \frac{\Delta T(t_o)}{T_o}$$

In order that T_m not be allowed to exceed some maximum allowable value, the single-pulse temperature rise must be limited to $(1 - \beta)\ T_m$, or

$$T_o = 1 - \exp\left[\left(\frac{\tau_p f_o - 1}{\tau_c f_o}\right)\right] T_m \qquad \text{(II-37)}$$

By inserting the single-pulse temperature rise given by Eq. (II-27) into Eq. (II-37) the maximum charge density that can be transmitted by convection cooled windows is found to be:

$$J_p \tau_p = \frac{C}{\psi}\left[\frac{1 - \exp\left(\frac{\tau_p f_o - 1}{\tau_c f_o}\right)}{1 + \frac{\psi_e}{\psi}\,\frac{\tau_r + \tau_f}{\tau_p}}\right] T_m \qquad \text{(II-38)}$$

Noting the similiarity between Eqs. (II-32) and (II-38) one may compare forced convection cooling and conduction cooling by forming the ratio,

$$\xi \equiv \frac{(J_p \tau_p)_{conv}}{(J_p \tau_p)_{cond}} = \frac{1-\exp\left(\frac{\tau_p f_o - 1}{\tau_c f_o}\right)}{1-\exp\left(\frac{1-\tau_p f_o}{\tau_d f_o}\right)\operatorname{erfc}\frac{1-\tau_p f_o}{\tau_d f_o}}^{1/2} \qquad \text{(II-39)}$$

where

$\tau_d = \rho C a^2/4k$

$\tau_c = CS/h$

$h = 0.023\ k/D\ R_e^{\ 0.8}\ P_r^{\ 0.4}$

$D = 2g$ = hydraulic diameter

$R_e = \rho DU/\mu$ = flow Reynolds Number

$U = Mc$ = flow velocity

M = Mach number

$c = \sqrt{\gamma g_o RT}$ = sound speed

$P_r = C_p/k\mu$ = Prandtl Number

$\rho = p/RT$ = gas density

Using values for these parameters that are typical for helium at 100°C, and choosing the double foil spacing, g so that the cooling gas e-beam losses are $\lesssim$ 10% of the 0.004 in. Al foil losses for gas pressures up to 10 atm,

$$h = 0.241\ (pM)^{0.8}\ \frac{W/cm^2}{^oC} \qquad \text{(II-40)}$$

where

the gas pressure p is expressed in atmospheres.

The ratio, ξ is shown in Figure II-47 as a function of repetition rate, so for values of (pM) between 0.1 and 10 atm. Notice that for any given (pM) - product, convection cooling is superior to conduction cooling for repetition rates below a characteristic cross-over frequency. For example, cooling with atmospheric pressure helium flowing at Mach - 1 is superior to conduction cooling for repetition rates < 25 Hz. By increasing this helium pressure to 10 atm at Mach 1, the cross-over frequency is increased to 1000 Hz and the maximum peak charge density transmitted with convection cooling is greater than twice that allowable with conduction cooling for repetition rates between 6 and 200 pps. Thus, forced convection cooled e-beam windows can offer some advantages over conduction cooled windows when extremely high average charge density e-beam are desired with high window transparency.

c. Failure Mode Criteria

In order to discuss heat loads and cooling methods it was necessary to select a specific failure mode criterion which, for

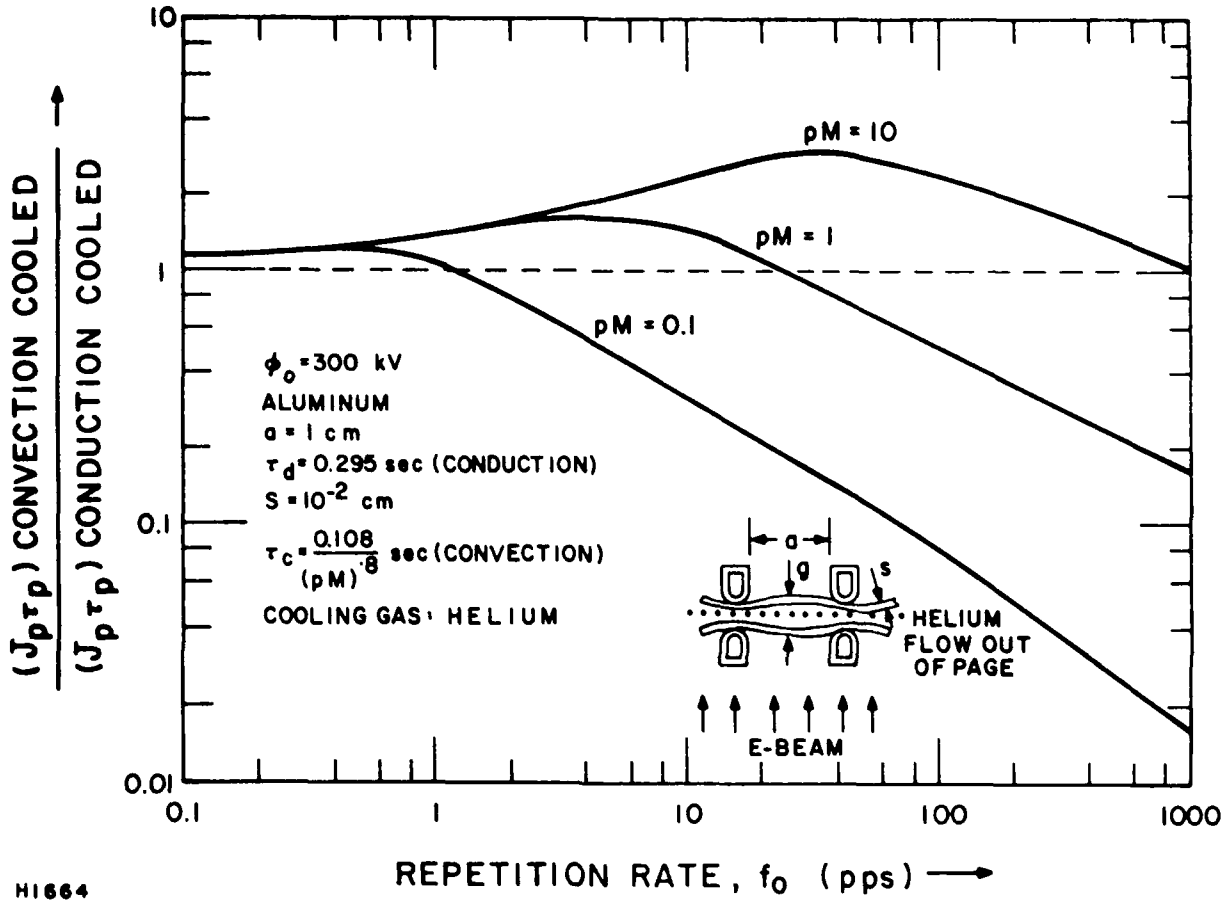

Figure II-47 Comparison of Convection Cooling and Conduction Cooling of E-Beam Windows as a Function of Cooling Gas Pressure and Flow Mach Number.

the material and parameters chosen, was simply that of not allowing the mid-foil temperature to exceed 200°C. The degree to which this is an adequate failure mode criterion depends upon how closely the ultimate failure mechanism is related to mid-foil temperatures. For example, consider the data shown by Figure II-48 which suggests that the $(J_p \tau_p)$ - product could be increased significantly by simply using Inconel 750 x or Nimonic 115 allowing T_m to approach 1000°C. While it is true that the e-beam window would probably survive (e.g., the ultimate stress of Nimonic 115 at 1000°C is 2-1/2 times that of aluminum operating at 200°C), operating the e-beam window at this temperature would adversely effect both vacuum conditions and laser medium homogeniety. It is clear, then, that the selection of the appropriate failure mode criteria must include total system considerations. Having integrated the system requirements into the e-beam window design procedure one may then consider the failure mode criteria for the window itself.

In establishing the e-beam window failure mode, one must decide if failure is caused by exceeding:

(1) maximum stress

(2) maximum strain

(3) maximum shear stress

(4) maximum distortion energy

The exact failure mode is also a function of the material used especially when composite or laminated foil construction is included. For example, a simple aluminum foil may fail when its maximum yeild strain is exceeded, but a laminated window (e.g., titanium clad with aluminum) may be limited by shear strain considerations.

Other factors which should be included in establishing a failure mode criteria include.

- Creep under long term loading
- Fatigue due to repetitively-pulsed and pressure cycling
- Surface conditions

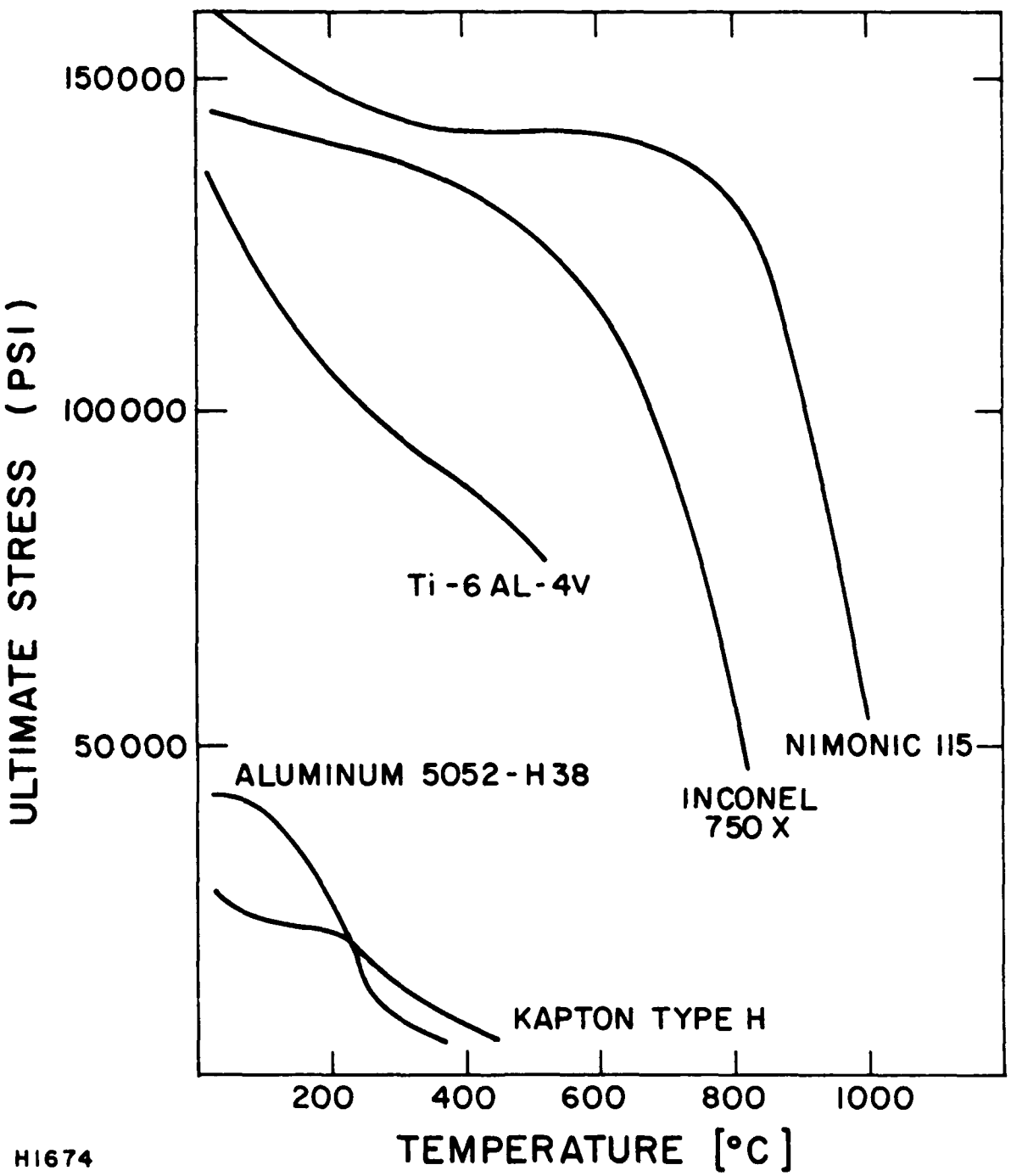

Figure II-48 Ultimate Stress Temperature Curves for Candidate Foil Materials.

- Vacuum thermal contact between foil and foil support
- Mechanical variation in foil thickness and support structure
- Pinholes
- Size and thickness availability
- Material impurities and alloys

Finally, when evaluating a variety of e-beam windows and cooling methods, the relative and absolute performance should be measured in in terms of:

(1) Transmitted e-beam current density

(2) Transmitted e-beam current density uniformity

(3) E-Beam window temperature relative to its effect on laser medium $\Delta\rho/\rho$

(4) Mean time between failure

(5) Mean time to repair

(6) Power required for cooling method

(7) Cost of e-beam window and cooling system

2. Foil Window Design

a. Foil Materials

The desirable properties for a foil material can be summarized as follows:

- Low atomic number - to minimize heat input
- High thermal conductivity - to minimize maximum temperature
- High resistance to creep at elevated temperatures - to prevent rupture

Beryllium

High purity beryllium combines the desirable attributes to a greater extent than any other material (atomic number 4, thermal conductivity 1.5 W $cm^{-1}{}^{o}K^{-1}$). Creep data available (for sheet) is only on a short-term basis (1/2 hr) but limited tests at AERL have shown encouraging results over longer times at temperatures of 550-600°C. Thin foils (< 0.004 in.) are expensive

(~ \$50/in.^{2}) and only available in small pieces. There is reason to believe that larger pieces could be produced if the interest of the manufacturers was encouraged.

Aluminum

Aluminum is long favored for low power e-beams because of its ready availability and low price. The atomic number of aluminum is relatively low (13). Aluminum also has a good thermal conductivity, however, its strength is unsatisfactory for laser mixture temperatures > 200°C. Cooling the foil support bars to 100°K may permit the use of aluminum. An alternate concept is a double aluminum foil with flowing helium cooling between them.

Titanium

Foil is available in both the pure form and as an alloy (Ti-3Al-2.5 V). The latter appears to have much better high-temperature strength but its thermal conductivity is lower (0.07 W cm^{-1} ^{o}K^{-1} vs 0.17 W cm^{-1} ^{o}K^{-1}). The atomic number for titanium is much higher (22) than that of beryllium which, in conjunction with the lower thermal conductivity, causes much higher foil temperatures. The energy dissipation of Ti foil is shown on Figure II-49.

Stainless Steel

Type 304 stainless steel is available in foil form down to 0.005 in. thickness and the thermal conductivity is comparable to pure titanium. Although the high atomic number (26) would cause an increase in foil temperature compared to titanium the high-temperature strength properties are superior.

Inconel 718

This is one of the nickel-based superalloys that is available in foil form. Its attractive property is the excellent elevated-temperature strength which warrants serious consideration of this material despite its high absorption of e-beam energy.

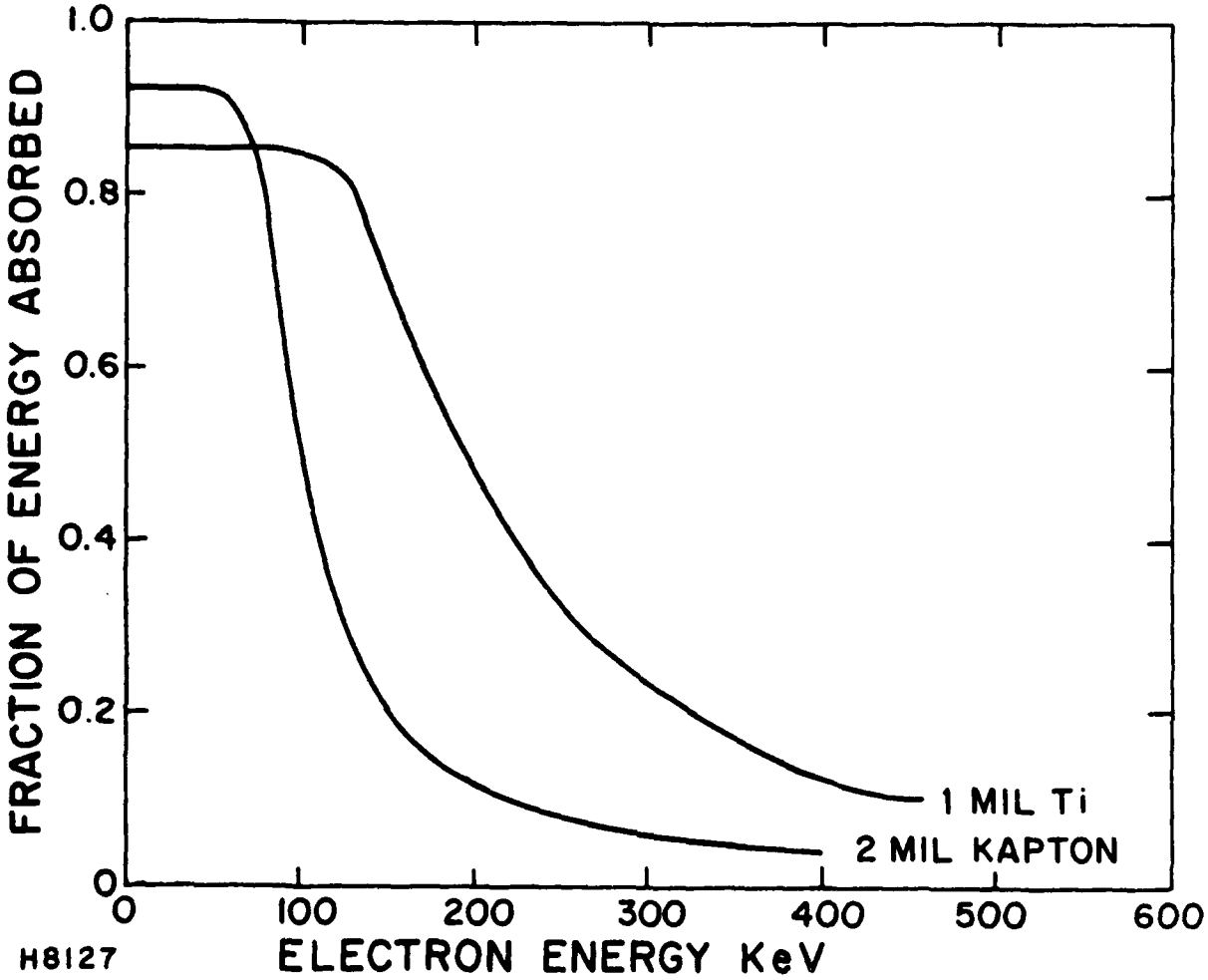

Figure II-49 Fraction of E-Beam Energy Absorbed

b. Clad Foils

A foil with a superior balance of properties could be produced by combining a high strength material with a high conductivity, low absorptivity, material. Cladding could be done by flame-spraying, for thickness of 0.001 in. and greater, or by electro-plating for thinner layers. If necessary an undercoat (e.g., nickel) may be applied to ensure good adhesion.

Technically, beryllium could also be applied by flame-spraying but this has not been done as yet due to the problems associated with the toxic fumes produced. Aluminum has a higher thermal conductivity than beryllium which offsets its greater absorption of e-beam energy, and aluminum coatings can be readily flame-sprayed on a wide variety of substrates. Copper has a very high thermal conductivity, but could only be used in very thin layers due to high electron absorption.

As an illustration of these properties Figure II-50 shows the steady-state thermal conditions for a foil of 0.001 in. titanium clad with 0.0002 in. of copper at a bar spacing of 0.10 in. (0.25 cm). The effect of bar spacing on the temperature at the center of the foil span is shown in Figure II-51. Although the heat absorbed by a plain titanium foil is only 75% of that for the clad foil the temperature is much higher due to the poor thermal conductivity. Because of the larger absorption by Ti at low voltages, the pulse length shown are 2 μsec at 100 Hz. Foil heating constraints on pulse repetition rate for a copper clad titanium foil is shown in Figure II-52. Assuming a 0.001 in. Ti - 0.0002 in. Cu foil supported on bars spaced by δ = 0.5 cm, about 100 W/cm^2 in the foil can be dissipated for an assumed allowable ΔT_{max} of 358°C.

Beryllium foil, if it were obtainable, only absorbs 30% as much energy as the clad foil and, with its superior thermal conductivity, reaches much lower temperatures for the same bar spacing.

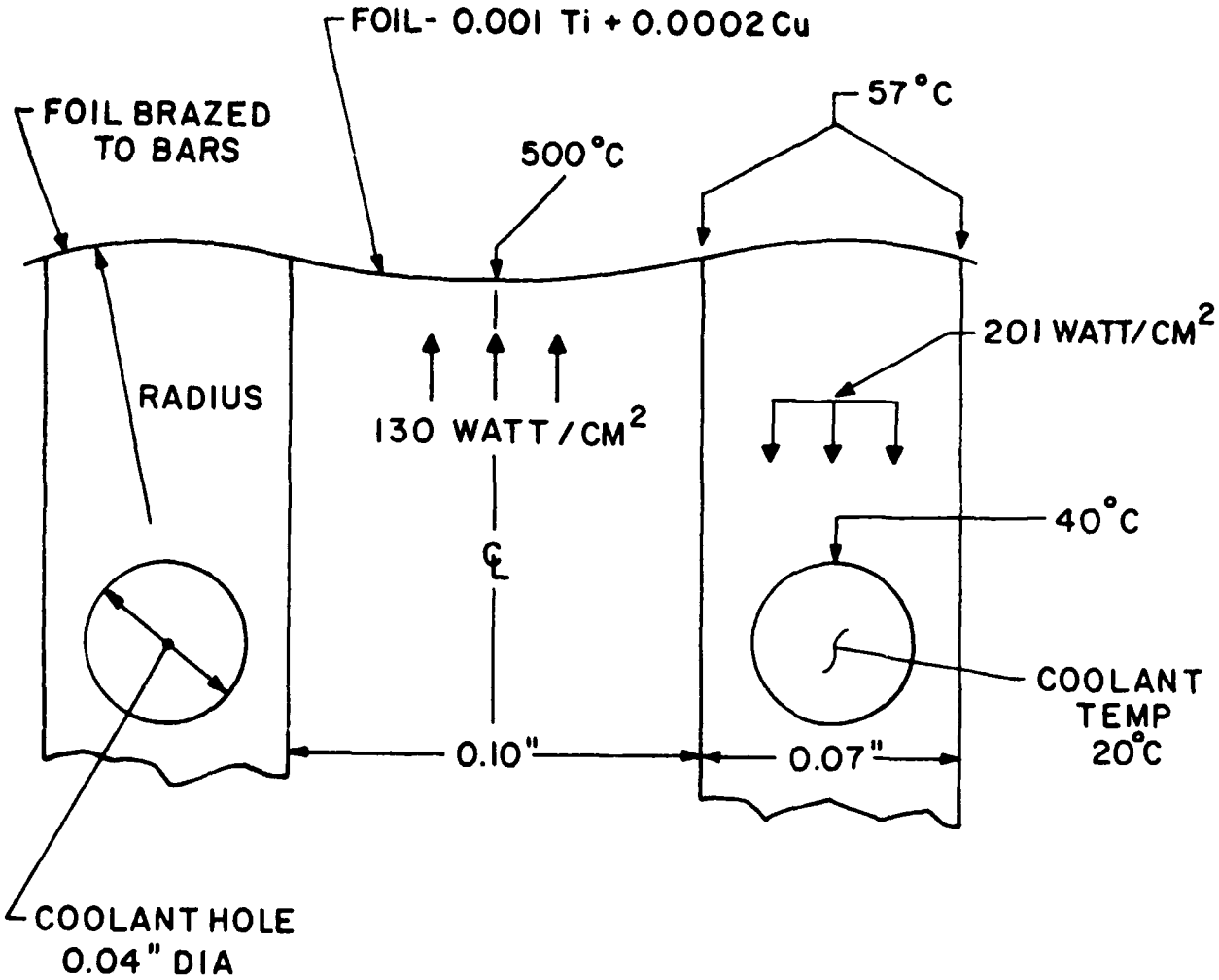

H6278

Figure II-50 Schematic Showing Foil and Support Bars, Showing Average Temperatures.

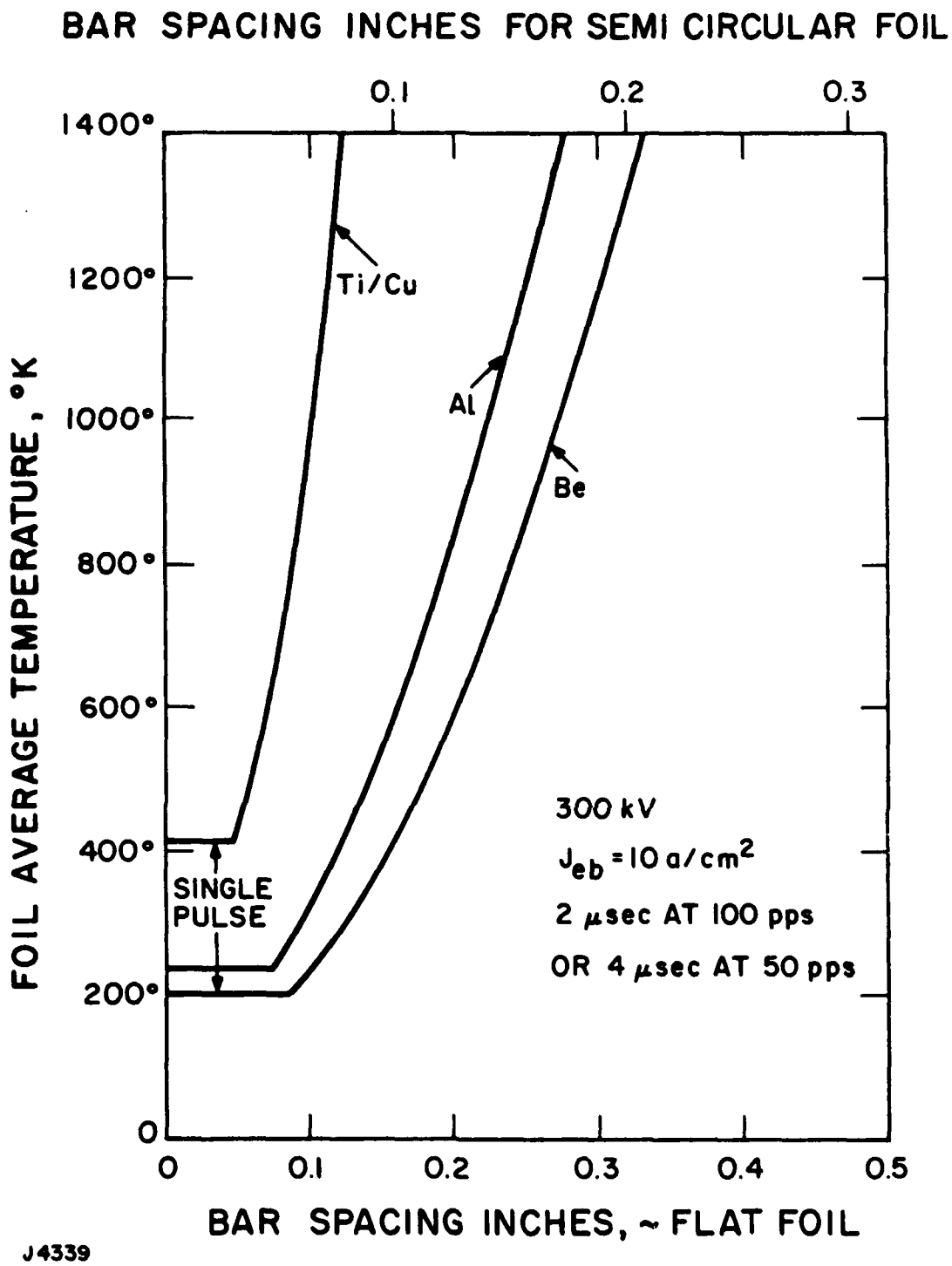

Figure II-51 Dependence of Foil Temperature on Support Bar Spacing. Initial temperatures are 100°K.

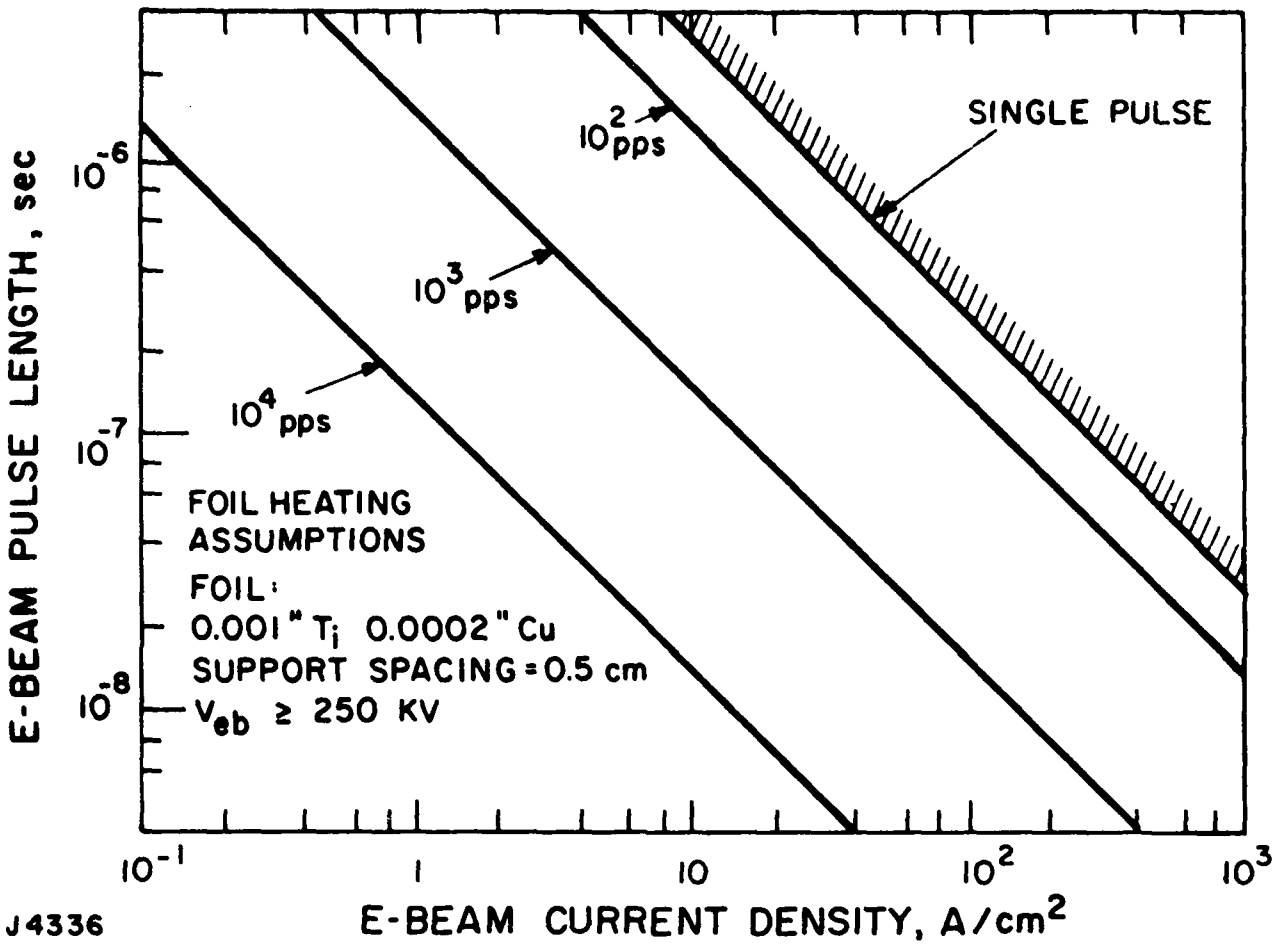

Figure II-52 Foil Heating Constraints on Pulse Repetition Rate as a Function of Beam Current Density, for a Copper Clad Titanium Foil.

c. Foil Stresses

Estimating foil lifetime for long repetitively-pulsed operation is uncertain since published creep data for suitable materials is given for forms other than foil (bar, sheet, etc.) under a constant applied stress. These data do not necessarily apply to thin foils and interpretation is further complicated by the fact that continuing elongation allows the foil to sag between the support bars, causing the stress to decline throughout the foil lifetime. In the calculations presented, a 10 hr creep strength was used but without using the additional creep elongation, which is conservative.

The cavity pressure on one side of the foil, with vacuum on the other, causes a static stress in the foil, given by

$$\sigma = \frac{p\delta}{2h \sin\theta} \qquad \text{(II-41)}$$

where p is the pressure, δ is the distance between the foil supports, h is the foil thickness, and θ is the angle tha the foil makes with the plane of the foil support plate, at the foil support holder. For an initially plane foil, the stress is also given by

$$\sigma = E\epsilon \qquad \text{(II-42)}$$

where ϵ is the elastic elongation of the foil,

$$\epsilon = \frac{\delta'}{\delta} - 1 \qquad \text{(II-43)}$$

and δ' is the length of the deflected foil. The relation to θ is given by

$$\frac{\theta}{\sin\theta} = \frac{\delta'}{\delta} \qquad \text{(II-44)}$$

The foil stress, σ, vs bar spacing, δ, is shown in Figure II-53. If an initial elongation is permitted, that is, the foil initially has slack, then the stress level is decreased considerably. In fact, the optimum initial elongation is 57%. However, the bar spacing cannot be icnreased without limit, because of the increased foil temperature with increasing spacing.

d. Experimental Validation

Single-pulse experiments have been made on 0.001 in. Ti alloy foil, initially at 250°C with an e-beam temperature rise of 250°C, an initial elongation of 5%, and bar spacing of 1.0 and 1.27 cm with no foil failure. The calculated stress for 6 atm pressure are shown below:

Bar Spacing cm	Predicted Foil Stress, kpsi Elongation	
	5%	Optimum (57%)
1.0	32	22.5
1.27	40	29

The ultimate tensile strength for various titanium alloys at that temperature is 50 to 10 kpsi. Thus, the experimental results are consistent with the predictions.

e. Foil Trade-Offs

The above discussion indicated that there exists a trade-off between stress and foil temperature. This trade-off is shown in Figure II-54. For a fixed bar-spacing, the effect of initial elongation on both stress and foil temperature was obtained and plotted. For a maximum foil temperature of 540°C, a stress of 70 kpsi can be sustained by several titanium alloys. This is also shown as the top line in Figure II-54. Based on this the average foil temperature rise can be calculated, which in turn limits the

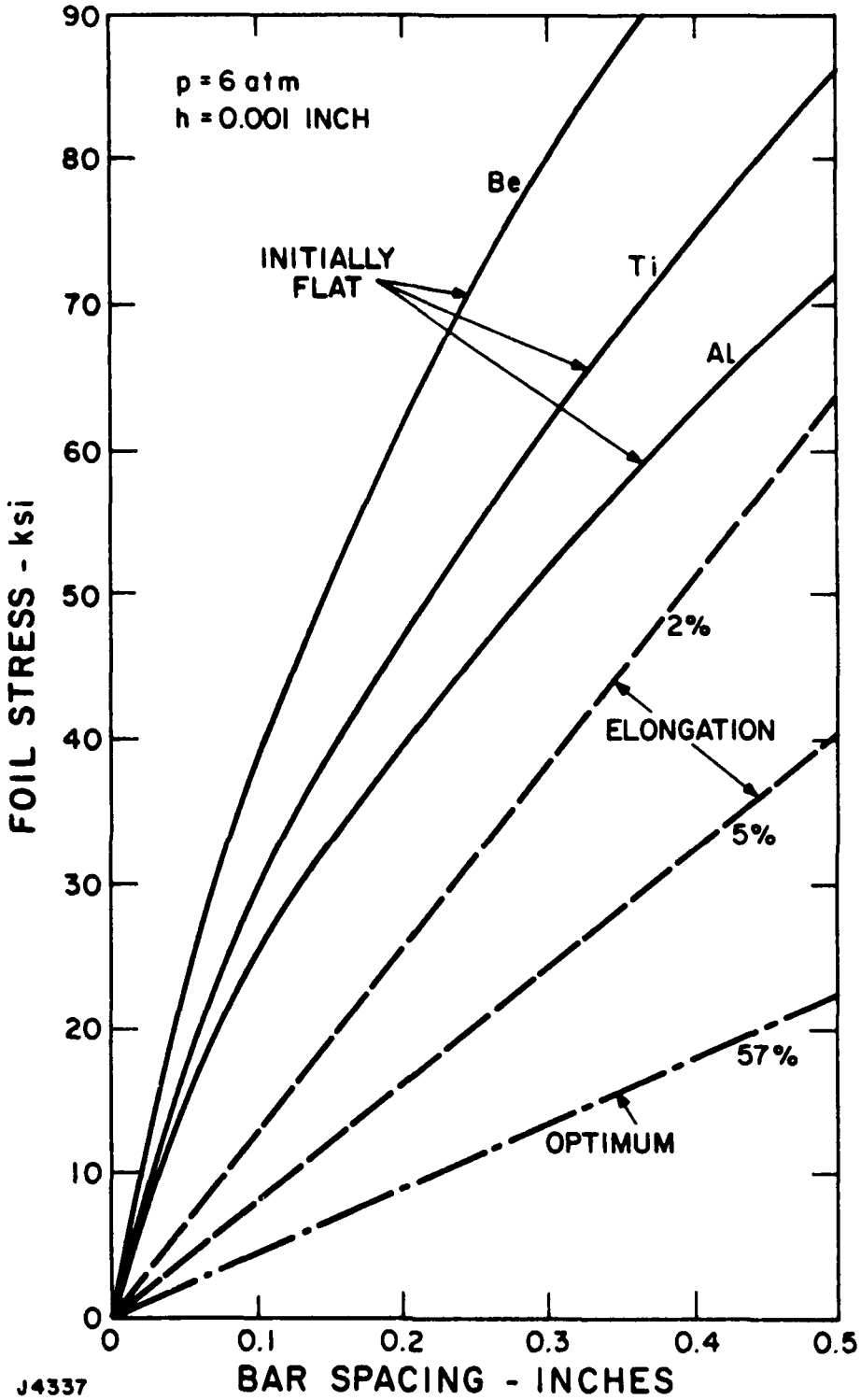

Figure II-53 Foil Stress as a Function of Support Spacing for Various Initial Elongations.

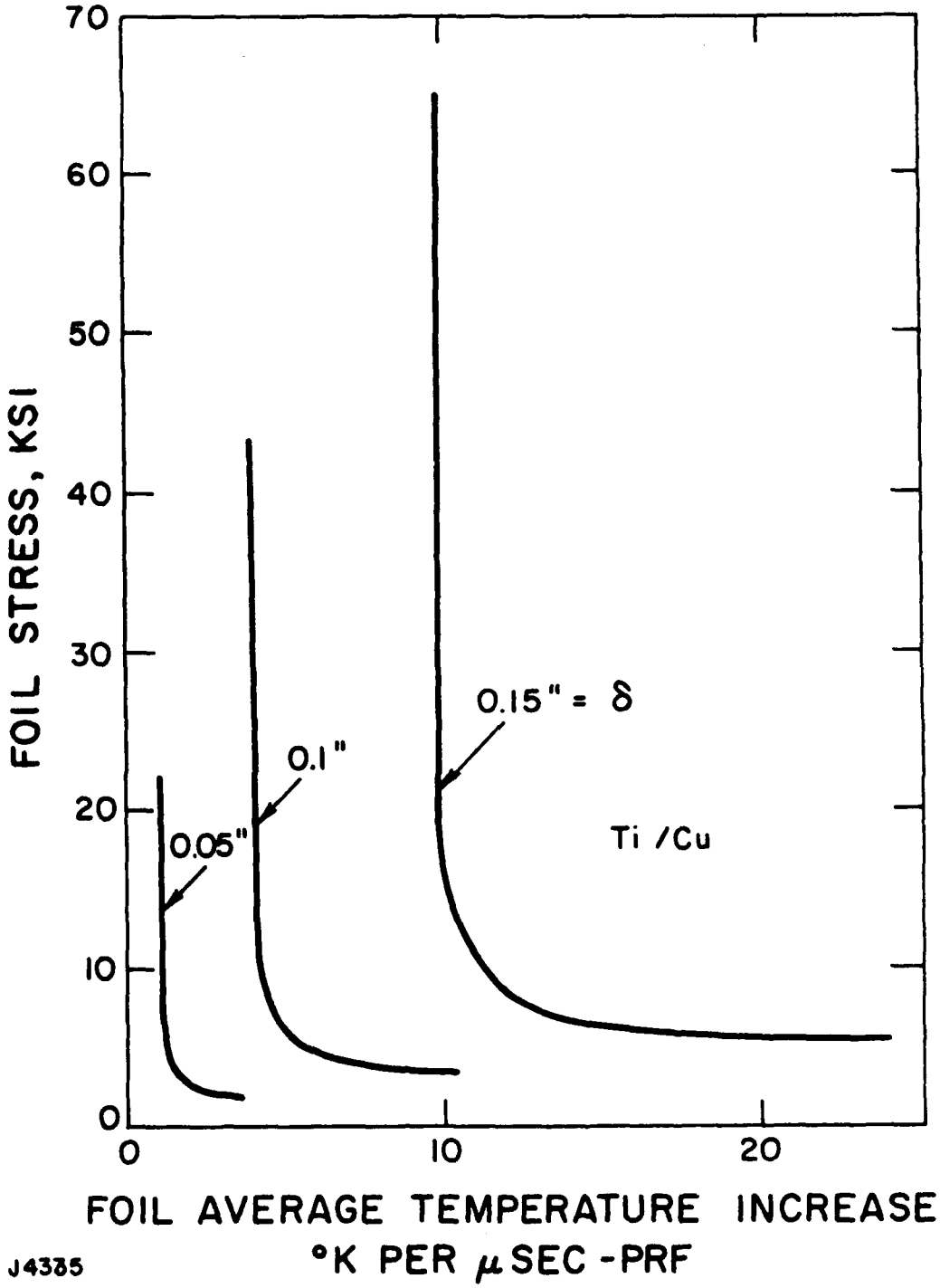

Figure II-54 Trade-off Between Foil Heating and Stress, for J_{eb} = 10 A/cm^2.

pulse repetition rate. This trade-off is shown in Figure II-55, for a Ti-Cu foil. To achieve a high repetition rate, a small bar spacing is required. However, if the length of the cavity in the flow direction can be increased, then smaller e-beam currents may be allowed, permitting a larger bar spacing.

A similar trade-off was made for 3003 H18 aluminum, also based on the use of LN_2 coolant in the foil support bars, so that the foil at the bars is at about $100^{o}C$. The maximum allowable temperature of the aluminum was varied and the results are shown in Figure II-55.

Figure II-55 also illustrates that the e-beam current or bar spacing is greater for aluminum, than for titanium assuming LN_2 cooled bars. In addition, the boundary layer in the cavity is thinner for lower temperatures, which must also be considered against the additional complexity of LN_2 cooling. Figure II-55 indicates that for an aluminum foil support spacing of 0.14 in., 100 Hz can be achieved for a 2 μsec pulse. To achieve the same PRF and a 4 μsec pulse, a bar spaicng of 0.1 in. is satisfactory. For a Ti-Cu foil whose support bars are LN_2 cooled, and a bar spacing of 0.1 in., 37 pps is achievable for 4 μsec, and 74 pps for 2 μsec pulses. As an alternative to copper clad titanium foil, AERL has determined that aluminum clad titanium foil is available, which may be superior to the Ti-Cu foil, because of the lower atomic number of aluminum on comparison to copper.

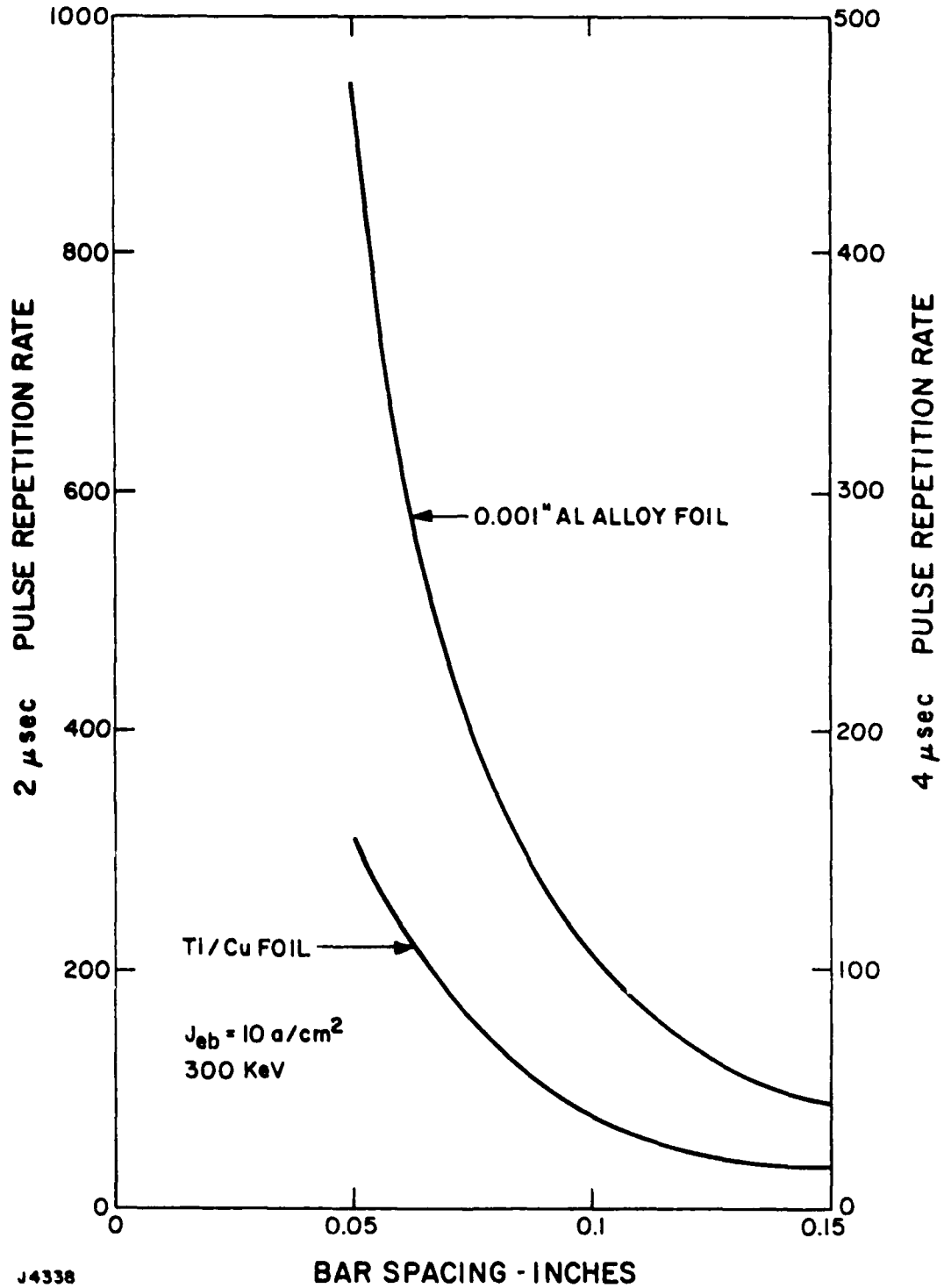

Figure II-55 Trade-off Between Foil Bar Spacing and PRF

SECTION II

REFERENCES

1. Parker, R.K., Anderson, R.E. and Duncan, C.V., J. Appl. Phys. 45, 2463 (1974).

2. Orzechowski, J.J. and Bekefi, G., Phys. Fluids, 19, 43 (1976).

3. Mesyats, G.A. and Proskurovskii, D.I., JETP Lett. 13, 4 (1971).

4. Bekefi, G., Private Communication.

5. Langmuir, L., Phys. Rev. 33, 954 (1929).

6. Hertz, H., Ann. Physik, 31, 983 (1887).

7. Einstein, A., Ann Physik, 17, 32 (1905).

8. Lawrence, E.O. and Beams, J.W., "Physics Review," 32, 478 (1928).

9. Furomoto, H.W., Ceccon, H.L., "Optical Pumps for Organic Dye," Applied Optics, 8, 8, p. 1613 (Aug. 1969).

10. Dobrestov, L.N., Gomoyunova, M.V., Emission Electronics, Israel Program for Scientific Translations, p. 194, (1971).

11. Beck, A.H., Proc. Inst. of Electrical Engineers, B106, 372 (1959).

12. Buck, J.G. and Clogston, A.M., "Microwave Magnetrons," Chapter 12 Edited by G.B. Collins, McGraw Hill Book Co., Inc., New York, 503 (1948).

13. Mangano, J.A. Private Communication.

14. Hull, "Barium Aluminate Dispenser," Phys. Rev. 56, 86 (July 1939).

15. Lafferty, "Design of Electron Gun," Nucleonics, 72 (April 1950).

16. Lemmens, "Cavity Type," Phillips Technical Review, 11, 341 (June 1950).

17. Hughes, "Chemical Reactions of Barium Oxide," J.A.P., 635 (June 1952).

18. Hughes, "Bariated Tungsten Emitters," J.A.P., 23, 1261 (Nov. 1952).

19. Levi, "Impregnated Structure," IRE Record, 6, 40 (1953).

20. Metson, "Heater-Cathode Insulation," Proc. IEE, 102, 678 (Sept. 1955).

21. Brodie, "Nature of the Surface," British J.A.P., 8, 27 (1957).

22. Brodie, "Evaporation of Barium," Jour. Electronics, 457 (Mar. 1957).

23. Rittner, "Mechanism of Operation," J.A.P., 1468 (Dec. 1957).

24. Rittner, "Emission from Barium on Molybdenum," J.A.P., 61 (Jan. 1958).

25. Beck, "High Current Density Cathode," P.I.E.E., 106B, 378 (July 1959).

26. Jenkins, "Poisoning of Impregnated Cathodes," J. of Elect. 393 (Nov. 1959).

27. Brodie, "Evaporation of Barium," J. of Elec. & Controls," 6, 149 (1959).

28. Dudley, "Emission and Evaporation," Tube Tech. Corp. 154 (1960).

29. Melnikov, "Emission from Barium Tungstate," F.T. Tela 2, 704 (1960).

30. Brodie, "Emission Fluctuations," J.A.P., 2039 (Oct. 1961).

31. Espersen, "Cathodes for Magnetrons," Phil. Tech. Rev. 23, 316 (1961).

32. Sandor, "View of Activation Process," J. Elect. Con. 13, 401 (Nov. 1962).

33. Beck, "Activation Process," J. Elect. Control, 623 (June 1963).

34. Druzhinin, "Barium Migration," Radio Eng. & Elec. Phy. 425 (Mar, 1965).

35. Alekseyev, "Secondary Emission," Radio Eng. & Elec. Phy. 500 (Mar. 1965).

36. Kucherenko, "Operation in Gases," Radio Eng. & Elec. Phy. 629 (Apr. 1965).

37. Gentry, "Heater Insulation Failure," Proc. IEE, 112, 1501 (Aug. 1965).

38. Greene, R.F., "The Surface Science of Cathodes," Appl. of Surface Science, 2, 2 (1979).

39. Shih, A., Hor, C. and Haas, G.A., "Auger Peak Height Calibrations of Ba, Sr and Ca in the Oxide Form," Appl. of Surface Science, 2, 2 (1979).

40. Rutter, V.E., Schimmel, D.G., Handy, R.A. and Smith, B.H., "Coated Powder Cathodes - Applications and Technology," Appl. of Surface Science, 2, 2 (1979).

41. Tuck, R.A., "Surface Studies of Thermionic Emitters by Methods Unique to Them," Appl. of Surface Science, 2, 2 (1979).

42. Brodie, I. and Spindt, C.A. "The Application of Thin-Film Field-Emission Cathodes to Electronic Tubes," Appl. of Surface Science, 2, 2 (1979).

43. Shih, A. and Haas, G.A., "CaO Surface Segregation as an Emission-Loss Mechanism," Appl. of Surface Science, 2, 2 (1979).

44. van Oostrom, A. and Augustus, L., "Activation and Early Life of a Pressed Barium Scandate Cathode," Appl. of Surface Science, 2, 2 (1979).

45. Thomas, R.E., Pankey, T., Gibson, J.W. and Haas, G.A., "Thermionic Properties of BaO on Iridium," Appl. of Surface Science, 2, 2 (1979).

46. Sickafus, E.N., Smith, M.A., Hammond, J.S., Artz, B.E. and Bomback, J.L., "Surface Phenomena of Potential Concern to Longevity of Dispenser Cathodes," Appl. of Surface Science, 2, 2 (1979).

47. Jones, D., McNeely, D. and Swanson, L.W., "Surface and Emission Characterization of the Impregnated Dispenser Cathode," Appl. of Surface Science, 2, 2 (1979).

48. Forman, R., "A Proposed Physical Model for the Impregnated Tungsten Cathode Based on Auger Surface Studies of the Ba-O-W System," Appl. of Surface Science, 2, 2 (1979).

49. Shih, A. and Haas. G.A., "Basic Cathode Poisoning Phenomena due to O_2, CO_2 and S," Appl. of Surface Science, 2, 2 (1979).

50. Maloney, C.E., Marrian, C.R.K. and Wyss, G., "Some Observations of Impregnated Tungsten Cathodes," Appl. of Surface Science, 2, 2 (1979).

51. Haas, G.A., Shih, A. and Thomas, R.E., "Electronic and Chemical Surface Studies in Oxide Cathodes," Appl. of Surface Science, 2, 2 (1979).

52. Haas, T.W. and Grant, J.T., "Scanning Electron Excited Auger Electron Spectroscopy," Appl. of Surface Science, 2, 2 (1979).

53. Trump. J.G. and Van de Graff, R.J., J.A.P. 18, p. 327, (1947).

54. Berger, M.J. and Seltzer, S.M., "Tables of Energy Losses and Ranges of Electrons and Positrons," NASA SP-3012, p.64.

III. DESCRIPTION OF EXPERIMENTAL APPARATUS AND TECHNIQUES

A. SINGLE-PULSE APPARATUS

The apparatus for the single-pulse test program, consists of a large vacuum box for the e-gun chamber, a Marx bank power supply and high-voltage table containing control electronics. The layout of the major components of the single-shot test configuration is shown in Figure III-1. The electrical schematic for the single-shot experiment is shown in Figure III-2. The 250 kV, 5.5 mA dc supply shown in Figure III-1 is used to condition the vacuum components for high-voltage operation. To do this, the supply is connected to the high-voltage table through a current-limiting resistor.

The 7.5 and 30 kVA isolation transformers are used to supply 60 Hz power to diagnostic equipment on the high-voltage table and to supply filament power for thermionic cathodes. The high-voltage table is simply a Faraday cage isolated from ground which is used to house instrumentation, controls, and diagnostic equipment that needs to be raised to cathode potentials ($\sim$ 300 kV).

The screen room shown in Figure III-1 serves two important functions; it provides $\sim$ 100 dB attenuation of EMI generated by high-current e-beam discharges, and serves a grounded conducting enclosure to protect personnel from the exposed high-voltage equipment in the e-beam test room.

The e-gun vacuum chamber is a 50 x 70 x 150 cm stainless steel enclosure which is large enough to accommodate a 20 x 100 cm cathode on the front surface of the inner box. Most of the inner box front surface has been blanked off with an aluminum plate which supports the 10 x 20 cm cathode candidates evaluated in the single-shot tests.

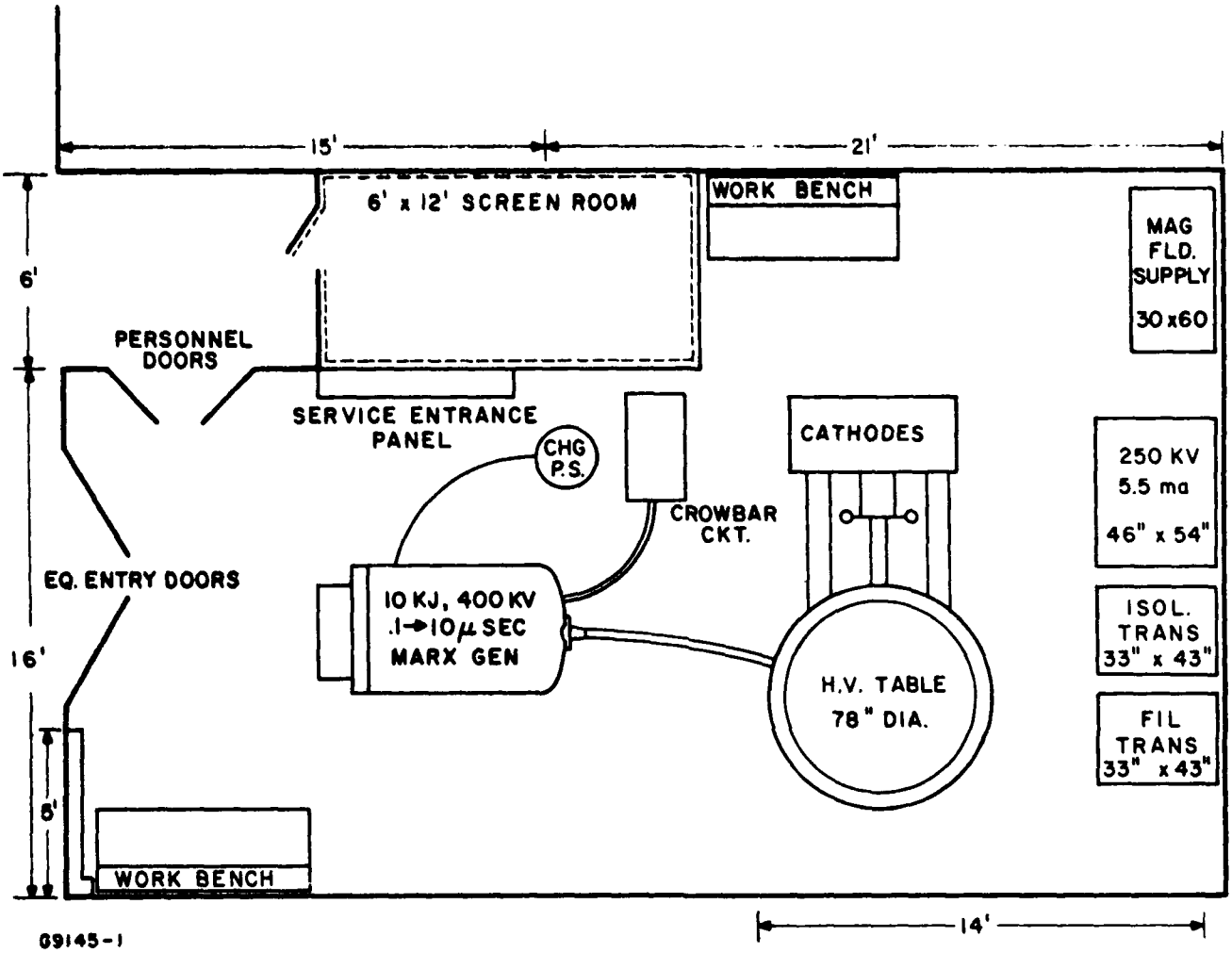

Figure III-1 Room Layout for the Single-Pulse Test Apparatus

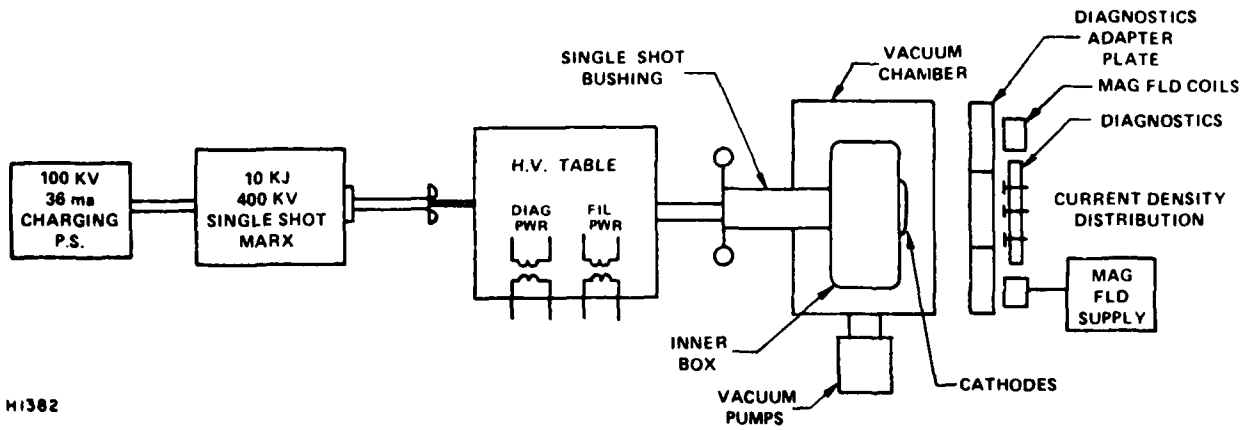

Figure III-2 Electrical Schematic for the Single-Shot Test Configuration.

The energy for these cathodes is supplied by the single-shot Marx generator as shown in Figure III-2. The four 0.5 μF capacitors are resistively charged in parallel to voltages up to 100 kV. When four series spark-gap switches are triggered, these capacitors are series connected across the e-gun anode-cathode gap connected to the Marx generator via the high-voltage table.

To terminate the pulse a smaller Marx generator is used to trigger the crowbar spark gap which uses the main Marx generator high-voltage terminal as one of the crowbar spark-gap electrodes. By adjusting the delay between the crowbar and main Marx generators, the load voltage pulse may be varied between 200 nsec to tens of microseconds. The voltage droop during the pulse, depends upon the current drawn by the e-gun so that the longer pulses are useful at reduced e-beam current. A typical current pulse for a 73 Ω resistive load is shown in Figure III-3.

The welding supplies which deliver 1500 A at 40 Vdc are used to energize the guide magnetic field coils. Maximum field strengths of ~ 4.5 kG are possible with this apparatus.

The anode-cathode voltage and total emission current waveforms are measured with a resistive divider and Rogowski current loop, respectively. Spatial distribution (time integrated) of the current density is measured by viewing the induced fluorescence in a polystyrene plate located just behind a Kapton foil as shown in Figure III-4.

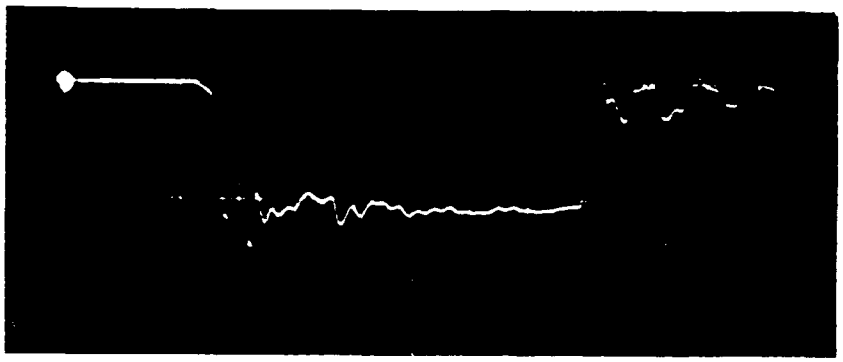

5 kA/div

H1840 200 ns/div

Figure III-3 Single-Shot Marx Generator Current Pulse into a 73 Ω Resistive Load.

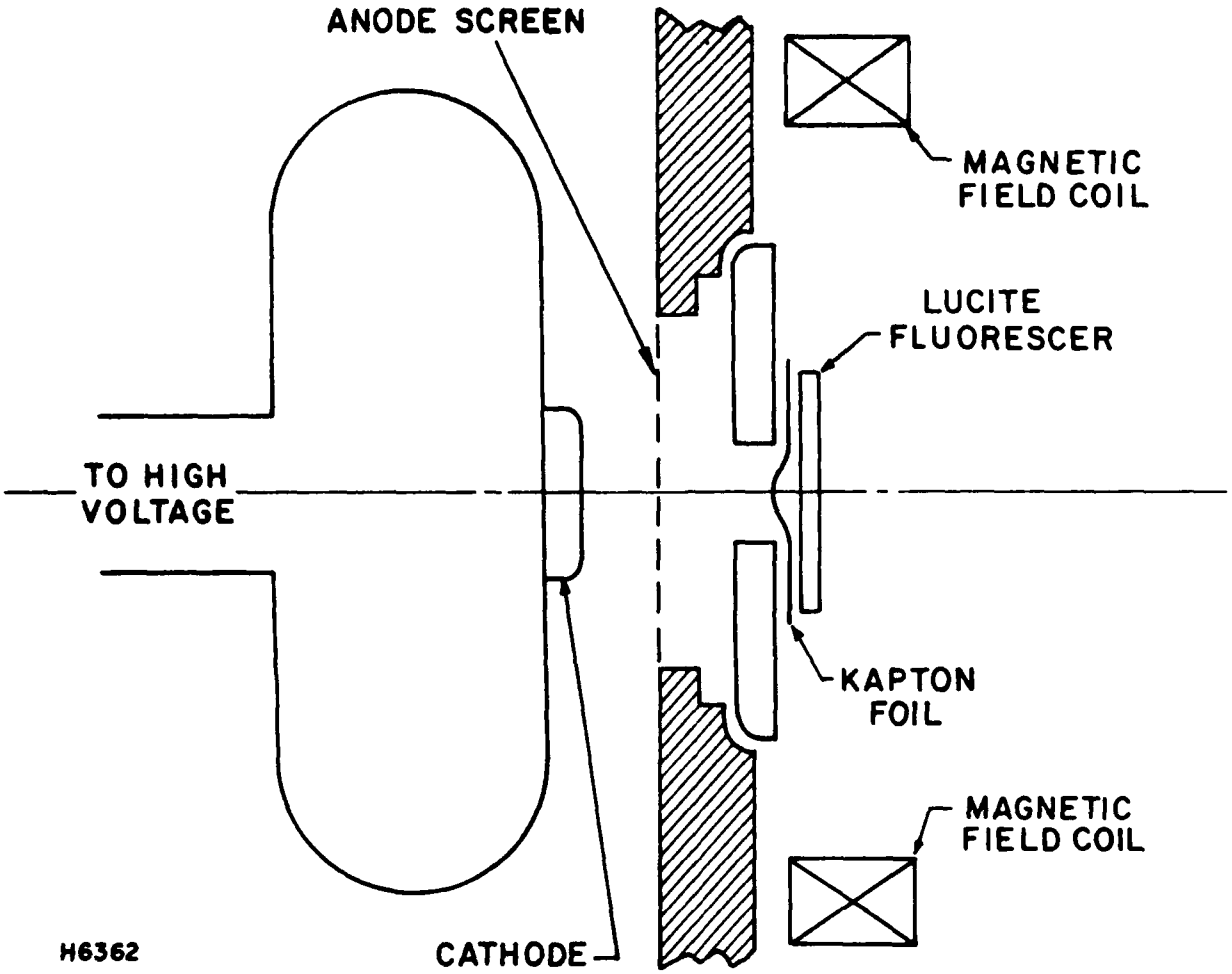

Figure III-4 Schematic of Experiment for Single-Pulse Tests

B. REPETITIVELY-PULSED E-GUN FACILITY

1. Line Pulser System

A repetitively-pulsed line pulser was procured by Systems, Science and Software (S^3), Hayward, CA, and included low-voltage power supplies, control and power conditioning equipment, a pulse forming network, isolation transformers and a high-voltage bushing for pulsed operation. The pulse generator system is designed to produce a 1 μsec pulse at 300 kV and 25 Hz into a 50 Ω load. To accommodate flexibility in load impedance, a variable resistance load consisting of a cupric sulfate solution, is connected across the load and cooled by a forced water heat exchanger. A schematic diagram of the pulser is shown in Figure III-5.

The e-beam vacuum chamber is bolted on to a mating flange at the output end of the pulse generator. A cast epoxy bushing provides the interface between the oil insulated pulse generator and the evacuated e-beam chamber. The bushing is sandwiched between the inside wall of the PFN (oil filled) tank and the high-voltage deck and is held in compression by a series of insulating threaded rods (not shown). The high-voltage deck which floats at the pulse generator output potential contains filament transformers and auxiliary supplies, e.g., for possible grid control. Filament, water cooling and other connections to the cathode pass within the hollow stem located within the output bushing and terminate in the high-voltage terminal. Power to the deck is provided by high-voltage isolation transformers located within the oil tank under the deck.

The pulse forming network consisting of a 10-section E-type configuration is charged to a maximum voltage of 650 kV through a pulse transformer also located within the oil tank. The PFN will deliver a 300 kV pulse of 1 μsec duration into a load of 50 Ω. To accommodate variations in the e-gun impedance, a variable matching resistor is connected in parallel with the diode load. The matching resistor is a water-cooled, copper sulfate solution located external to the oil tank. Isolating the high-voltage deck from

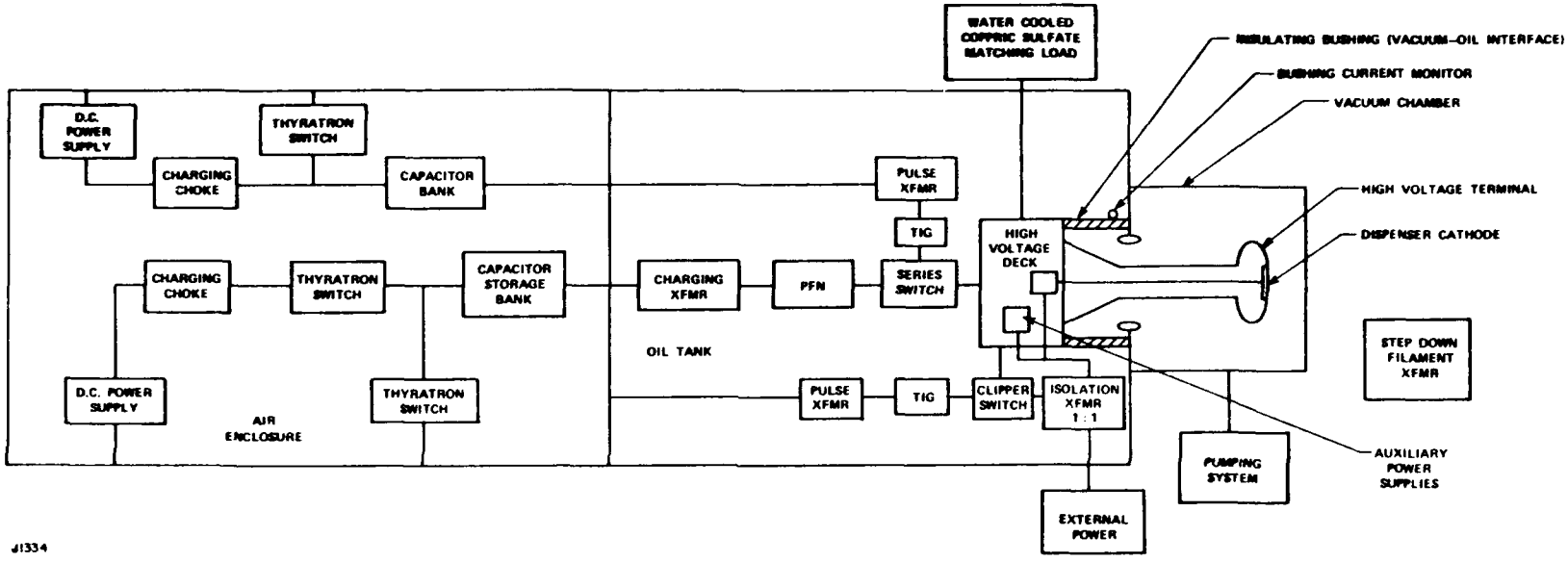

Figure III-5 Schematic Diagram of the Repetitively-Pulsed E-Gun Facility.

the PFN is a series switch consisting of a SF_6 pressurized, mid-plane triggered spark gap. A trigger pulse to the series switch is provided by a pulse transformer isolated by a trigger isolation gap (TIG) operated in an overvolted mode. To insure a short fall time of the output voltage pulse, a clipper switch, similar to the series switch, is provided as crowbar across the load. In both cases, the SF_6 flow was substantially increased over that provided with the system originally in order to achieve reliable operation under repped conditions.

The charging circuit is located in an air enclosure behind the oil tank and consists of a power supply, charging reactor and thyratron switch as shown in Figure III-5. The power is derived from a multistage variac with rectifying diode stack and a filter capacitor. A primary capacitor bank is resonantly charged to nearly twice the voltage of the filter capacitor through a series charging choke and series thyratron switch. The series thyratron also serves as a back biased diode preventing the primary capacitor bank from discharging back through the power supply. The charging time for the resonant cycle is ~ 30 msec allowing system repetition rates up to 25 Hz. After peak charge condition is reached, a parallel thyratron switches the primary capacitor into the primary of a pulse transformer with turns ratio of 18:1. The secondary of the pulse transformer charges the PFN to high-voltage levels in times of the order of ~ 20 μsec. For a maximum filter capacitor voltage of ~ 22 kV, the primary capacitor voltage is raised to ~ 37 kV and the secondary of the pulse transformer charges the PFN to ~ 650 kV. A series spark gap switches the PFN into the diode load with matching resistor of 50 Ω in parallel. A clipper gap terminates the pulse thereby shortening the fall time of the pulse voltage. Two similar charging systems are provided for the trigger pulses for the series and clipper spark gaps.

The diagnostic monitors include a resistive voltage divider network for both the capacitor storage bank and the high-voltage deck and a Rogowski current loop for the total diode current. The current monitor supplied by S^3 proved to be too insensitive for current values which were lower than originally anticipated and a new Rogowski loop with more turns but somewhat slower time response was installed.

The performance of the pulser was tested with the cathode inoperative, i.e., cold, by adjusting the dummy load to 50 Ω. For single pulses, output voltages of 300 kV were achieved both with and without the clipper gap. The pulser was operated at 270 kV at 25 Hz for several successive one-minute runs with a prefire rate of between 1 and 2%. At lower output voltages, 240 kV, a long duration run of 4000 shots was made before a prefire terminated the run. After final modification of the spark gap gas flow system, several 100 shot bursts at 270 kV and 25 Hz were made with no prefires indicating a prefire rate of < 1%.

The shape of the output voltage pulse for one 100 shot burst is shown in Figure III-6 where all pulses are overlayed. The clipper gap which truncates the trailing edge of the pulse appears to have a 100 nsec jitter when the signal is viewed in real time but the leading edge appears stable. The width of the output pulse under repped operation is shorter than for single shot as shown in Figure III-7, thus indicating a drift in the clipper gap timing.

The output current shape across the 50 Ω resistive load was measured with the more sensitive Rogowski loop. In this measurement, the loop was moved from the bushing to the lead connecting the dummy load to the high-voltage deck. This probe has a sensitivity of 0.55 V/kA and is a factor of 8 times more sensitive than the coil supplied by S^3. Minimum observable current with this probe is ~ 100 A. The time response of the probe is shown in Figure III-8 in comparison with the voltage pulse across the 50 Ω dummy load. This rise and fall times of the current signals is ~ 2 times greater than the voltage signal which is a result of the higher internal inductance of the probe.

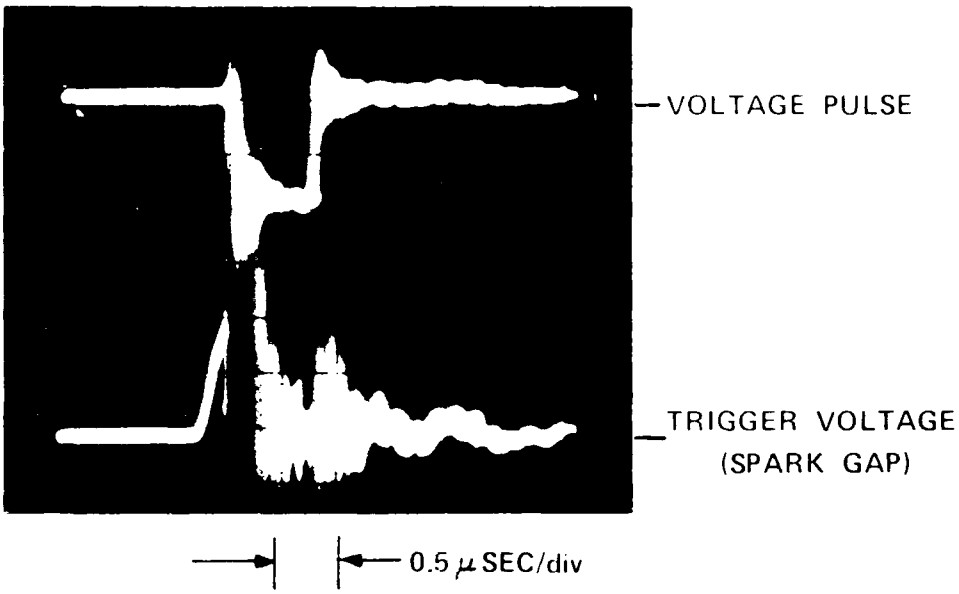

REPPED OPERATION

J4173

Figure III-6 Output Voltage Across a 50 Ω Resistive Load Under Repetitively-Pulsed Conditions.

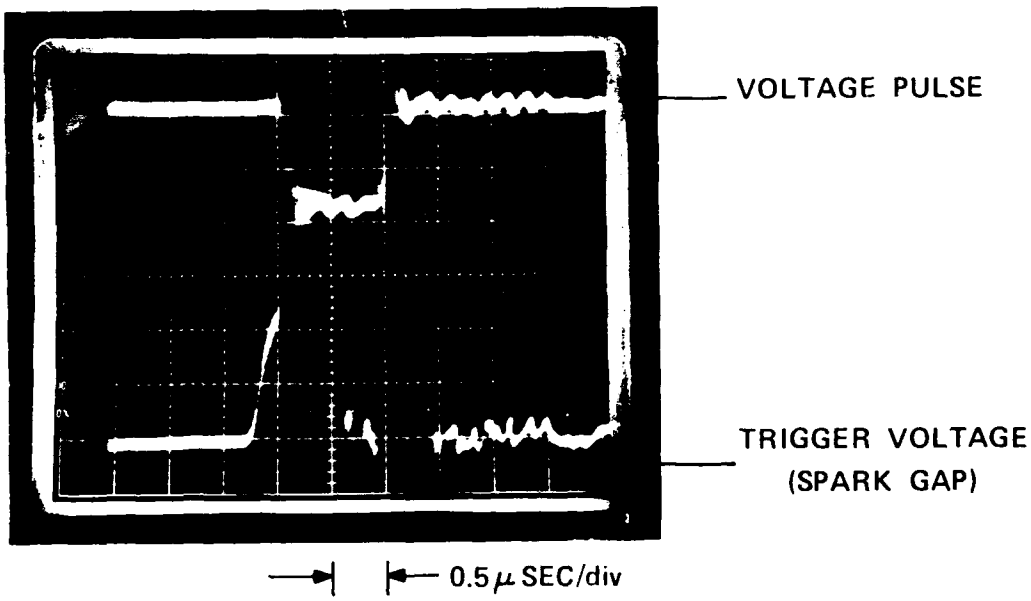

SINGLE PULSE OPERATION

J 4171

Figure III-7 Output Voltage Across a 50 Ω Resistive Load for Single-Shot Conditions.

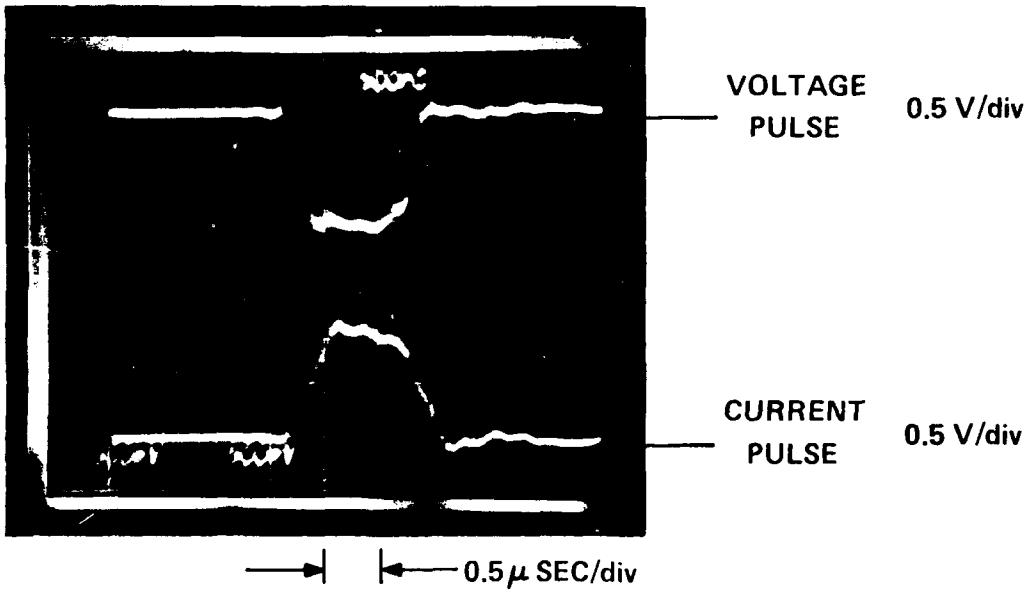

J4172

Figure III-8 Time Response of a Sensitive Rogowski Current Probe.

2. Vacuum Chamber

The vacuum chamber which houses the dispenser cathode is a stainless steel cylindrical vessel bolted onto the end wall of the oil tank of the pulser. A schematic diagram of the tank showing the pumping system, view ports, high-voltage terminal, bushing and anode is shown in Figure III-9. The primary pump for the chamber is a 1500 ℓ/sec turbomolecular pump (Sargent-Welch Model No. 3132C) which also serves to rough the chamber from atmosphere. A 2000 ℓ/sec closed-cycle cryopump (CTI-Cryotorr 7) was added later along with a 6 in. LN_2 cold trap to aid in removing the major residual gas, water vapor. A small cold-trapped diffusion pump was used periodically to evacuate the cryopump and therefore prevent condensed gases from re-entering the vacuum chamber upon shutdown. Eight view ports surround the high-voltage terminal, and the anode could also be replaced by a view window for temperature measurements. A magnetic mass spectrometer (Aerovac Monotorr 702) sampled the background gas both prior to and during cathode activation. After continued pumping alternated with heating cycles (of the cathode arrray), a base pressure of $\sim 8 \times 10^{-8}$ torr was achieved. A mild bakeout cycle was performed by wrapping the chamber with heater tapes and insulation, however, this mode of baking is not truly effective since the bushing surface and cathode stem cannot be heated and water vapor driven off the chamber will condense on these cool surfaces.

Details of the high-voltage terminal, cathode mounts and water-cooled anode foil support structures are shown in Figures III-9 and III-10. The two circular magnetic field coils placed in the Helmholtz configuration give a uniform dc guide magnetic field up to 2 kG in the anode-cathode region.

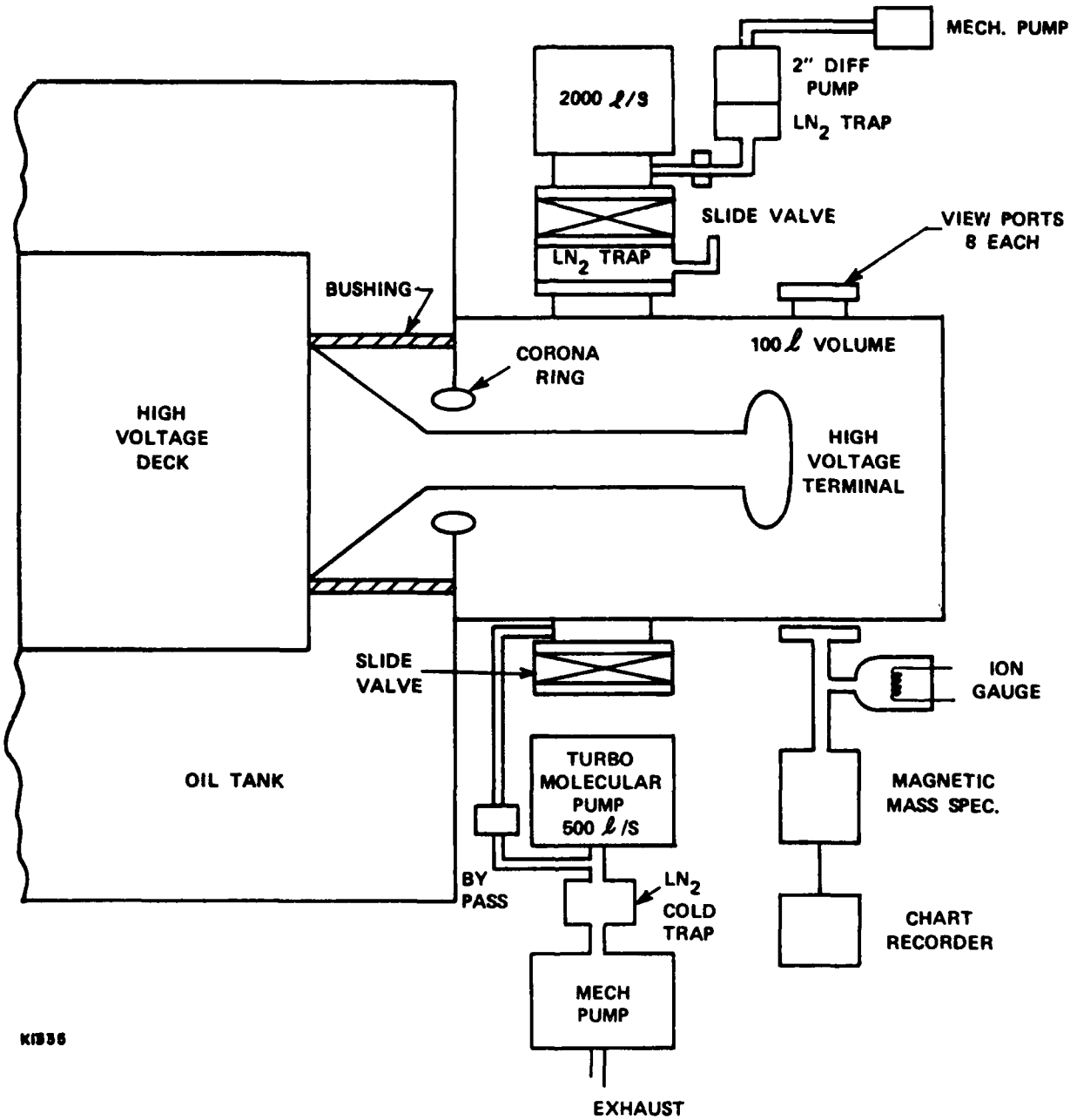

Figure III-9 Schematic Diagram of the Vacuum Chamber

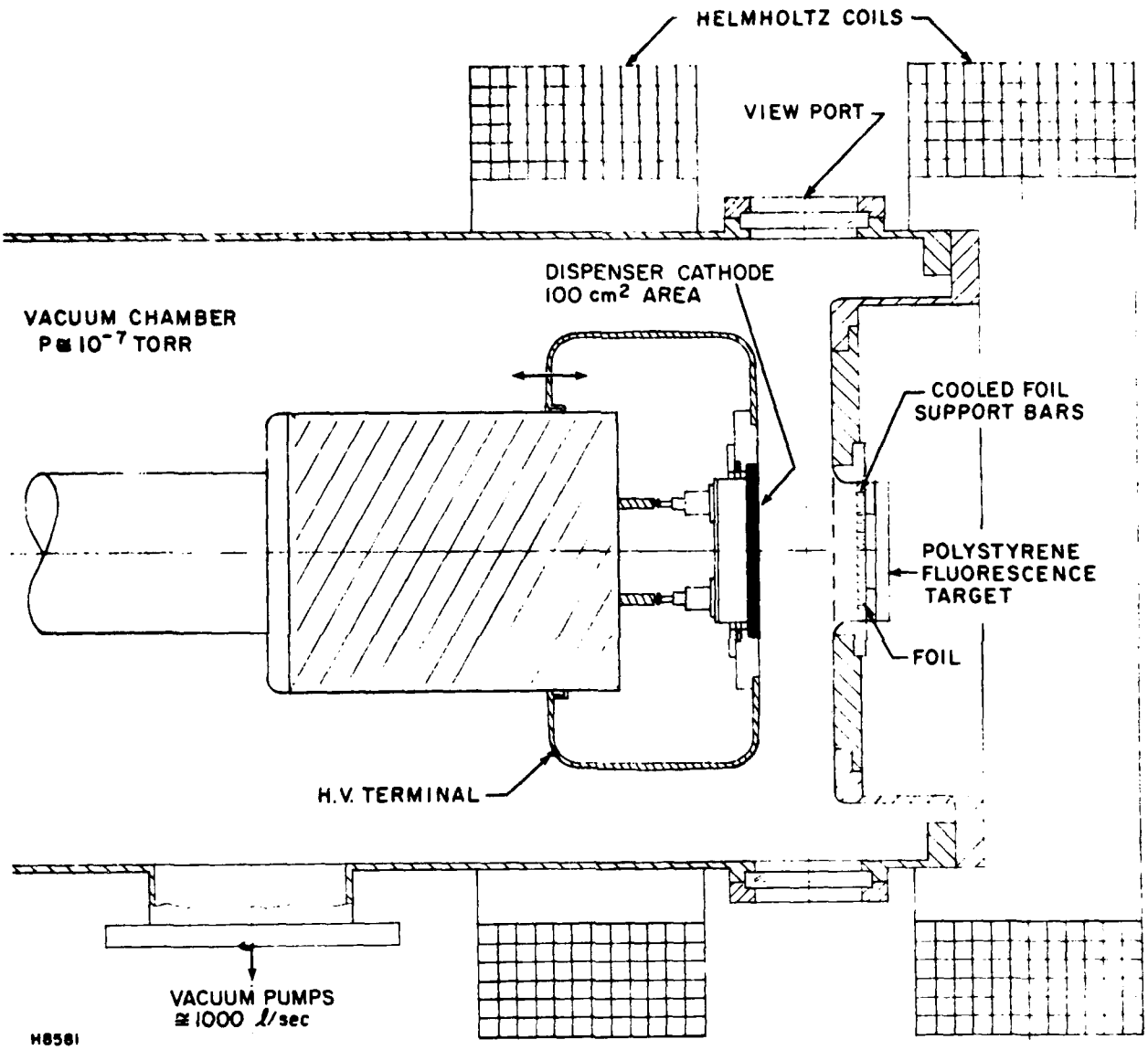

Figure III-10 E-Gun Test Chamber

The insulating bushing is made of cast epoxy, EPON 828-A with a vapor pressure curve shown in Figure III-11. Although this curve indicates that good vacuums should be attainable, given sufficient pumping time, we feel that unless the bushing-tank interface is redesigned to allow sufficient bakeout, this material is unsuitable. Mass spectra indicate that the major component of the residual gas in the base vacuum is water vapor, as shown in Figure III-12. In this situation, a full bakeout will usually lower the base pressure by at least an order of magnitude providing all surfaces are heated. Most dispenser cathodes used in commercial tubes are baked at $\geq 450^{\circ}C$, however, this temperature is clearly beyond the capability of the viton O-rings used in the present system. Metal seals or an all welded construction are needed at this temperature. A lower temperature bakeout, say $200^{\circ}C$ (viton limited) may be sufficient to remove water vapor from the vacuum chamber surfaces especially if only moderate cathode lifetimes, 100s of hours, are required. The subject of base vacuum, bakeout procedures and compatible materials requires further investigation.

Two types of anodes were used in the present tests: (1) a solid, water-cooled plate, and (2) a thin metal foil window supported by a water-cooled bar structure made of copper (see Figure III-13). Both aluminum and copper were tried for the solid anode; however, aluminum appears to poison dispenser cathodes and copper is the preferred material for this application. Both copper and titanium foils have been used and performance of each will be discussed in the following sections.

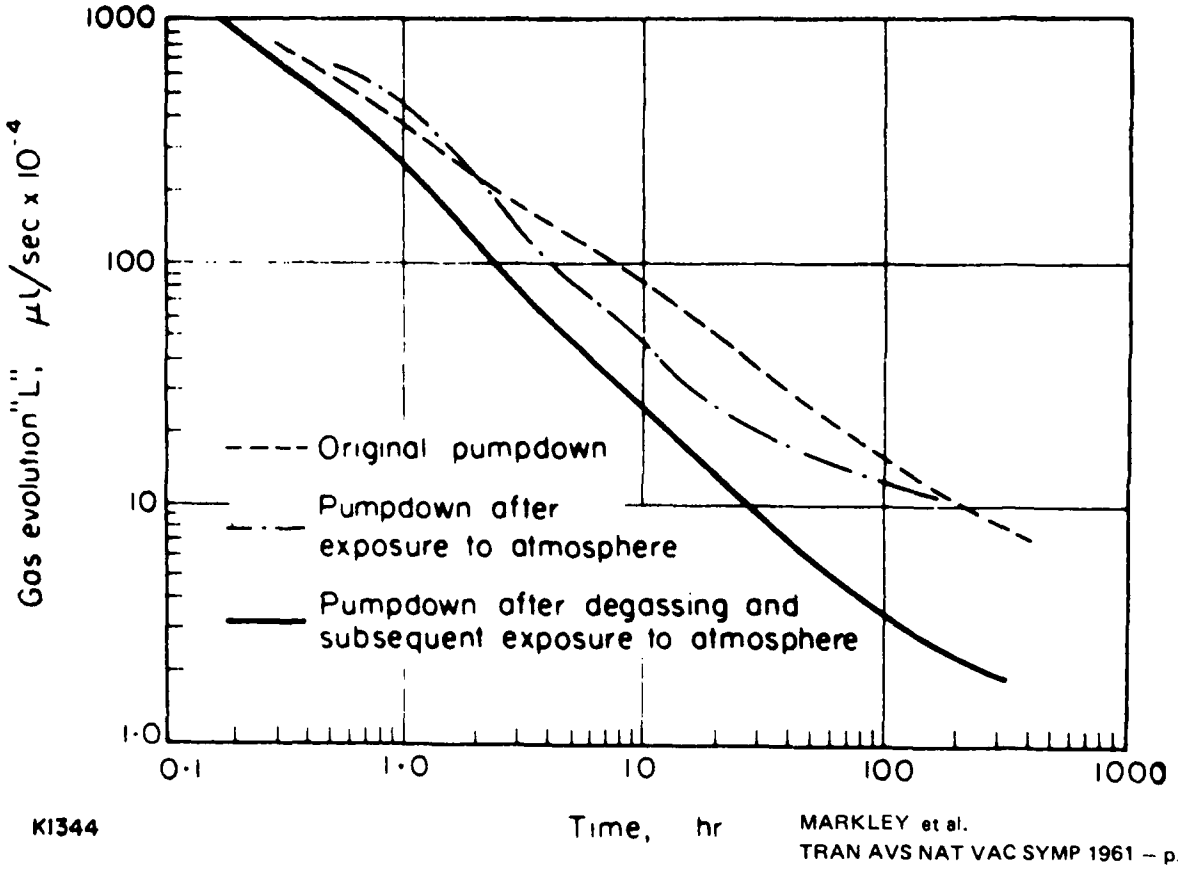

MARKLEY et al.
TRAN AVS NAT VAC SYMP 1961 – p. 78
PERGAMON PRESS OXFORD 1962

Figure III-11 Vapor Pressure Curve of EPON 828

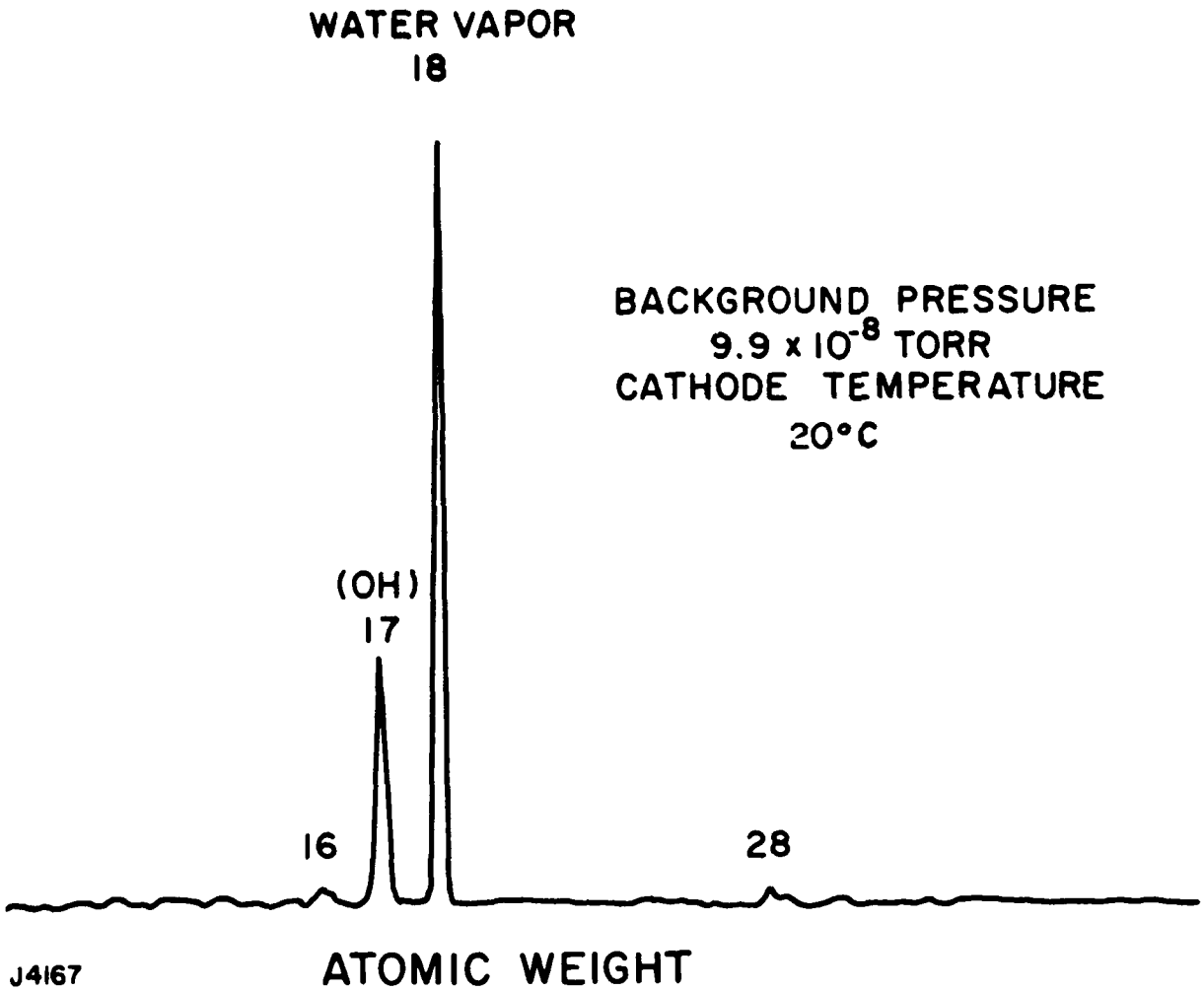

Figure III-12 Mass Spectrometer Scan of the Base Vacuum in the Vacuum Chamber.

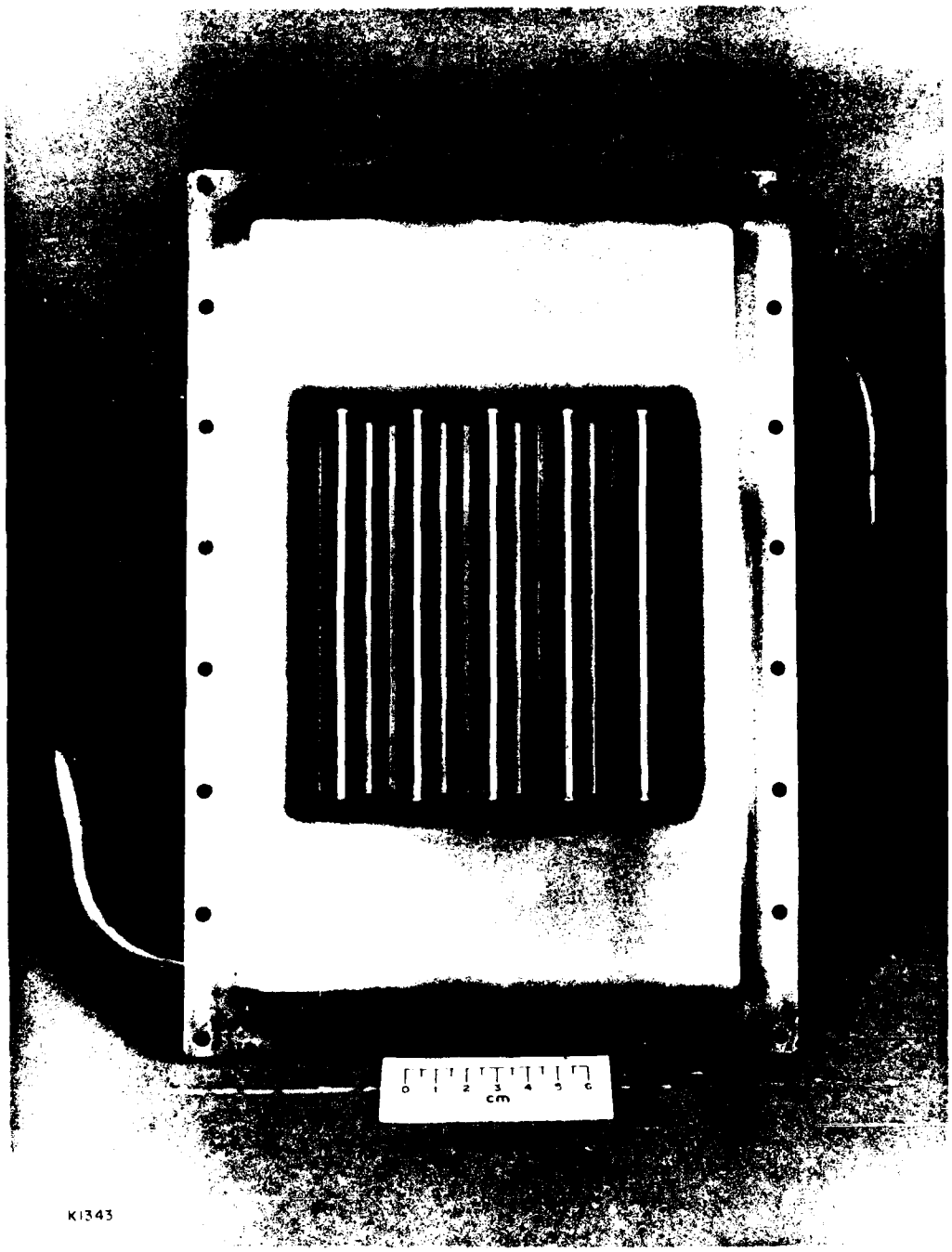

CONDUCTION COOLED
FOIL SUPPORT STRUCTURE

Figure III-13 Photographs of the Water-Cooled Foil Anode and Support Bars

C. FIELD EMISSION CATHODES

1. Tantalum Blade Cathode

A cold cathode array, 10 x 20 cm, with provision for preheating of the blades is shown schematically in Figure III-14 and photographically in Figure III-15. Each blade is spring loaded to account for thermal expansion and is separated electrically by mounting on a ceramic insulator, shown in Figure III-16. The entire subassembly is mounted behind the electrostatic cover plate shown in Figure III-17 and the complete unit is mounted on the cathode surface of the e-gun.

2. Carbon Felt Cathodes

Another broad area cold cathode concept is illustrated in Figure III-18. Here, carbon felt is attached to the flat portion of a high-voltage terminal and the many fine carbon fibers serve as field emission sites. The relative simplicity of this concept is evident from the lack of structural components, mounting hardware, etc. The measured performance in terms of closure velocity, spatial uniformity and emission density as a function of magnetic field is discussed in Section IV.

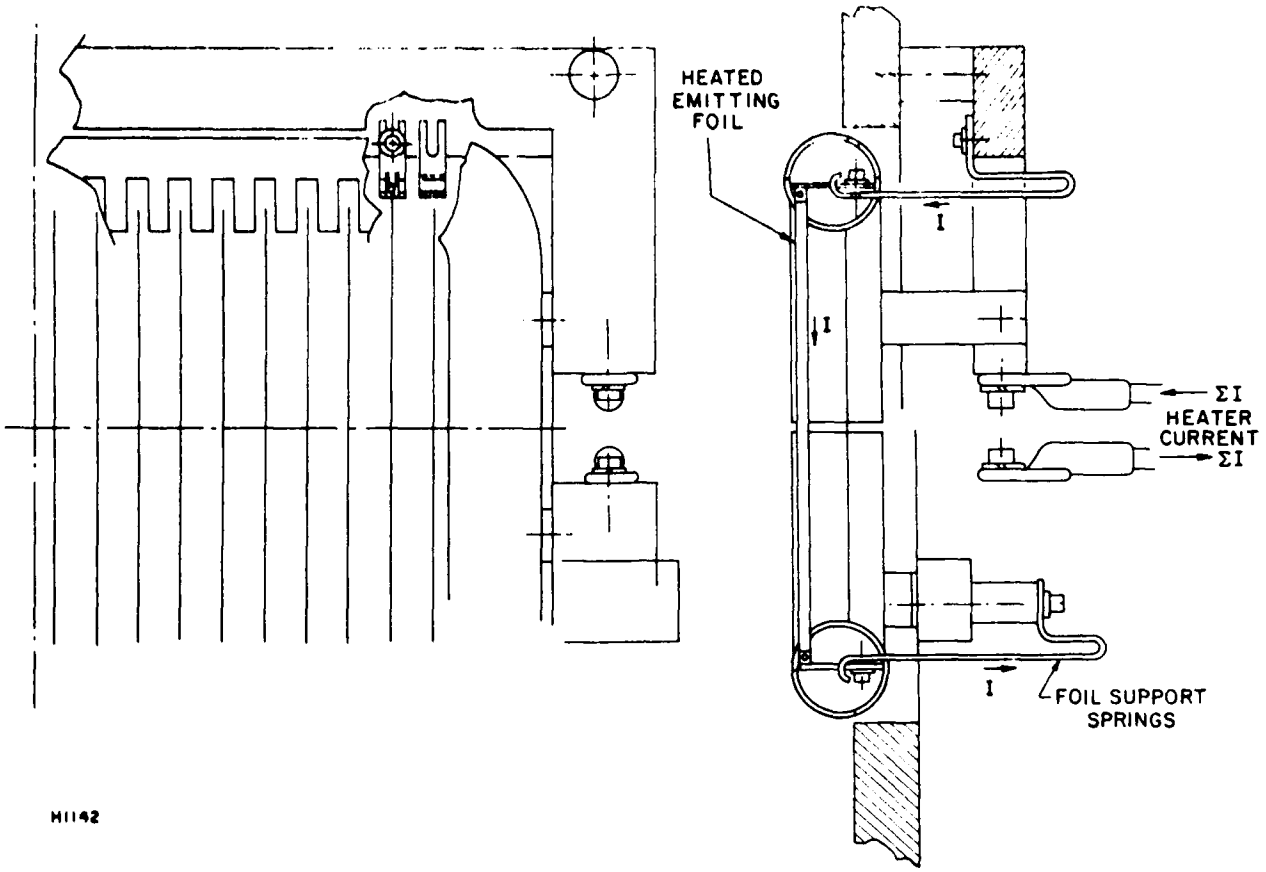

Figure III-14 Cold Cathode Concept with Outgassing Capability.

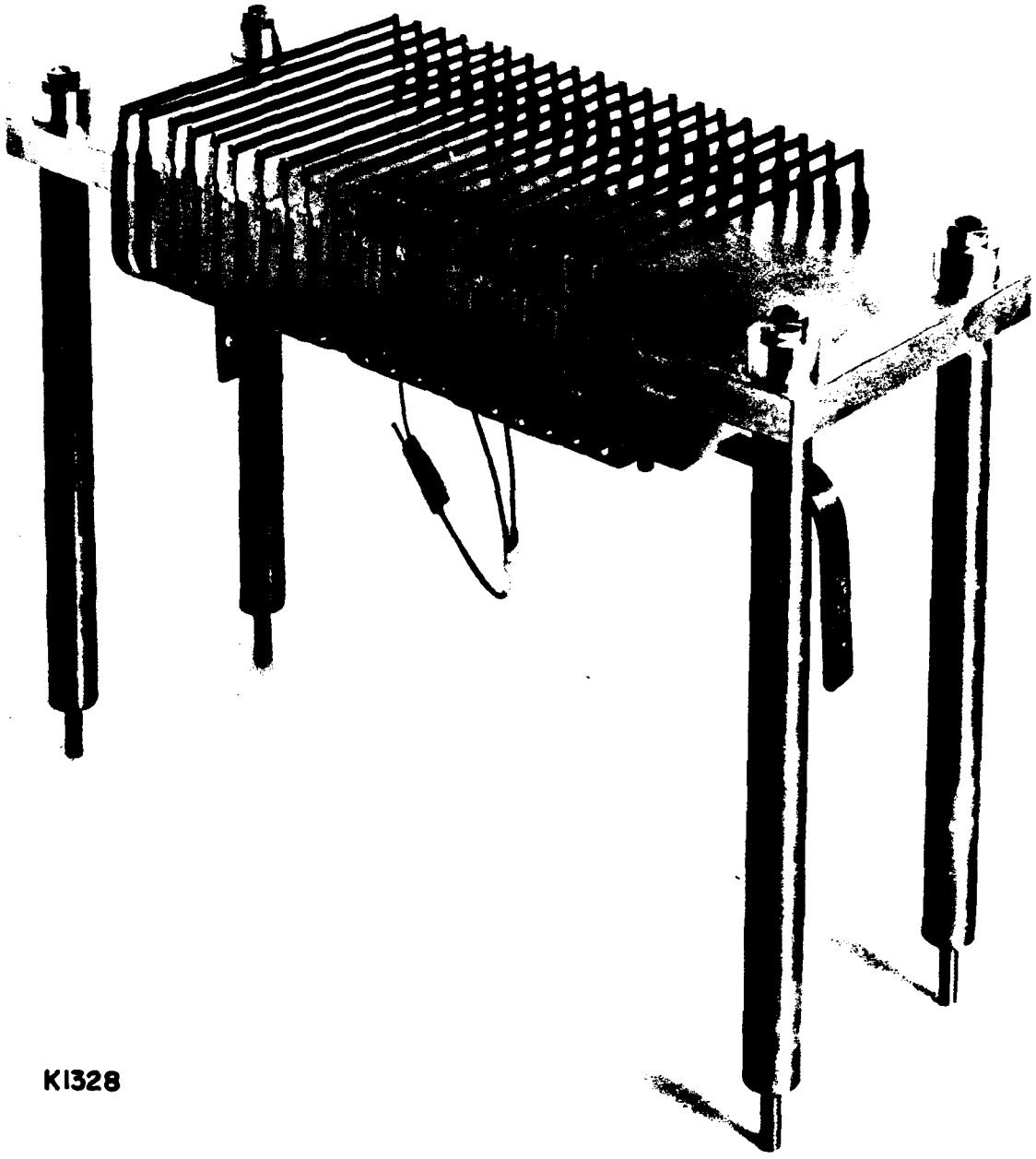

Figure III-15 Cold Cathode Array with Outgassing Preheaters

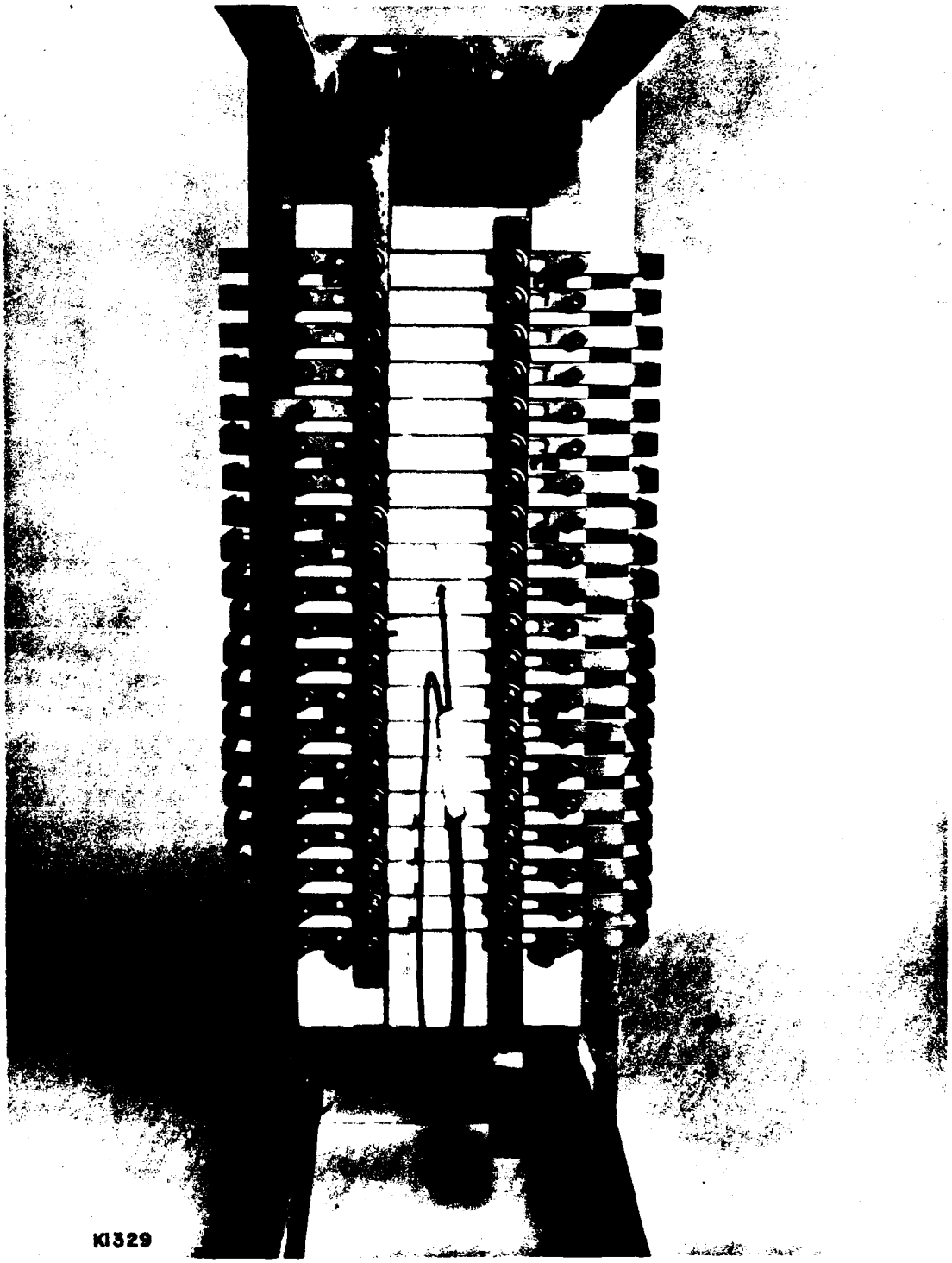

Figure III-16 Electrical Isolation of Heated Blades

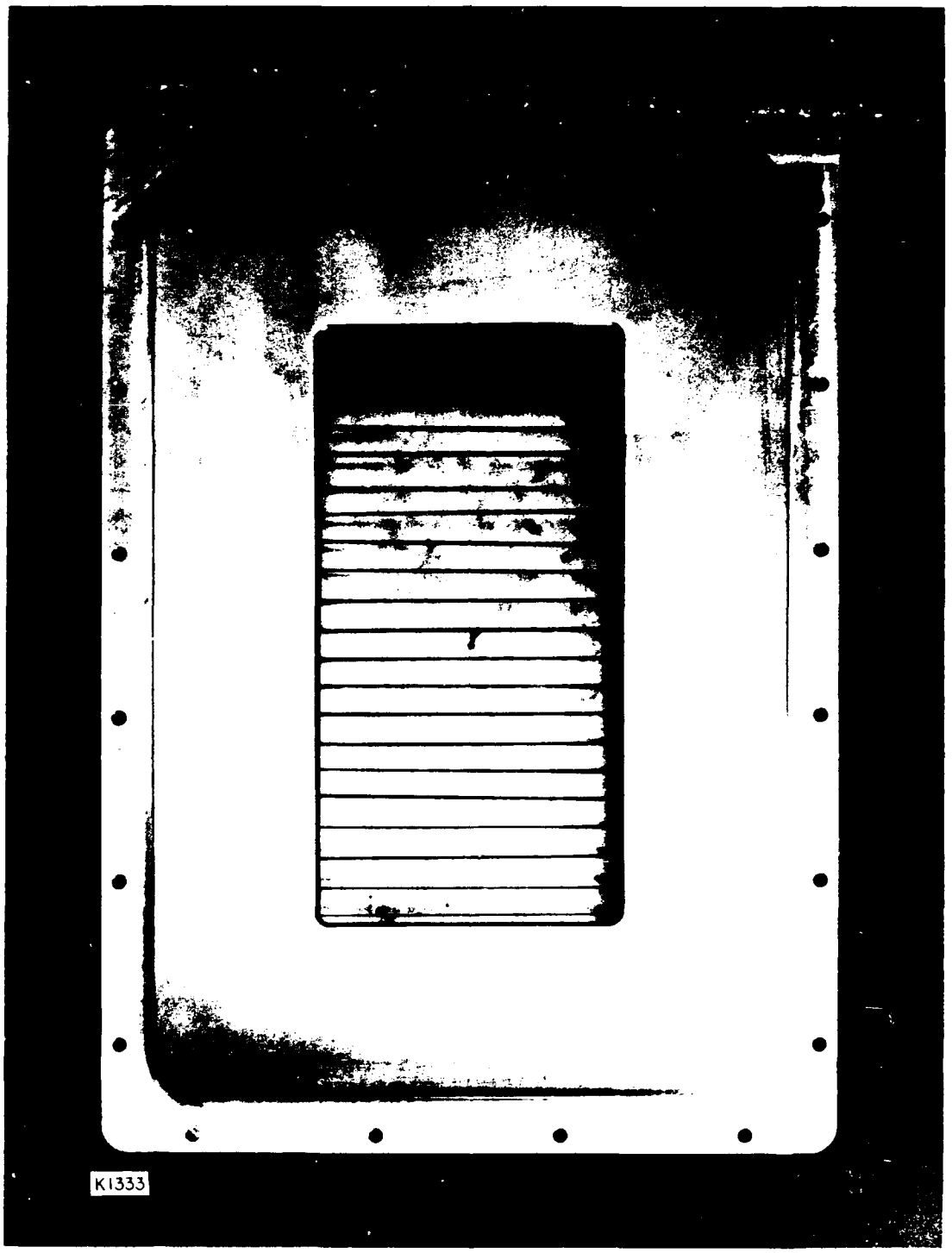

Figure III-17 Cold Cathode Mounted Behind Electrostatic Cover Plate.

100 cm

CARBON FELT COLD CATHODE

J4563

Figure III-18 Carbon Felt Cold Cathode

D. PHOTOEMISSIVE CATHODES

Photoemissive cathodes also require no heater structures, but rely on photoelectron emission initiated in this case by high-power, pulsed flashlamps. Metals such as aluminum and magnesium are studied in this effort because they are not poisoned upon contact with air. A simple implementation of the photoemissive cathode technology is shown in Figure III-19. The 10 x 20 cm magnesium cathode was mounted on an aluminum plate as shown in Figure III-20 which was then mounted to the face of the high-voltage terminal of the diode structure. The cathode configuration was illuminated by the flashlamps shown in Figure III-21. No shielding structures, magnetic or material, were provided and some darkening of the flashlamp envelope (quartz) was evident after 40-50 shots. The spatial distribution of the current density was monitored by a series of current buttons (Figure III-22) and the total current waveform was measured with a Pearson current transformer located in the ground return of the diode. Rectangular cavities provide access to the high-voltage terminals of the flashlamp so that all these connections can be made outside the vacuum system. The round porthole just above the right-hand rectangular cavity is the quartz window through which flashlamp to pulse duration was measured with a vacuum photodiode. This quartz window was also darkened by the e-beam.

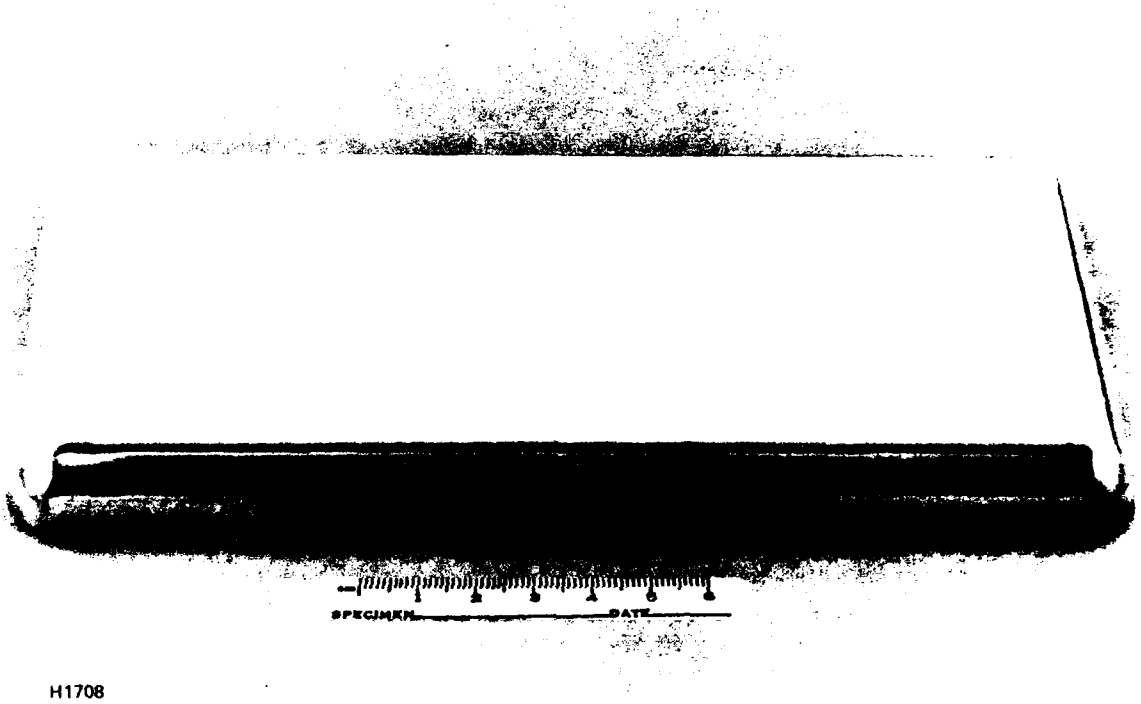

Figure III-19 Magnesium Photoemissive Cathode (10 x 20 cm)

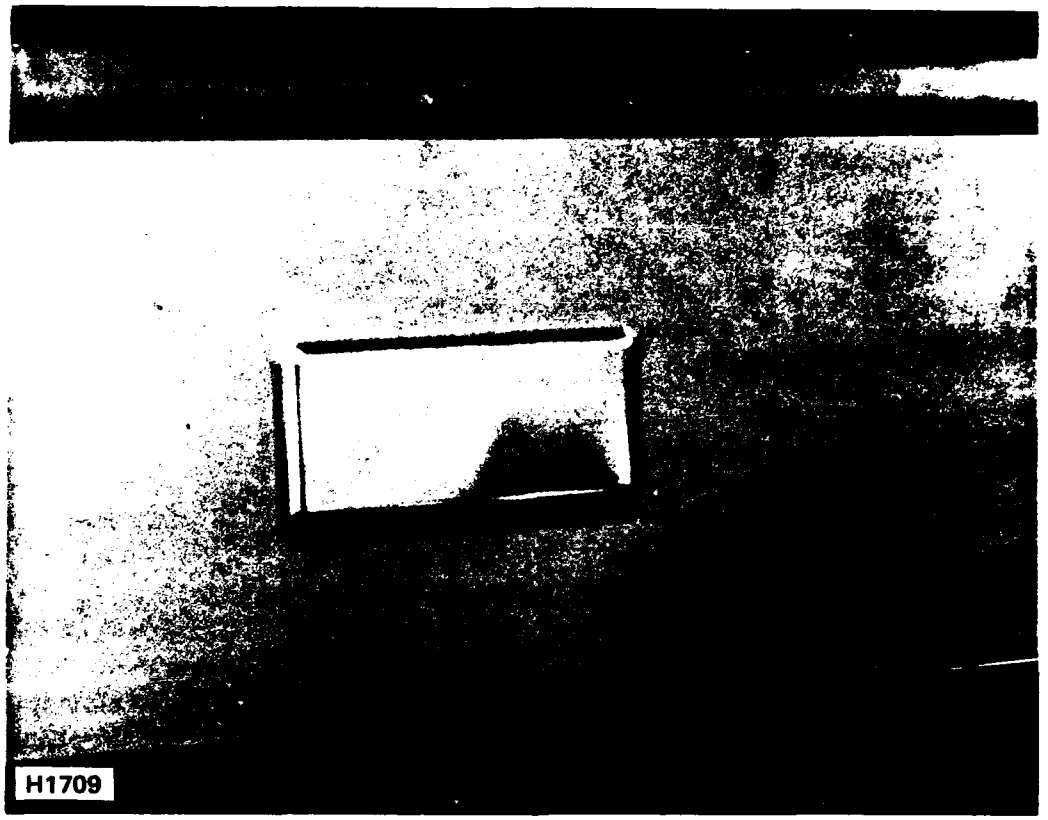

Figure III-20 Magnesium Photocathode Mounted on Aluminum Support Plate which is Attached to the High-Voltage.

Figure III-21 Coaxial Flashlamps Used to Farodiate the Photocathode.

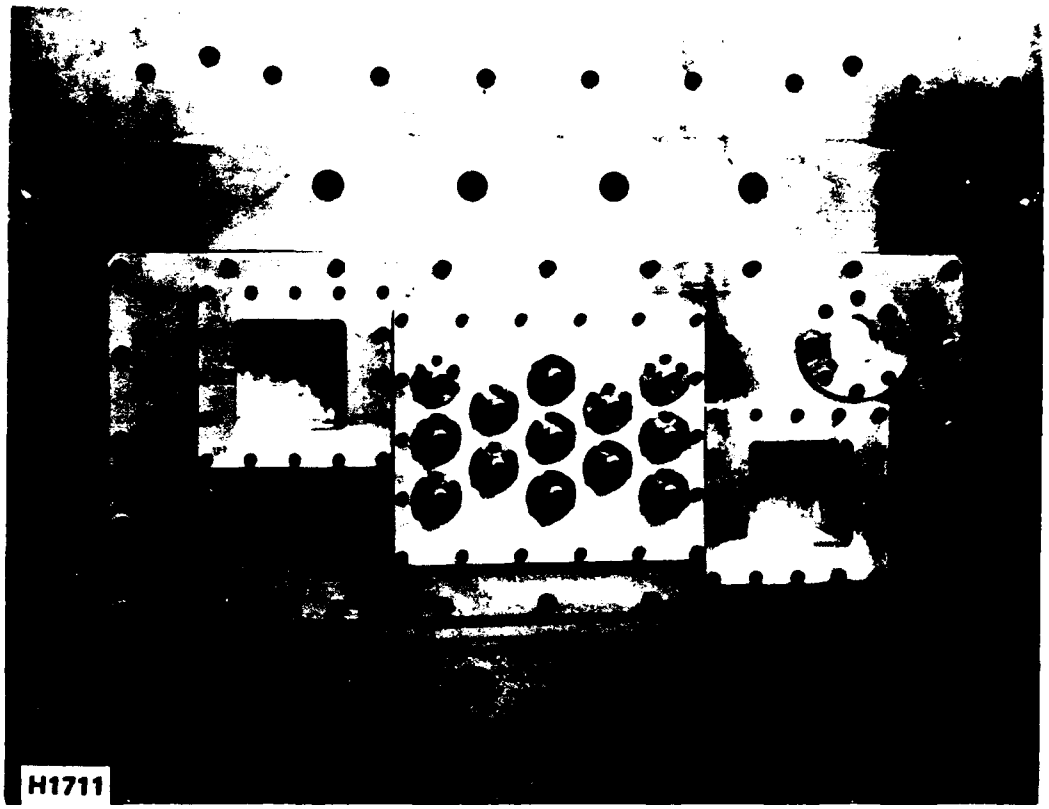

Figure III-22 Current Button Plate Used to Measure E-Beam Current Density Distribution.

E. SMALL AREA THERMIONIC CATHODES

The experimental configuration for the 5 cm^2 area dispenser cathode is shown schematically in Figure III-23. The dispenser cathode in Figure III-24 consists of a cylindrical tube holding the heater structure which is encased in ceramic and the 1 in. diameter face plate of barium impregnated porous tungsten. The dispenser cathode is held in place by three spring clips of molybdenum which provide a high thermal resistance means of support and the entire structure is mounted on a copper plate on the face of the high-voltage terminal. Clearance is provided between the cathode barrel and the copper face plate to minimize conduction losses in the heater.

The face of the cathode is placed ~ 2.8 cm away from a perforated nickel screen which serves as the electrostatic anode of the e-gun. The electrons leaving the cathode pass through the holes in the nickel attenuator and strike the polystyrene which is located inside the vacuum chamber of the e-gun. The electrons striking the polystyrene causing it to fluoresce and this fluorescence is photographed through a quartz window in order to observe the activation and electron emission characteristics of the cathode. The surface of the polystyrene nearest the cathode is aluminized to remove the electronic charge from the polystyrene just after the e-beam pulse. If this is not done, large electric fields would develop which would destroy the polystyrene target.

A similar mounting structure was used to test these small area dispenser cathodes in the repped facility where the base vacuum was lower. In this arrangement, the heater power as a function of cathode temperature was measured and found to be significantly greater than reported by the manufacturer (Spectra-Mat, Watsonville, CA). The Spectra-Mat measurement was obtained in a bell jar with the dispenser cathode hanging from the leads with no other support. The observation that all the temperature dependencies are linear with input power agrees with the calculation that radiation cooling is negligible at these

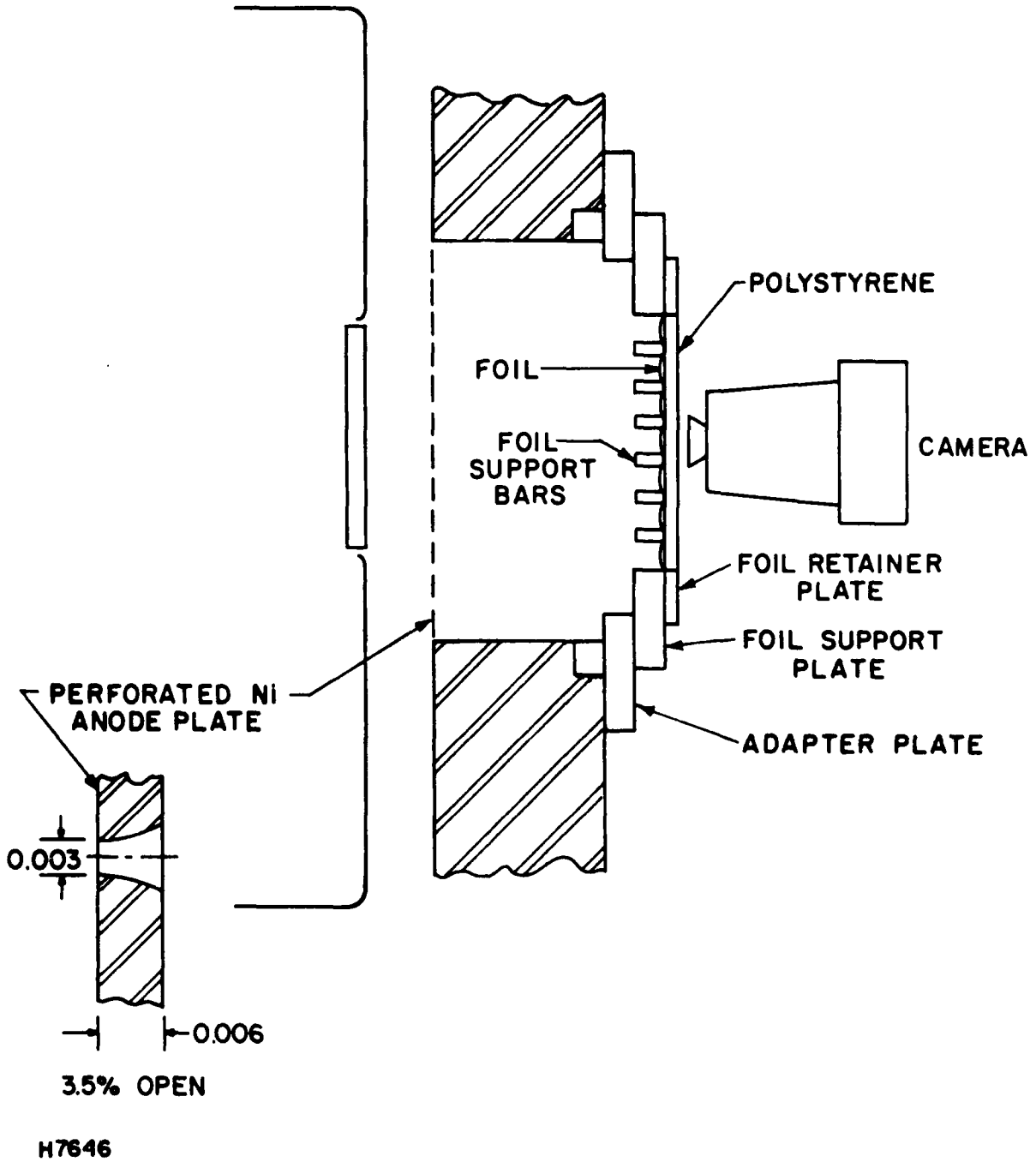

Figure III-23 Experimental Configuration for the Small Area Dispenser Cathode.

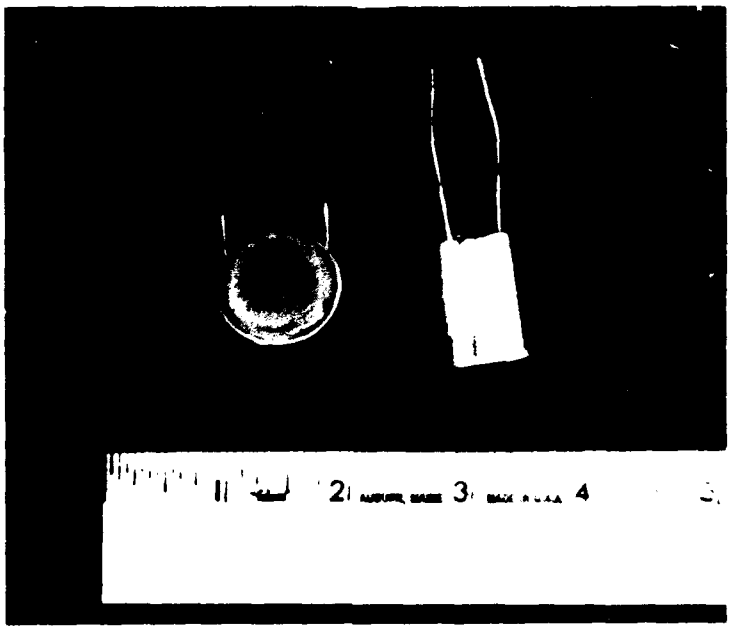

SMALL AREA DISPENSER CATHODE

J4563 (THERMIONIC)

Figure III-24 Small Area Dispenser Cathode

temperatures and, hence, all heat losses are from conduction through the support and heater structure. On one occasion, the heat loss through the molybdenum spring clips was sufficiently great that the heater structure failed at high temperature. This situation was alleviated by removing most of the molybdenum surface contact by milling the clips to two 1/8 in. wide strips at the tangent points. The lower heating curve results, which is in better agreement with the unsupported case.

For the measurement series taken in the repped facility, the total current signal was too low to be measured by the Rogowski loop located around the bushing. In this case, the PFN was disconnected and the anode-cathode voltage provided by the thyratron pulse normally used to trigger the spark gaps. The cathode was then placed closer to the anode (1.75 cm) to reach the several A/cm^2 regime.

F. LARGE AREA THERMIONIC CATHODES

The large area cathodes shown in Figure III-25 measures 10 x 10 cm, having an active area of 100 cm^2. The heater structure consists of tungsten filaments surrounded by ceramic tubes which are inserted into holes drilled through the dispenser cathode block as shown in Figure III-25. The filaments are connected in series by means of small tantalum clips which are swaged on to the tungsten and connected to the step down filament transformer in the high-voltage deck. The filament current is brought into the high-voltage terminal through the water cooling lines and voltage isolation is achieved via small ceramic insulating sections.

The large area dispenser cathode is mounted to the high-voltage terminal by means of thin molybdenum tabs which are pinned to the cathode sides. Molybdenum is used because its high-temperature capability and compatibility with barium dispenser cathodes, and the tabs are made thin to reduce heat conduction. Attached to the mounting tabs and directly behind the cathode surface are several sheets of molybdenum which serve as radiation shields to minimize the heat loss from the rear cathode surface.

The wire size and length of the heater structure is chosen to present an impedance which matches the power capabilities of the transformer coupled power supply. The temperature of the cathode surface was measured with an optical pyrometer (Leeds and Northrup) and the resultant (midpoint) temperature is plotted as a function of total input power in Figure III-26. At low temperatures, conduction losses through the moly tabs and heater structure dominate while at high-temperatures radiation losses become significant and the temperature rises more slowly as shown by the calculated curve in the figure. At the highest temperature of operation, 1360°C, the measured input power is 1550 W with a relatively large error bar due to an uncertainty in the primary current measurement. The error bar in measured temperature reflects the temperature variation across the cathode surface and the fact that the emissivity of the surface is not known precisely.

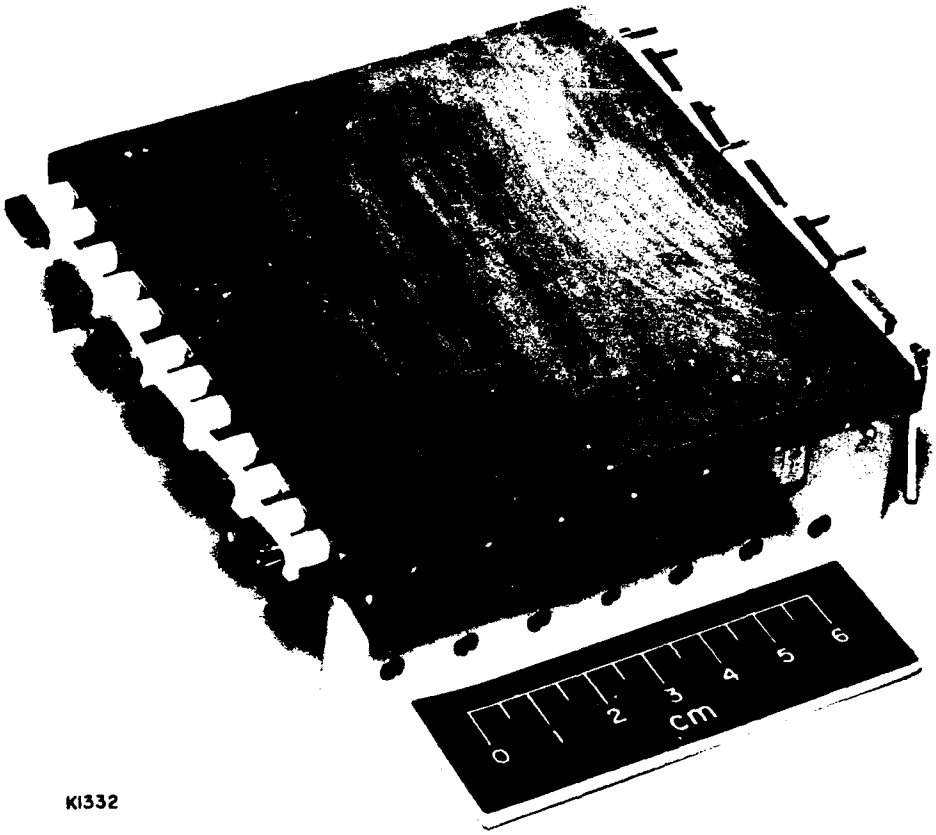

Figure III-25 Large Area Dispenser Cathode

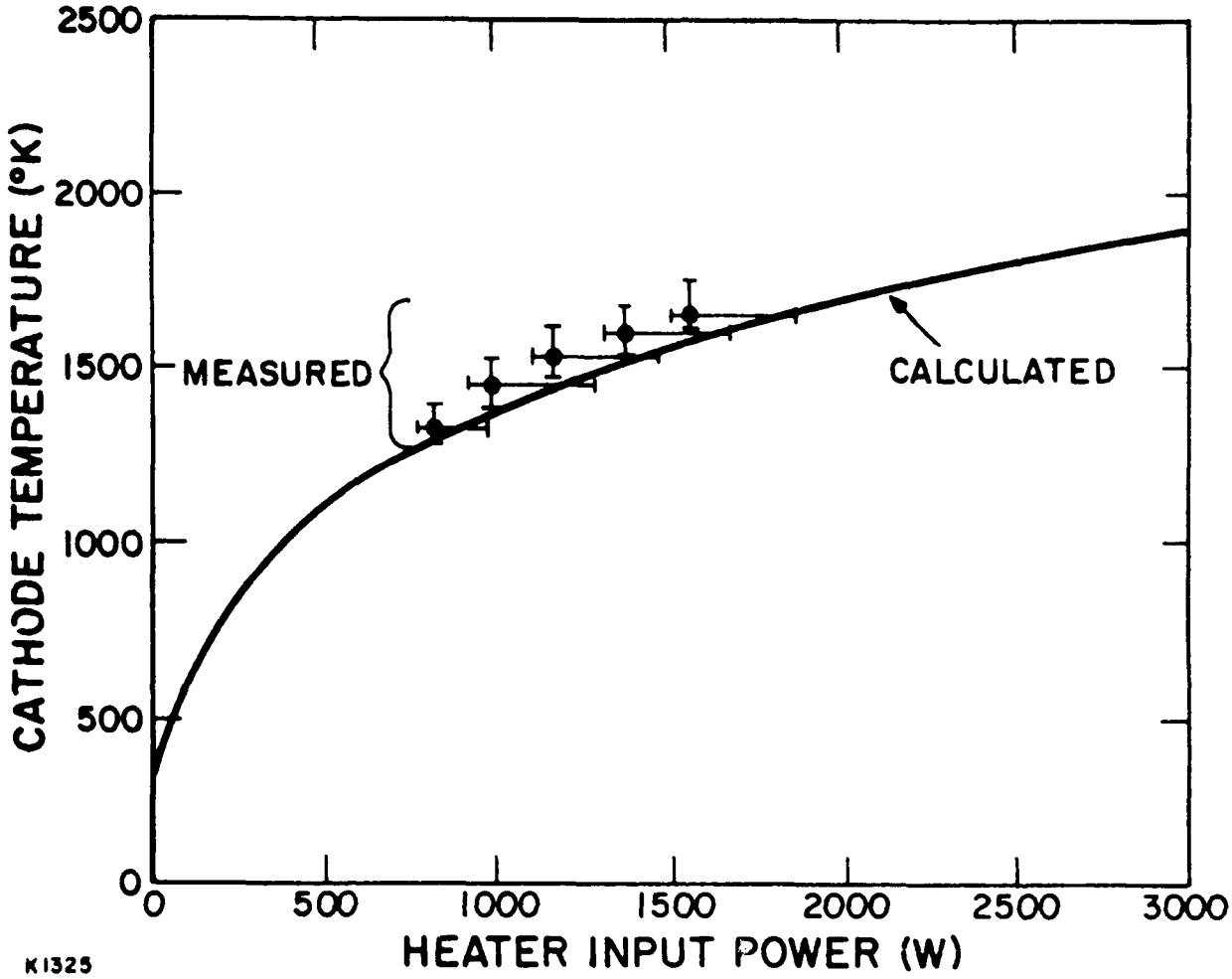

Figure III-26 Large Area Cathode Temperature vs. Input Power

The temperature profiles along horizontal and vertical scans through the midpoint are shown in Figure III-27. The observed temperature variation of $\sim 75^{\circ}C$ could represent as much as a factor of two in current density if the cathodes were operated emission limited. However, for most applications, the cathodes would be operated space charge limited with the edge temperature limit set above the desired emission. Also, in a larger scale system a heated ring surrounding the cathode would improve temperature uniformity.

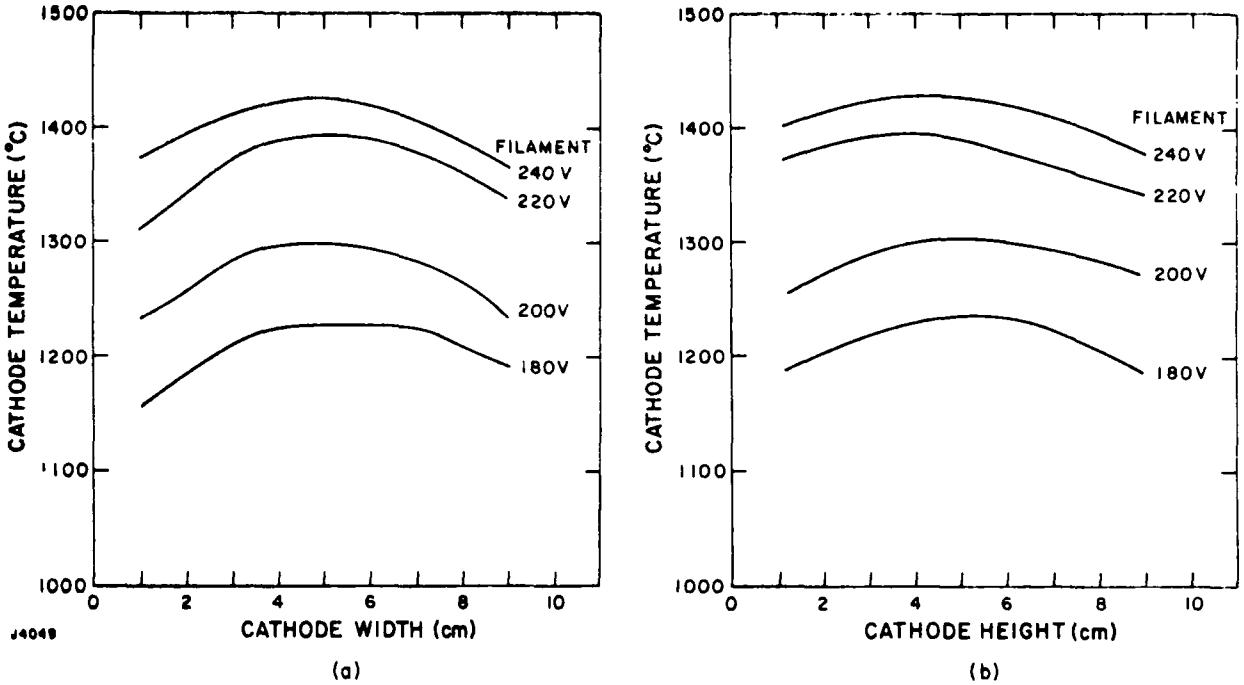

Figure III-27 Temperature Profiles of 150 cm^2 along Horizontal and Vertical Scans.

G. FOIL AND FOIL SUPPORT STRUCTURE (REPPED FACILITY)

The foil support structure (Figure III-28) together with its associated thin metallic foil was designed not only to test the cooling capability of the combination but also to permit diagnosis of the beam under repped conditions outside the vacuum chamber. The support structure is constructed of OFHC copper plates and tubes and is vacuum brazed and helium leak checked before installation. The foil support bars are spaced 5 mm apart, and 3 mm wide, and 8 mm high. Water cooling is supplied by manifolds located at either end of the bars.

For high-average current applications such as would be encountered in a long pulse repped XeF laser, the power which must be dissipated in the foil can exceed 100 W/cm^2 and, hence, a material with high thermal conductivity is required. For some applications, the laser gas is operated at elevated temperature ($\sim 200^{o}C$) for higher performance, and hence, the foil material must also be capable of high ambient temperatures. Titanium foil has high-temperature capabilities, is of moderate atomic number (and therefore moderate electron stopping power), but has very low thermal conductivity. To improve the thermal conduction of titanium foil, other materials, e.g., copper, can be deposited on the surface in thin layers.

Another reason for cladding titanium foils is the incompatibility of titanium with dispenser cathodes. Since copper is the only metal with high conductivity which is compatible with dispenser cathodes, copper is the cladding material at least for the surface facing the cathode. Aluminum which has lower electron stopping power could be used on the high pressure side of the foil.

The cladding thickness of copper required to appreciably raise the thermal conductivity of the titanium foil is $\sim 5\ \mu m$. Several methods of plating these thick layers of copper on titanium were investigated under this program, e.g., electro-plating and vapor deposition, were as yet unsuccessful

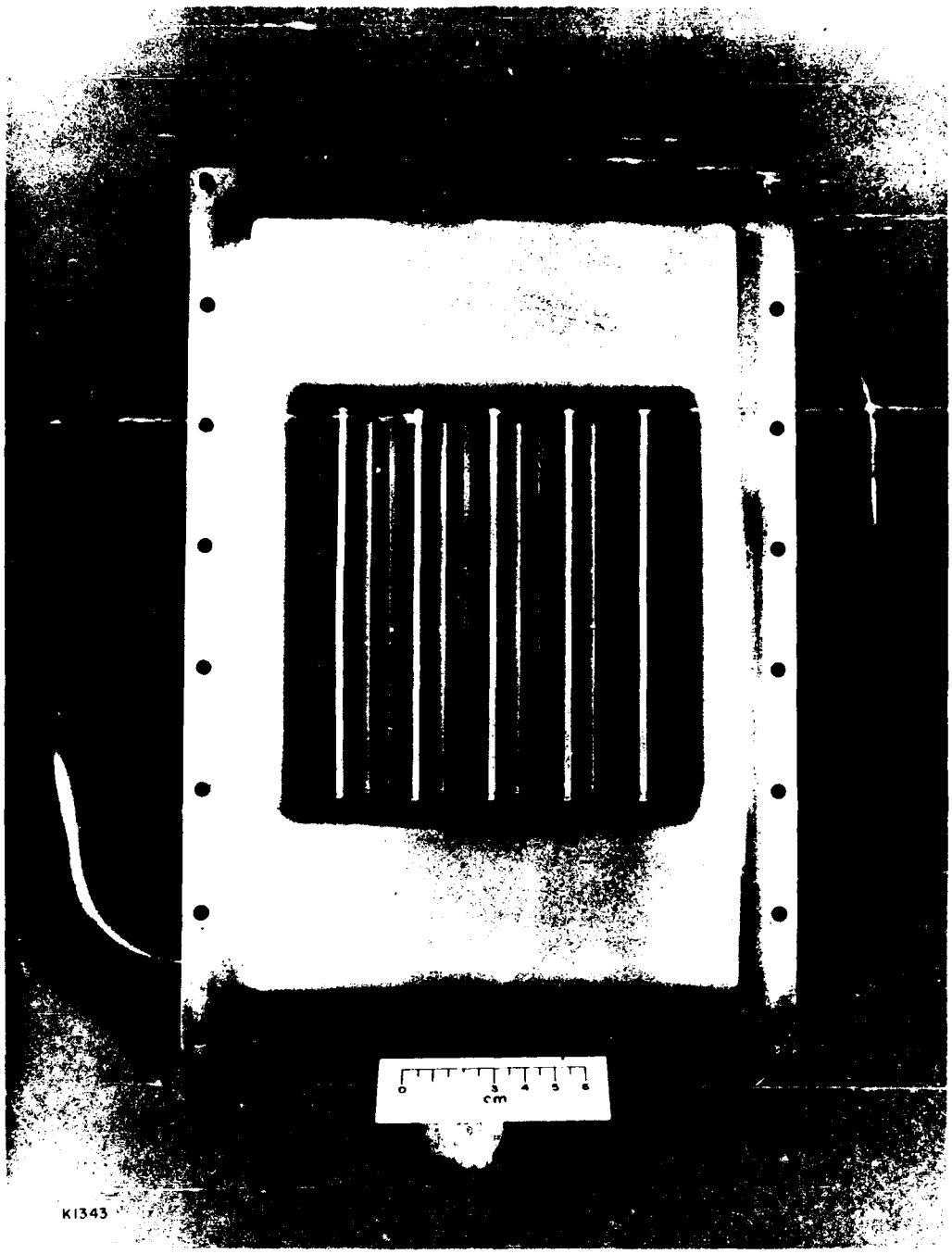

CONDUCTION COOLED
FOIL SUPPORT STRUCTURE

Figure III-28 Foil Support Structure

results. Titanium forms oxides which are strongly bound to the surface and cladding of thick layers is difficult. Thin coatings, 0.5-1 μm, were achieved with relatively good adhesion and tests show that this thickness is sufficient to overcome the poisoning associated with pure titanium. Figure III-29 shows photomicrographs of 25 μm titanium foil with ~0.5-2 μm thick layers of vacuum deposited copper with varying degree of adhesion. Figure III-30 shows an attempt to coat the same thickness of titanium foil with aluminum by plasma spraying on two sides. The bond appears to be good, however, the uniformity is very poor and deemed unacceptable for the present application.

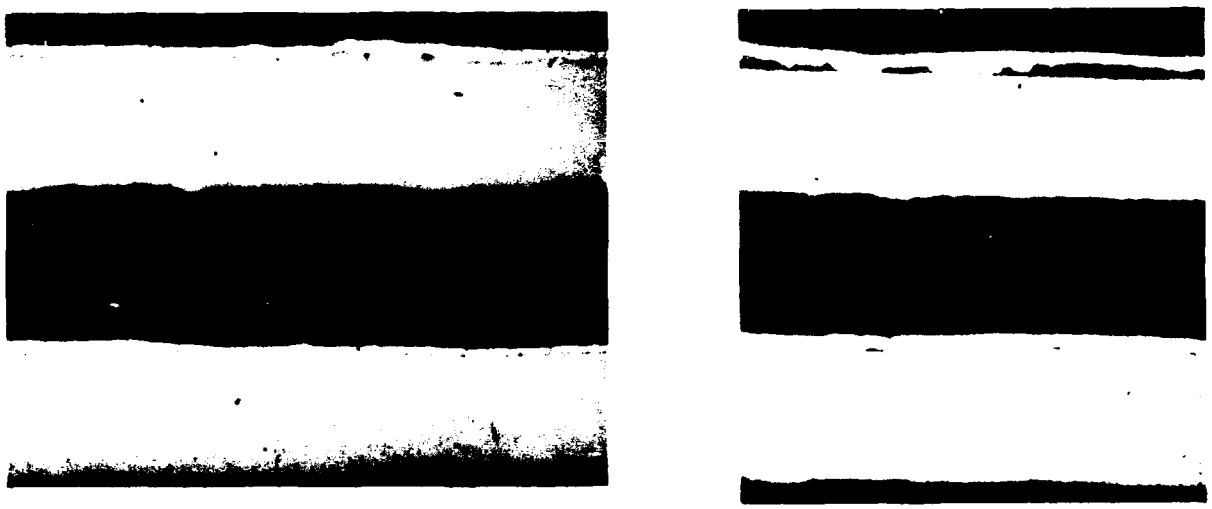

(A) (B)

K1324

Figure III-29 Photomicrograph of Copper Clad Titanium Foil (Vapor Deposition).

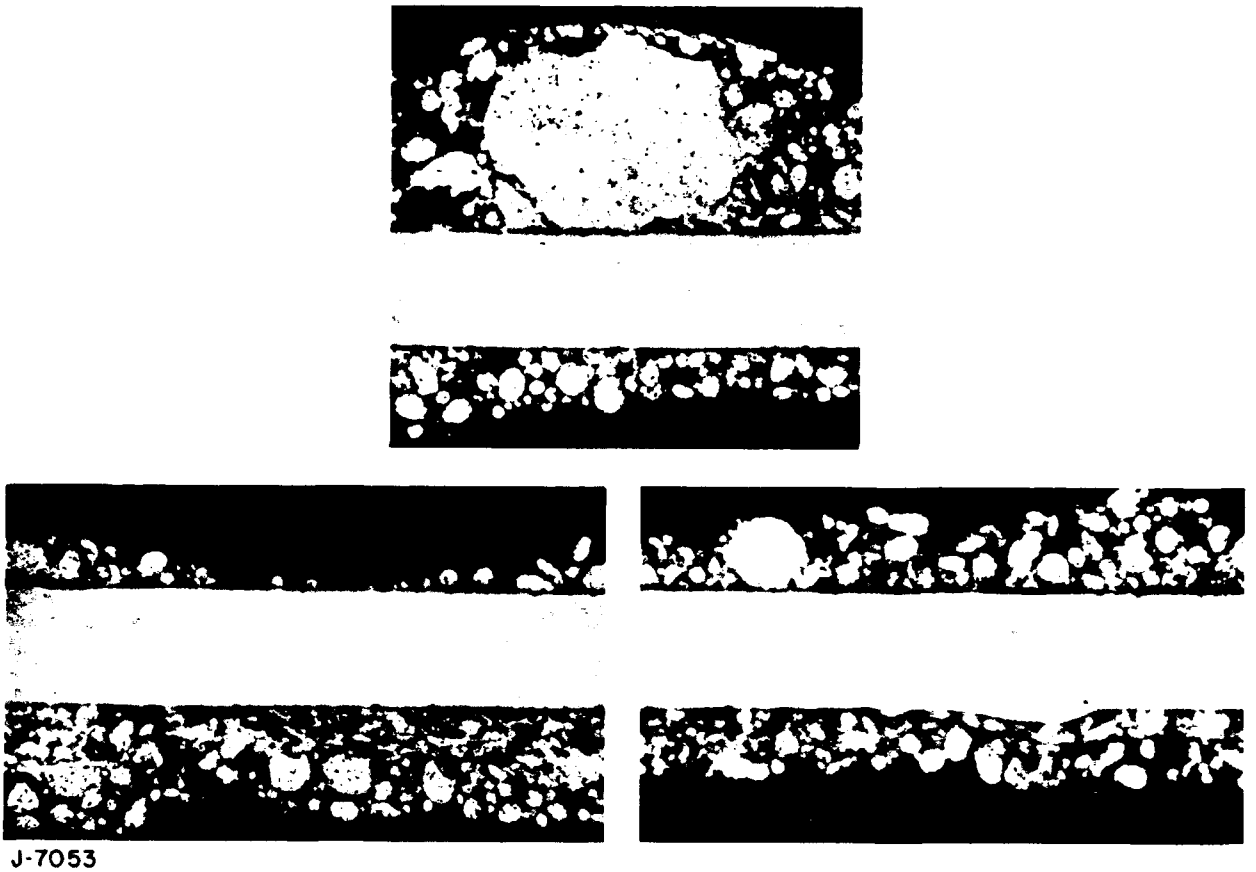

J-7053

Figure III-30 Photomicrograph of Aluminum Clad Titanium Foil (Plasma Spraying).

IV. EXPERIMENTAL RESULTS

A. TANTALUM BLADE CATHODES

The tantalum blade cathode array shown in Figure III-15 was operated with and without preheating. Without preheating, the current waveform of Figure IV-1a shows significant diode closure as evidenced by the rising current in the presence of constant applied voltage. With preheat of the cathode blades (Figure IV-1b), there is no evidence of diode closure during the first microsecond of this pulse indicating that the closure velocity has been substantially reduced by heating the cathode blades. The anode-cathode spacing for this experiment was ~ 2.5 cm and would have been almost completely transversed in one microsecond by a cathode plasma traveling at ~ 2 cm/μsec.

Longer pulse data was not taken successfully because of substantial arcing between anode and cathode. This arcing is worsened by three factors associated with heated cold cathodes. First, field emission from the cathode blades prevents dc conditioning of the cathode structure above 50 to 70 kV. Thus, microparticles which could ordinarily be removed by high dc voltage aging remain and can cause arcing. Second, it is possible to feed energy from the low impedance blade heating source into the anode-cathode arc plasma once this arc is established. This can lead to sustained anode and cathode energy dissipation and hence damage. Third, cathode inductance may have been large enough to cause arcing between the blades and their electrostatic cover plate which must be placed close to but not touching the cathode blades. Such local arcing can initiate an anode-cathode arc.

A preliminary design effort was initiated for a low inductance, high thermal resistance connection between the cathode blades and their electrostatic cover plate. The energy feed into

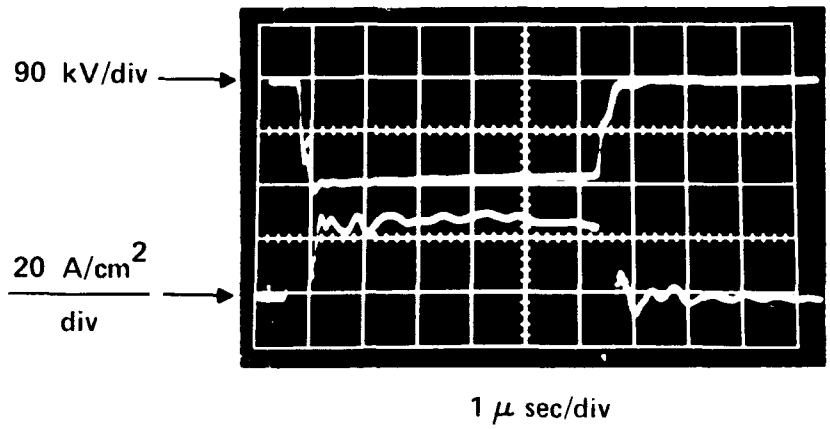

- NO ANODE OR CATHODE DIODE CLOSURE
  - CONSTANT IMPEDANCE
  - NO ANODE OUTGASSING REQUIRED

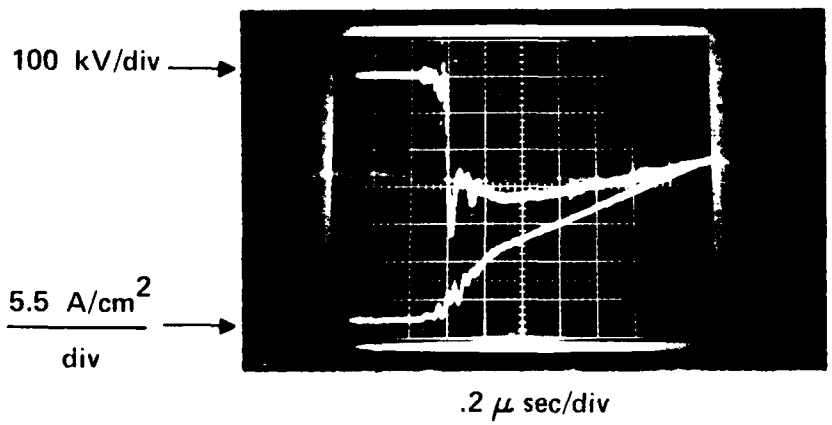

COLD CATHODE

H7831

Figure IV-1 Effect of Cathode Outgassing on the Closure. Characteristics of a Tantalum Blade, Cold Cathode Array (a) No Preheat (b) Preheat.

the plasma arc from the heater source can be eliminated by synchronizing the pulses with the zero crossing of the ac heater current. However, substantial blade vibration is expected when ac heater power is applied in the presence of the guide magnetic field. Since this could lead to premature blade failure due to flexure fatigue, dc heater power is preferred. To prevent energy coupling, the dc power must be turned off prior to the e-beam pulse and turned on again after several recombination times. To accommodate high voltage dc conditioning of the cathode structure a suitable removable cathode shield would be required. Low energy, high impedance pulsed aging is also a possible solution. These complications, however, detract from the inherent simplicity of a blade cathode, and their effectiveness for long pulse durations is questionable.

The spatial and temporal distributions of the current density were resolved as a function of the externally applied guide magnetic fields. Typical volt-ampere characteristics of the diode are shown in Figure IV-2. The spatial distribution of current density as a function of increasing magnetic fields is shown in Figure IV-3. The most noteable features in this photograph are the imaging of individual blades, the slant angle of the e-beam which decreases with increasing applied magnetic field, and the nonuniform emission along several of the cold cathode blades.

The tilting of the e-beam is caused by the interaction of the current density with the self-magnetic field, and since the guide field inhibits transverse spreading of the beam, the tilt is observed. As the applied guide field is increased, the beam is constrained to follow a more nearly axial path thereby reducing the slant angle as shown in Figure IV-3. However, the increased guide field also inhibits transverse spreading of the beam making the individual emitters more pronounced. This increase in current nonuniformity has severe consequences on both foil heating and pumping processes within the laser gas. The slant effect caused by the self-field can be compensated by tilting the blades at the

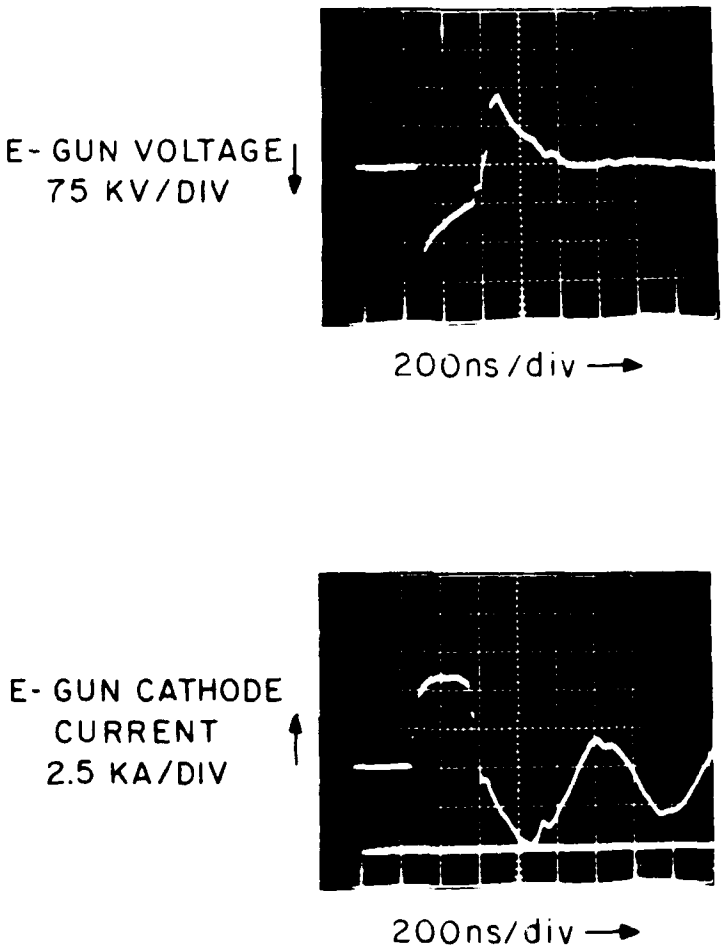

H6391

Figure IV-2 E-Gun Voltage and Current Waveforms of Tantalum Blade Cathode.

ANODE/CATHODE SPACING = 1.9 cm
E-BEAM CURRENT DENSITY = 40A/cm^2
E-BEAM ENERGY = 150 keV
FOIL 2 MIL KAPTON
TANTALUM CATHODES SPACED 1.2 cm APART

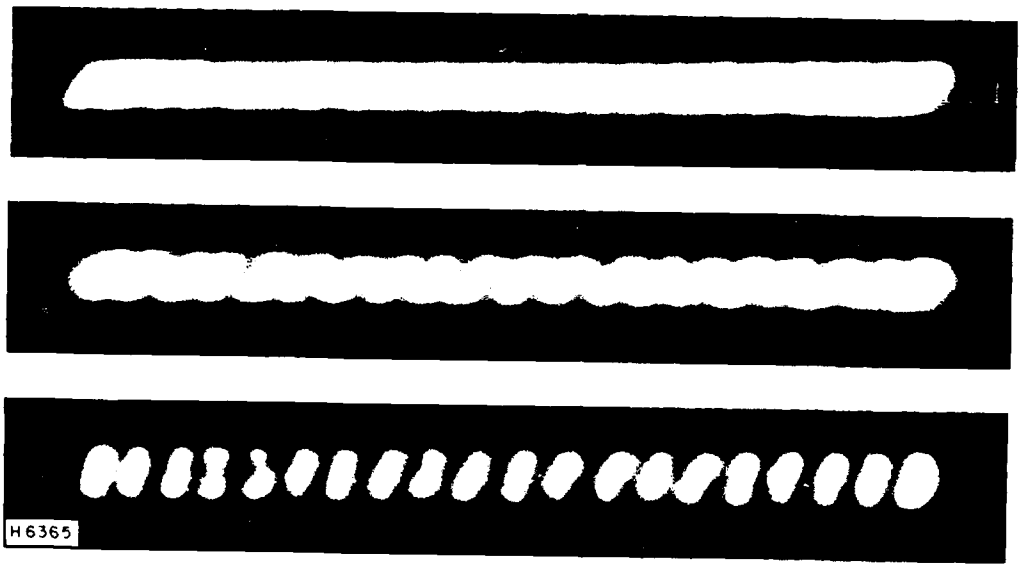

B = 0.75 kG

B = 1.5 kG

B = 3.4 kG

Figure IV-3 Spatial Distribution of Current Density in a Tantalum Blade Cold Cathode with Guide Magnetic Fields.

appropriate angle as shown in Figure IV-4, but the lack of uniformity across the blade array remains a serious problem for guided e-beams.

The transverse plasma spreading along each blade and between blades is shown in the time resolved photographs of Figure IV-5. Frame #1 is a 10 nsec exposure occurring near the beginning of the current pulse. Plasma spreading is noted to increase with time and to be constrained with increasing applied magnetic guide field.

The lack of uniformity that is evident along the blade can be caused by randomness of emission from sites that are apparently grown during pulsed operation. Figure IV-6 shows an electron microscope picture of the edge of a 1/2 mil tantalum blade as it appears after ~ 50 shots of 300 nsec duration. In the presence of a strong applied guide magnetic field, emission from such sites can cause nonuniform emission from the cathode plasma and lead to high local energy deposition in both the foil and laser medium.

Due to the practical problems associated with apparatus which might alleviate the diode closure effects and the inherent nonuniformity of these blade cathodes in the presence of strong guide fields, we believe that blade cathode arrays are not suited to long pulse applications, i.e., > 1 μsec. For short pulses, the following performance parameters have been demonstrated in this study:

Current density - 60 A/cm^2
Pulse duration - 300 nsec
Anode-cathode voltages - 150 kV
Guide magnetic field - 1 kG
Peak Ti foil temperature - 505°K
Peak Ti foil pressures - 5.2 atm
Foil deposition - 1.44 J/cm^2

B. CARBON FELT CATHODES

In contrast to the blade cathodes, the broad area carbon felt cathode produces a uniform emission profile even in the presence of guide magnetic fields. In Figure IV-7, the emission profile at

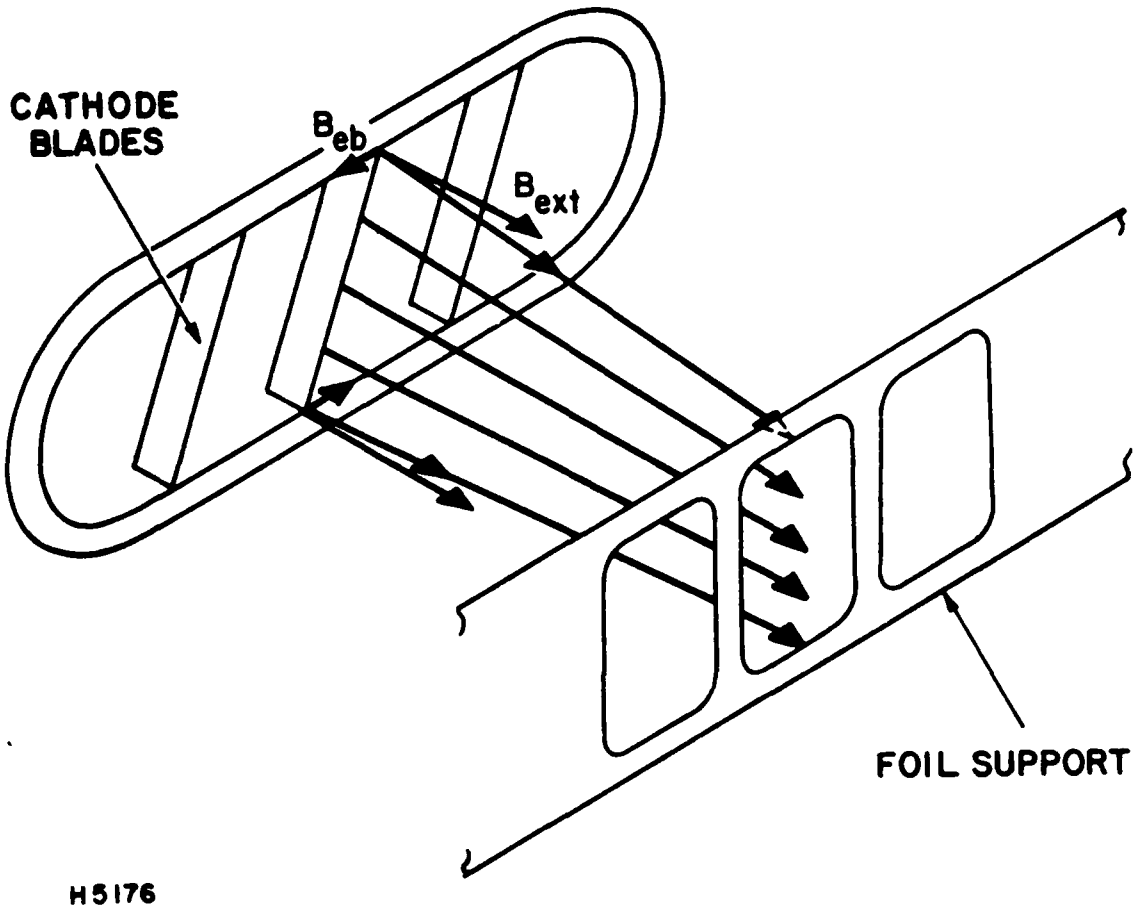

Figure IV-4 Tilt Compensation in a Blade Cathode Array

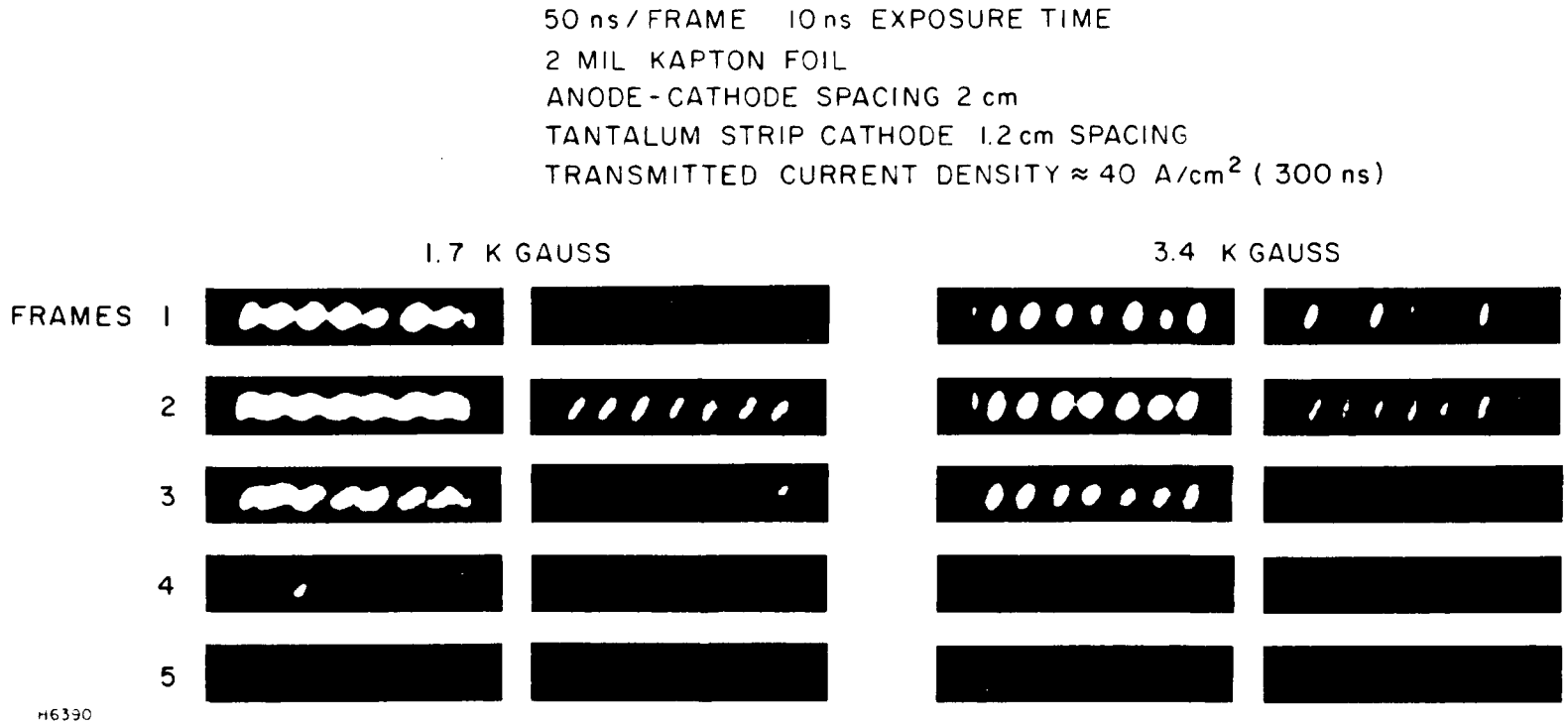

Figure IV-5 Time Resolved E-Beam Current Density Distributions

AVCO EVERETT

Figure IV-6 Emission Sites "Grown" along the Edges of a 1/2 mil Tantalum Cold Cathode Blade After ~ 50 (Single-Pulse).

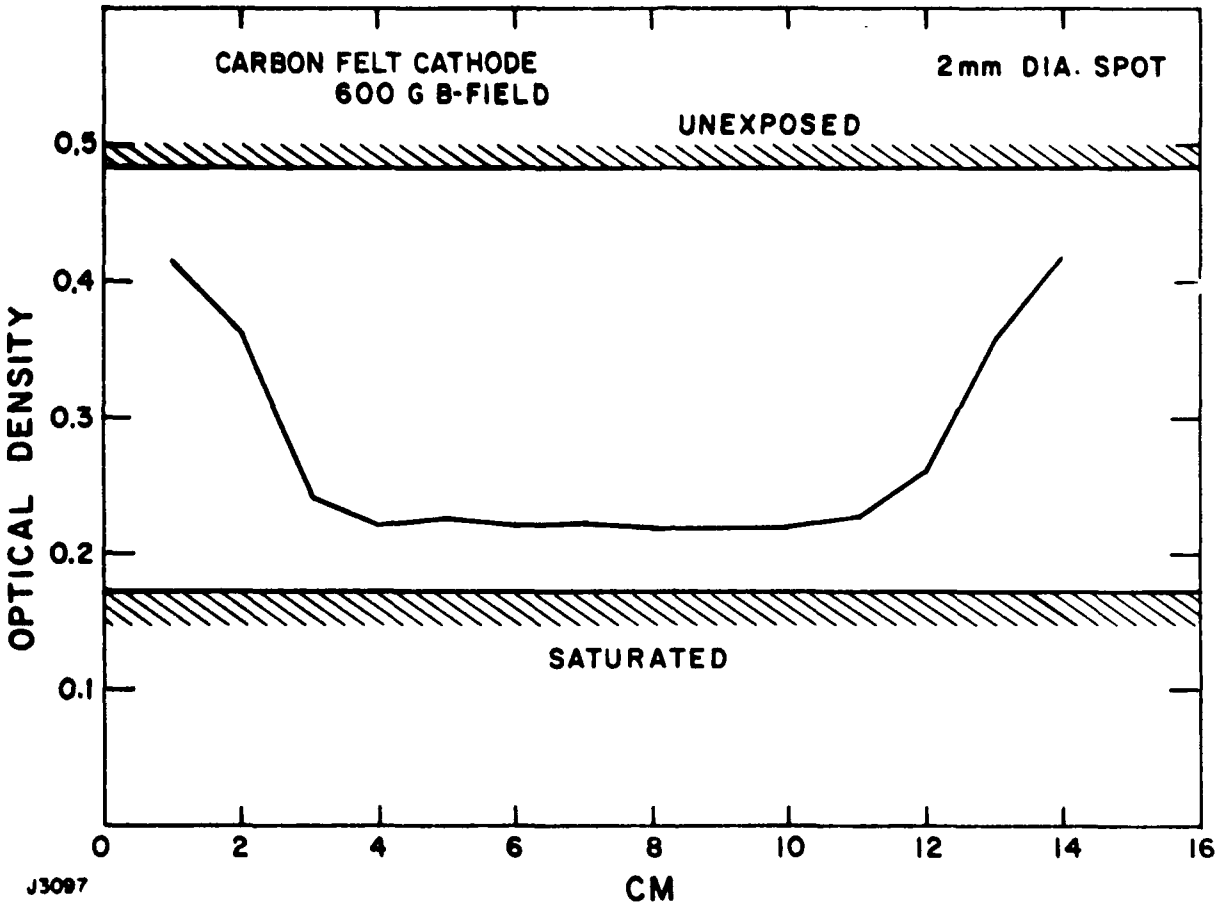

Figure IV-7 Emission Profile of a Carbon Felt Cathode

a guide field of 0.6 kG is measured by densitometering a sheet of blue cellophane which has been irradiated with the beam.

In the absence of guide field, the carbon felt cathode also has lower closure velocity than does the tantalum blade cathode. The measurement technique is illustrated in Figure IV-8. The V-I characteristics are plotted and the value of the closure velocity, v_c, is extrapolated point by point during the pulse. In this way, not only is the value of v_c obtained but its constancy during the pulse is confirmed.

Plots of the closure velocity versus guide field for felt and tantalum blade cathodes are shown in Figure IV-9. Although the closure velocity for felt cathodes is lower than that for blade cathodes at zero applied field, both cathodes show increasing closure velocity as the guide field is increased. Hence, the utility of felt cathodes is also limited to short pulses, i.e., < 1 μsec as illustrated in Figure IV-10.

C. PHOTOEMISSIVE CATHODES

During this cathode test sequence, one of the flashlamps malfunctioned so that the cathode was illuminated unsymmetrically by the remaining lamp as shown in Figure IV-11. The total e-beam current is seen in Figure IV-12 to be synchronous with the flashlamp pulse reaching a peak value of 20 A. The flat portion of the magnesium cathode shown in Figure III-19 has an area of 130 cm^2 which implies an average current density of 0.15 A/cm^2. Just prior to this test, the flashlamp brightness was measured to be 150 W/cm^2 Å for 300 J stored in the flashlamp driver capacitor. Thus between the cutoff wavelength of 2000 Å and the cathode emission threshold of 3000 Å the effective average quantum efficiency is

$$\gamma = \frac{hc}{e} \frac{J}{\langle\lambda\rangle \; G \; B_o \Delta\lambda} = 5.1 \times 10^{-5} \text{ electrons/incident photon.}$$

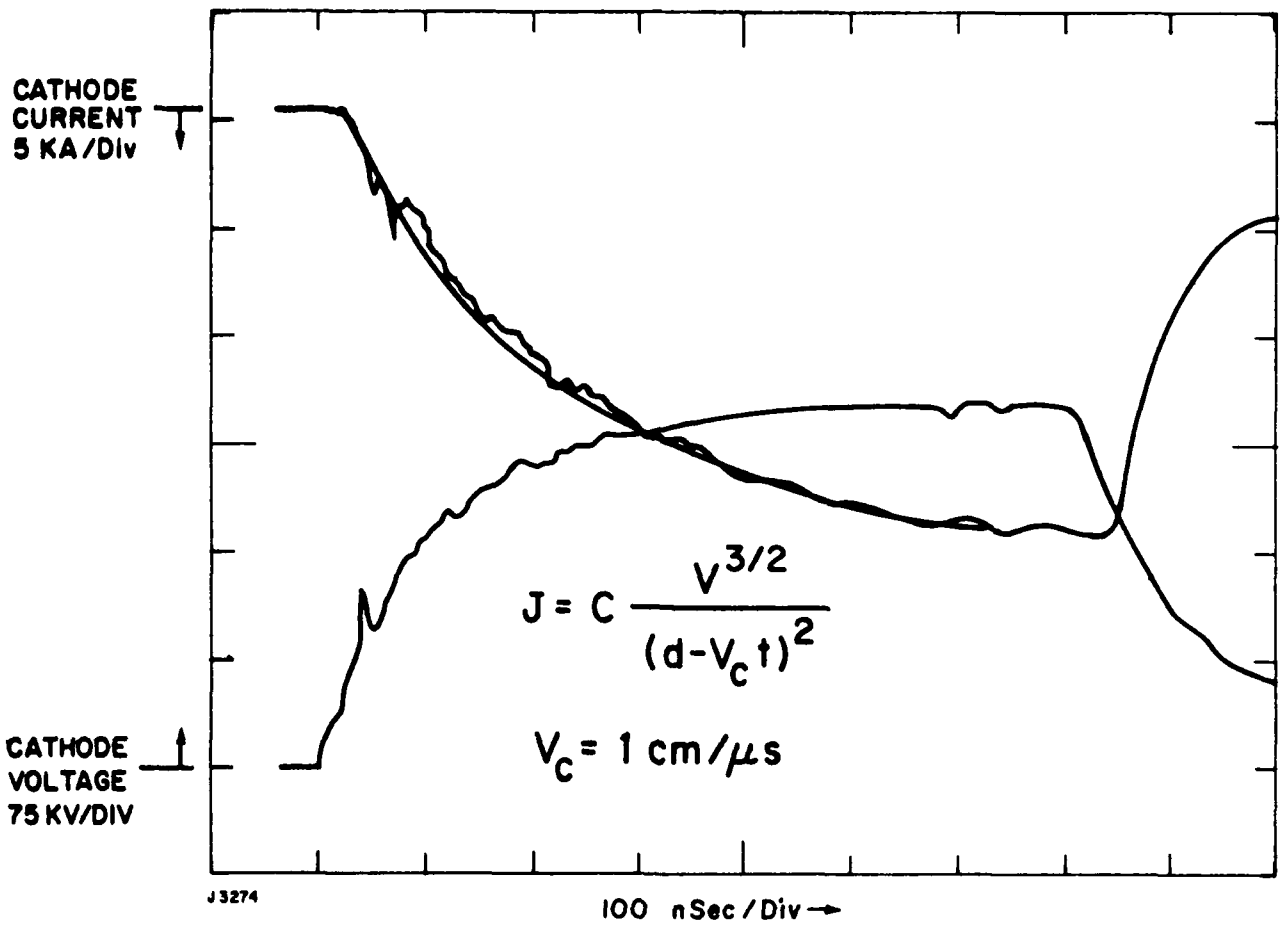

Figure IV-8 V-I Characteristics for a Space Charge Limited Diode with Diode Closure Present.

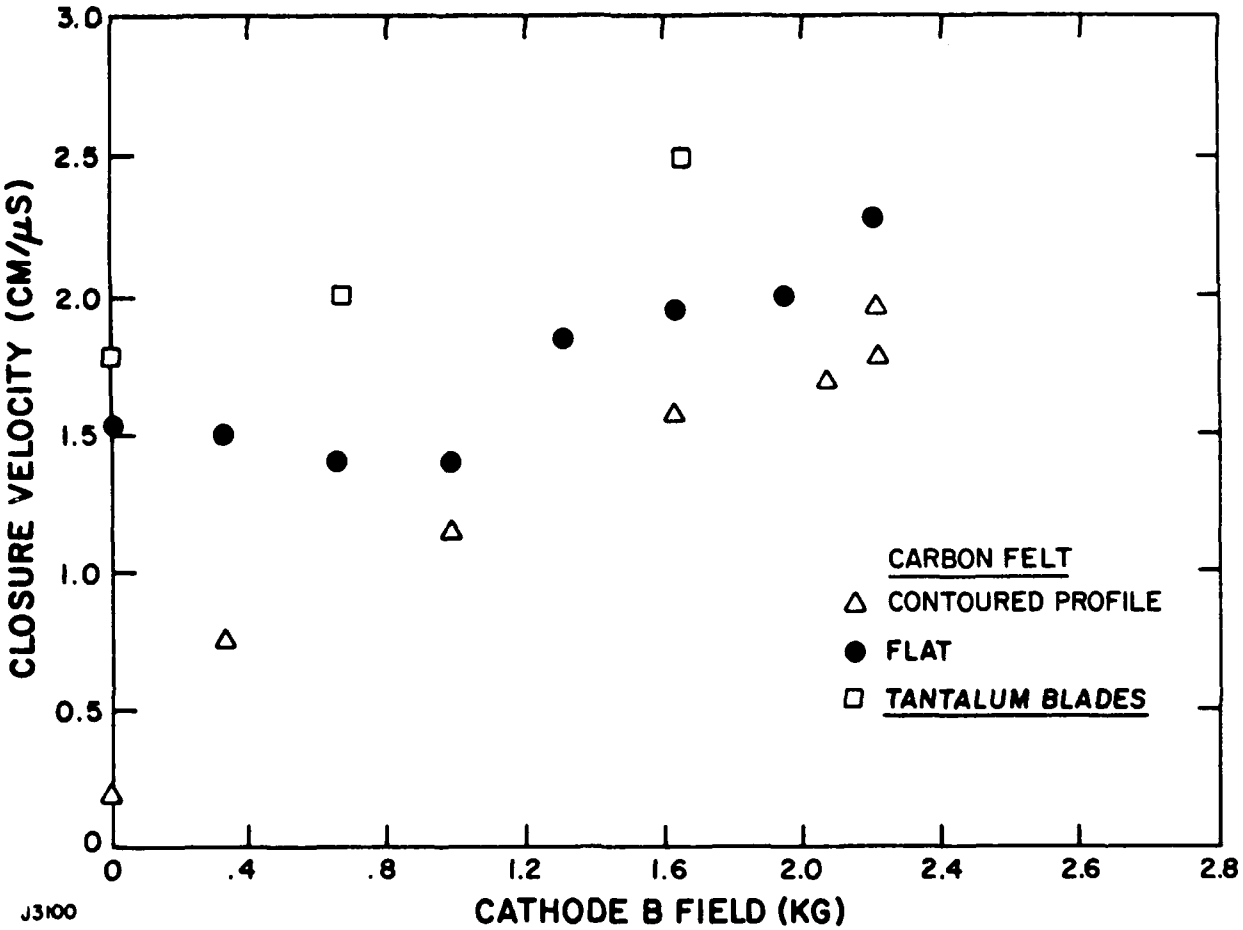

Figure IV-9 Diode Closure Velocity vs. Guide Field

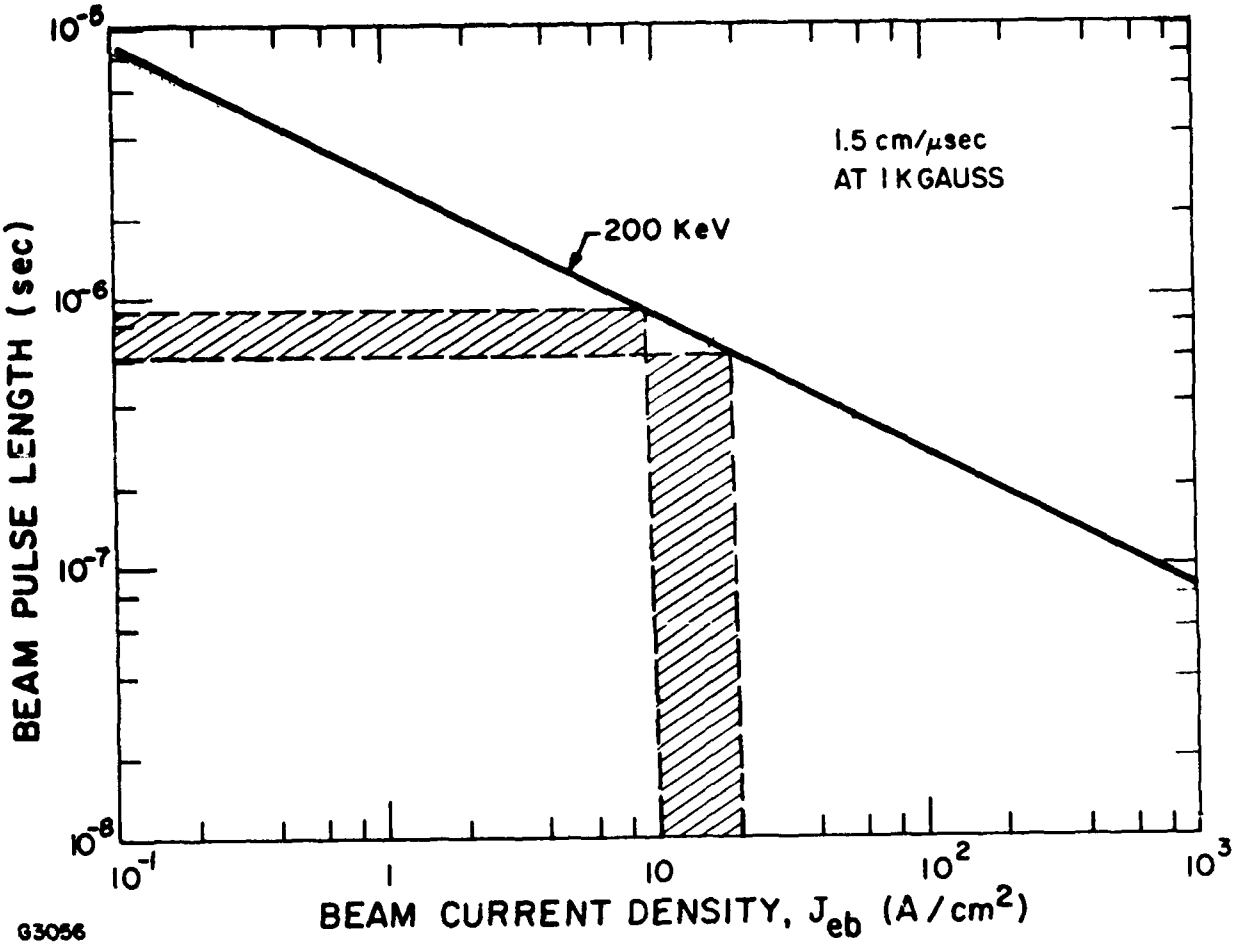

Figure IV-10 Constraint on E-Beam Pulse Length as a Result of Diode Closure.

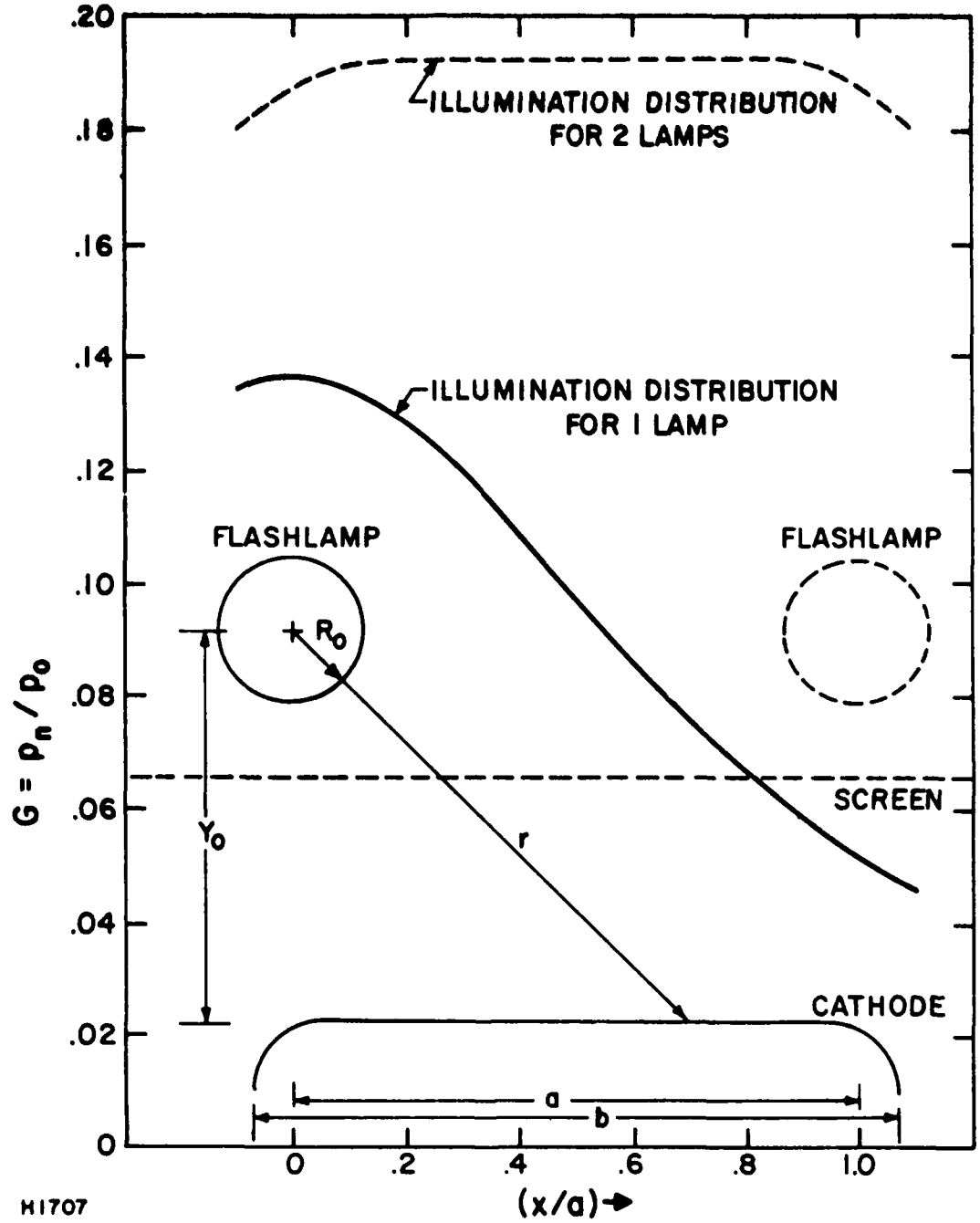

Figure IV-11 Cathode Illumination Due to One and Two Flashlamps, Including the Effects of r^{-1} Fall Off and the Oblique Capacity of the Screen.

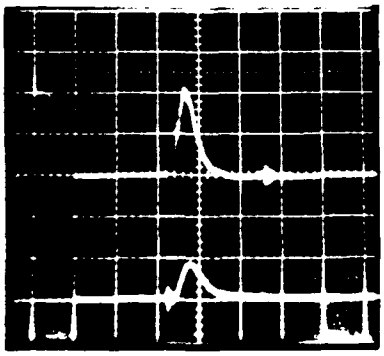

TOTAL CURRENT
10 A/div

PHOTODIODE VOLTAGE
1 V / div

200 ns/div

H1710

Figure IV-12 Total E-Beam Current Flowing to 13 Current Buttons

This quantum efficiency is within the range of 10^{-5} to 10^{-3} electrons/photon which has been measured[1] for pure metals. The wide variations in the measured quantum efficiency has been attributed to variations in the purity and outgassing characteristics of the surface. By careful surface preparation, e.g., electron bombardment or ion backstreaming, current densities of the order of 6 A/cm^2 may be possible for the double lamp initiation. Increasing the flashlamp input energy to the full 470 J rating should increase the useful lamp brightness to 225 W/cm^2 and thereby increase the cathode emission to ~ 9 A/cm^2.

The main elements of a program to develop photoemissive cathodes to their fullest potential would involve the following tasks:

(a) Investigate the technology required to develop air-exposable, high current density photoelectric cathodes with quantum efficiencies > 1% in the spectral range between 2000 and 3000 Å.

(b) Develop high intensity (> 100 W/cm^2 Å) repetitively-pulsed flashlamps with efficiencies > 10% in the spectral range between 2000 and 3000 Å.

(c) Investigate the use of reflectors and highly transparent anode screens to increase cathode irradiation (G factor).

(d) Investigate methods to increase e-beam window transparency. This has the same effect as increasing quantum efficiency and will be part of the foil cooling program.

(e) Investigate the effectiveness of shields to protect the flashlamps from high energy electron bombardment. This will minimize darkening of the quartz flashlamps envelope which will prolong flashlamp life.

D. SMALL AREA DISPENSER CATHODES

1. Cathode Activation

The activation procedure of dispenser cathodes is critical for good performance, i.e., high emission at low surface temperature. The recommended procedure[2] involves slow heating of the cathode to the minimum temperature for barium diffusion ~ 1185°C and then prolonged heating at somewhat lower temperature ~ 1150°C.

A vacuum of 10^{-8} to 10^{-7} torr is preferred, higher levels may result in only partial activation and lower emission. The single-pulse test chamber was not built for vacuums in this range; the use of an oil diffusion pump and rubber O-rings limited this system to $> 10^{-6}$ torr, and it was found necessary to increase the cathode temperature well above the recommended value in order to achieve the desired level of emission. The activation heating cycle typically used for the 5 cm^2 cathode in this system is shown in Figure IV-13. In Figure IV-14, photographs of the polystyrene target fluorescence of the cathode emission at increasing temperatures are shown together with current waveforms. The three photographs are for cathode temperatures of 1190°C, 1300°C and 1360°C, and are interpreted as follows. At the lowest temperature, the cathode is not yet activated as evidenced by zero current in the oscilloscope trace to the left. At 1190°C, the pressure is 5×10^{-6} torr due to outgassing of the cathode and surrounding structures. For this temperature and pressure combination, the arrival rate of (poisoning) background neutrals is higher than the arrival rate of barium diffused to the surface and, therefore, activation is inhibited and no emission is observed. As the temperature of the cathode is raised to 1300°C, the flow of barium increase to overcome the poisoning effects, activation is initiated, and there is partial emission from the central portion of the cathode where the temperature is highest. The oscilloscope trace confirms a small value of current emission. As the temperature is raised to 1360°C, the cathode surface becomes significantly more activated, the current distribution becomes more uniform and the measured average current density of ~ 20 A/cm^2 corresponds to the space charge limit.

2. Beam Expansion

It can be observed in Figure IV-14 that the beam diameter at the fluorescent polystyrene is $\sim 30\%$ larger than the cathode diameter. This is due in part to the electron optics near the

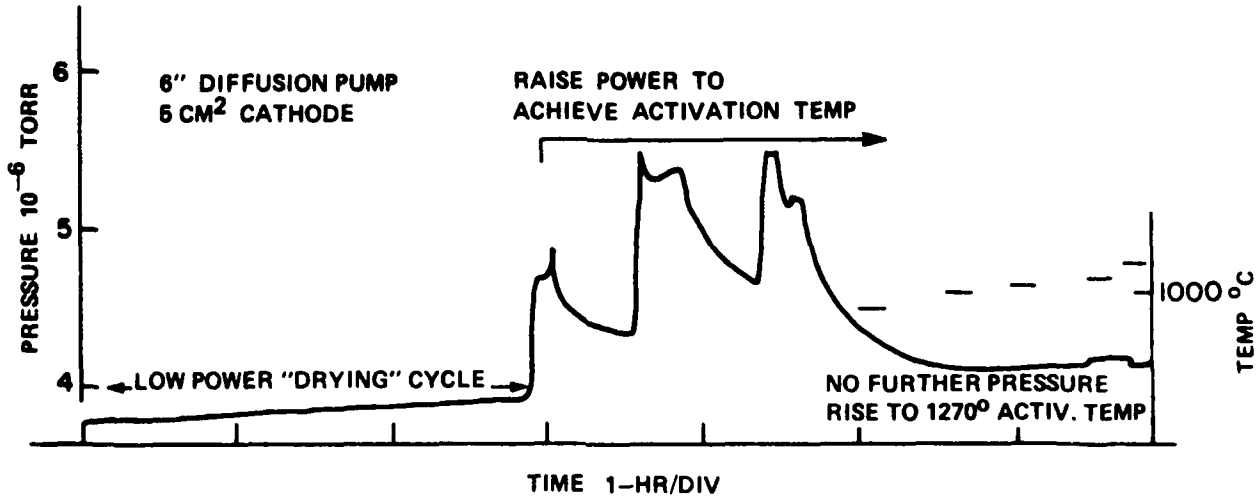

H7741

Figure IV-13 Activation of the Small Area Dispenser Cathode

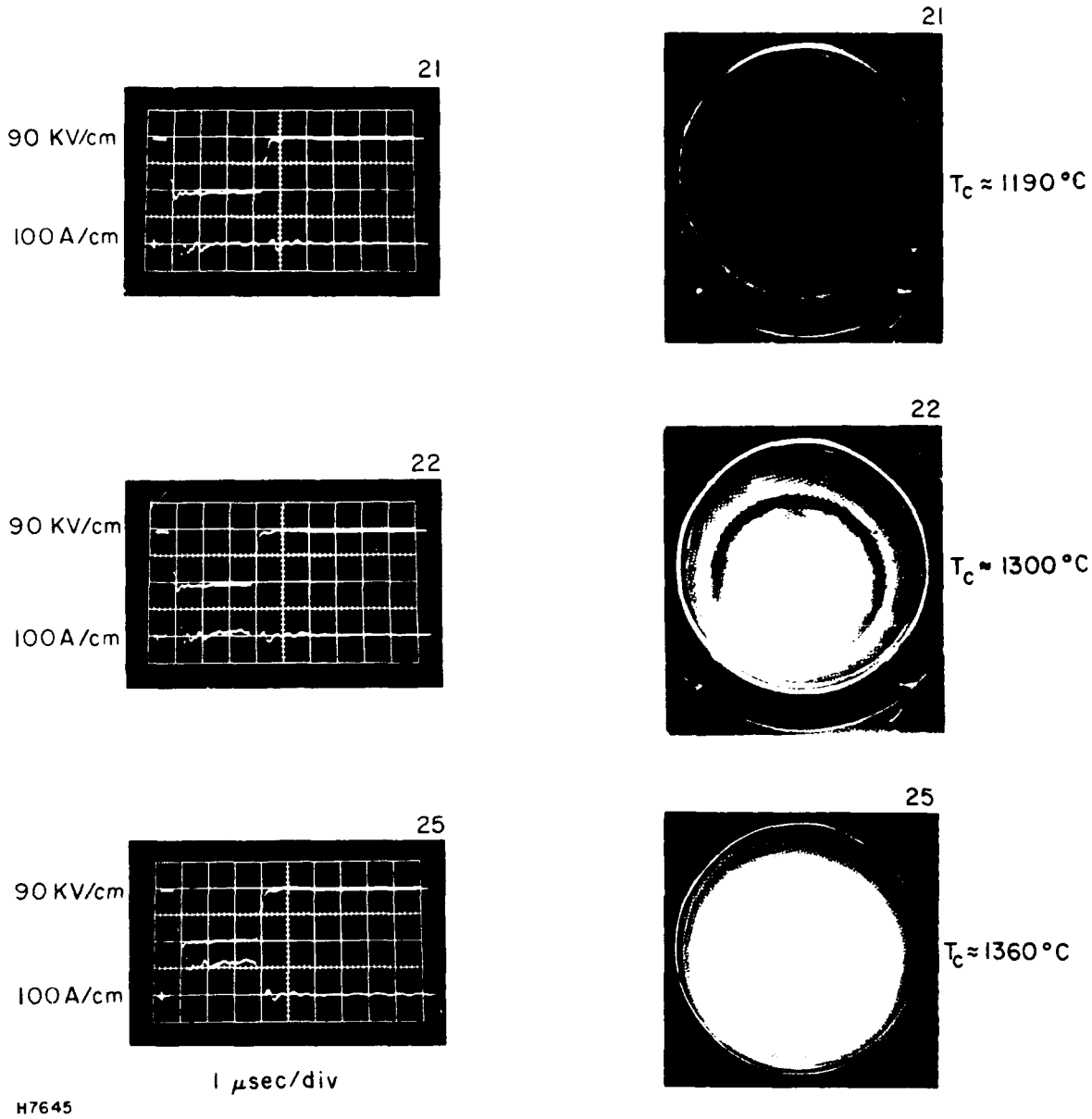

Figure IV-14 Small Area Dispenser Cathode at Different Temperatures.

cathode surface as illustrated schematically in Figure IV-15. At the centerline of the cathode operated in the space charge limited mode the electric field is zero. Beyond the cathode surface, the emission is zero and the potential will vary linearly from cathode to anode and will have a net positive value at the elctrostatic plane of the cathode. In making the transition between a high positive field and a zero field at the emitting surface of the cathode a diverging lens effect is established. Since the energy of the electron leaving the cathode it is quite low in this region, the electrons will approximately follow the electric field lines and hence diverge radially outward, thereby expanding the beam.

Space charge repulsive forces also expand the beam but a rough estimate of the space charge field, i.e.,

$$\phi = Jr^2/4v\varepsilon_o \approx 3 \text{ kV}$$

where

J = current density

r = beam radius

v = electron velocity $\approx c$

ε_o = permitivity of free space

indicates that space charge forces are insufficient to expand the beam by the observed amount. In Figure IV-14 a bright ring around the outer edge of the cathode is observed. This ring is caused by a higher than average current density around the edge of the cathode associated with the transition from zero field at the emitting surface of the cathode to a higher positive field where there is no emission. At this transition point which is near the edge of the cathode, the field is higher than that associated with the space charge limited conditions, and hence higher current density is extracted. The ratio of current density at the edge to current density of the interior of the cathode surface was measured to be ~ 1.4. This above average emission will occur at the edge of any

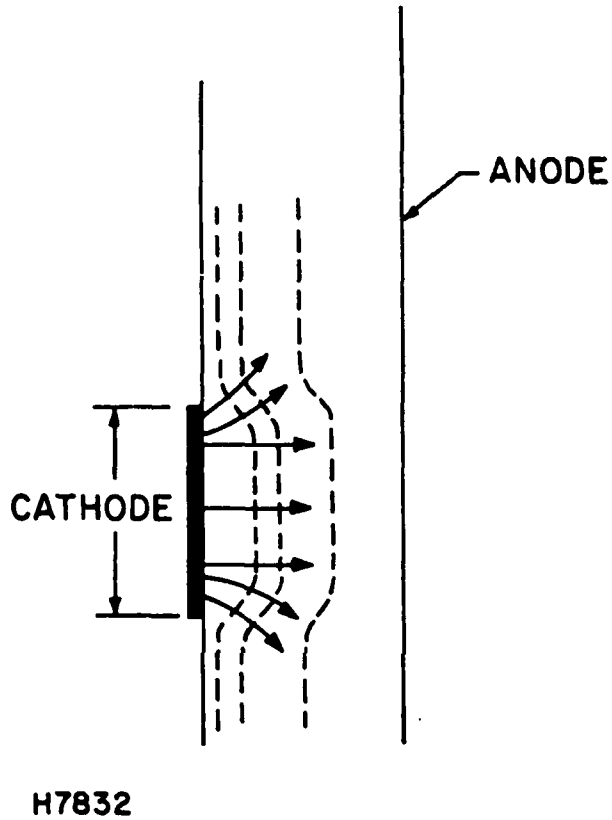

Figure IV-15 Defocussing Effects in the Diode Region

cathode surface regardless of area, unless thermal or mechanical grading is used at the periphery.

3. Magnetic Field Effects

The effects of the axial magnetic guide field on the emission of the small area cathode were investigated and the results are shown in Figure IV-16. As the B-field is increased from zero to 720 G it can be seen that the e-beam diameter at the polystyrene target decreases from a large diameter at zero field to a diameter very nearly that of the actual cathode diameter. The egg shape observed in Figure IV-16 is associated with the self-magnetic field of the cathode current flowing in the rectangular cathode holder as shown in Figure IV-17. The combination of the applied guide magnetic field in the axial direction and the transverse self-magnetic field of the cathode current act to skew the beam into the egg shape as shown schematically in Figure IV-17 and shown in the photographs of the experimental result shown in Figure IV-16.

4. No Diode Closure

One of the primary objectives of this program was to demonstrate a technology which would eliminate diode closure and thereby permit long pulse width at high current density. This goal has been accomplished using the dispenser thermionic cathode. In Figure IV-18 pulse widths in excess of 6 μsec at 15 A/cm^2 and 160 kV are shown with and without a guide magnetic field. No evidence exists for the presence of diode closure, i.e., the current traces are flat. When compared with the cold cathode performance shown in Figure IV-19 it is clear that the diode closure problem can be completely eliminated by the use of the dispenser thermionic cathode.

5. Comparison of Cathode Performance

Testing of the 5 cm^2 area cathodes was extended to the repped facility. One objective was to investigate the influence of vacuum conditions on cathode emission and hopefully improve the

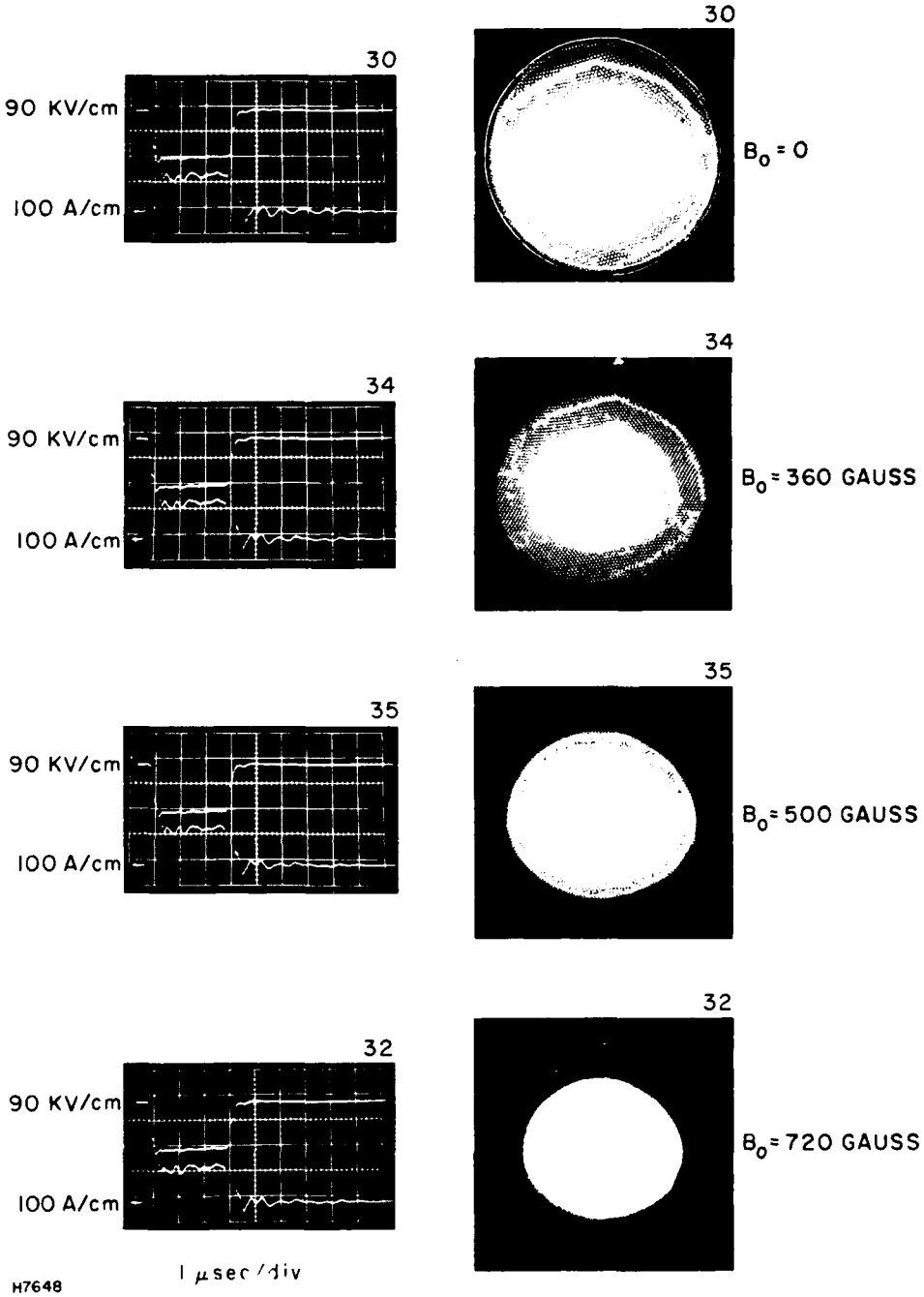

Figure IV-16 Effects of Axial Magnetic Guide Field on the Current of the Small Area Dispenser Cathode.

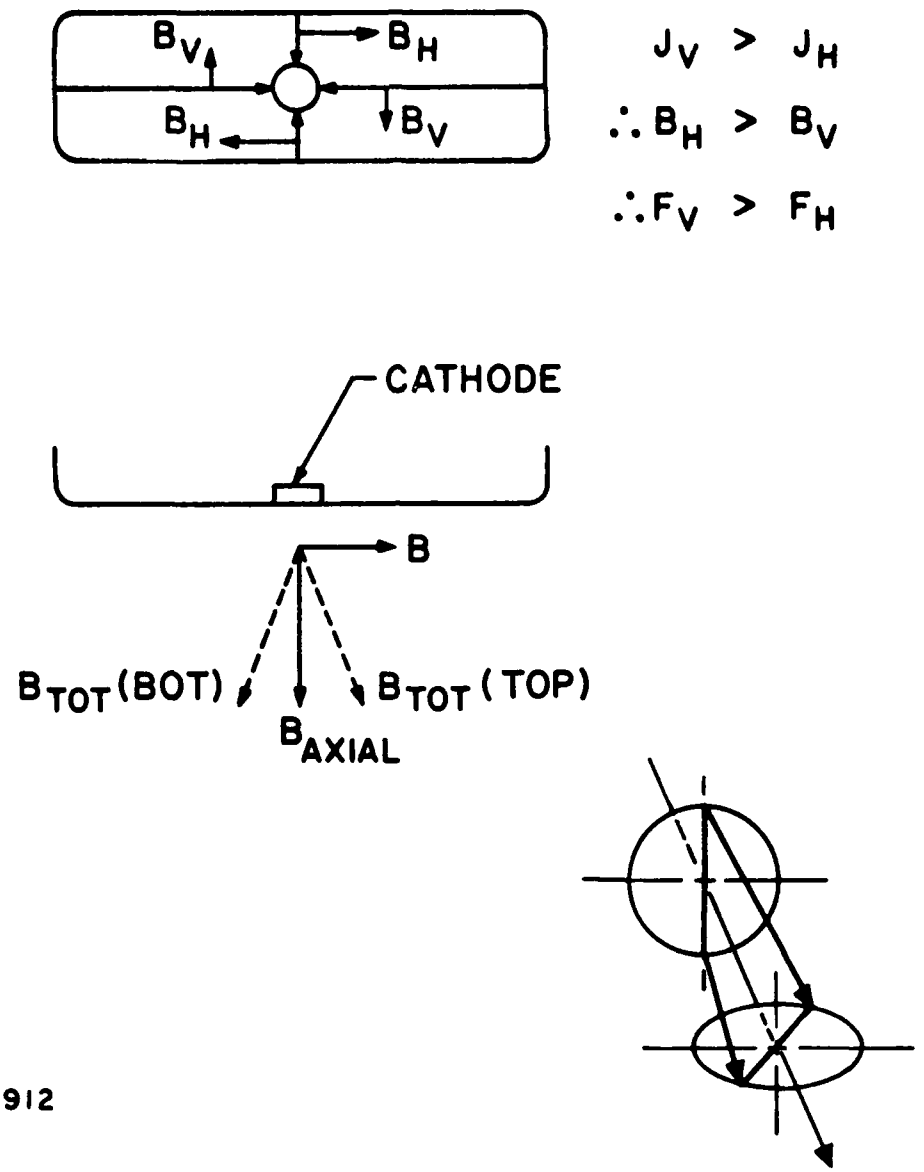

Figure IV-17 Distorted Beam Profile Resulting from Interaction of the Current with the Self-Magnetic Field.

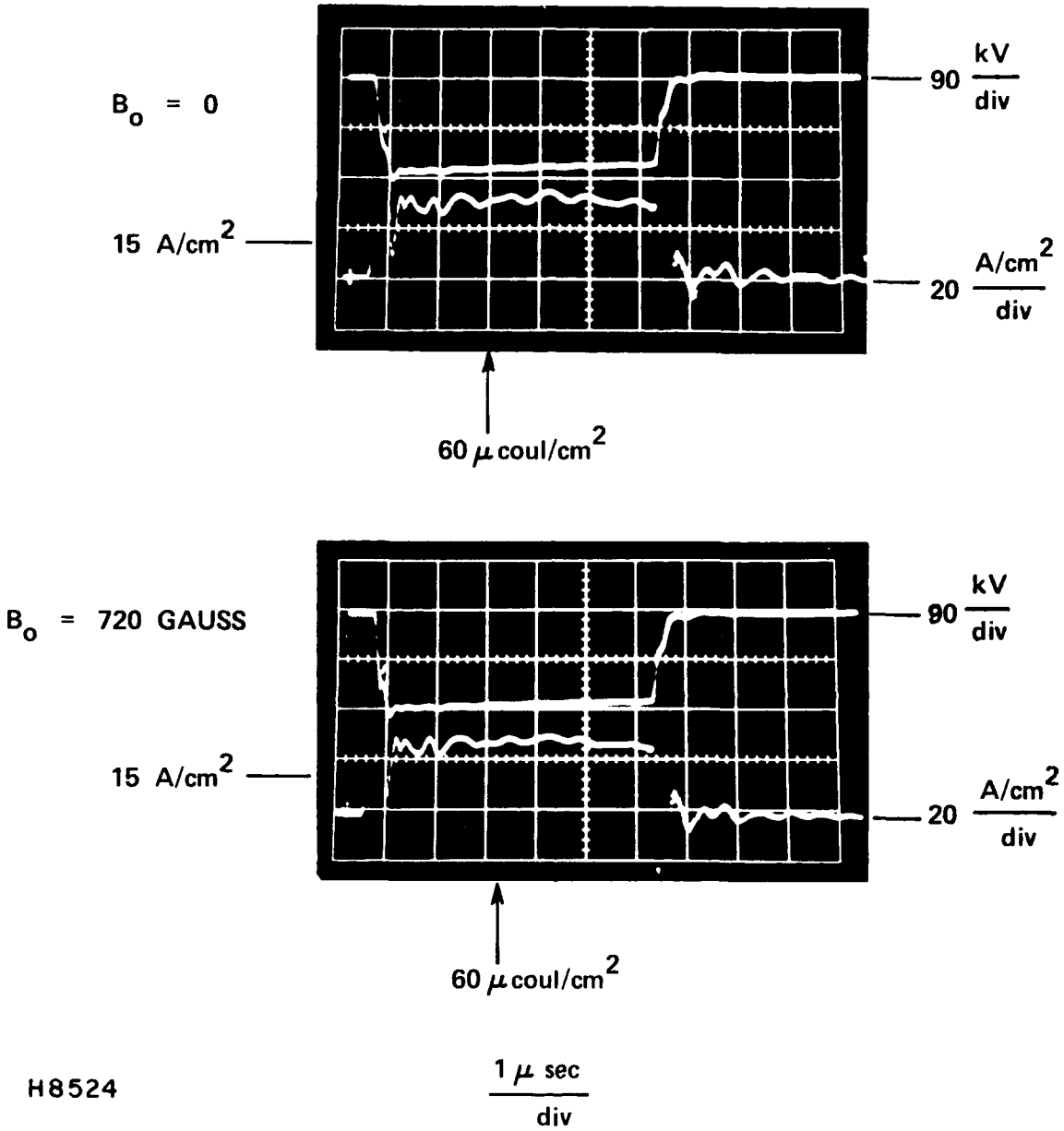

Figure IV-18 Long Pulse, High Current Density Results from the Small Area Dispenser Cathode.

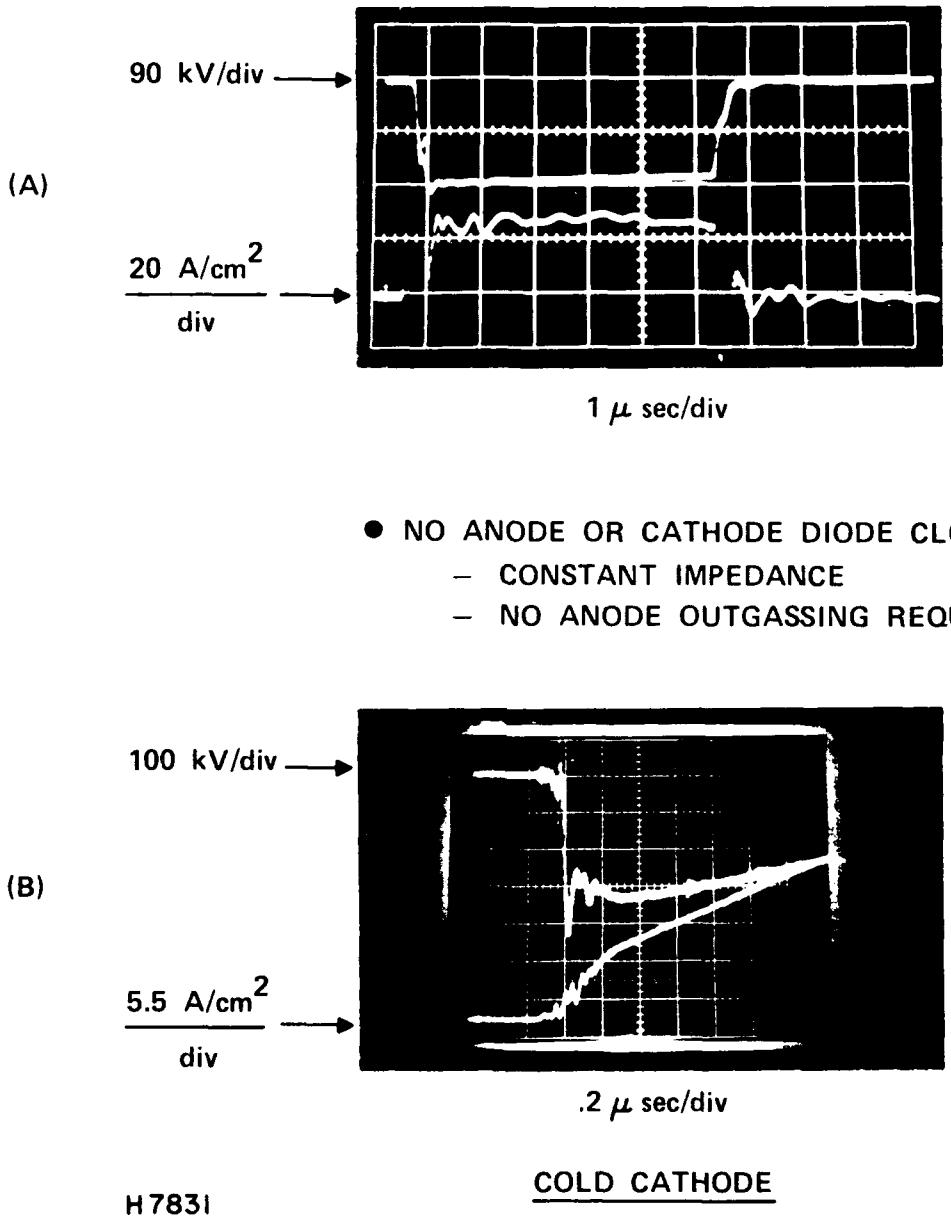

Figure IV-19 Volt-Ampere Characteristics of E-Guns Using (a) Dispenser and (b) Field Emission Cathodes.

performance as a result of the nearly ten times lower base pressure of $\sim 10^{-7}$ torr achievable in the new chamber. Another objective was to test Scandate-type impregnants, which should give the same emission densities as the standard B type cathode but at $\sim 100^{\circ}C$ lower cathode temperature.[2] As mentioned in Section III, these tests were performed with a thyratron pulser at voltages up to 30 kV, compared with the 160 kV used in the single pulse apparatus, and the main reason for this was to allow the use of a more sensitive current probe. The difference in voltage made it hard to determine the dependence of cathode performance on the vacuum conditions, because the emission generally depends on both the temperature and the diode voltage (and electric field) in a complex manner. This is particularly true if the cathode surface is only partially activated, and emission characteristics should be extrapolated to zero field conditions in order to compare the data of different experiments. Tentative conclusions are that activation appears easier to achieve and that the emission is higher and more stable with the lower base vacuum, however, the improvements cannot be quantified based on the presently available data. The performance of the Scandate cathode was found to be slightly better than for the type B. Thus, for emission levels of up to ~ 5 A/cm^2, the Scandate was found to give the same emission as the B at $\sim 30^{\circ}C$ lower temperature (but not $\sim 100^{\circ}C$ lower temperature as the manufacturer[2] specifies).

E. LARGE AREA DISPENSER CATHODES

Large area (100 cm^2) dispenser cathodes were operated in both the single-pulse and repped-pulse facilities. The single-pulse apparatus was found to be inadeqaute for high current operation, being seriously limited by vacuum conditions (aggravated by additional heat load of the large cathode), and by the high impedance of the Marx bank. For these reasons, preliminary tests achieving ~ 5 A/cm^2 at 100 kV in 6 μsec pulses were aimed at development of diagnostics, awaiting the procurement of the 300 kV, 25 Hz line pulser and construction of the new test chamber.

The repped facility was operated initially with a base pressure of about 1×10^{-6} torr, rising to about 5×10^{-6} torr with the cathode heated. After addition of a cryopump and a LN_2 cold trap, a mild external bakeout and prolonged pumping, the base vacuum was lowered to 1×10^{-7} torr with unheated cathode and 2×10^{-7} torr with the 100 cm^2 dispenser cathode at 1300°C. The rate at which the filament power is increased depends upon the maximum allowable background pressure. In early experiments, the background pressure was kept below $\sim 5 \times 10^{-6}$ torr but subsequent experiments showed that better cathode performance resulted when the background pressure was kept below 10^{-6} torr during initial heating and activation. A typical time history of the activation process is shown in Figure IV-20. The residual gas in the vacuum chamber shows a high concentration of CO as evidenced by the mass spectrometer scan of Figure IV-21. (The presence of N_2 can be ruled out by the absence of the corresponding signal at AMU = 14.)

After the initial activation period, the cathodes are tested for emission using a low current, moderate voltage power supply. Typical voltage and currents during this period are 15 kV and 500 mA (supply limited) and serve as a verification of emission onset rather than quantified performance level.

The emission of the 100 cm^2 area cathode was measured as a function of temperature and diode voltage with the anode-cathode spacing initially set at 4 cm. Figure IV-22a shows the results obtained initially with relatively poor vacuum. In these early runs, the base pressure (cold) was $\sim 5 \times 10^{-7}$ torr and cathode was activated at relatively high pressure, i.e., $> 10^{-6}$ torr during heating. The pressure rises immediately after the pulse to the 10^{-5} torr range indicating high outgassing rates. In a later test series, the base pressure was improved to the 1×10^{-7} torr level and the pressure during activation was kept

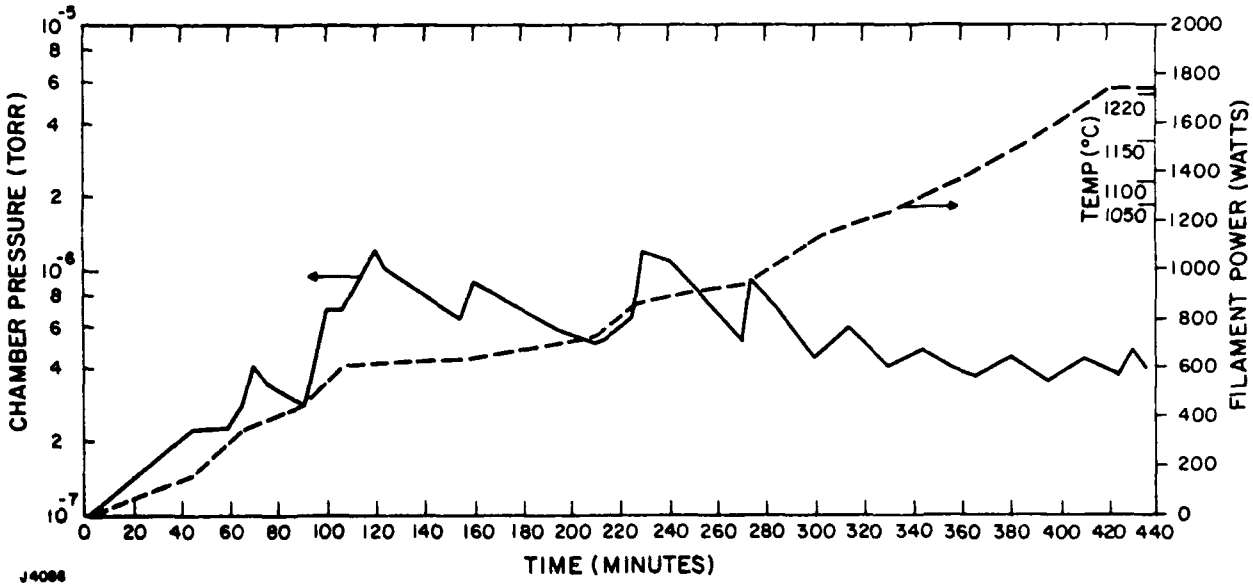

Figure IV-20 Temperature and Pressure History of Large Area Dispenser Cathode Activation.

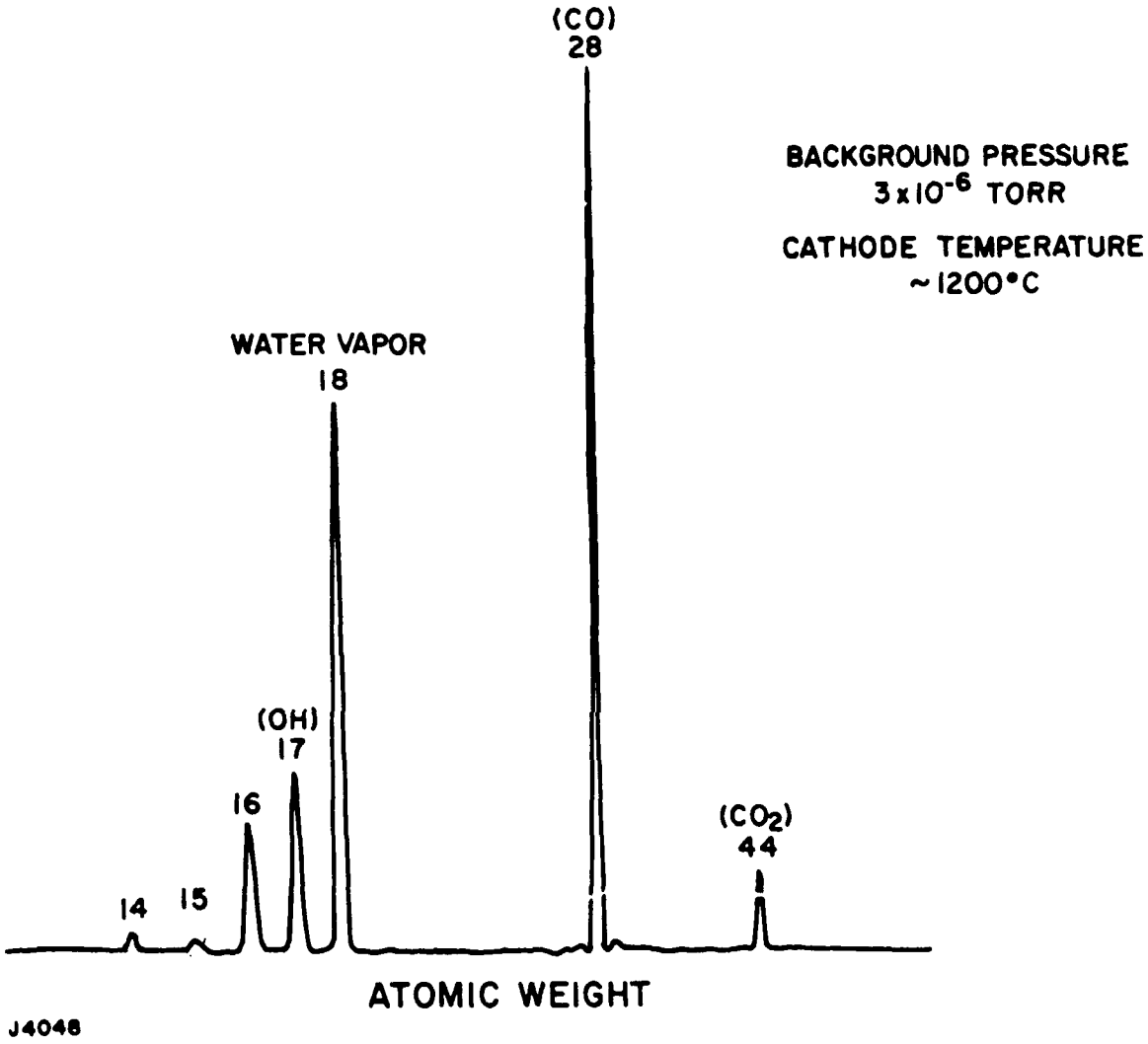

Figure IV-21 Mass Spectrometer Scan During the Activation Process.

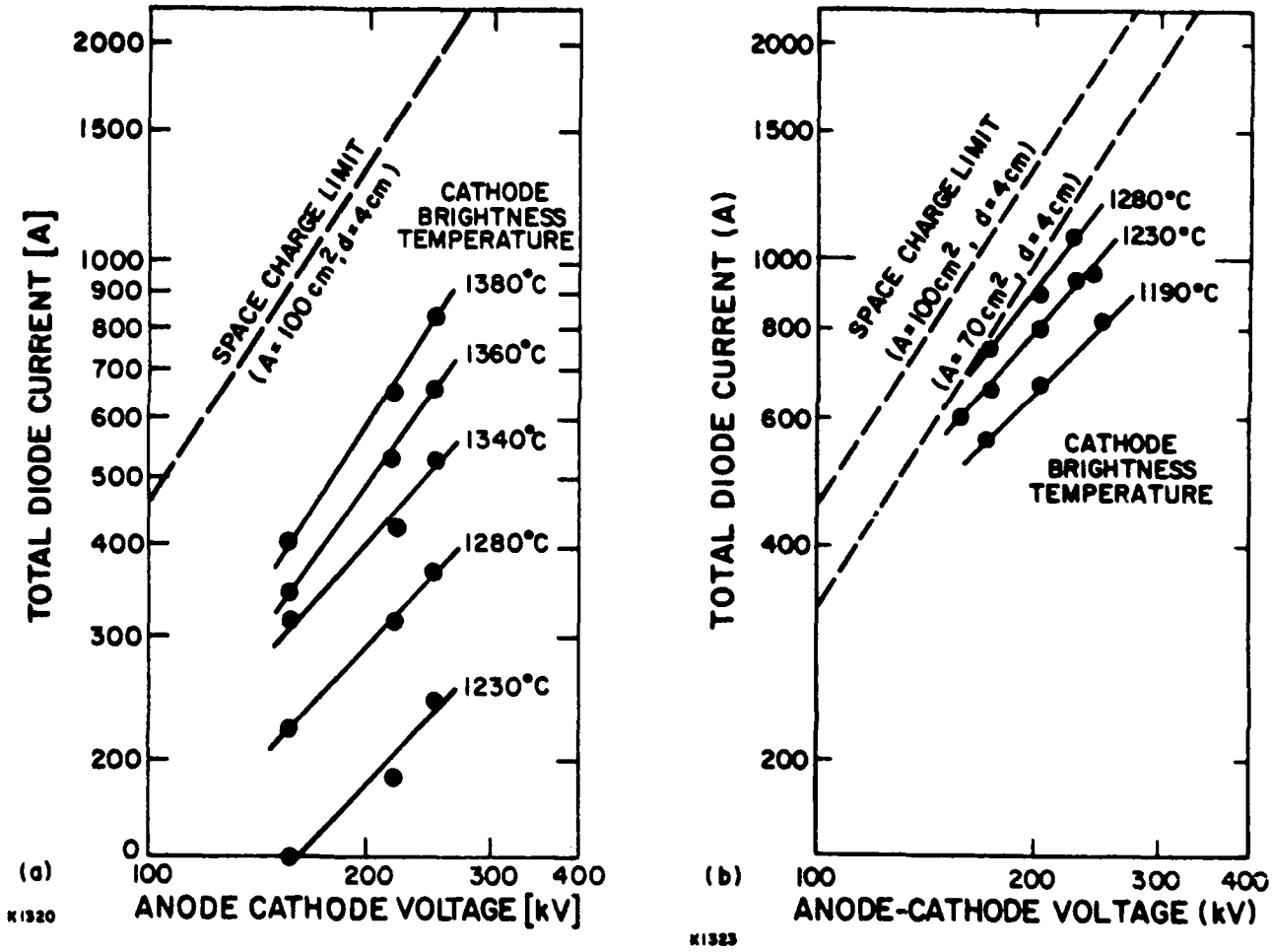

Figure IV-22 Voltage and Current Characteristics Measured for a 100 cm^2 Dispenser Cathode (d_{ak} = 4 cm)

a) ~ 10^{-6} torr

b) ~ 10^{-7} torr

below 10^{-6} torr. Figure IV-22b shows the data for these conditions. Compared to Figure IV-22a, a significant increase in emission at a fixed temperature is observed. At a diode voltage of 250 kV, the highest pulse current measured here was 1080 A which represents an average of ~ 11 A/cm^2 for the 100 cm^2 cathode. (The effective emitting area for this cathode is shown later to be ~70 cm^2, thus giving an actual current density of ~ 15 A/cm^2.

The variation of pulse current with voltage as indicated in Figure IV-22 is generally less than the $V^{3/2}$ which would result from a space charge limited operating region. To estimate the comparison of this data with the one-dimensional space charge limited theory, the Child-Langmuir law,

$$I = AKV^{3/2}/d^2$$

is plotted where:

I = total cathode current

A = effective cathode area

K = $2.33\ 10^{-6}$ A $(V)^{-3/2}$

d = anode-cathode spacing.

As seen in Figure IV-22b, the 1280°C data approaches the space charge limit for an effective cathode area of 70 cm^2.

To achieve higher emission density, the anode-cathode spacing was reduced from 4 to 3 cm. The resulting data is plotted in Figure IV-23. At the highest voltage, 300 kV (corresponding to an average electric field of 100 kV/cm), a total cathode current of 2200 A was achieved. The voltage and current pulse shapes at this operating point are shown in Figure IV-24. For the same estimated effective area, 70 cm^2, the cathode again is operating close to the space charge limit. (At these high values of electric field it was found necessary to operate the cathode at high current in order to avoid arcing. Under conditions of no current, the electric field in the anode-cathode space is roughly constant at a

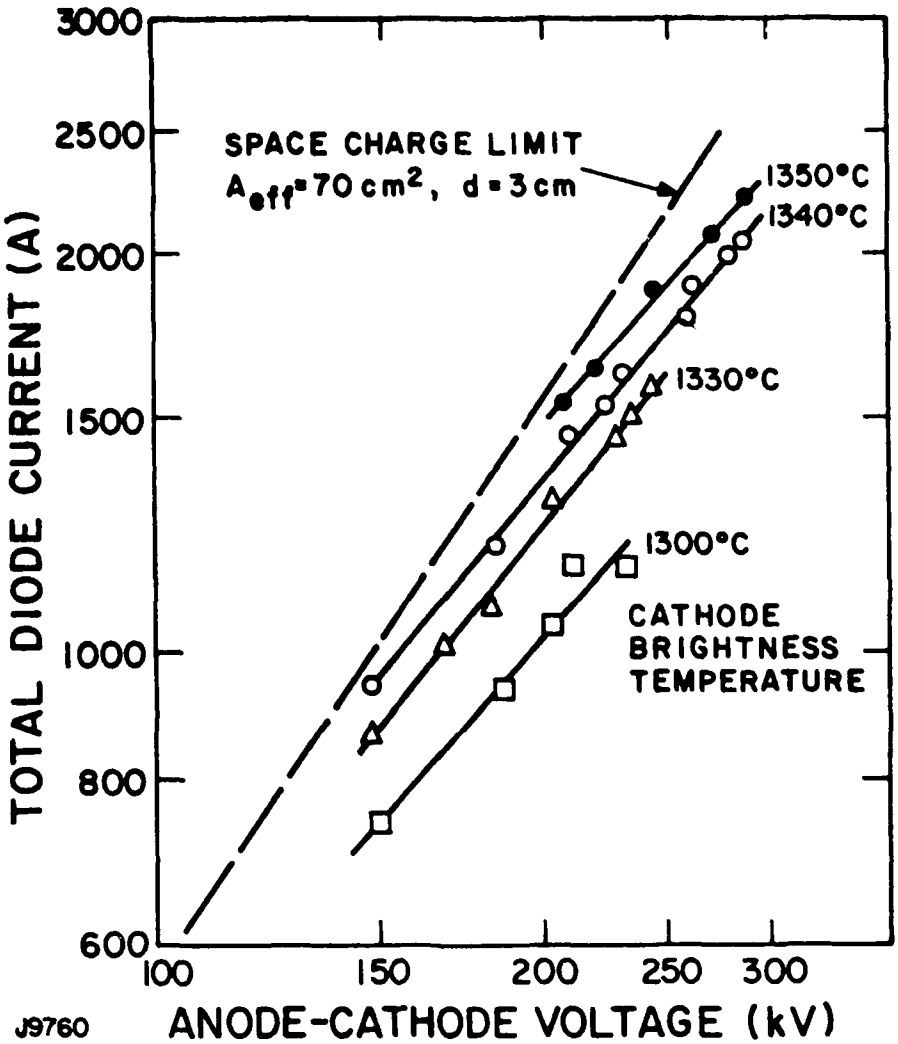

Figure IV-23 Voltage and Current Characteristics at Reduced Spacing (d_{ak} = 3 cm).

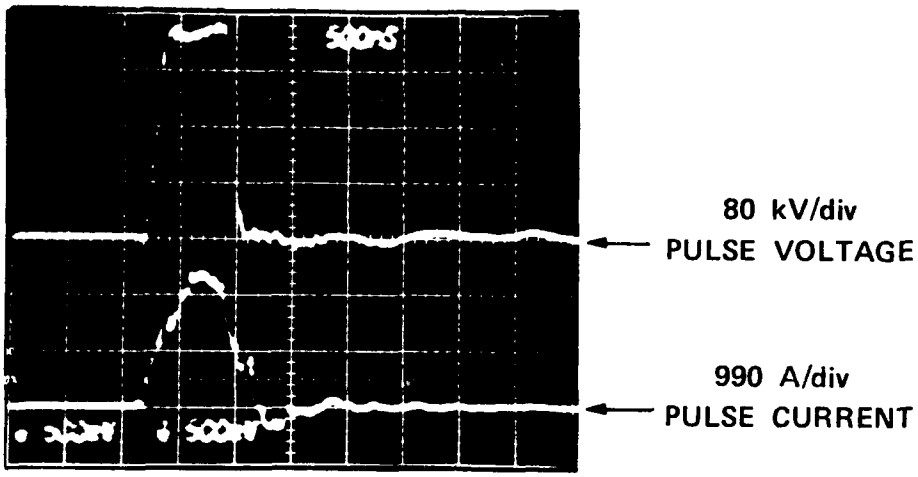

J6025

Figure IV-24 Voltage and Current Waveforms at 2200 A Emission

value of voltage divided by distance. In the presence of current, the space charge shields the cathode from the high electric fields and the electric field at the cathode surface is reduced. In the fully space charge limited regime, the field at the cathode is ≈ 0, and the cathode surface is fully shielded. Operating the cathode fully space charge limited, yields maximum voltage standoff.)

A cross-plot of the voltage-current characteristics of Figures IV-22 and IV-23 showing the surface temperature and lifetime aspects of the data is given in Figure IV-25.

It should be noted that, for the current densities of interest, 10-30 A/cm^2, the cathode temperature required is about 100^oC higher than specified by the manufacturer (and achieved for smaller size cathodes under superior vacuum conditions). Although the projected life times for the presently tested cathodes according to Figure IV-25 is between 100 and 1000 hr and therefore should be sufficient for relevant DARPA applications, it is important to realize that 100^oC reduction in cathode temperature increase its life by a factor of ten. From the arguments presented in the following as well as the observation that emission increases with improvements in base vacuum as well as operating vacuum levels, it can be concluded that more complete activation of the dispenser cathode surface will result in lower required surface temperatures commensurate with longer lifetimes.

Further evidence of only partial activation comes from analysis of the emission data. The emission from thermionic cathodes is given by Richardson's equation:

$$J = AT^2 \exp(-e\phi/kT)$$

where

J = emission density

$A = 4\pi mek^2/h^3 = 120\ A/cm^2\ {}^oK^2$

T = cathode surface temperature

Φ = work function.

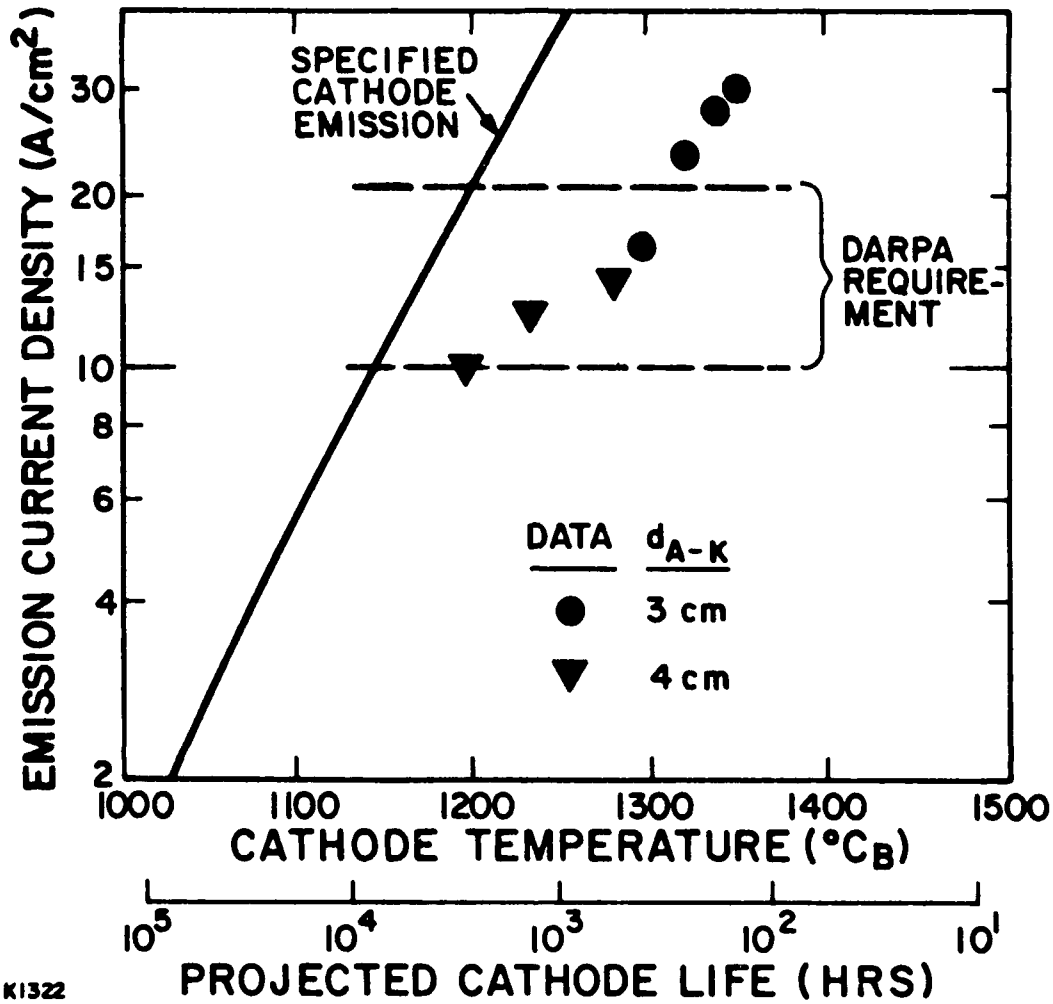

Figure IV-25 Thermionic Dispenser Cathode Emission Characteristics, Measured and Projected.

By plotting the quantity J/T^2 versus T^{-1} on a log-linear plot, the slope of the line yields the work function while the intercept should give the constant, A. In practice, however, the experimental value of A is far lower than calculated and can be interpreted as a figure of merit related to the effective area which has been successfully activated. To illustrate these concepts, the plot of Figure IV-26 is based on the data given in Figure IV-22a. The current is corrected to the zero field condition by the Schottky relation,

$$J = J_o \exp\left(0.44\ E^{1/2}/T(^oK)\right)$$

where

J = measured current density

J_o = zero field current density

E = electric field (vacuum) in volts/meter

The slope of the line gives a value for the work function of $\phi \cong 1.61$ which is in agreement with earlier measurements.[3] The intercept, however, yields $A \approx 5 \times 10^{-2}$ $[A/cm^2(^oK)^2]$. This discrepancy would indicate that there are emission sites with the correct barium-oxygen-tungsten configuration, i.e., correct work function; however, that also the effective area of these emission sites is a small fraction of the cathode area.

It is true, however, that the projected performance[2] shown in Figure IV-25 does not correspond to full area activation. The values of ϕ and A for this cathode (53280 on tungsten cathode) is 1.67 eV and 2.6 $A/cm^2/(^oK)^2$, respectively. The work function is in good agreement, however, the effective area is still ~ 50 times lower than expected for full surface activation.

1. Spatial Uniformity

The spatial uniformity of the cathode current was monitored by open shutter photographs (single-pulse mode) of the e-beam induced fluorescence from a polystyrene target placed against the

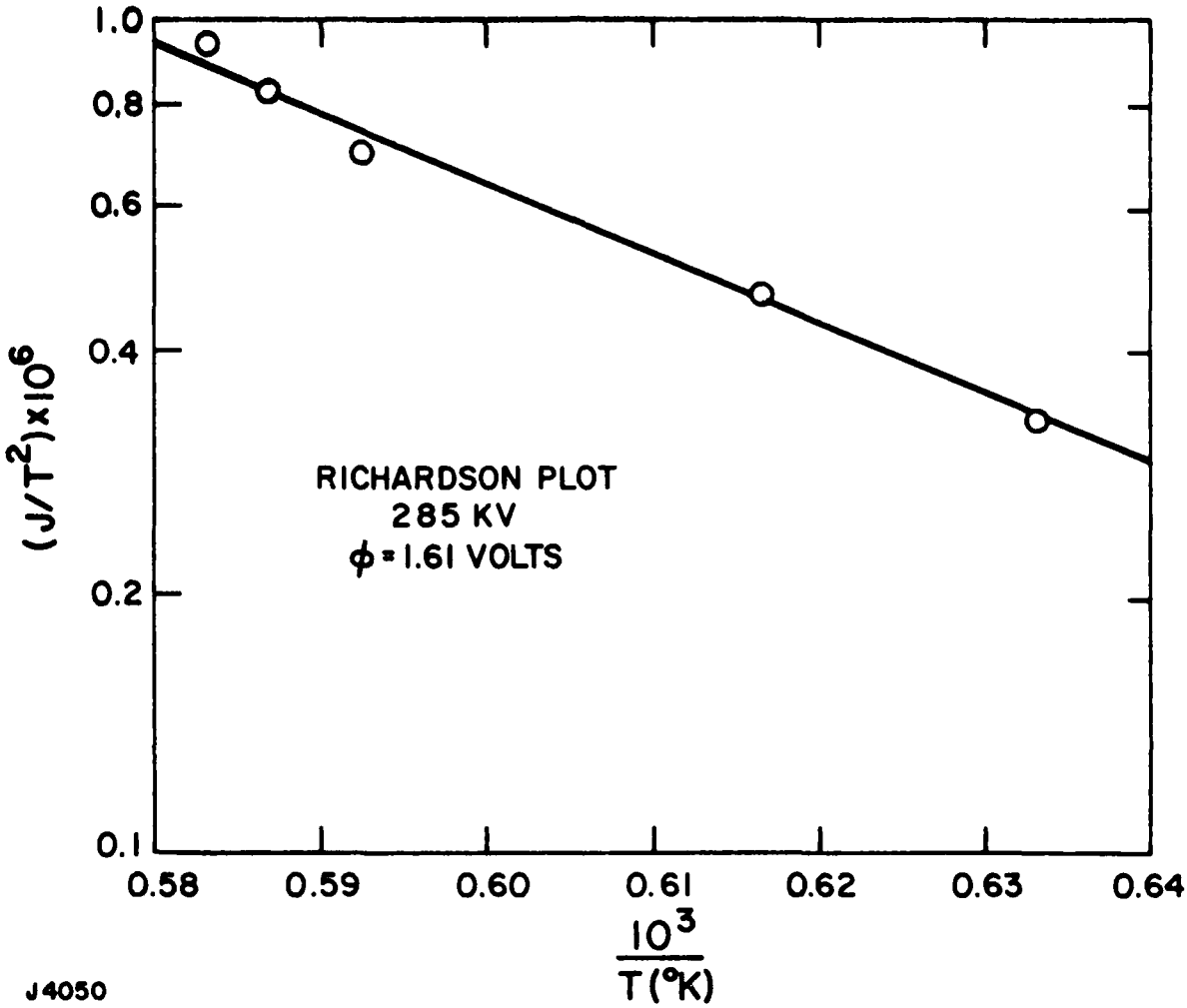

Figure IV-26 Richardson Plot for the Dispenser Cathode

metallic foil. A photograph of the fluorescence and densitometer traces parallel and perpendicular to the foil support ribs are shown in Figures IV-27 and IV-28. The corresponding data in the presence of an externally applied guide magnetic field are shown in Figures IV-29 and IV-28, respectively. Figure IV-27 shows that without the magnetic field, the beam spreads laterally so that the fluorescent image is wider than the 10 cm cathode dimension. The opposite is true with the magnetic field applied, as shown by Figure IV-29 where the 1:1 image of the cathode indicates that the effective emitting area of the cathode is $\sim 70\ cm^2$. This is also evident from the densitometer traces in Figure IV-28, and reflects the measured $\sim 75^oC$ temperature gradient across the cathode surface due to edge radiation and heat conduction through the molybdenum supports. Another feature of the magnetically immersed cathode evident in Figures IV-27 and IV-28 is the enhancement of current at the beam edges and dip in the center, which can be attributed to beam space charge effects.

Also evident from the densitometer traces (e.g., Figure IV-28) that the total emission from the cathode is decreased as a result of a guide field in excess of ~ 400 G. A possible explanation for this suppression of current is linked with the incomplete activation of the dispenser cathode surface in the following manner. If the emission is originating from discrete sites rather than from a truly board area, the geometrical nature of the emission would change as a function of the guide magnetic field. For a discrete emission site, the zero field geometry would be that of a three-dimensional expansion whereas under high guide fields the emission is forced to be one-dimensional due to collimation of the current. Under space charge limited conditions, the one-dimensional current is smaller than that for three dimensions since for three-dimensional spreading, the retarding effect of the space charge cloud is diminished. This effect should decrease as the degree of surface activation is increased.

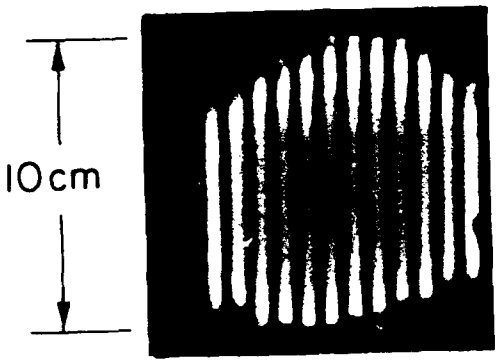

Figure IV-27 Fluorescence From Dispenser Cathode Emission Without Guide Magnetic Field (B=0).

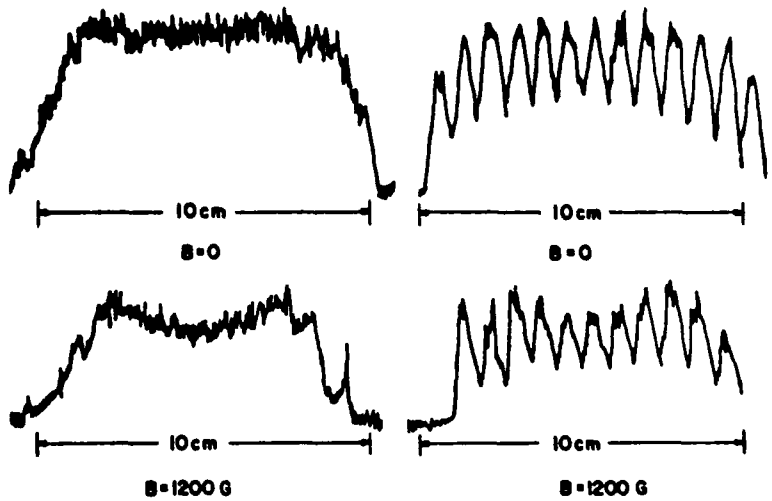

Figure IV-28 Densitometer Traces at Dispenser Cathode Emission. Centerline Profiles Perpendicular and Parallel to Foil Support With and Without B-field.

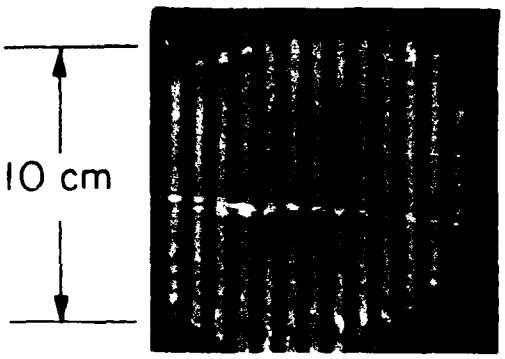

J5612

Figure IV-29 Fluorescence from Dispenser Cathode Emission in a Guide Magnetic Field (B = 800 G).

2. Repped Testing

The 100 cm^2 area thermionic cathode was repetitively-pulsed to determine the pulse-to-pulse stability, lifetime, average power capabilities, as well as to test foil cooling concepts. A table of parameters showing the range of operating conditions as well as the parameters of a long duration test series ("concurrent" column) is presented in Figure IV-30. In this repped series, total cathode currents of 100-2200 A corresponding to current densities of up to ~ 30 A/cm^2 were achieved at voltages of up to 300 kV. Pulse repetition rates of up to 25 Hz were used and pulse burst durations of up to 1100 pulses were achieved. In the long duration run, the current density was ~ 10 A/cm^2 at a voltage of 215 kV (dictated by pulser reliability) across an anode-cathode spacing of 4 cm. The pulse duration was 0.8 μsec at a repetition rate of 25 Hz. Several long duration runs of ~ 1000 pulses each were made in rapid succession with no degradation seen in the cathode current.

Two sets of oscillograms illustrate the stability and repeatability of the dispenser cathode. In Figure IV-31, the voltage and current waveforms for 100 shot bursts are shown with and without the clipper gap in operation. In Figure IV-32, the waveforms of a 1000 shot burst are overlayed showing the excellent pulse-to-pulse reproducibility. Not visible in this photograph are the line pulser prefires which are observed visually on the oscilloscope in real-time and were counted to be ~ 1% of the total. The limitation of ~ 1000 pulse burst is not caused by the cathode but rather by the pulser. At about 1000 pulses, a prefire or other fault would trip the protective circuitry causing the pulser to shut down. The pulser was started as fast as possible, usually within a minute and another long burst was run. In subsequent tests, the anode-cathode spacing was reduced to 3 cm and higher current densities were achieved by raising the cathode temperature as well as the anode-cathode voltage. At the maximum current density of 30 A/cm^2, the pulser was run for short bursts of 10 pulses at 25 Hz with no degradation in current, however, pulser unreliability made longer duration testing difficult.

PARAMETER	RANGE	CONCURRENT
• PULSE VOLTAGE	100 – 300 kV	215 kV
• PULSE CURRENT	100 – 2200 A	725 A
• PULSE DURATION	0.8 – 1.0 μs	0.8 μs
• REP. RATE	10 – 25 Hz	25 Hz
• PULSES / BURST	5 – 1100	1100

J5664

Figure IV-30 Test Conditions for Repped, Large Area Dispenser Cathode.

80 kV/DIV

0.5 μ SEC/DIV

370 A/DIV

(A)

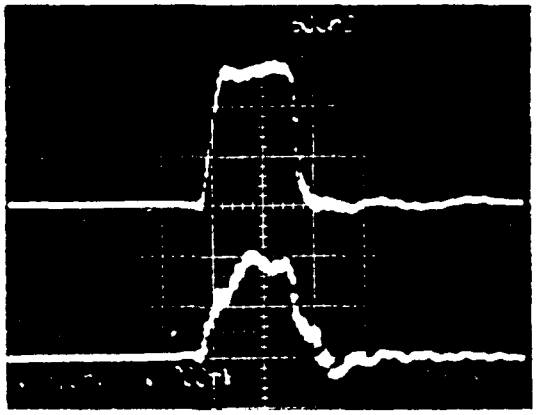

100 SHOTS, 25 Hz
215 kV

80 kV/DIV

0.5 μ SEC/DIV

370 A/DIV

(B)

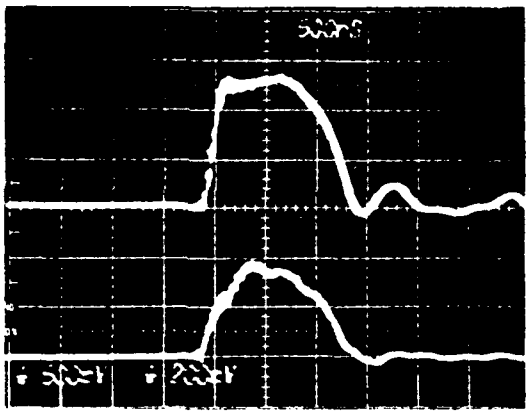

100 SHOTS, 25 Hz
215 kV

J9761

Figure IV-31 Voltage and Current Waveforms of a Dispenser Cathode a) With and b) Without a Clipper Gap (100 Shot Overlay).

CLIPPER GAP

80 kV/DIV

1 μSEC/DIV

250 A/DIV

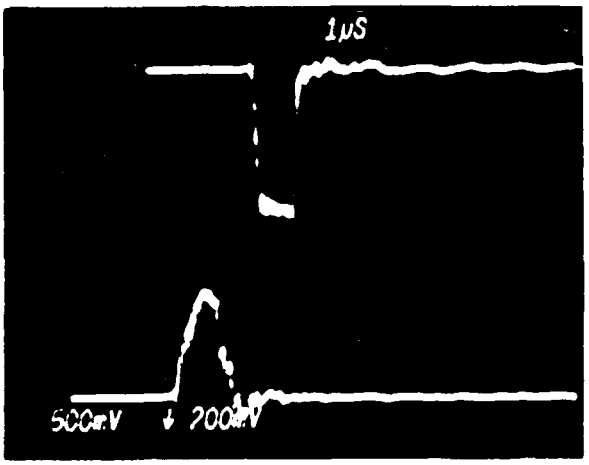

1000 SHOTS, 25 Hz
215 kV, 1390°C

J5625

Figure IV-32 Voltage and Current Waveforms of a 1000 Shot Overlay

In summary, repped operation for long duration bursts has been demonstrated at an emission of ~ 10 A/cm^2, 215 kV, and 25 Hz. The pulse-to-pulse reproducibility is excellent and no long term degradation was seen after ~ 5000 pulses. The vacuum level during the long duration bursts was stable at ~ 3 x 10^{-6} torr.

3. Outgassing

An important operating parameter which bears directly on the pumping requirements for scaled repped systems is the outgassing rate. In a full scale system, a high outgassing rate will require large pumps to maintain proper operating pressure. Carbon felt cathodes have been observed to produce outgassing of ~ 10 molecules/electron and at that rate, an ~ 1000 cm^2 diode system was limited to burst durations of ~ 100 pulses.[4] With the 100 cm^2 dispenser cathode, the steady pressure level observed during the long duration burst correspond to an outgassing rate of ~ 1 molecule/electron. This rate is compared to that which would be required for a practical large-scale system in Figure IV-33. A reduction of three orders of magnitude in the outgassing rate is needed for large-scale operation and this requirement may be the most compelling reason for a bakeable, high vacuum system.

F. FOIL TESTING

The deposition of any metallic layer on titanium foils is complicated by the reactive nature of titanium. A tenacious oxide layers quickly forms which prevents a good bond between the layers in all but very thin coatings. Coating thickness of up to 5 μm of copper have been obtained on 25 μm titanium foils but their adhesion under stress is poor for thicknesses over ~ 1 μm and the thermal quality of the contact is questionable, see Figure III-26. Other metallic layers, e.g., aluminum, may be used to improve the heat conductivity of titanium but the surface quality is uneven and a good vacuum seal would be difficult. An example of the rough quality of these aluminum cladded is shown by the cross-

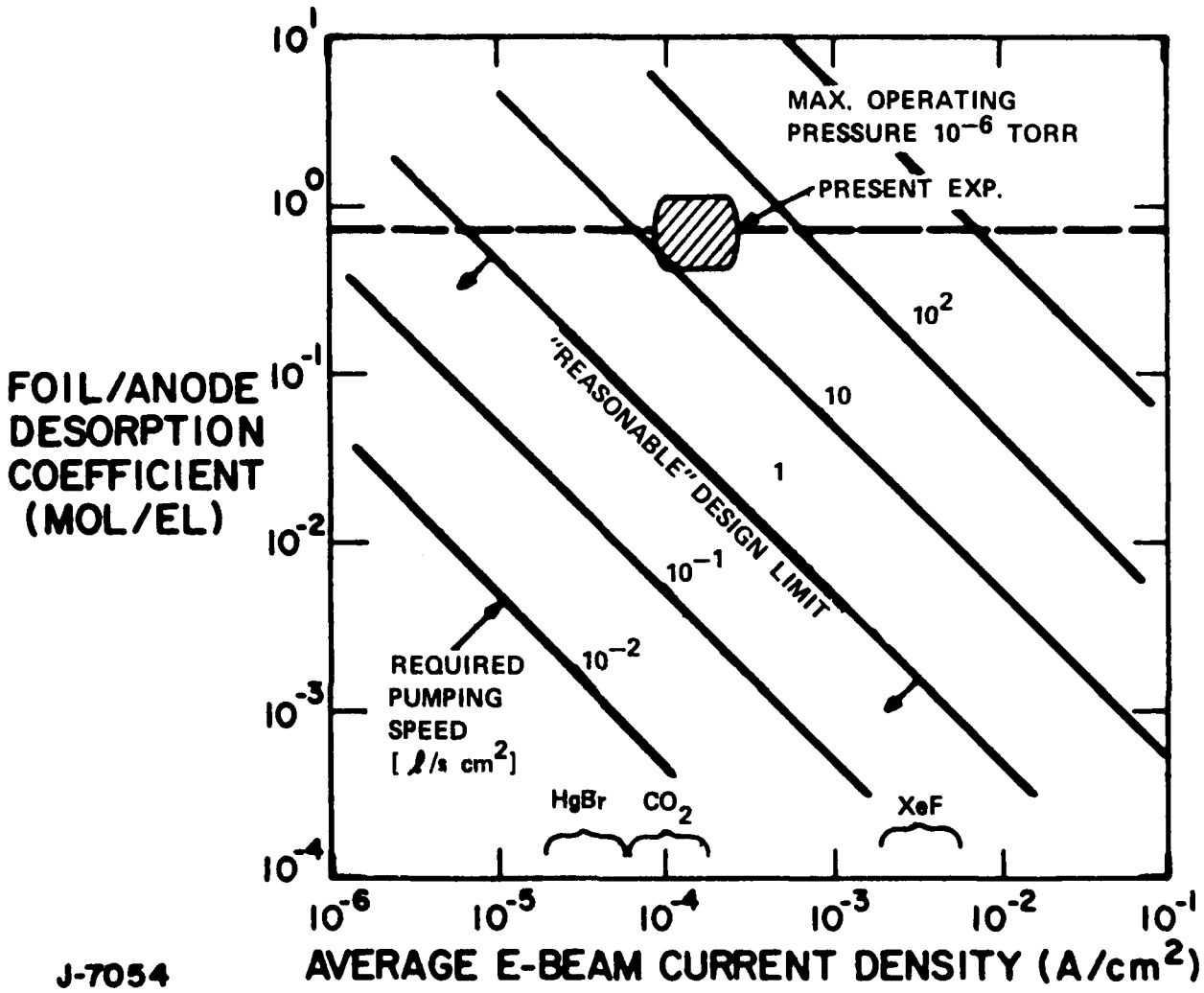

Figure IV-33 Outgassing Constraints for Large-Scale Dispenser Cathodes.

sectional photographs of these foils in Figure III-26. Another reason for rejecting aluminum as a cladding material is its incompatibility with dispenser cathodes, although it could be applied on the high-pressure side of the foil.

Incompatibility with dispenser cathodes is also the reason that pure titanium foils cannot be used on the vacuum side as evidenced by the drop in emission observed under repped conditions. (See Figure IV-34.) The exact nature of the poisoning mechanism is not known. For example, the current shows no degradation for single or a few pulse bursts. For bursts of 10 Hz or more, the current drops after a few pulses. No sharp rise in vacuum level is observed as compared to the pure copper foil case and the first few pulses of subsequent bursts do recover to the original level. Analysis of the outgassing products during the pulse burst is complicated by the high electrical noise level; however, it should be possible to capture some of the gas products and analyze a sample immediately following a run. Titanium is known to absorb oxygen and a gas analysis should differentiate between outgassing and other mechanisms such as ion bombardment.

The deleterious effects of pure titanium foil were cured by coating the foil with a very thin copper flash, 0.5 μm thick. At this thickness, the coating can be well bonded to the titanium and also improves the heat conductivity, albeit only by a factor of two.

At higher e-beam fluences, the foils overheats and the copper cladding fails by melting and flaking. This situation was demonstrated by removing the trigger signal to the clipper gap and, hence, increasing the power deposition in the foil by almost 40%. With the high e-beam fluences, the foil temperature rises and the copper layer degrades and exposing titanium which poisons the cathode. This conclusion is further borne out by the observations that the pressure during the burst with no clipper present is $\sim 4.2 \times 10^{-6}$ torr as compared to $\sim 3.5 \times 10^{-6}$ torr with the

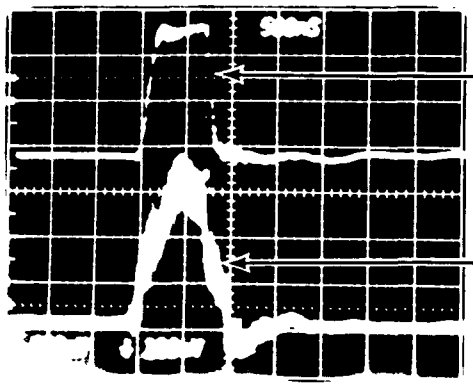

CATHODE TEMPERATURE – 1390°C

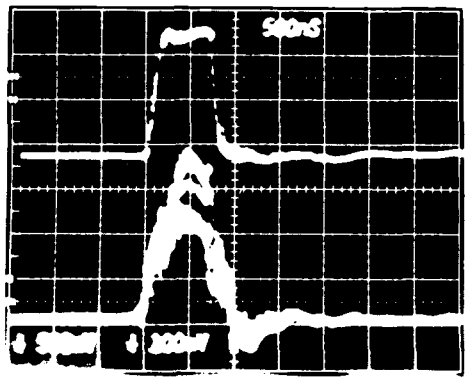

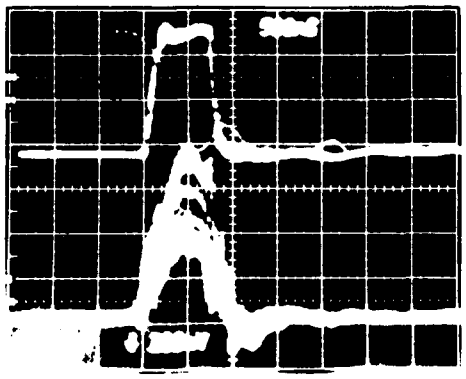

J6012

Figure IV-34 Poisoning by Pure Titanium Foils

shortened pulse. After these runs, the foil runs was removed and significant burning and degradation of the copper layer was observed. The photograph of Figure IV-35 shows the copper clad side of the titanium foil and the lifted portions of the copper cladding. The average e-beam current corresponds to a power dissipation in the foil of ~ 30 W/cm^2 which raises the foil temperature to near the melting point of copper. The relationship between cladding, average power dissipated in the foil and cathode emission needs further investigation.

G. GAS POISONING TESTS

The poisoning tests were conducted in several stages. The first test was the (accidental) exposure of the large area dispenser cathode at an operating temperature of 1230°C and emission density of 10 A/cm^2 to a mixture of argon and air. This situation occurred as a result of the failure of the pure copper foil under repped conditions. After reactivation which consisted of a prolonged heating cycle (4-5 hr) at a temperature in excess of the operating temperature, the full emission current was obtained at the original voltage and cathode temperature.

The second poisoning test was the exposure of both heated and unheated dispenser cathodes to a 50/50 mix of N_2/CO_2 at one atmosphere to simulate an ABEL-type laser mix. For these tests, the cathode was operated at a baseline level of 7 A/cm^2 at 160 kV (3 cm anode-cathode spacing) in a single-pulse mode. The cathode temperature for this baseline condition was ~ 1230°C. The cathode was first exposed to the laser gas mix in the unheated state and then repumped and reactivated by the normal procedure. The cathode emission was restored to its prepoisoned operating condition, i.e., at the same voltage and cathode temperature.

The cathode was then exposed to the laser gas mix while hot (1230°C). The chamber was repumped and the cathode reactivated in the usual manner with the current density restored to about 70% of its original value. Full current could then be achieved by

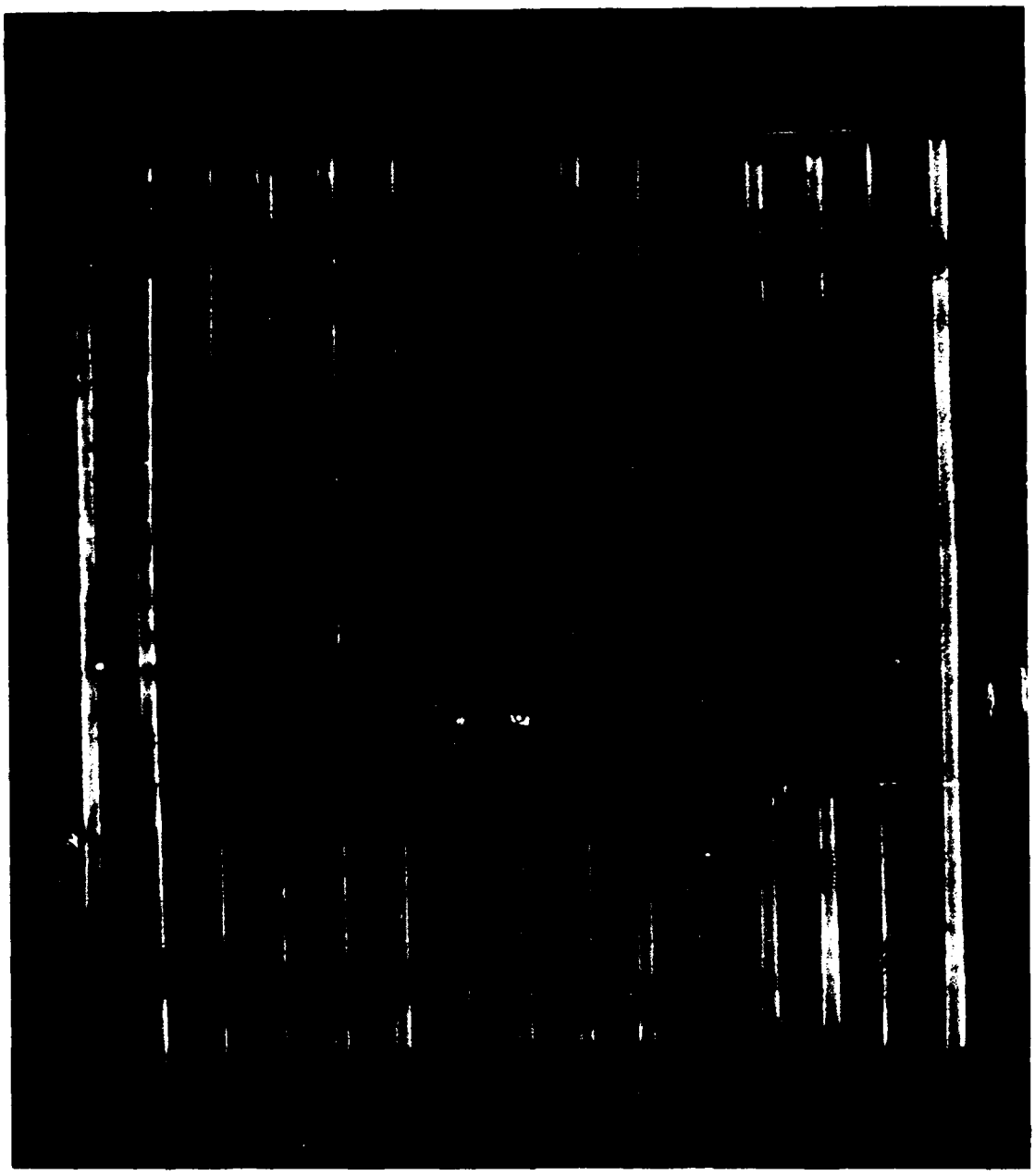

K1321

Figure IV-35 25 μm Titanium Foil Clad with 0.5 μm Thick Copper Operated up to 30 W/cm^2.

operation at higher voltage (at 1230°C) or at the same voltage at higher temperatures (~ 1330°C). After prolonged operation at the higher temperature and a longer pumping time, the chamber pressure stabilized to its initial level and full current operation was restored at the baseline voltage and cathode temperature conditions.

The final poisoning test in the series was the exposure of both heated and unheated cathodes to a simulated laser mix of 0.5% NF_3 and the remainder argon. Since all the noble gases are known not to be deleterious to dispenser cathode operation, the diluent was kept to argon rather than neon, xenon, krypton or helium. After exposing the unheated cathode to the gas mix (at one atmosphere) the chamber was repumped and the cathode reactivated in the normal manner. Full current emission was restored at the baseline conditions. After the heated cathode was exposed to the (one atmosphere) HN_3, Ar mixture, repumped and reactivated in the usual manner, the current level was restored to ~ 60% of the original baseline condition. Higher temperature operation and/or higher voltage did restore the cathode to ~ 95% of its original value and again, prolonged operation at the higher temperature in conjunction with pumping did restore the cathode emission to ~ 90% of original value at baseline conditions.

The poisoning tests have shown that dispenser cathodes can survive exposure to laser gases, especially those containing NF_3 and still retain the ability to be reactivated. Further tests are needed to explore the full degree of resistance to poisoning.

SECTION IV

REFERENCES

1. Dobrestov, L.N and Gomoyunova, M.V., Emission Electronics Israel Program for Scientific Translations, 1971, p 194.

2. Spectra-Mate, Inc., Watsonville, CA.

3. Beck, H.W., Inst. El. Eng., 106B, July 1959, p 393.

4. Shannon, J., Maxwell Labs, Inc., presentation at the DARPA Eximer Laser Technology Review Meeting, Naval Research Laboratory, 1-2 July, 1980.

DISTRIBUTION LIST

Director Defense Advanced Research Projects Agency, 1400 Wilson Boulevard, Arlington, VA 22209, Attn: Directed Energy Office
Lt. Col. Benedict (1 copy)

Director, OUSDRE (R & AT), The Pentagon, Washington, DC 20301, Attn: Directed Energy Office (1 copy)

Commander, Headquarters AFSC (DLCAM), Andrews AFB, Washington, DC 20334, Attn: Capt. T. J. Dyble (1 copy)

Commander, AF Wright Aeronautical Laboratories, Aero Propulsion Laboratory, Wright-Patterson AFB, OH 45433, Attn: POOC-3
Dr. A. Garscadden
(1 copy)

Commander, Air Force Weapons Lab, Kirtland AFB, New Mexico 87117, Attn: AR Colonel John G. Rich (1 copy)
AL Dr. L.A. Schlie, and Lt. Col. T. Meyer (1 copy)

Commander, US Army Missile Command, Redstone Arsenal, AL 35889, Attn: DRSMI-RH Colonel W.R. De Leuil (1 copy)
DRSMI-ROC Mr. Charles Cason (1 copy)
DRSMI-RHST Dr. T. G. Miller (1 copy)
DRSMI-RHSS Dr. G. Dezenberg (1 copy)
DRSMI-RHE Mr. Myron Cole (1 copy)
DRSMI-RAS Dr. F. Haak (1 copy)
DRSMI-RRD Dr. H. Howgate (1 copy)

Commander, Ballistic Missile Defense Advanced Technology Center, P.O. Box 1500, Huntsville, AL 35807, Attn: BMD ATC-O
Mr. M. Lavan (1 copy)

Commander, Airforce Space Division, P.O. Box 92960, Worldway Postal Center, Los Angeles, CA 90009, Attn: YND (1 copy)
Colonel H. A. Shelton

Commander, US Army Electronics and Devices Lab, Fort Monmouth, NJ 07703, Attn: DELET-BG Mr. W. Wright (1 copy)

Director, Central Intelligence Agency, Washington, DC 20505, Attn: Mr. Greg Bock (1 copy)

Director, Defense Intelligence Agency, Washington, DC 20301, Attn: Mr. Seymour Berler (1 copy)

Director, Department of Energy, Washington, DC 20545, Attn: Dr. G. Canavan, OIF (1 copy)

Commander, Naval Reserach Laboratory, Washington, DC 20375, Attn: Code 112 Dr. N. Djeu (1 copy)
Dr. S Searles (1 copy)

Commander, Office of Naval Research, 1030 E. Green Street, Pasadena, CA 91106, Attn: Code 402 Dr. R. Behringer (1 copy)

Commander, Naval Sea Systems Command, Department of the Navy, Washington, DC 20362, Attn: PMS-405 Capt. A. Skolnick (1 copy)

Commander, Naval Ocean Systems Center, 271 Catalina Boulevard, San Diego, CA 92152, Attn: Code 8105 L. Stotts (1 copy)

Aerospace Corporation, P.O. Box 92957, Los Angeles, CA, Attn: Dr. R. Hoffland (1 copy)

Avco Everett Research Laboratories, 2385 Revere Beach Parkway, Everett, MA 02149, Attn: Dr. J. Daugherty (1 copy)

Hughes Aircraft Company, Centinela [illegible] Teale Streets, Culver City, CA 90230, Attn: R. Hill (1 copy)

The Boeing Company, P.O. Box 3999, M. S. 8C16, Seattle, WA 98124, Attn: M. Weisbach (1 copy)

GTE Sylvania, Inc., Electronic Systems Group - Western Division, Mountain View, CA 92042, Attn: Dr. L. Braverman (1 copy)

Lawrence Livermore National Laboratory, P.O. Box 5508, Livermore, CA 94550, Attn: Code L470 Dr. J.R. Murray (1 copy)
Dr. L. Pleasance (1 copy)

Los Alamos Scientific Laboratory, P.O. Box 1663, Los Alamos, New Mexico 87545, Attn: Dr. Charles Brau (1 copy)

Mathematical Sciences Northwest, Inc., P.O. Box 1887, Bellevue, WA 98009, Attn: Dr. Peter H. Rose (1 copy)

Maxwell Laboratories, Inc., 8835 Balboa Avenue, San Diego, CA 92123, Attn: Dr. A Kolb (1 copy)

Physics International Company, 2700 Merced Street, San Leandro, CA 94577, Attn: Dr. M. Kolpin (1 copy)

Poseidon Research, 11777 San Vincente Boulevard, Los Angeles, CA 90049, Attn: Dr. S. Crow (1 copy)

Rockwell International, Rocketdyne Division, 6633 Canoga Avenue, Canoga Park, CA 91304, Attn: Mr. R. Siegler (1 copy)

Northrop Corporation, Research and Technology Center, One Research Park, Palos Verdes Peninsula, CA 90274, Attn: Dr. M. Baumik
(1 copy)

Riverside Research Institute, 1701 North Fort Meyer Driver, Arlington, VA 22209, Attn: Space Laser Library (1 copy)

Sandia Laboratories, P.O. Box 5800, Albuquerque, New Mexico 87115, Attn: J. Gerado, (1 copy)

W.J. Schafer Associates, Inc., 607 N Avenue, Door 14, Wakefield, MA 01880, Attn: Dr. J. Reilly (1 copy)

W.J. Schafer Associates, Inc., 1901 North Fort Myer Drive, Suite 803, Washington, DC 20036, Attn: Dr. J. Hammond (1 copy)

Stanford Research Institute, Menlo Park, CA 94025, Attn: Dr. D. Huestis (1 copy)

TRW Defense and Space Systems Group, 2030 M Street NW, Suite 800, Washington, DC 20036, Attn: R. Foster (1 copy)

TRW Defense and Space Systems Group, One Space Park, Building R1, Room 1032, Redondo Beach, CA 92078, Attn: Dr. J. Schwartz
(1 copy)

United Technologies Research Center, 400 Main Street, East Hartford, CT 06108, Attn: Dr. W. Brown (1 copy)

Western Reserach Corporation, 8616 Commerce Avenue, San Diego, CA 92121, Attn: R. Hunter (1 copy)

R&D Associates, 6400 Uptown Boulevard, NE, Albuquerque, New Mexico 87110, Attn: Dr. J. Colbert (1 copy)

Los Alamos National Laboratory, P.O. Box 1663, Los Alamos, New Mexico 87544, Attn: Dr. C. Fenstermacher (MS 527) (1 copy)